

Computational Analysis and Methods for Electromagnetic Exposure Limits, Antenna Optimization and Cell Phone Design

THÈSE N° 5984 (2013)

PRÉSENTÉE LE 30 OCTOBRE 2013

À LA FACULTÉ DES SCIENCES ET TECHNIQUES DE L'INGÉNIEUR
LABORATOIRE D'ÉLECTROMAGNÉTISME ET ACOUSTIQUE
PROGRAMME DOCTORAL EN GÉNIE ÉLECTRIQUE

ÉCOLE POLYTECHNIQUE FÉDÉRALE DE LAUSANNE

POUR L'OBTENTION DU GRADE DE DOCTEUR ÈS SCIENCES

PAR

Chen XI LIN

acceptée sur proposition du jury:

Prof. P. Vandergheynst, président du jury
Prof. J. R. Mosig, Dr N. Chavannes, directeurs de thèse
Prof. M. Okoniewski, rapporteur
Prof. M. Popovich, rapporteur
Prof. F. Rachidi-Haeri, rapporteur



ÉCOLE POLYTECHNIQUE
FÉDÉRALE DE LAUSANNE

Suisse
2013

我喜欢的哲理名言

~ 庄周梦蝶~

昔者庄周梦为胡蝶

栩栩然胡蝶也

不知周也

俄然觉

则蘧蘧然周也

不知周之梦为胡蝶与

胡蝶之梦为周与

出自庄子齐物论

首先要感谢我的父母，陈光和胡友安，一路走来你们的教育，照顾和关爱是我能完成学业的动力。感谢我的太太卢燕，为了让我走完博士学业这条路，辛苦老婆了！谢谢你给予我的爱和支持。给我刚出世的女儿妍心，我们的世界因你而更加精彩！我仅此把这篇论文献给我可爱的家人们！

陈希临

苏黎世, 二零一三年六月

Acknowledgements

The very first person, to whom I would like to express my sincerest gratitude, is my thesis co-supervisor Dr. Nicolas Chavannes. He has been a true mentor and a dear friend during my doctoral study. This thesis will not be possible without his invaluable support. Many thanks to my thesis co-supervisor Prof. Dr. Juan Mosig for accepting me as his Ph.D student and assisting me patiently with many research and administrative issues. I would also like to especially thank Prof. Dr. Niels Kuster for reviewing my publications and providing me with invaluable comments and suggestions. Sincere gratitude goes to Dr. Roger Tay for been a valuable mentor throughout my earlier career in Motorola and my current doctoral study. I would also like to take this opportunity to thank my thesis internal examiner Prof. Dr. Farhad Rachidi and external examiners Prof. Dr. Michal Okoniewski and Prof. Dr. Milica Popovich for their much appreciated involvements in my thesis review and defence.

There are many friends, co-workers and fellow students I would like to thank for their help, advice and friendships during my stay in Zurich and Lausanne. I enjoy your accompanies very much. In SPEAG and IT'IS, I would like to thank Dr. Stefan Benkler, Dr. Stefan Schild, Dr. Elaine Barretto, Dr. Pedro Crespo-Valero, Dr. Esra Neufeld, Dr. Valerio De Santis, Dr. Erdem Ofli, Dr. Can Akgun, Dr. Guillermo Del Castillo, Dr. Eugenia Cabot, Dr. Tomas Stefanski, Dr. Andreas Christ, Dr. Mark Douglass, Maria del Mar Miñana Maiques, Emilio Cherubini, Peter Futter, Maximilian Futterer, Yijian Gong, Adamos Kyriakou, Johanna Wolf, David Adekayode, Dr. Chung-Huan Li, XiaoWei Liao, Manuel Murbach, Jane Roth, Marie-Christine Gosselin, Yvonne Maeder, Jacqueline Pieper and Martin Daellenbach. In LEMA, I would like to thank Prof. Dr. Anja Skrivervik, Dr. Michael Mattes, Dr. Eden Sorolla, Jean-François Zurcher, Ioannis Koufogiannis, Jovanche Trajkovikj and Apostolos Sounas. In Singapore, my gratitude goes to Tan Yu Chee, who has been my mentor and friend for many years, for helping me with questions regarding antenna fixture and measurements. Special blessing goes to Dr. Jurriaan Bakker and Dr. A.E. Umenei for the valuable collaborations and fruitful research results generated from the joint projects. To all the people who have helped me in one way or another during my doctoral study, but due to space limitation can not be included in this acknowledgement, thank you!

Zurich, June 2013

X.L. Chen

Abstract

In recent years, the advancements of wireless technologies have led to rapid developments in the field of telecommunication, power delivery and bio-medical applications. During the evolution of a wireless technology, the electromagnetic compatibility (EMC) between a radiating source (e.g., an antenna) and nearby active or passive elements (e.g., a closely integrated electronic component or a human body) often introduces challenging design requirements.

This thesis focuses on the applications of state-of-the-art computational electromagnetic compatibility (CEMC) techniques in multidisciplinary engineering design tasks, with an emphasis on computational bio-electromagnetic compatibility (CBEMC). The analyses reported in this thesis span practical applications from power frequency (Hz) to radio frequency (GHz), providing research outcomes which significantly benefit the understandings of low-frequency human body exposure safety and radio-frequency antenna integration and optimization. The research aspect of the thesis is initiated with a thorough review of the existing low-frequency exposure safety guidelines recommended by international regulatory committees. The subsequent analyses suggest essential scientific basis for the update and revision of the existing exposure limits. Practical exposure scenarios (e.g., magnetic resonant wireless power transfer) are investigated with novel assessment techniques. Subsequently, a computer-aided optimization scheme based on network-distributed genetic algorithms is applied to highly detailed numerical mobile phone model and human body phantoms. The investigated optimization technique is proven to be superior than traditional empirical approaches. Finally, the CEMC techniques are applied in the context of non-dosimetry related engineering design environment by investigating the integration of a miniature loudspeaker (acoustic component) and a mobile device antenna (radio frequency component). Based on simulation and measurement data, the coupling mechanisms are determined to establish the fundamental design guidelines for optimum antenna-speaker co-existence and performance.

In summary, this thesis details several novel applications of CEMC in the most stringent and complex industrial design environments. The presented research findings serve as indispensable basis for future research oriented towards the exposure-compliant and electromagnetic-compatible designs for novel wireless technologies.

Abstract

Keywords: low frequency exposure, wireless power transfer, magnetic induction, high-voltage detector, exposure limit, specific absorption rate, quasi-static approximation, antenna optimization, genetic algorithms, speaker integration, coupling, radiation loss.

Résumé

Ces dernières années, l'évolution des technologies sans fil ont permis des développements rapides dans les domaines des télécommunications, transmission de puissance et applications en biomédecine. En cette évolution, la compatibilité électromagnétique (EMC, par son acronyme en anglais) entre une source de rayonnement (par exemple, une antenne) et un élément passif ou actif (par exemple, un composant électronique intégré ou le corps humain) introduit souvent des exigences de conception difficiles.

Cette thèse se centre sur l'applications de techniques de compatibilité électromagnétique computationnelle avancées (CEMC en anglais) dans des tâches d'ingénierie multidisciplinaires, avec une emphase sur la compatibilité bio-électromagnétique computationnelle (CBEMC en anglais). Les analyses présentées dans cette thèse couvrent des applications pratiques allant des fréquences typiques du réseau électrique (quelques Hz) aux hyperfréquences (GHz) et mènent à des résultats qui bénéficieront de manière significative la compréhension de la sûreté de l'exposition de basse fréquence sur le corps humain et l'intégration de l'antenne radiofréquence. La thèse commence par une révision compréhensive des consignes de sécurité d'exposition aux basses fréquences recommandées par les comités de réglementation internationaux. L'analyse subséquente suggère une base scientifique pour mettre à jour et réviser les limites d'exposition existantes. Scénarios d'exposition pratiques (par exemple, le transfert d'énergie sans fil par résonance magnétique) sont étudiés avec les nouvelles techniques d'évaluation. Par la suite, un schéma d'optimisation assisté par ordinateur et basé sur des algorithmes génétiques distribués en réseau est appliqué à un modèle de téléphone mobile numérique très détaillée, qui incorpore des "human body phantoms". La technique d'optimisation s'est avérée supérieure aux approches empiriques traditionnelles. Enfin, les techniques CEMC sont appliquées dans des contextes de d'ingénierie non liés à la dosimétrie en étudiant l'intégration d'un haut-parleur miniature (composant acoustique) e d'une antenne de téléphone mobile (composant radiofréquence). A partir des simulations et des données de mesure, les mécanismes de couplage ont pu être déterminés et ont servi à établir les lignes directrices de conception fondamentale pour optimiser la coexistence entre l'antenne et les haut-parleurs. En résumé, cette thèse détaille plusieurs nouvelles applications de la CEMC dans les environnements les plus rigoureux et complexes du design industriel. Les résultats de recherche présentés servent comme base indispensable pour de futures recherches orientées vers les limites d'exposition conformes et vers les technologies sans fil novatrices et compatibles du point de vue électromagnétique.

Résumé

Mots-Clés: exposition de basse fréquence, transfert d'énergie sans fil, induction magnétique, détecteur de haute tension, limite d'exposition, taux d'absorption spécifique (SAR), approximation quasi-statique, optimisation d'antenne, algorithmes génétiques, intégration de haut-parleur, couplage, perte de rayonnement.

List of Acronyms

AP	Action Potential
BEM	Boundary Element Method
B-Field	Magnetic Field
BR	Basic Restriction
CAD	Computer Aided Design
CBEM	Computational Bio Electromagnetic
CEM	Computational Electromagnetic
CF	Conversion Factor
CL	Compliance Level
CNS	Central Nervous System
CSF	Cerebrospinal Fluid
CT	Computed Tomography
CTIA	Cellular Telecommunications Industry Association
DCS	Digital Cellular Service
E-Field	Electric Field
EQS	Electro Quasi Static
EMC	Electromagnetic Compatibility
EMI	Electromagnetic Interference
FDTD	Finite Difference Time Domain
FICA	Folded Inverted Conformal Antenna

List of Acronyms

FMA	Folded Monopoles Antenna
GA	Genetic Algorithms
GPU	Graphic Processing Unit
GSM	Global System for Mobile Communications
HAC	Hearing Aid Compatibility
IEEE	Institute of Electrical and Electronics Engineers
ICNIRP	International Commission on Non-Ionizing Radiation Protection
LF	Low Frequency
MPE	Maximum Permissible Exposure
MQS	Magneto Quasi Static
MRI	Magnetic Resonance Imaging
OTA	Over the Air
PCS	Personal Communications Service
PIFA	Planar Inverted F Antenna
PNS	Peripheral Nervous System
RL	Reference Level
RF	Radio Frequency
SAM	Specific Anthropomorphic Mannequin
SAR	Specific Absorption Rate
SENN	Spatially Extended Non-linear Node
SPFD	Scalar Potential Finite Difference
SPFE	Scalar Potential Finite Element
TRP	Total Radiated Power
UV	Ultra Violet
WPT	Wireless Power Transfer

List of Figures

1.1	Low frequency exposure scenarios: (a) high-voltage power lines, (b) electronic article surveillance gate, (c) wireless power and (d) transcranial magnetic stimulation.	2
1.2	The numerical modelling of a mobile phone with a head phantom and a posable hand phantom which depicts a realistic device-in-use condition.	4
1.3	(a) A typical antenna-speaker assembly module and (b) miniature speakers to be integrated.	5
2.1	The external E-field, B-field and <i>in situ</i> E-field distributions for (a) vertically aligned E-field and (b) vertically and horizontally aligned B-field, copyright Reilly 1998 pp.346 [70].	11
2.2	The basic restriction levels for the central nervous system (CNS) and peripheral nerve system (PNS), under the general public and occupational exposure conditions, recommended in ICNIRP-2010.	19
2.3	The basic restriction levels for the brain, heart, other tissue and extremities, under the general public and controlled exposure conditions, recommended in IEEE Std. C95.6-2002.	19
2.4	The magnetic flux density reference levels (maximum permissible exposure), under the general public and occupational (controlled environment) exposure conditions, recommended in ICNIRP-2010 and IEEE Std. C95.6-2002.	20
2.5	The electric field reference levels (maximum permissible exposure), under the general public and occupational (controlled environment) exposure conditions, recommended in ICNIRP-2010 and IEEE Std. C95.6-2002.	20
2.6	(a) A B-field meter and (b) a dual-element E-field and B-field meter, copyright Narda Safety Test Solutions GmbH.	26
2.7	A scaled-down human model made of styrofoam cast and filled with saline solution, copyright Kaune and Forsythe 1985 pp.17 [21].	27
2.8	The anatomical models employed in this study, from left to right, Roberta, Dizzie, Duke, Ella and Fats.	28
2.9	The Duke model with (a) detailed skeleton and tissue composition and (b) 2 mm grid resolution voxel slices.	29
2.10	A posable anatomical model manipulated into various postures, copyright IT'IS Foundation, Zurich, Switzerland.	29

List of Figures

2.11	3D Yee cell showing the E- and H-field components in the staggered grid.	34
2.12	The ellipsoidal body employed in the validation study.	39
2.13	The perturbed vertically-polarized external E-field distribution at 100 kHz computed by (a) the SPFE solver and (b) the FDTD solver.	41
2.14	The weighted average values of the relative permittivity and conductivity for an adult male body.	43
2.15	The left-hand-side values of (2.31), (2.32) and (2.33) calculated based on the adult male tissue composition data.	43
2.16	A simplified human body model (based on the dimensions of Duke) with brain, cerebralspinal fluid, spinal cord, heart and body shell represented by rectangular blocks.	44
3.1	The E-field distribution in a sphere with a diameter of (a) 10 cm and (b) 2 cm, exposed to a uniform 50 Hz B-field in the x direction and the peak induced E-field (normalized to the respective analytical value) as a function of grid size.	51
3.2	The induced E-field distribution on the upper left corner of the sphere (with 10 cm diameter) for (a) E_{voxel} , (b) $E_{V,\text{avg}}$ and (c) $E_{L,\text{avg}}$, the E-field values are normalized to the peak induced E_{max} value.	52
3.3	The E-field distribution (on the xz plane, at $y = +5$ cm, $y = 0$ mm at the cubic center) in a $10 \times 10 \times 10$ cm ³ cube with a missing octant exposed to a uniform 50 Hz B-field in the x direction and the peak induced E-field value (normalized to the $E_{V,\text{avg}}$ value at the grid size of 0.05 mm) as a function of grid size.	53
3.4	The peak induced E-field values (normalized to the $E_{V,\text{avg}}$ value at 0.5 mm) in the brain of Duke as a function of grid size due to 50 Hz LAT (side-to-side) uniform B-field exposure.	54
3.5	(a) A canonical head model with a dish layer of thickness d , for a conductivity ratio of $\sigma_1:\sigma_2 = 100:1$, the $E_{V,\text{avg}}$ field distributions in (b) a homogeneous model, (c) $d = 2$ mm and (d) $d = 10$ mm.	57
3.6	The enhancement factor for the peak $E_{V,\text{avg}}$ value in the heterogeneous spherical model due to tissue conductivity contrast and model variation (when compared to the homogeneous sphere case) as a function of conductivity contrast ratio and layer thickness (d).	58
3.7	The ICNIRP-2010 BR levels for the CNS tissues and the peak $E_{V,\text{avg}}$, E_{99} values for (a) general public and (b) occupational exposure, and (c) the IEEE.Std.C95.6-2002 BR levels for the brain and the peak $E_{L,\text{avg}}$ values for general public exposure, in the brain of Duke exposed to a uniform LAT (side-to-side) B-field at the respective reference level.	59
3.8	The compliance levels for the peak induced $E_{V,\text{avg}}$, E_{99} for ICNIRP-2010 and $E_{L,\text{avg}}$ for IEEE Std. C95.6-2002, in the brains of the five anatomical models due to uniform LAT B-field exposure at (a) 50 Hz and (b) 10 Hz for general public exposure.	62

3.9	(a) Tissue conductivity value and (b) conductivity contrast ratio ($\sigma_{CSF} : \sigma_{Tissue}$) with respect to the cerebrospinal fluid (CSF) for selected biological tissues at low frequency.	63
3.10	The sagittal 0.5 mm voxel slice views (at the peak induction location) of Duke and Roberta and the $E_{V,avg}$ field distributions at 50 Hz due to uniform LAT (side-to-side) B-fields.	64
3.11	Skin anatomy and layer structure (copyright 2009 Pearson Education, Inc., publishing as Benjamin Cummings).	66
3.12	(a) A multi-layer skin structure, (b) a single-layer skin structure and (c) an overlapped skin model (note that the skin layer dimensions are not drawn to scale).	67
3.13	The normalized peak induced E-field in the dermis layer as a function of the conductivity (S/m) and thickness (mm) of (a) stratum corneum, (b) cellular epidermis, (c) dermis and (d) hypodermis.	69
3.14	(a) The normalized peak induced E-field in the single-layer skin model as a function of the skin conductivity (S/m) and layer thickness (mm), and (b) a comparison with the peak E-field values (horizontal lines) computed in the dermis of the multi-layer skin model.	71
3.15	The peak E-field induced in Duke due to 0.1 mT 50 Hz uniform front-to-back B-field as a function of grid size with two skin conductivity values, “G” stands for a conductivity of 0.0002 S/m and “M” stands for 0.23 S/m, “Skin” stands for E-field in the skin and “Sat” stands for E-field in the hypodermis.	72
3.16	The ICNIRP-2010 BR levels for the PNS tissue and the peak $E_{V,avg}$, E_{99} values for (a) general public and (b) occupational exposure, and (c) the IEEE.Std.C95.6-2002 BR levels for the extremities and the peak $E_{L,avg}$ values for general public exposure, in the skin of Duke exposed to a uniform AP (front-to-back) B-field at the respective reference level, “G” stands for a skin conductivity of 0.0002 S/m and “M” stands for 0.23 S/m.	73
4.1	Human body models (Duke and Dizzie) with the investigated sites of exposure and system positions (torso and hand) for location sensitivity analysis, the encircled area indicates the region exposed to the WPT system.	78
4.2	The quasi-static approximation validity conditions computed by 2.31, 2.32 and 2.33, based on weighted average tissue dielectric properties and a characteristic length of 335 mm.	81
4.3	The structure of the investigated WPT system (not drawn to scale): (a) L1 to L4 coil positions, (b) top view of the system with B-field measurement line and (c) side view of the system.	82
4.4	The measured and simulated B-field along the central horizontal axis, 9.7 mm above the top of the Rx subsystem.	84
4.5	The peak $E_{V,avg}$ and $E_{L,avg}$ values (V/m) for the Duke model at P2 exposure location as a function of grid size.	84

List of Figures

4.6	The compliance factors for (a) the peak $E_{V,avg}$ (ICNIRP 2010), (b) the peak $E_{L,avg}$ (IEEE C95.1-2005), (c) the peak SAR_{10g} (ICNIRP 1998) and (d) the peak SAR_{1g} (IEEE C95.1-1991).	85
4.7	(a) The E-field distribution in an adult hand due to the exposure to the WPT system operating at 100 kHz with 5 W received power, and (b) the peak E-field values (maximum and mean $\pm 2\sigma_{sd}$) in the torso and hand with respect to the relevant basic restrictions.	87
4.8	The peak rms E-field values normalized to 1 A peak current for the homogeneous phantom at 100 kHz as a function of coil dimension and coil-to-body distance (D), $E_{Analytical}$ is the analytically calculated E-field and $E_{Simulation}$ is the result of the SPFE solver.	88
4.9	The K_E and K_{psSAR} factors at 100 kHz to convert the peak field values in a homogeneous Duke model to values of a heterogeneous Duke model as a function of coil diameter (d) for two coil-to-body distances (D = 5 and 10 mm) at P2.	89
4.10	(a) The normalized source power (W) and (b) the normalized permissible B-field (T) with respect to the basic restrictions ($E_{ind-limit}$, $psSAR_{limit}$) based on the simulation results ($E_{sim.}$ and $psSAR_{sim.}$) and approximation results ($E_{approx.}$ and $psSAR_{approx.}$) of a 150 mm coil at 5 mm coil-to-body distance for the Duke model at P2, the vertical dashed lines indicate the frequencies to achieve the maximum WPT source power and permissible B-field.	91
4.11	The analytically calculated normalized B-field at 200 kHz along: (a) the central vertical axis, (b) the central horizontal axis 0.1 m away from a Tx coil and (c) the central horizontal axis 1 m away from a Tx coil, for Tx coils with radius in the range of 0.5 to 2.5 m.	96
4.12	The Tx coil locations with body positions and orientations: (a) 3D-view, (b) side-view and (c) top-view with labelled body positions (P1 to P9).	97
4.13	The normalized maximum permissible power (W) at the middle vertical level for (a) a ceiling-level Tx coil with a ground-level standing body and (b) a floor-level Tx coil with a lying-down body, as a function of frequency.	101
5.1	The external E-field distribution (a) front view, (b) side view, (c) top view, and (d) the induced E-field ($E_{V,avg}$) distribution, (e) the configuration of ground-to-sole contact.	107
5.2	The ICNIRP-2010 BR levels for the CNS tissues and the peak $E_{V,avg}$, E_{99} values for (a) general public and (b) occupational exposure, and (c) the IEEE Std. C95.6-2002 BR levels for the brain and the peak $E_{L,avg}$ values for general public exposure, in Duke exposed to a uniform vertically polarized E-field at the respective reference level.	110

5.3	The ICNIRP-2010 BR levels for the PNS tissues and the peak $E_{V,avg}$, E_{99} values for (a) general public and (b) occupational exposure, and (c) the IEEE Std. C95.6-2002 BR levels for the extremities and the peak $E_{L,avg}$ values, in Duke (excluding skin) exposed to a uniform vertically polarized E-field at the respective reference level.	111
5.4	(a) The IEEE Std. C95.6-2002 BR levels and the peak $E_{L,avg}$ values for the heart, and (b) the ICNIRP-2010 (occupational), IEEE.Std.C95.6-2002 (controlled environment) threshold limits for contact current and the computed short-circuit current (I_{SC}) in Duke exposed to a uniform vertically polarized E-field at the respective reference level.	112
5.5	The outline of a person operating a voltage detector (left) and a photograph depicting a realistic operation (right), copyright Pfisterer AG.	114
5.6	Three body postures for the simulation of a person operating a voltage detector, from left to right, body posture P_1 , P_2 and P_3	115
5.7	The posable hand grip of the voltage detector handle.	115
5.8	The induced current density distribution for the three investigated body postures, from left to right, body posture P_1 , P_2 and P_3	117
6.1	The mobile phone model employed in this study: the photograph of the actual phone (far left) and the CAD derived model.	122
6.2	The Folded Monopoles Antenna (FMA).	123
6.3	The Planar Inverted F Antenna (PIFA).	124
6.4	The Folded Inverted Conformal Antenna (FICA).	125
6.5	The parametrization configuration for the optimization of the Planar Inverted F Antenna (PIFA) design.	125
6.6	The SAM head phantom cheek placement and a CTIA-compliant hand phantom grip for the investigated mobile phone.	126
6.7	The antenna S_{11} of the optimized antennas in free space.	127
6.8	The band-averaged total radiated power values of the optimized antennas in free space.	128
6.9	The PIFA geometries before and after optimization with the total fitness chart.	128
6.10	The antenna S_{11} of the PIFA design in free space before and after optimization.	129
6.11	The band-averaged total radiated power values of the optimized antennas with SAM head phantom only.	129
6.12	The band-averaged total radiated power values of the optimized antennas with head-and-hand phantom loading.	130
6.13	The antenna S_{11} optimized against head-and-hand phantom frequency detuning for the PIFA design.	130
6.14	The peak 1-gram SAR values normalized to the conducted powers for equal total radiated power under the SAM head phantom loading condition for the GSM900 and DCS1800 bands.	131

List of Figures

6.15	The magnetic field distributions extracted at the frontal (keypad side) phone surface at 849 MHz for the FMA (left), PIFA (center) and FICA (right) under the SAM head phantom loading condition; the red-color squares indicate the SAR hot spot locations.	132
6.16	The HAC electric (upper row) and magnetic (lower row) field distributions at 849 MHz for the FMA (left), PIFA (center) and FICA (right).	133
6.17	The HAC electric (upper row) and magnetic (lower row) field distributions at 1910 MHz for the FMA (left), PIFA (center) and FICA (right).	133
7.1	The basic structure and components of the investigated moving-coil speaker (components are not drawn to scale and plastic frame is not shown).	138
7.2	The equivalent circuit of a single-resonant antenna-speaker assembly, the mutual couplings are classified as free-space and conductive couplings.	140
7.3	(a) A printed circuit board with a center-positioned speaker and an antenna-speaker assembly with (b) a PIFA, (c) a conformal loop antenna and (d) a vertical PIFA, the speaker is conductively-coupled to the PCB ground.	142
7.4	The antenna S_{11} for (a) PIFA with a center-positioned terminal-isolated speaker, and (b) PIFA, (c) loop antenna and (d) vertical PIFA, each with a center-positioned conductively-coupled speaker.	144
7.5	(a) The radiation efficiency of the PIFA with a center-positioned conductively-coupled speaker and (b) the voice coil reactance of the respective speaker.	145
7.6	(a) The radiation efficiency of the vertical PIFA with a center-positioned conductively-coupled speaker and (b) the voice coil reactance of the respective speaker.	145
7.7	(a) The dual-band PIFA antenna with a center-positioned speaker, (b) PIFA antenna S_{11} and (c) antenna radiation efficiency due to a conductively-coupled (grounded) or a capacitively-coupled (floating) speaker.	147
7.8	(a) The dual-band FICA antenna with a center-positioned speaker, (b) FICA antenna S_{11} and (c) antenna radiation efficiency due to a conductively-coupled (grounded) or a capacitively-coupled (floating) speaker.	148
7.9	The RMS E-field distributions of the FICA at 1875 MHz with a center-positioned (a) capacitively-coupled speaker and (b) conductively-coupled speaker, the E-field values are normalized to the peak value in the capacitively-coupled case.	149
7.10	The RMS H-field distributions of the FICA at 1875 MHz with a center-positioned (a) capacitively-coupled speaker and (b) conductively-coupled speaker, the H-field values are normalized to the peak value in the capacitively-coupled case.	149
7.11	(a) The CAD model of a PIFA-speaker assembly for numerical simulation and (b) the corresponding physical model.	150
7.12	The simulation results of (a) PIFA S_{11} , (b) PIFA radiation efficiency, (c) speaker impedance (R for resistance, X for reactance) and (d) PIFA input impedance with a center-positioned terminal-isolated (floating) or conductively-coupled (grounded) speaker.	151

- 7.13 The measurement results of PIFA radiation efficiency with a center-positioned conductively-coupled speaker for (a) low band, (b) high band and with a right-positioned conductively-coupled speaker for (c) low band and (d) high band. . . 153
- 7.14 The measurement results of (a) PIFA S_{11} , (b) PIFA radiation efficiency for the low band, (c) PIFA radiation efficiency for the high band and (d) speaker coil reactance for the high band, with left-located conductively-coupled speakers. . . 154

List of Tables

2.1	Basic restrictions for the human body exposure to low frequency f (Hz) electric and magnetic field in ICNIRP-2010.	16
2.2	Reference levels for the human body exposure to low frequency f (Hz) electric and magnetic field in ICNIRP-2010.	17
2.3	Reference levels for low frequency f (kHz) contact current from conductive objects in ICNIRP-2010.	17
2.4	Basic restriction, E_o (V/m), for the human body exposure to low frequency f (Hz) electric and magnetic field in IEEE Std. C95.6-2002.	18
2.5	Maximum permissible exposure levels for the human body exposure to low frequency f (Hz) electric and magnetic field in IEEE Std. C95.6-2002.	18
2.6	Maximum permissible exposure levels for 0 kHz to 3 kHz induced and contact current for continuous sinusoidal waveforms in IEEE Std. C95.6-2002.	18
2.7	A list of exposure limits at 50 Hz for ICNIRP-2010 and IEEE Std. C95.6-2002.	25
2.8	Dielectric property values of selected human body tissues at 50 Hz.	30
2.9	The peak induced E-field (V/m) at 100 Hz, Δ denotes the difference between the analytical and SPFE solutions in percentage ($\Delta = \frac{ E_{SPFE} - E_{analytical} }{E_{analytical}} \%$).	41
2.10	The tissue composition of adult male and female as a percentage of the total body weight.	43
2.11	The variation of the computed peak induced E-fields of the simplified body model between the SPFE solver and the FDTD solver ($\Delta = \frac{ E_{SPFE} - E_{FDTD} }{E_{FDTD}} \%$).	45
3.1	The conversion factors between a 1 T uniform LAT (side-to-side) B-field and the computed peak induced E-field in the brain of Duke.	61
3.2	The range of the investigated skin layer conductivity values and thickness values, the typical values are shown in the parenthesis.	68
3.3	The conversion factors between a 1 T uniform AP (front-to-back) B-field and the computed peak induced E-field in the skin of Duke when the conductivity value of muscle is applied to the skin layer.	75
4.1	The ICNIRP and IEEE exposure limits relevant for WPT operating between 0.1–10 MHz, f in Hz.	79

List of Tables

4.2 The mean, maximum and standard deviation values of the K_E and K_{psSAR} scaling factors based on the sensitivity analysis of a 150 mm coil placed at 24 locations on the body with 5 and 10 mm coil-to-body distances at 100 kHz. 90

4.3 Compliance factors versus approximations, d is coil diameter and D is coil-to-body distance. 90

4.4 The mean (μ), maximum (max) and standard deviation (σ_{sd}) of the B-field intensity in the center of the room at the middle and quarter levels before the induced E-field exceeds the ICNIRP 2010 and IEEE C95.1-2005 basic restrictions at 200 kHz. 99

4.5 The mean (μ), maximum (max) and standard deviation (σ_{sd}) of the B-field intensity in the center of the room at the middle and quarter levels before the induced SAR exceeds the ICNIRP 1998, IEEE C95.1-1991 and IEEE C95.1-2005 basic restrictions at 6.78 MHz. 100

4.6 The maximum power (W) obtainable by a small ($50 \times 100 \text{ mm}^2$) and large ($200 \times 300 \text{ mm}^2$) Rx coil ($Q = 100$) 1.3 m above the floor tangential to a $5.2 \times 5.2 \text{ m}^2$ Tx coil (a) 2.7 m above the floor (assume floor-bound body), (b) 0.1 m below the floor, at 200 kHz and 6.78 MHz, based on the $\mu \pm 2\sigma_{sd}$ of the calculated maximum permissible B_{Tx} , while maintaining compliance with the ICNIRP and IEEE basic restrictions. 102

5.1 The conversion factors between a 1 kV/m uniform vertically polarized E-field and the computed peak induced E-fields in the brain of Duke. 107

5.2 The conversion factors between a 1 kV/m uniform vertically polarized E-field and the computed peak induced E-fields in the body of Duke (excluding the skin layer). 107

5.3 The conversion factors between a 1 kV/m uniform vertically polarized E-field and (a) the computed peak induced E-field in the heart of Duke and (b) the short-circuit current (I_{SC}) across the ankles of Duke. 108

5.4 The measured resistance of a hand-to-hand configuration for dry skin and large contact areas, with respect to the contact voltage (V) and population percentile (%) at 50 Hz. 116

5.5 The computed body resistance R_b with respect to posture variation, the corresponding peak induced E-field ($E_{V,avg}$) and the short-circuit current (I_{SC}), for R_i of $300 \text{ M}\Omega$ and V_{source} of 110 kV at 50 Hz. 116

6.1 The relative permittivity ϵ_r and conductivity σ (S/m) of the SAM head and hand phantoms. 127

6.2 Computation settings and optimization time requirement. 134

7.1 The conductivity (σ) and relative permittivity (ϵ_r) of the speaker components. . . 139

Contents

Abstract	i
Résumé	iii
List of Acronyms	v
List of Figures	vii
List of Tables	xiii
Table of Contents	xx
1 Introduction	1
1.1 Low Frequency Exposure Dosimetry Assessment	1
1.2 Mobile Device Antenna Optimization with Genetic Algorithms	3
1.3 Analysis and Design of Antenna-Speaker Integration	4
1.4 Outline and Original Contributions	5
2 Review of LF Exposure and Dosimetry Techniques	9
2.1 Introduction	9
2.2 Biological System Interaction with Low Frequency Fields	10
2.2.1 Electric and Magnetic Induction	10
2.2.2 Contact Current Induction	12
2.2.3 Protective Measures against Low Frequency Exposure	12
2.2.4 Biological Effects due to Low Frequency Exposure	13
2.3 ICNIRP-2010 and IEEE Std. C95.6-2002 Exposure Limits	14
2.3.1 Basis of the Exposure Limits	14
2.3.2 Basic Restrictions and Reference Levels	16
2.3.3 Rationales for the Basic Restrictions	18
2.3.4 Spatial Averaging and 99th Percentile	22
2.3.5 Conversion Factors between <i>ex situ</i> and <i>in situ</i> Fields	23
2.3.6 Summary on the ICNIRP and IEEE Exposure Limits	25
2.4 Low Frequency Field Measurement Techniques	26
2.4.1 Free Space Electric and Magnetic Field Measurement	26
2.4.2 Limitations of Induced Field Measurement	27

Contents

2.5	Anatomical Model and Tissue Dielectric Property	28
2.5.1	High-Resolution MRI-based Anatomical Models	28
2.5.2	Posable Anatomical Model	28
2.5.3	Low Frequency Human Body Tissue Dielectric Property	30
2.6	Low Frequency Numerical Dosimetry Techniques	31
2.6.1	Electromagnetic Quasi-Static Approximation	31
2.6.2	Existing Low Frequency Numerical Dosimetry Techniques	33
2.6.3	Scalar Potential Finite Element (SPFE) Method	37
2.7	Validation of the SPFE Method	38
2.7.1	Comparison with Analytical Solutions	38
2.7.2	Comparison with FDTD Solutions	40
2.8	Quasi-Static Approximation for a Full-Body Exposure	41
2.8.1	Quasi-Static Frequency Limit	41
2.8.2	Quasi-Static Approximation Uncertainty above 200 kHz	44
2.9	Conclusion	44
3	LF Magnetic Field Exposure Analysis - Theory and Fundamentals	47
3.1	Introduction	47
3.2	Post-processing Techniques for the <i>in situ</i> E-field	48
3.2.1	Spatial Averaging	48
3.2.2	99th Percentile Value	50
3.3	Discretization Uncertainty for the Peak Induced E-field	50
3.3.1	Background	50
3.3.2	Discretization Uncertainty due to Stair-Casing Error	50
3.3.3	Discretization Uncertainty due to Field Singularity	53
3.3.4	Discretization Uncertainty for an Anatomical Model	54
3.3.5	Summary of the Discretization Uncertainty Analysis	55
3.4	Analysis of Human Brain Exposure	56
3.4.1	Background	56
3.4.2	Canonical Head Model	56
3.4.3	Computational Results of Anatomical Models	58
3.4.4	Summary of the Human Brain Exposure Analysis	63
3.5	Analysis of Human Body Exposure	65
3.5.1	Background	65
3.5.2	Skin Anatomy and Tissue Dielectric Property	65
3.5.3	Multi-layer Skin Modelling	67
3.5.4	Computational Results of an Anatomical Model	71
3.5.5	Summary of the Human Body Exposure Analysis	75
3.6	Conclusion	75

4	LF Magnetic Field Exposure Analysis - Practical Investigations	77
4.1	Introduction	77
4.2	Exposure to Close-Range Wireless Power Transfer System	78
4.2.1	Methods and Materials	78
4.2.2	Investigation of a Practical WPT System	82
4.2.3	Characterization of Generic Coils	86
4.2.4	Summary of the Short-range Wireless Power Transfer System Analysis	92
4.3	Theoretical Assessment of the Maximum Obtainable Power for Mid-range Wireless Power Transfer Based on Exposure Limits	93
4.3.1	Background	93
4.3.2	Methods and Materials	94
4.3.3	Incident B-field based on Tx Coil Size	95
4.3.4	Maximum Permissible B-field Intensity	98
4.3.5	Estimation of the Maximum Obtainable Power	100
4.3.6	Summary of the Mid-range Wireless Power Transfer Analysis	102
4.4	Conclusion	103
5	LF Electric Field Exposure Analysis	105
5.1	Introduction	105
5.2	Analysis of the Exposure to Uniform E-field	105
5.2.1	Background	105
5.2.2	Computational Results of an Anatomical Model	106
5.2.3	Summary of the Uniform E-field Exposure Analysis	108
5.3	Analysis of Contact Current	113
5.3.1	Background	113
5.3.2	High Voltage Detector	113
5.3.3	Analysis of the Contact Current due to a High Voltage Detector	114
5.3.4	Summary of the Contact Current Analysis	117
5.4	Conclusion	118
6	Mobile Device Antenna Optimization with Genetic Algorithms	119
6.1	Introduction	119
6.2	Methods and Materials	120
6.2.1	FDTD-based Simulation Platform	120
6.2.2	Genetic Algorithms and Network Distributed Optimization	120
6.2.3	Antenna Optimization Methodology	121
6.3	Antenna Models	122
6.3.1	Folded Monopoles Antenna (FMA)	123
6.3.2	Planar Inverted F Antenna (PIFA)	123
6.3.3	Folded Inverted Conformal Antenna (FICA)	124
6.4	Parametrization and Optimization	125
6.4.1	Antenna Modelling and Parametrization	125
6.4.2	Optimization Process	126

Contents

6.5	Optimization Results and Discussions	127
6.5.1	Radiation Performance in Free Space	127
6.5.2	Radiation Performance with Head and Hand Phantoms	129
6.5.3	Specific Absorption Rate (SAR)	131
6.5.4	Hearing Aid Compatibility (HAC)	132
6.5.5	Computation Requirement and Optimization Time	134
6.5.6	Optimization Validation	135
6.6	Conclusion	135
7	Analysis and Design of Mobile Device Antenna-Speaker Assembly	137
7.1	Introduction	137
7.2	Background	138
7.2.1	Moving-Coil Speaker Model	138
7.2.2	Equivalent Circuit of an Antenna-Speaker Assembly	139
7.2.3	Mutual Coupling and EMC/EMI Issues	140
7.2.4	Existing Design Techniques and Limitations	141
7.3	Numerical Analysis of a Simplified Speaker Structure	141
7.3.1	CAD Model and Simulation Tool	141
7.3.2	Conductively Coupled or Isolated Speaker	143
7.3.3	Capacitively Coupled Speaker	146
7.4	Investigation of a Practical Antenna-Speaker Assembly	149
7.4.1	Numerical Simulation of a PIFA-Speaker Assembly	150
7.4.2	Measurement of a PIFA-Speaker Assembly	152
7.5	Summary and Proposed Design Guidelines	155
7.6	Conclusion	156
8	Conclusions and Future Work	157
8.1	Thesis Assessment	157
8.1.1	Recommendations for the Existing Low Frequency Exposure Guidelines	158
8.1.2	Exposure Safety Analysis for Emerging Wireless Technologies	158
8.1.3	Virtual Prototyping of Antenna Optimization	159
8.1.4	Design Guidelines for Cross-Frequency Component Integration	159
8.2	Perspectives	160
8.2.1	Stimulation Threshold of Biological System	160
8.2.2	MRI Gradient Coil Peripheral Nerve Stimulation	160
8.2.3	Reduce the Exposure Level of a Wireless Power Unit	160
8.2.4	Alternative Antenna Optimization Algorithms	160
	Bibliography	171
	Curriculum Vitae	173
	List of Publications	177

1 Introduction

This chapter outlines the research objectives, analysis procedures and original contributions of this thesis. Based on the operating frequency range of the investigated wireless applications, the research work is organized into three sections: (1) low frequency exposure assessment, (2) mobile device antenna optimization with network-distributed genetic algorithms and (3) analysis of cross-frequency component integration (i.e., antenna-speaker assembly). Detailed literature reviews, analysis and research outcomes are presented in the respective chapters.

1.1 Low Frequency Exposure Dosimetry Assessment

Public concern over possible biological effects due to the exposure to low frequency electric (E) field and magnetic (B) field emerged in the 1960s with the introduction of ultra high voltage (UHV) transmission line systems. At low frequency, artificial B-fields are frequently encountered in many aspects of daily life, e.g., near power lines, electronic article surveillance gate, wireless charging and therapeutic/medical treatment (see Figure 1.1). With the advancements of wireless technology, more low frequency exposure sources are emerging. To prevent acute and adverse biological effects due to the exposure to electromagnetic fields, various international committees have published exposure guidelines: e.g., ICNIRP-1998 [1] and ICNIRP-2010 [2] by the International Commission on Non-Ionizing Radiation Protection (ICNIRP), and IEEE Std. C95.6-2002 [3], IEEE Std. C95.1-1992 [4] and IEEE Std. C95.1-2005 [5] by the Institute of Electrical and Electronics Engineers (IEEE).

To gain a better understanding of the interactions between electromagnetic fields and a human body, it is critical to obtain information pertaining to both the magnitude and distribution of the induced fields. Dosimetry, the process of determining the induced fields in body tissues through measurement or numerical techniques, becomes indispensable in the process of wireless technology development. As a human body is composed of highly inhomogeneous biological tissues, the measurement of the induced fields in such a complex environment is limited by the existing phantom modelling and sensor technology. As a result, numerical dosimetry is often employed when detail *in situ* field information are required.

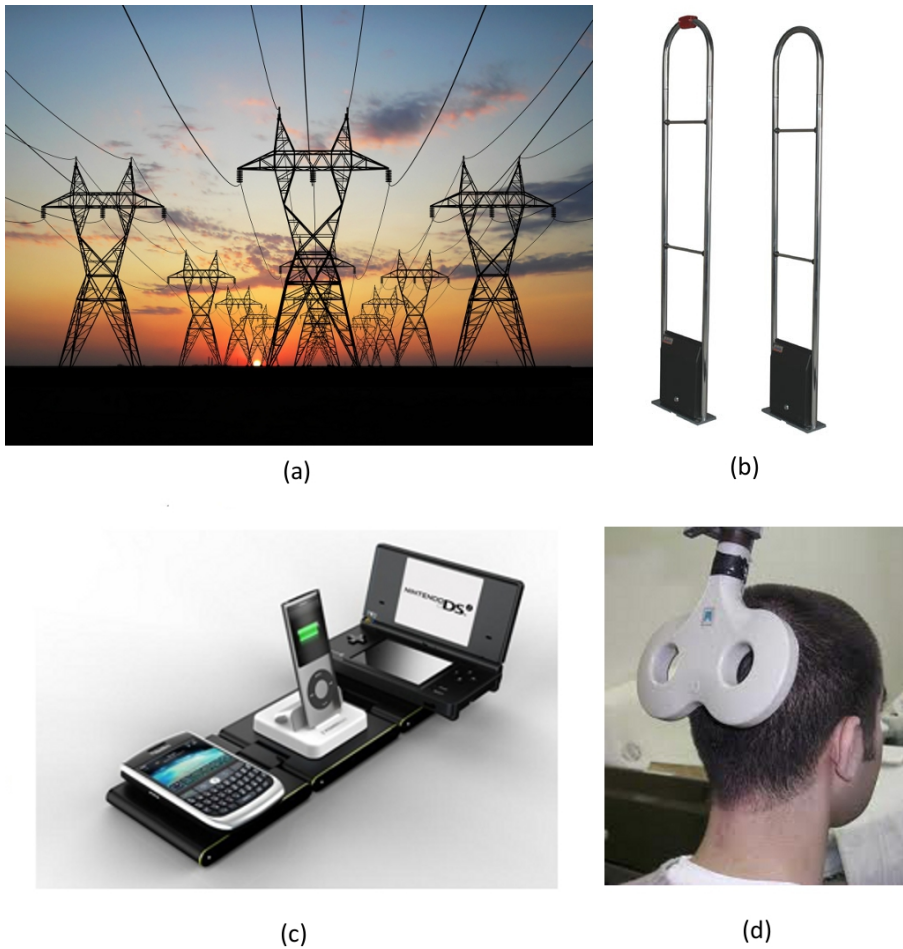


Figure 1.1: Low frequency exposure scenarios: (a) high-voltage power lines, (b) electronic article surveillance gate, (c) wireless power and (d) transcranial magnetic stimulation.

Considerable research efforts [6–41] have been invested in the field of numerical dosimetry for low frequency electric and magnetic field inductions. By numerically determining the induced field distribution and peak magnitude inside a human body, the conversion factors between the *ex situ* fields and *in situ* fields can be established. As the low frequency exposure limits suggested by the aforementioned guidelines and standards [1–5] are often based on the results of numerical dosimetry, realistic modelling and computational accuracy play important roles. Based on quasi-static approximation, several numerical techniques, e.g., Boundary Element Method (BEM) [41], Finite Difference Time Domain (FDTD) method [14] and Scalar Potential Finite Difference (SPFD) method [6] were proposed to compute the induced fields (i.e., current density and electric field) inside a human body.

Previously published numerical dosimetry studies are often based on pre-voxellized anatomically realistic models. The typical grid resolutions employed in the past studies are in the range of 2 to 5 mm, which are coarse and inadequate in view of the current computational capability. To advance the knowledge of low frequency numerical dosimetry, research work is conducted

in this thesis with novel applications of an up-to-date low frequency numerical technique. Exposure scenarios involving uniform and non-uniform incident low frequency fields are investigated with canonical models and statistical approach. By applying state-of-the-art computational techniques, the research objectives of this study are to examine the validity of the existing exposure limits [1–5] and investigate the exposure safety of various complex low frequency electromagnetic sources (e.g., wireless power transfer and high-voltage power-line detector).

1.2 Mobile Device Antenna Optimization with Genetic Algorithms

In this section, the application of computational techniques on mobile device antenna optimization is investigated. With the increasing demands for portable devices (e.g., mobile phone and tablet computer), product engineers have to realize a wireless design in a short time frame while achieving high performance requirements including compliance with Over The Air (OTA), Specific Absorption Rate (SAR) and Hearing Aid Compatibility (HAC) product standards. Following the trend of slimmer and smaller form factor, the available space for antenna design shrinks. Inevitably, engineers face great difficulty implementing multi-band antenna for a mobile device with small chassis and limited antenna volume. Without proper optimization, a poorly designed antenna could cause shorter battery life, inadequate signal coverage and frequent call drops.

A typical mobile device antenna design cycle consists of initial concept validation, prototyping and numerous optimization iterations based on the mechanical and electrical design changes. The traditional optimization process relies on empirical tuning, e.g., iteratively tweaking an antenna structure to improve bandwidth and radiation performance. Such approach demands engineering expertise, measurement equipments (e.g., vector network analyzer and anechoic chamber) and time-consuming measurement iterations. In light of the ever shortening product design cycle, a computer-aided automatic antenna optimization approach is highly valued as an important complement to the traditional empirical method.

In recent years, emphasis has been placed on computer-aided antenna optimization using numerical techniques [42–44]. Optimization algorithms such as the Genetic Algorithms (GAs) have been widely applied to antenna optimizations [45–47]. Complex antenna optimization task should benefit from the advancements in computer hardware architecture (e.g., memory and processing speed), electromagnetic numerical modelling technique and optimization algorithms. The research objective of the current study is to investigate the practicability of a numerical-based antenna optimization scheme which is capable of completing an optimization task within the shortest possible time. To this aim, an antenna optimization analysis, utilizing a Finite-Difference Time-Domain (FDTD) based computational platform [48] and network-distributed GAs, is conducted. A mobile phone structure is accurately represented by a detail computer-aided-design (CAD) phone model. In addition, realistic operating condition is considered with anatomical phantoms (see Figure 1.2).

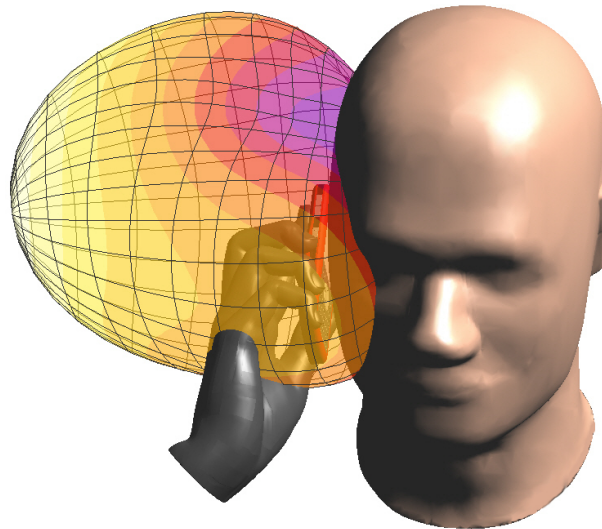


Figure 1.2: The numerical modelling of a mobile phone with a head phantom and a possible hand phantom which depicts a realistic device-in-use condition.

1.3 Analysis and Design of Antenna-Speaker Integration

The design of an audio-radio component integration for wireless device is investigated in this section. In the development of a wireless device, removing unwanted coupling and interference sources is a critical design requirement. The presence of electronic components, e.g., speaker, vibrator and camera, can significantly influence the antenna radiation performance. When these components are placed in close vicinity to an antenna element, electromagnetic near-field coupling could lead to radiation efficiency deterioration when certain amount of input power is “absorbed” by the components instead of radiated out [49]. With the trend of smaller and slimmer device form factor, components are forced to be packed closer together in order to maximize the use of available device volume. This inevitably leads to severe electromagnetic compatibility and interference (EMC and EMI) issues. To overcome such problems, proper electromagnetic screening is required to achieve optimum performance. The research objective of this section focuses on understanding and improving the performance of an antenna-speaker assembly (i.e., a typical cross-frequency component integration).

For a wireless device, a common design practice is to place a miniature speaker within the antenna volume so that the same volume can serve both as acoustic resonant chamber and antenna carrier [50–53] (see Figure 1.3). A poorly integrated loudspeaker can interact with the near fields of an antenna and give rise to non-radiative resonances. In addition to antenna radiation efficiency degradation, harmonic signals produced by the speaker can be coupled through the antenna to the radio frequency (RF) receiver which leads to receiver de-sense (i.e., increased receiver noise level). It is therefore critical for an antenna-speaker assembly design to adapt an effective decoupling scheme.

Nevertheless, the complexity of a speaker structure has made electromagnetic modelling of coupling mechanisms difficult and therefore nearly impossible to optimize using numerical approach [54]. As a result, in the previously published antenna studies [55–59], speakers are often modelled as simplified metal blocks (i.e., either isolated or grounded to the printed circuit board). To address complex coupling mechanisms and determine the best available design approach, the RF resonance characteristics of highly realistic speaker models are investigated in the current study. The research aims to derive a set of design guidelines through a combination of hardware prototyping and numerical simulations using realistic speaker models. By achieving an in-depth understanding of the coupling characteristics, the optimization cycle and design cost of such cross-frequency component integration can be significantly improved.



Figure 1.3: (a) A typical antenna-speaker assembly module and (b) miniature speakers to be integrated.

1.4 Outline and Original Contributions

This section illustrates the contents and original contributions of individual chapters. Each chapter includes introduction, research progress, discussion and conclusion.

Chapter 2: Low Frequency Exposure and Dosimetry Techniques

Description: A literature review on low frequency electric and magnetic exposure is presented in this chapter. The interaction of biological systems with low frequency fields and the associated biological effects are discussed to establish the significance of exposure limits and numerical dosimetry. The methods and materials (e.g., anatomical models, measurement and numerical techniques) for low frequency dosimetry assessment are reviewed, followed by an introduction of the computational techniques employed in this study. The applied solver is validated with analytical solutions to establish the basis for subsequent analyses.

Chapter 1. Introduction

Original contribution: The Scalar Potential Finite Element (SPFE) solver is introduced for the first time to illustrate the specific numerical approach employed in this thesis. The discussions of the existing exposure guidelines (ICNIRP and IEEE) establish the motivations for the extensive low frequency exposure research work subsequently conducted in the thesis.

Chapters 3 and 4: Low Frequency Magnetic Field Exposure Analysis

Description: These chapters illustrate the exposure analysis of low frequency B-field induction. First, the spatial averaging and percentile filtering approaches recommended by the exposure guidelines and standards [1–3, 5] are interpreted and implemented. Next, the effects of the averaging and filtering techniques on the induced peak E-field in an exposed body are investigated with respect to numerical artefacts such as stair-casing errors and field singularities. Following that, in-depth analyses of the human brain and whole body exposure are conducted for uniform B-field exposure scenarios. Compliance assessments with the published exposure limits are conducted to verify the validity of these limits. Practical low frequency B-field exposure sources, e.g., wireless power transfer (WPT), are also analyzed to demonstrate the industrial applications of the applied techniques.

Original contribution: The brain exposure analysis leads to the identification of ill-defined exposure limits due to erroneous assumptions of frequency scaling and tissue homogeneity. In the whole body exposure analysis, the modelling of a multi-layer skin model is investigated for the first time for low frequency B-field induction. The results suggest that a single-layer homogeneous skin layer can be employed to estimate the worst-case E-field in a multi-layer skin model for a limb-non-touching posture. The research results lead to an up-to-date reference for the revisions of low frequency B-field induction exposure limits.

The analyses conducted for wireless power transfer (WPT) exposure provide crucial information for the implementation of an exposure-compliant wireless power system. Both close-range localized exposure and mid-range whole-body exposure scenarios are considered. The compliance assessment of a practical 100 kHz close-range WPT prototype is investigated for the first time to reveal the exposure safety of such wireless power system and establish the design parameters (e.g., optimum operating frequency range and effects of coil design) for improved exposure compliance. Furthermore, by estimating the maximum power obtainable through WPT without exceeding exposure limits in a room-size environment, a theoretical assessment for the power budget of loosely-coupled magnetic resonant WPT based on human body exposure limits is presented.

Chapter 5: Low Frequency Electric Field Exposure Analysis

Description: In this chapter, the application of numerical techniques is extended to the exposure analysis of low frequency E-field induction and contact current scenarios. A grounded human body exposed to uniform E-field and a practical exposure scenario of a person operating a high voltage detector below a power distribution line are investigated.

Original contribution: The computational results provide up-to-date estimation of the spatially averaged induced peak E-field in the human brain, heart and body due to uniform E-field induction. With reference to the published exposure guidelines, revision is suggested for the non-conservative exposure limits. From the high-voltage detector exposure assessment, the computational results of several body postures reveal no tangible exposure safety concerns towards the operation of a high-voltage detector, provided that the device exhibits a proper safety operating resistance.

Chapter 6: Mobile Device Antenna Optimization with Genetic Algorithms

Description: A numerical-based antenna optimization approach is demonstrated in this chapter. The research objective is to investigate the practicability of a fully automated computer-aided optimization for the antenna design of a commercial mobile device. A highly detail physical mobile phone model is imported to simulate a complex design environment which is typical for modern telecommunication device development. Three multiple-resonance internal antenna designs are optimized by employing a simulation platform which utilizes genetic algorithms, network cluster distribution and a finite difference time domain solver. The optimization task aims to achieve simultaneous optimum antenna radiation performance (OTA), minimum RF energy absorption in a user's head (SAR) and reduced interference with hearing aid devices (HAC).

Original contribution: The research work presented in this chapter provides the frame work of a novel antenna optimization scheme. The complexity of a detail mobile phone structure is for the first time modelled with up-to-date computational capability. The variety of internal antenna designs investigated in this study provides insightful information pertaining to the near-field and far-field performance characteristics. This information allows an antenna designer to determine the most suitable antenna structure based on the targeted device form factor. The individual antenna performance, with respect to the achievable bandwidth, total radiated power (TRP), specific absorption rate (SAR) and hearing aid compatibility (HAC) performance, is investigated by considering realistic operating conditions, e.g., placed next to a human head phantom and held by a hand grip phantom. Based on the optimization requirements (e.g., hardware resource and iteration time) and optimization results, it is demonstrated that a fully automated computer-aided antenna optimization process is superior to the traditional empirical approach and can significantly improve a mobile device antenna development cycle.

Chapter 7: Analysis and Design of Mobile Device Antenna-Speaker Assembly

Description: The mutual coupling between an antenna and a closely integrated moving-coil speaker is investigated in this chapter. The analysis focuses on the speaker voice coil radio-frequency harmonic resonance characteristics and the antenna radiation efficiency degradation due to the presence of a speaker. Antenna structures with a simplified speaker model are first employed to assess the impacts of design parameters, e.g., speaker resonance, antenna shape and speaker location, on the antenna radiation performance. Subsequently,

Chapter 1. Introduction

practical antenna-speaker assemblies are investigated with respect to variable speaker location and voice coil design through numerical simulations and hardware prototyping.

Original contribution: The speaker high frequency harmonic resonance and potential coupling mechanisms are first illustrated with an equivalent circuit to outline the sensitive design parameters. Next, with simplified speaker models, the fundamental coupling characteristics between an antenna element and a closely integrated speaker are determined through numerical simulations. The simulation results indicate that the degradation of antenna radiation efficiency is associated with the non-radiative energy stored in a conductively or capacitively coupled resonant speaker. The trend of coupling characteristics is then analyzed with highly complex numerical speaker models and verified with hardware prototype measurements. Based on the research outcomes, practical design guidelines are proposed to achieve cost-effectiveness, antenna-speaker co-existence and optimum antenna radiation efficiency even under the most stringent industrial design constraints.

Chapter 8: Conclusions and Future Work

Summary and general assessment of the work achieved in this thesis are presented in this chapter. Based on the research findings, possible future research directions are discussed.

2 Review of LF Exposure and Dosimetry Techniques

2.1 Introduction

In contemporary society, the tremendous growth in the use of electrical energy inevitably results in an increase in the intensity of electric and magnetic fields in both rural and urban environments. Electro-smog could originate from various sources, e.g., power grids, base stations, radio and television broadcast stations, cellular phones and domestic electrical appliances. The likelihood and level of exposure to biological systems from man-made electromagnetic fields has increased by orders of magnitude over the past century. Based on the oscillating frequency, electromagnetic radiation can be classified as non-ionizing or ionizing. The distinction is generally drawn at the wavelength of around 1 nm in the ultraviolet (UV) region. Non-ionizing radiation refers to the electromagnetic radiation that does not carry sufficient energy to cause ionization in living systems. Natural sources of non-ionizing radiation are, for instance, solar radiation from the Sun, cosmic radiation from distant stars and terrestrial activities, e.g., lightning. Compared to the intensity of the man-made electromagnetic fields, the natural sources are in general much weaker. The non-ionizing part of the electromagnetic spectrum can be further divided into the following categories: low frequency, radio wave, microwave, infra-red (IR) and visible light.

First part of the research in this thesis focuses on the exposure of a human body in the lower frequency (LF) range, covering a spectrum from 10 Hz up to 100 kHz. It should be noted that the range of low frequency spectrum is not strictly defined. It depends on specific application and the wavelength-to-domain ratio. In the context of radio communication, the low frequency spectrum is defined from 30 kHz to 300 kHz. In the past decades, studies have been conducted in defining the physical interactions of LF electric (E) and magnetic (B) fields with living organisms and describing the biological effects emerged from these interactions. Particular interest has been focused on the E-fields and B-fields at power frequencies (i.e. 50 and 60 Hz) since the strongest man-made LF E-field and B-field are often found near electric power facilities (e.g., over-head and underground power lines). The terms *magnetic field*, *magnetic flux density* and *B-field* are used interchangeably in this thesis with the assumption

of constant permeability (μ). In this chapter, the LF E-field and B-field exposure and the associated biological effects, dosimetry assessment techniques and published exposure limits are reviewed. The content is organized as follows: an overview of the LF E-field and B-field exposure to the human body, with an emphasis on the published exposure limits [1–5], is introduced to provide a theoretical background for the forthcoming investigations. Following that, various existing measurement and numerical dosimetry techniques are reviewed. A LF numerical solver based on the electromagnetic quasi-static approximation and the Finite Element Method (FEM) is introduced. This LF solver is validated with respect to its computational accuracy through a comparison with analytical solutions and alternative numerical solutions of an electromagnetic full-wave solver [48]. The upper frequency limit of the electromagnetic quasi-static approximation for a full-body LF exposure scenario is derived based on the reported human body tissue dielectric property values [60] and tissue composition data [61]. The numerical uncertainties of the LF solver, when applied to a frequency up to 10 MHz, are investigated through a comparison study with a full-wave FDTD solver [48].

2.2 Biological System Interaction with Low Frequency Fields

The sensory and regulatory organs in a human body function as sophisticated electrical systems. The human body itself produces subtle electromagnetic fields. The associated electrical signals are responsible for the control of biological processes and the transportation of information from one part of the body to another. Some of the biological field quantities can be measured directly. For instance, the electrical activity along the scalp can be captured on an electroencephalography (EEG). When exposed to a LF E-field or B-field, *in situ* E-fields (current flow) are induced inside a human body. If the induced E-field strength is high enough to affect the body's natural E-fields, the stimulation of nerves and muscles would occur. This could trigger numerous biological effects on the electrical activities of the human body, e.g., *visual phosphenes* (i.e., visible flashing light) and *peripheral nerve stimulation* (i.e., sensation) [62]. Based on the nature of induction, two types of interaction can be classified: *direct* field induction and *indirect* contact induction.

2.2.1 Electric and Magnetic Induction

Based on the electromagnetic quasi-static approximation (to be discussed in details in Section 2.6.1), the interaction between a human body and LF fields can be interpreted separately for the external E-fields and B-fields.

E-field Induction

As a human body exhibits high and finite conductivity (σ) at low frequency, two phenomena arise when a human body is placed in a slowly time-varying E-field: (1) the human body perturbs the external E-field significantly and (2) a relatively small amount of E-field (typically

5 to 6 orders of magnitude lower than the external E-field at 50-60 Hz) is induced in the body due to the surface charges introduced on the body by the external E-field. The external E-field perturbation can be explained as follows: a conductive human body leads to a small E-field inside the body due to direct E-field induction. As a boundary condition requirement, the tangential components of the E-field must be equal at the air-body interface. Since the *in situ* E-field is small, the tangential E-field in the air on the body surface must be small as well. This implies that the external E-field on the body surface is predominantly aligned vertically to the surface. It follows that the E-field vectors can be “crowded-in” based on the contour of the body shape. Hence, the magnitude of the external perturbed E-field can be much greater with the presence of the body. The degree of E-field enhancement depends on the shape of the body and body posture. For a slender and pointy shape, the concentration of the external E-field is greater. The oscillating electric charges on the surface of an exposed human body lead to current flow inside the body. The strongest E-field induction occurs when a human body is standing straight with grounded feet in a vertically oriented external E-field (i.e., E-field lines are aligned parallel to the principal body height axis) as shown in Figure 2.1(a). It should be noted that this worst-case claim ignores the effect of body posture.

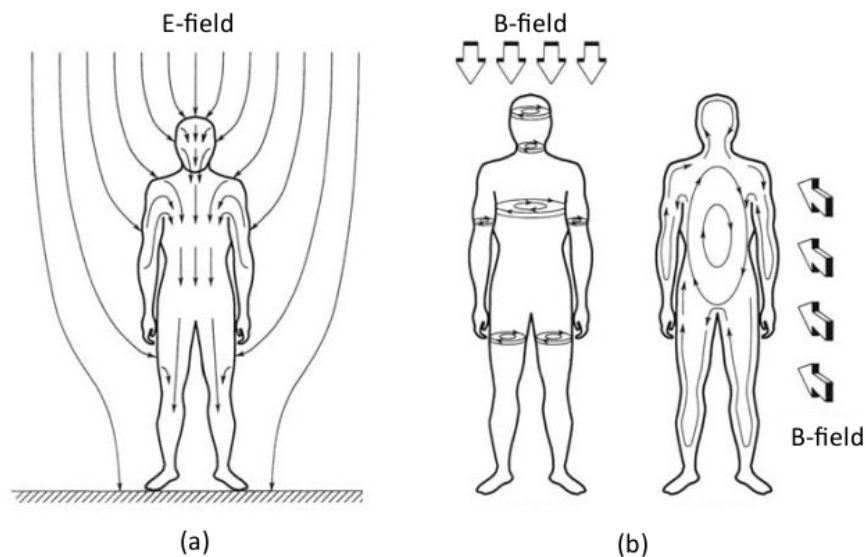


Figure 2.1: The external E-field, B-field and *in situ* E-field distributions for (a) vertically aligned E-field and (b) vertically and horizontally aligned B-field, copyright Reilly 1998 pp.346 [70].

B-field Induction

For the exposure to a slowly time-varying B-field, according to *Faraday's law of induction*, E-fields and hence currents will be induced in a conductive body. Such currents are known as *eddy currents*, and they circulate in closed loops which tend to lie in the planes normal to the direction of the applied B-field (see Figure 2.1(b)). The induced currents are the smallest at the center of the perpendicular plane and gradually increase with ascending distance from the center. Higher induced E-field is expected in larger object since the peripheral conduction

Chapter 2. Review of LF Exposure and Dosimetry Techniques

loops are larger. In contrast to the E-field induction case, a human body causes virtually no perturbation to an external B-field at low frequency. This is mainly because most of the living tissues are non-magnetic (i.e., exhibit weak susceptibility to a B-field). As a LF B-field can not be effectively shielded by conventional conductive screening techniques, the prevention of B-field induction in a human body received more attention than the E-field induction case. To conclude, the exposure to LF E-field or B-field results in induced E-fields (current flow) in a human body. The magnitude and distribution of the induced E-field depend on the orientation, distribution, magnitude of the external field and the shape, size and posture of the exposed body. The induction of E-field due to the exposure to external E-fields or B-fields is considered as a direct effect of LF exposure and is referred to as *direct induction*.

2.2.2 Contact Current Induction

A conductive object, when placed in a LF E-field, experiences induced electric charges on it. The exposed object carries electrical energy which is stored in the form of capacitance. When two conductive objects at different electric potentials are brought into contact with each other, two phenomena arise: (1) Right before making physical contact, when the two objects are extremely close to each other, a capacitive discharge occurs in which transient pulses pass between the two objects in order to equalize the potential difference between them. If the potential difference is large enough, the discharge could trigger sparks at the point of contact. This discharge is commonly referred to as *spark discharge*. (2) Once physical contact is made, a steady-state current with the same frequency as the external E-field starts to flow between the objects. This current is known as *contact current* and it can be triggered when a human body comes into contact with a conductive object at a different electric potential level. For instance, in the vicinity of an electric power facility where intensive E-fields are present, a grounded human body (i.e., at the Earth potential) touching a large ungrounded charged conductive object (e.g. the metal frame of a vehicle with dry tires) could result in a *short-circuit* current (i.e., the current that would flow through a short-circuit path into the ground). If such current is strong enough, it can produce perception, muscular tetanus and cardiac fibrillation. The *let-go* threshold is defined as the largest amount of current that is allowed to pass through a person's hand without causing muscular contraction severe enough such that the person loses his or her ability to let go of the current-conducting object. Currents exceeding this threshold are potentially fatal and should be avoided at all cost. The induction of contact current is considered as an indirect effect of LF E-field exposure and is often referred to as *indirect induction*.

2.2.3 Protective Measures against Low Frequency Exposure

The protection against LF E-field exposure can be readily achieved through conductive shielding. At low frequency, virtually any conductive surface will provide substantial shielding effect against E-field exposure. One practical example is for personnels working in high-voltage

power line areas, protective suits known as the *Faraday suit* which are made from electrically conductive materials are often worn by workers. On the contrary, there is no convenient way to achieve effective shielding against the exposure of LF B-field. Ferromagnetic coating is sometimes applied on high-current power lines. The most practical approach for B-field exposure protection is to limit the access to the areas with intensive B-field or limit the strength of B-field under a certain threshold level. For the protection against contact current, the most common and effective protective measure is to bring the conductive objects to the same electric potential level. For instance, during a “hot-wire” operation on a high-voltage power line, the worker will bring his body potential to the same level as the energized power line. This lowers the danger of electrocution due to spark discharge or contact current.

2.2.4 Biological Effects due to Low Frequency Exposure

The fact that LF E-field and B-field exposures are classified as non-ionizing implies that these fields generally transfer minute amounts of energy to a biological cell when compared to ionizing radiation. As a result, the induced E-fields are unable to disrupt the chemical bonds in a cell. In addition, all the cells in a human body maintain large natural E-fields across their outer membranes, hence weakly induced E-fields are often passed on as noise without significant impact. Nevertheless, studies over the past few decades have demonstrated that under certain circumstances, the membranes of cells can be sensitive to even fairly weak externally imposed fields: *extremely small signal changes can trigger major bio-chemical responses critical to the functioning of a cell* [63]. The biological effects triggered by LF exposure have been observed in a large number of *in vitro* experiments inside culture medium. Human volunteer experiments also provided substantial evidence for exposure-induced stimulation. As a result, the accumulated findings warrant further research in identifying the mechanisms and effects of LF E-field and B-field exposure.

Based on the reported findings, some biological effects due to LF exposure are well quantified and understood while some remain unclear and debatable. A generally accepted mechanism of interaction between LF field and biological tissues is the direct stimulation of excitable cells [64]. This phenomenon occurs when an electric potential, known as the *action potential*, is induced across the membranes of excitable cells. One of such phenomenon is *peripheral nerve stimulation* in which nerve excitation is triggered by the field-induced depolarization of the neural membrane. This activates the voltage-gated ion channels, which in term produces a propagating action potential down the length of the neuron. As a consequence, sensation can be perceived. Another important interaction is *cardiac excitation* which is associated with the stimulation of a contraction (systole). It is associated with *ventricular fibrillation*, a symptom that could lead to a life-threatening condition. Considerable debate was raised in the past decades over the question of whether LF exposure may be linked to an elevation in the risk of cancer. In particular, the risk of childhood leukaemia, nervous tissue tumours and breast cancer [65–68]. Due to the lack of convincing evidence and the identification of biologically plausible mechanism, it is believed that if LF exposure is indeed associated

with the development of cancer, it only acts as an agent of promotion instead of cause [68]. On the one hand, the established biological effects indicate a need to restrict or limit the exposure of LF E-field and B-field to prevent unintentional nerve stimulation. On the other hand, diagnostic and therapeutic medical treatment techniques, e.g., neuromuscular electrical stimulation and transcranial magnetic stimulation, have been developed based on the neuron and synaptic stimulation phenomenon due to LF induction.

2.3 ICNIRP-2010 and IEEE Std. C95.6-2002 Exposure Limits

To prevent acute and adverse biological effects, international committees, e.g., the Institute of Electrical and Electronics Engineers (IEEE) and the International Commission on Non-Ionizing Radiation Protection (ICNIRP) have published low frequency exposure guidelines and standards [1–5] based on numerical and experimental dosimetry data. The purpose of these guidelines and standards is to recommend exposure assessment procedures and to suggest field intensity limits for the external E-field and B-field such that the induced E-field in the human body is below the threshold levels that could trigger the known biological effects. In the low frequency range, the interactions of E-field and B-field with the human body through direct induction are mostly of non-thermal nature. As a result, the stimulation effect due to the induced E-fields are generally investigated for LF exposure instead of the heating effect, i.e., the Specific Absorption Rate (SAR). This section discusses the rationales behind the derivations of the ICNIRP-2010 [2] and IEEE Std. C95.6-2002 [3] low frequency exposure limits.

2.3.1 Basis of the Exposure Limits

Definition of Field Quantity

Two types of exposure limit are employed in the exposure guidelines and standards: *basic restriction* and *reference level* (known as *maximum permissible exposure* in the IEEE standards). The basic restriction (BR) refers to the threshold level of the internal E-field strength. The *in situ* E-field is generally accepted to be the field quantity that directly affects nerve cells and other electrically sensitive cells, instead of the current density (J) which is employed in earlier exposure guidelines [69]. The rationales for employing the induced E-field instead of the induced current density for the BR field quantity are given as follows: (1) the fundamental force responsible for electro-stimulation effects is the *in situ* E-field rather than the induced current density [70, 71]; (2) the current density can be expressed in terms of the E-field (E) as σE where σ is the conductivity of the medium, therefore basing an exposure standard on current density introduces an additional parameter with uncertainty [3]. The basic restriction levels are determined through numerical nerve models such as the Spatially Extended Non-linear Node (SENN) model [71] or experimental data from human volunteers. The reference level (RL) refers to the threshold level of the external unperturbed E-field and B-field strength. The reference levels are provided for practical exposure assessment purposes since the internal

E-field strength is relatively difficult to be determined. Most reference levels are derived from the relevant basic restrictions using measurement or computational techniques. For certain biological effects, e.g., magneto-phosphenes (i.e., the perception of faint flickering light in the periphery of the visual field due to the exposure to LF B-field), the threshold of the external B-field is first determined through experiments and then the basic restriction is derived numerically from human body models.

General Public and Occupational Exposure

Based on the exposed population, two categories of exposure limits are defined: *general public* and *occupational* (known as *controlled environment* in the IEEE standard) exposure. In IEEE Std. C95.6-2002, the definition of controlled environment is given as: *an area that is accessible to those who are aware of the potential for exposure as a concomitant of employment, to individuals cognizant of exposure and potential adverse effects, or where exposure is the incidental result of passage through areas posted with warnings, or where the environment is not accessible to the general public and those individuals having access are aware of the potential for adverse effects*. The definition of general public in IEEE Std. C95.6-2002 is: *all individuals who may experience exposure, except those in controlled environments*. In ICNIRP-2002, the occupational environment is described as: *occupational circumstances in which, with appropriate advice and training, it is reasonable for workers voluntarily and knowingly to experience transient effects such as retinal phosphenes and possible minor changes in some brain functions*. The definition of general public in ICNIRP-2010 refers simply to *members of the general public*.

Exposure Assessment Procedure

The procedures to perform a LF exposure assessment are recommended by the exposure guidelines and standards as follows: (1) determine the external field intensity (e.g., through field measurements); (2) if the external field intensity is below the RL (MPE) level, compliance with the exposure limits is achieved; (3) if the external field intensity exceeds the RL (MPE) level, dosimetry technique should be applied to assess the induced E-field; (4) If the induced E-field is below the BR level, compliance is achieved, otherwise non-compliance is declared. It should be noted that due to the inclusion of conservative safety factors, non-compliance of the exposure limits does not immediately warrant nerve stimulation in an actual exposure scenario. It is stated in ICNIRP-2010 that *the reference levels are calculated for the condition of maximum coupling of the field to the exposed individual, thereby providing maximum protection*. A similar statement can be found in IEEE Std. C95.6-2002: *compliance with the maximum permissible exposure level ensures compliance with the basic restrictions*. It is therefore clear that the conversion between the basic restriction and the reference level, which relies on numerical computations, plays a critical role in achieving scientifically sound and effective exposure limits for stimulation prevention.

2.3.2 Basic Restrictions and Reference Levels

In this section, the basic restrictions and reference levels suggested in ICNIRP-2010 [2] and IEEE Std. C95.6-2002 [3] are presented in tabular and graphic forms. For the IEEE exposure limits above 3 kHz, the BR and RL values are adopted from IEEE Std. C95.1-2005 [5]. It can be observed that the exposure limits are inconsistent between the two standardization committees. The main differences are: the definition of exposed tissue group, the conversion factors between the external field and the induced field, and the safety factors which are applied to account for scientific uncertainties. In ICNIRP-2010, the exposed tissues are grouped into the central nervous system (CNS) and the peripheral nerve system (PNS). It should be noted that the CNS tissues defined in ICNIRP-2010 include the brain and retina only (i.e., excluding the spinal cord). The PNS tissues defined in ICNIRP-2010 include all tissues of head and body, with the skin suggested to be the worst-case target tissue. In IEEE Std. C95.6-2002, the exposed tissues are grouped as brain, heart, extremities (i.e., hands, wrists, feet and ankles) and other tissue. The rationales behind the derivations of the basic restrictions will be discussed in Section 2.3.3 and the conversion factors will be discussed in Section 2.3.5.

ICNIRP-2010

The basic restrictions and reference levels of ICNIRP-2010 are presented in Tables 2.1, 2.2 and 2.3. The graphic representations are shown in Figures 2.2, 2.4 and 2.5. The field quantities are expressed in terms of rms values.

Table 2.1: Basic restrictions for the human body exposure to low frequency f (Hz) electric and magnetic field in ICNIRP-2010.

Exposure characteristic	Frequency range	Internal electric field (V/m)
Occupational exposure		
CNS tissue of the head	1 Hz -10 Hz	$0.5/f$
	10 Hz - 25 Hz	0.05
	25 Hz - 400 Hz	$2 \times 10^{-3} f$
	400 Hz - 3 kHz	0.8
	3 kHz - 10 MHz	$2.7 \times 10^{-4} f$
All tissues of head and body	1 Hz - 3 kHz	0.8
	3 kHz - 10 MHz	$2.7 \times 10^{-4} f$
General public exposure		
CNS tissue of the head	1 Hz -10 Hz	$0.1/f$
	10 Hz - 25 Hz	0.01
	25 Hz - 1 kHz	$4 \times 10^{-4} f$
	1 kHz - 3 kHz	0.4
	3 kHz - 10 MHz	$1.35 \times 10^{-4} f$
All tissues of head and body	1 Hz - 3 kHz	0.4
	3 kHz - 10 MHz	$1.35 \times 10^{-4} f$

Chapter 2. Review of LF Exposure and Dosimetry Techniques

Table 2.2: Reference levels for the human body exposure to low frequency f (Hz) electric and magnetic field in ICNIRP-2010.

Frequency range	Electric field (kV/m)	Magnetic flux density (T)
Occupational exposure		
1 Hz - 8 Hz	20	$0.2/f^2$
8 Hz - 25 Hz	20	$2.5 \times 10^{-2}/f$
25 Hz - 300 Hz	$5 \times 10^2/f$	1×10^{-3}
300 Hz - 3 kHz	$5 \times 10^2/f$	$0.3/f$
3 kHz - 10 MHz	0.17	1×10^{-4}
General public exposure		
1 Hz - 8 Hz	5	$4 \times 10^{-2}/f^2$
8 Hz - 25 Hz	5	$5 \times 10^{-3}/f$
25 Hz - 50 Hz	5	2×10^{-4}
50 Hz - 400 Hz	$2.5 \times 10^2/f$	2×10^{-4}
400 Hz - 3 kHz	$2.5 \times 10^2/f$	$8 \times 10^{-2}/f$
3 kHz - 10 MHz	8.3×10^{-2}	2.7×10^{-5}

Table 2.3: Reference levels for low frequency f (kHz) contact current from conductive objects in ICNIRP-2010.

	Frequency range	Contact current (mA)
Occupational exposure	up to 2.5 kHz	1.0
	2.5 - 100 kHz	$0.4f$
	100 kHz - 10 MHz	40
General exposure	up to 2.5 kHz	0.5
	2.5 - 100 kHz	$0.2f$
	100 kHz - 10 MHz	20

IEEE Std. C95.6-2002

The basic restrictions and maximum permissible exposure levels of IEEE Std. C95.6-2002 are presented in Tables 2.4, 2.6 and 2.5. The graphic representations are shown in Figures 2.3, 2.4 and 2.5. The field quantities are expressed in terms of rms values. To determine the basic restriction value (E_i) at a frequency f (Hz), Table 2.4 is interpreted as follows:

$$E_i = E_o \quad \text{for } f \leq f_e \quad (2.1)$$

$$E_i = E_o \frac{f}{f_e} \quad \text{for } f \geq f_e \quad (2.2)$$

Chapter 2. Review of LF Exposure and Dosimetry Techniques

Table 2.4: Basic restriction, E_o (V/m), for the human body exposure to low frequency f (Hz) electric and magnetic field in IEEE Std. C95.6-2002.

Exposed tissue	f_e (Hz)	General public	Controlled environment
Brain	20	5.89×10^3	1.77×10^{-2}
Hear	167	0.943	0.943
Extremities	3350	2.1	2.1
Other tissue	3350	0.701	2.1

Table 2.5: Maximum permissible exposure levels for the human body exposure to low frequency f (Hz) electric and magnetic field in IEEE Std. C95.6-2002.

Frequency range (Hz)	General public	Controlled environment
Magnetic flux density (mT)		
< 0.153	118	353
0.153 - 20	$18.1/f$	$54.3/f$
20 - 759	0.904	2.71
759 - 3350	$687/f$	$2060/f$
3350 - 100000	0.205	0.615
Electric field (kV/m)		
1 - 368	5	-
368 - 3000	$1.84 \times 10^3/f$	-
3000 - 100000	0.614	-
1 - 272	-	20
272 - 3000	-	$5.44 \times 10^3/f$
3000 - 100000	-	1.813

Table 2.6: Maximum permissible exposure levels for 0 kHz to 3 kHz induced and contact current for continuous sinusoidal waveforms in IEEE Std. C95.6-2002.

Condition	General public (mA)	Controlled environment (mA)
Both feet	2.70	6.0
Each feet	1.35	3.0
Contact, grasp	-	3.0
Contact, touch	0.50	1.5

2.3.3 Rationales for the Basic Restrictions

ICNIRP-2010

In ICNIRP-2010, the perception of surface electric charge, the direct stimulation of nerve and muscle tissue and the induction of retinal phosphenes are quoted as the well established biological effects which serve as a basis for the recommended basic restrictions. Based on the results of human volunteer experiments, the external E-field thresholds for direct perception by the most sensitive 10% of volunteers at 50–60 Hz are found to be in a range between 2

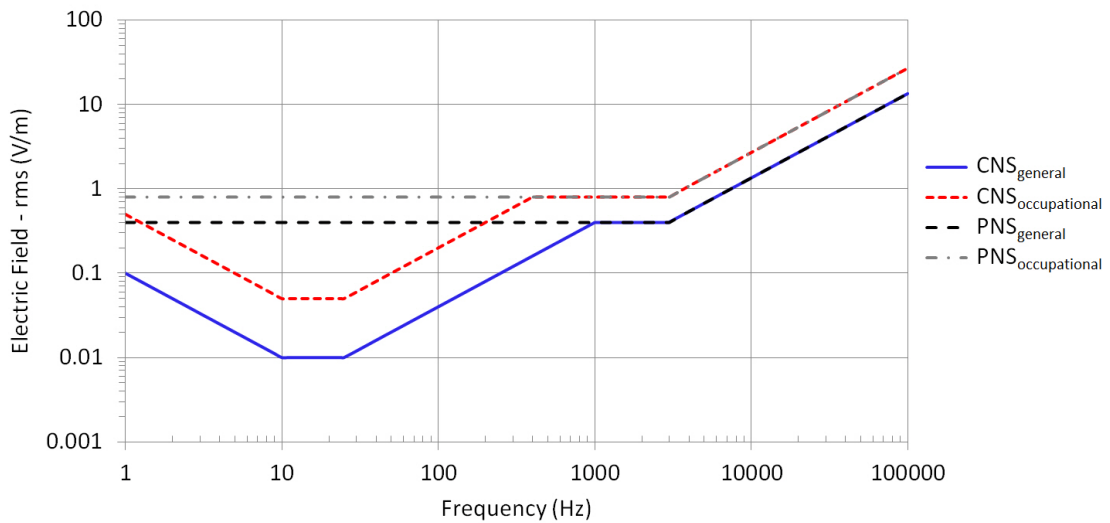


Figure 2.2: The basic restriction levels for the central nervous system (CNS) and peripheral nerve system (PNS), under the general public and occupational exposure conditions, recommended in ICNIRP-2010.

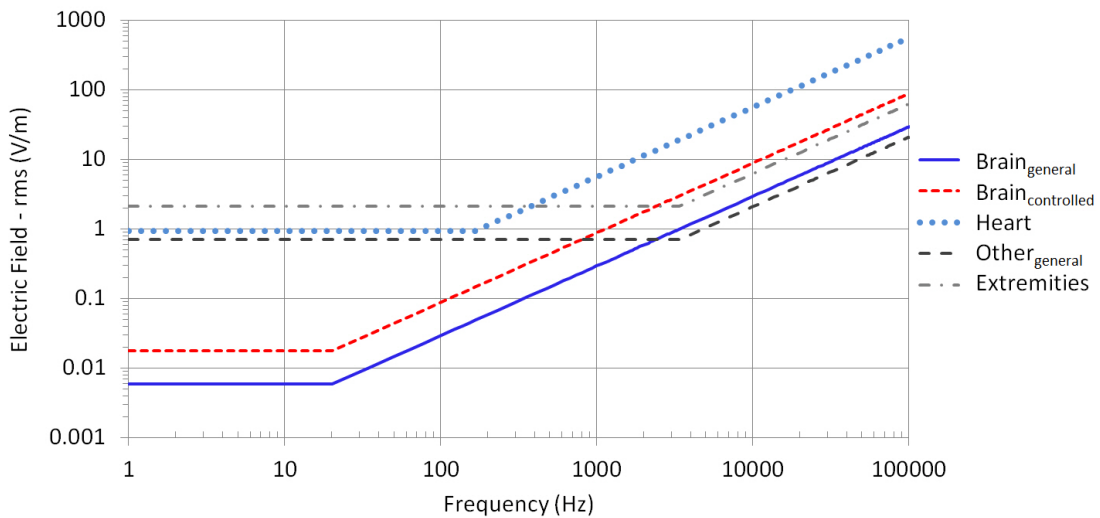


Figure 2.3: The basic restriction levels for the brain, heart, other tissue and extremities, under the general public and controlled exposure conditions, recommended in IEEE Std. C95.6-2002.

kV/m and 5 kV/m and 5% found 15 kV/m to 20 kV/m annoying. Based on a numerical nerve model [70, 71], myelinated nerve fibres of the human peripheral nervous system (PNS) have been estimated to have a minimum threshold value of induced E-field at around 6 V/m (non-rms peak). Experimental results obtained from volunteers exposed to the switched gradient B-fields of magnetic resonance (MR) systems suggest that the threshold for perception may be as low as about 2 V/m (based on the computational results of a homogeneous human

Chapter 2. Review of LF Exposure and Dosimetry Techniques

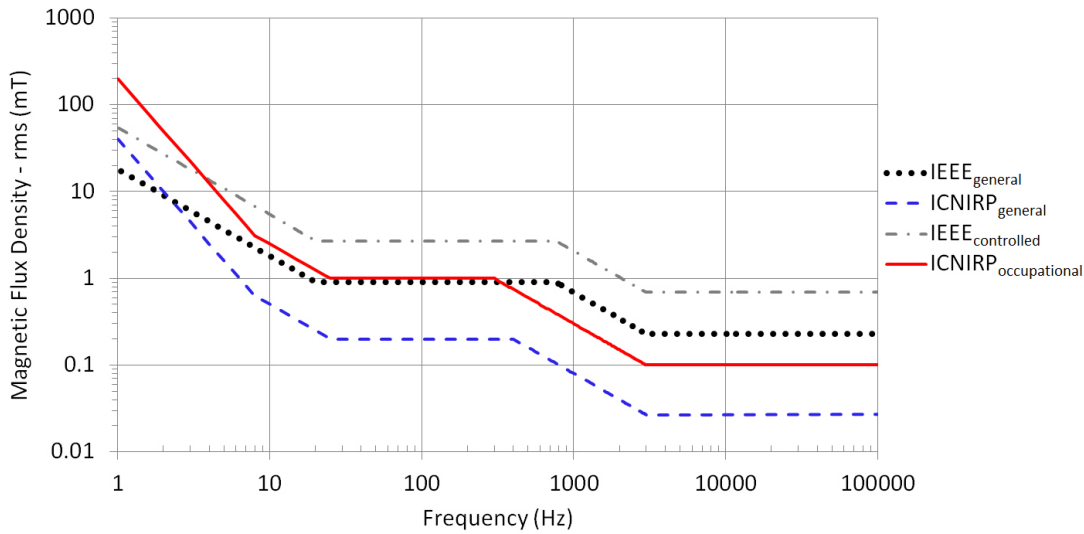


Figure 2.4: The magnetic flux density reference levels (maximum permissible exposure), under the general public and occupational (controlled environment) exposure conditions, recommended in ICNIRP-2010 and IEEE Std. C95.6-2002.

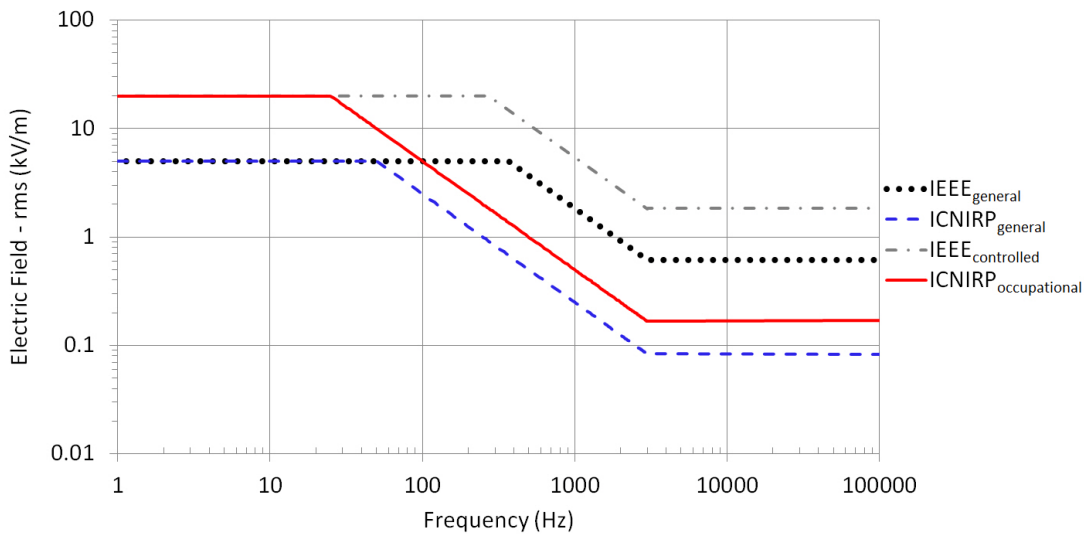


Figure 2.5: The electric field reference levels (maximum permissible exposure), under the general public and occupational (controlled environment) exposure conditions, recommended in ICNIRP-2010 and IEEE Std. C95.6-2002.

model) and 4 V/m to 6 V/m (based on the computational results of a heterogeneous human model). Another basis is that the myelinated nerve fibres of the central nervous system (CNS) was found to be stimulated by the E-fields induced during transcranial magnetic stimulation (TMS). Based on the experimental B-field strength, theoretical calculation suggests that the minimum stimulation threshold values may be close to 10 V/m (non-rms peak).

The stimulation thresholds rise above around 1 kHz to 3 kHz due to the progressively shorter time available for the accumulation of electric charge on the nerve membrane (this explains the frequency-dependent ascend of ICNIRP basic restriction above 3 kHz) and below about 10 Hz due to the accommodation of a nerve to a slowly depolarizing stimulus. Note that this accommodation effect is not considered in the IEEE Std. C95.6-2002 standard, this explains the shape difference between the basic restriction curves in Figure 2.2 and Figure 2.3 for frequencies below 10 Hz. Below the threshold for direct nerve or muscle excitation, a well established effect of induced E-field is the induction of magnetic phosphenes in the retinas of volunteers exposed to LF B-fields. The minimum threshold magnetic flux density is found to be around 5 mT at 20 Hz, rising at higher and lower frequencies. Based on this experimental data, the threshold for induced E-field strengths in the retina was estimated to be between about 50 mV/m to 100 mV/m at 20 Hz. As the retina is considered as part of the CNS (together with the brain), the magnetic phosphenes threshold is employed as a basis for the basic restriction of the CNS in ICNIRP-2010. As shown in Table 2.1, the value 50 mV/m is employed as the occupational exposure basic restriction value for the CNS tissues at a frequency from 10 Hz to 25 Hz. The magnetic phosphene thresholds rise rapidly at higher frequencies, intersecting with the thresholds for peripheral and central myelinated nerve stimulation at 400 Hz. The threshold on peripheral nerve stimulation for all parts of the body is determined based on the threshold for perception (i.e., 4 V/m) obtained from the switched gradient magnetic field experiment. A reduction factor of 5 is applied to the 4 V/m threshold, this gives rise to the basic restriction of 0.8 V/m for all tissues of head and body up to 3 kHz in occupational exposure scenario. In order to be conservative, additional reduction factors of 2 (for all tissues of head and body) and 5 (for the CNS tissues) are applied for the general public exposure.

IEEE Std. C95.6-2002

In IEEE Std. C95.6-2002, it is stated that the maximum exposure limits are based on the avoidance of the following biological effects: aversive or painful stimulation of sensory neurons, muscle excitation, direct alteration of synaptic activity within the brain, cardiac excitation and adverse effects associated with induced forces on rapidly moving charges within the body. As the threshold of excitation is known to be inversely proportional to the diameter of a nerve axon, it is assumed in the IEEE standard that the nerve fibre diameter is at the outer limit of the distribution of fibre sizes found in humans. Accordingly, a maximum diameter of 20 μm is assumed for a peripheral nerve and 10 μm for a CNS neuron. Based on a theoretical model of myelinated nerve [70, 71] and experimental data, the median *in situ* E-field threshold (non-rms peak) is estimated to be 0.075 V/m for synapse activity alteration in the brain at 20 Hz (based on the experimental data from magnetic phosphenes due to gradient coil of MR systems), 12.3 V/m for 10- μm brain nerve excitation at 3350 Hz, 6.15 V/m for 20- μm body nerve excitation at 3350 Hz and 12 V/m for cardiac excitation at 167 Hz. These threshold values serve as a basis for the IEEE basic restriction levels. As shown in Table 2.4, the exposure tissues in IEEE Std. C95.6-2002 are classified as brain, heart, extremities (i.e., hands, wrists, feet and ankles) and other tissue. The aforementioned median threshold values are converted

to the actual basic restriction values (rms) by applying multipliers such as the safety factor (e.g., a reduction factor of 3 for the brain and other tissue in general public exposure), probability factor and median-to-adverse threshold conversion factor. A comparison between Table 2.1 and Table 2.4 reveals that the fundamental differences between the ICNIRP and IEEE basic restrictions are: (1) the variation in safety factor and threshold conversion factors (only applicable in the IEEE standard), (2) the classification of the exposed tissue group, (3) the assumption of accommodation effect (only applicable in the ICNIRP guidelines) and (4) the frequency-dependent transition points.

2.3.4 Spatial Averaging and 99th Percentile

In ICNIRP-2010 and IEEE Std. C95.6-2002, both biological and numerical rationales are given for the spatial averaging of the induced E-fields. The biological rationales are: (1) a point-wise peak E-field is unlikely to occur during a LF exposure (i.e., excluding the effect of conductive implants); (2) induced E-fields across a certain distance along an axon are required to activate an action potential (AP) [71]. The numerical rationale is: due to computational artefacts such as stair-casing errors, the maximum E-field value of a single voxel element tends to overestimate the actual peak and is less stable than the average of neighbouring voxel values.

ICNIRP-2010

In ICNIRP-2010, a vector average of the E-field within a contiguous tissue volume of $2 \times 2 \times 2$ mm³ is suggested. It is followed by a statement: *for a specific tissue, the 99th percentile value of the electric field is the relevant value to be compared with the basic restriction.* The 99th percentile value refers to the value exceeded by 1% of the total voxel elements. While the choice of 2 mm is stated to be based on the maximum inter-nodal distance between the nodes of Ranvier, ICNIRP acknowledged that a biologically reasonable averaging distance is from 1 mm to 7 mm. The choice of 2 mm can be understood as a practical compromise since at the time of ICNIRP guidelines setting, i.e., the year 2010, the best available numerical dosimetry results are based on anatomical models with 2 mm grid resolution. Hence, no $2 \times 2 \times 2$ mm³ volume-averaged dosimetry results were in fact available at that time since no averaging can be performed on the computational results obtained from a 2 mm grid resolution. This is speculated to be the main reason why the 99th percentile value is suggested in the first place. The rationale for the 99th percentile value is stated in ICNIRP-2010 as: *maximal values in one voxel in a specific tissue are prone to large stair-casing errors associated with sharp corners of the cubical voxel. A solution to obtain more stable peak approximations is based on choosing for the peak value a value representing the 99th percentile value of the induced field in a specific tissue.* ICNIRP also acknowledged that from a biological point of view, the decision of 99th percentile is a *somewhat arbitrary choice.*

While an arbitrary choice is strictly speaking unsuitable for an international exposure guideline, the ICNIRP-recommended instructions for volume averaging and 99th percentile filtering are

ambiguous. For instance, the definition of a contiguous tissue volume is not clearly stated in ICNIRP-2010. One possible interpretation is that the exposed tissue groups defined by ICNIRP: *CNS tissue of the head* (i.e., brain and retina) and *all tissues of body and head* can be treated as target tissues. Alternatively, each individual segmented tissue can be regarded as one target tissue. The lack of clear tissue definition for averaging may lead to uncorrelated findings from different research groups. For the 99th percentile approach, the definition of *specific tissue* is unclear as well. For instance, to assess the induced E-field in the brain, one could take the 99th percentile of the entire brain or take the 99th percentile value of each segmented brain tissue and then choose the maximal value. Since the 99th percentile value is dependent on tissue size and applied grid resolution, the whole-brain 99th percentile value is expected to be less conservative than the maximal 99th percentile value taken from individual brain tissues. In a more extreme case when less than 100 voxels are assigned to a tissue, a 99th percentile value will be invalid unless interpolation is allowed.

IEEE Std. C95.6-2002

In IEEE Std. C95.6-2002, the averaging distance 5 mm is determined with the use of a non-linear model of a myelinated nerve [72]. It is stated that: *The basic restrictions on the in situ electric field apply to an arithmetic average determined over a straight line segment of 0.5 cm length oriented in any direction within the tissue.* A biological rationale is attached to the line averaging: *the most sensitive means of exciting a nerve fibre is via an in situ electric field oriented with the long axis of the nerve fibre, and acting at its terminus.* Both the spatial averaging and its associated biological rationale are coherent. It is relatively easy to define a 5 mm straight line within an investigated tissue, however to comply with the *any direction* orientation requirement, a brute-force approach will require a complete rotation of the line at each pivot point. As a practical compromise, a possible approach is to assume that when the line is centred on a grid and aligned with the direction of the vectorial E-field at that grid, then an averaging along this line would lead to the maximal averaged E-field. An erroneous statement is noted in IEEE Std. C95.6-2002: *the in situ electric field can be determined as the average over a distance $d_a = 5$ mm, which can be readily determined from the potential difference at a spacing of 5 mm.* This statement is only valid for the E-field induction and contact current induction cases. In a B-field induction scenario, the induced E-field is a product of both the magnetic vector potential and electric scalar potential, hence the averaged E-field cannot be obtained solely from electric potential difference.

2.3.5 Conversion Factors between *ex situ* and *in situ* Fields

ICNIRP-2010

To derive a reference level based on an established basic restriction level (or vice versa), the results of computational models are often employed. In ICNIRP-2010, it is stated that the maximum local peak E-field induced in the brain by a 50 Hz uniform B-field is approximately

Chapter 2. Review of LF Exposure and Dosimetry Techniques

23 mV/m to 33 mV/m per mT. As there was no conversion factor for peripheral nerve tissue available at the time of guideline setting for ICNIRP-2010, the skin, which contains peripheral nerve endings, was chosen as a worst-case target tissue. The E-field induced in the skin by a 50 Hz uniform B-field is approximately 20 mV/m to 60 mV/m per mT. For the external E-field exposure, the maximum local E-field induced by a 50 Hz E-field in the brain is approximately 1.7 mV/m to 2.6 mV/m per kV/m. The maximum E-field in the skin is approximately 12 mV/m to 33 mV/m per kV/m. These conversion factors are based on the 99th percentile computational results of anatomical models reported in [11, 12]. The ICNIRP-2010 reference levels are derived based on the 99th percentile values with an additional reduction factor of 3 to account for dosimetric uncertainty. In another word, the conversion factors between the ICNIRP-recommended $2 \times 2 \times 2\text{mm}^3$ volume-averaged E-field and the external field are not applied due to the lack of computational results. It is therefore unclear if the the existing ICNIRP conversion factors can offer sufficient safety margins for stimulation prevention.

IEEE Std. C95.6-2002

In IEEE Std. C95.6-2002, the maximum permissible exposure for the external B-field is derived from ellipsoidal induction models. The use of anatomical model is dismissed due to the lack of model validation and a large variation in reported dosimetry values. It should be noted that the setting of IEEE Std. C95.6-2002 is eight years ahead of ICNIRP-2010. At the time of IEEE standard setting, an analytical model was indeed a more reliable choice than an anatomical model for the derivation of exposure limits. The magnetic induction model treats an exposed human body as an elliptical shape with homogeneous conductivity. Large body dimensions were assumed to provide conservatism. Based on the basic restriction values, magnetic flux density values are analytically computed. Subsequently, the maximum permissible exposure limits are derived after applying multiplying factors such as the safety factor, probability factor and adverse reaction factor. Due to the use of different numerical models (analytical vs. anatomical), a large variation is observed between the ICNIRP and IEEE conversion factors.

For the external E-field, the maximum permissible exposure limits are mainly derived based on the contact current induced in an erect person touching a grounded conductor in a vertically polarized E-field. Experimental data on the threshold of perception for individuals exposed in 60 Hz E-field are also referred. It is stated in IEEE Std. C95.6-2002 that the threshold E-field required to limit the threshold contact current is significantly lower than what is required to directly induce the threshold *in situ* E-field. A conversion example is given by IEEE as follows: *to induce a 17.7 mV/m E-field in the brain of an erect person at 60 Hz, an external vertically polarized E-field of about 59 kV/m is required* [73]. The computational results of anatomical models [11] quoted in ICNIRP-2010 indicate that to induce the same amount of E-field in the brain, the external E-field threshold limit may be as low as 10 kV/m. Similar discrepancy between the ICNIRP and IEEE conversion factors can be observed through further comparison. As shown in Table 2.7 the external 50 Hz B-field limit is 0.904 mT in IEEE Std. C95.6-2002 and 0.2 mT in ICNIRP-2002, while the induced E-field limit is 0.0147 V/m (for IEEE) and 0.02 V/m

Table 2.7: A list of exposure limits at 50 Hz for ICNIRP-2010 and IEEE Std. C95.6-2002.

	IEEE Std. C95.6-2002	ICNIRP-2010
General public		
Basic restriction (V/m)		
Brain (CNS tissues)	1.47×10^{-2}	0.02
Extremities (PNS tissues)	2.10	0.4
Reference level		
E-field (kV/m)	5	5
B-field (mT)	0.904	0.2
Occupational (controlled environment)		
Basic restriction (V/m)		
Brain (CNS tissues)	4.42×10^{-2}	0.1
Extremities (PNS tissues)	2.10	0.8
Reference level		
E-field (kV/m)	20	10
B-field (mT)	2.71	1.0

(for ICNIRP), respectively. This indicates that the conversion factors at 50 Hz differ by more than a factor of 4 between IEEE and ICNIRP. Such discrepancy should be closely investigated to assess the validity of the recommended reference levels with respect to the associated basic restrictions.

2.3.6 Summary on the ICNIRP and IEEE Exposure Limits

This section provides an in-depth discussion on the derivations of the ICNIRP and IEEE exposure limits. Limited by the scope of research objectives, the details pertaining to the exposure assessment of pulsed (non-sinusoidal) fields, additive exposure (both E-field and B-field), and contact-induced current threshold are not included in the discussion. By analyzing the rationales behind the derivations of the basic restriction and reference levels, a clear frame work of the exposure limit setting is presented. A comparison between the ICNIRP-2010 exposure guidelines and the IEEE Std. C95.6-2002 exposure standard reveals that there are significant discrepancies between the two sets of exposure limits. Recall the ICNIRP-2010 statement: *the reference levels are calculated for the condition of maximum coupling of the field to the exposed individual, thereby providing maximum protection* and the IEEE Std. C95.6-2002 statement: *compliance with the maximum permissible exposure level ensures compliance with the basic restrictions*. Both ICNIRP and IEEE claim that the recommended exposure limits provide maximum protection against LF E-field and B-field exposure. To assess the validity of these claims, up-to-date scientific evidences should be provided to support the derivations of exposure limits.

2.4 Low Frequency Field Measurement Techniques

2.4.1 Free Space Electric and Magnetic Field Measurement

For the measurement of low frequency E-field and B-field, field meters are often employed [74]. There are in general two types of E-field meter. One type is known as the self-contained or free-body meter which measures the current flow between two halves of an isolated conductive body (probe) immersed in an E-field. The other type is the ground reference meter which measures the current flow from a probe placed inside an E-field to the ground. The free-body type is portable and often used for outdoor measurements, e.g., area near power lines. An E-field meter consists of two parts: probe and detector. During a measurement, the probe is introduced into an E-field on an insulating handle while the detector measures the current induced between the two conducting halves of the probe. Precaution should be taken to minimize E-field perturbation from the probe and the person making the measurement. For the measurement of the E-field acting on a conductive surface (e.g., surface of a human body), a small surface element can be placed directly over the surface of interest. The current induced in this element is directly related to the average E-field acting on it. A B-field meter typically consists of electrically shielded coils of wire. When the coils are immersed in a time-varying B-field, a current is induced corresponding to the applied B-field. The induced current is assumed to be sufficiently small so that the opposing secondary B-field generated by it can be neglected. The B-field can then be extrapolated from the measured induced current value. In the context of a LF exposure guideline compliance assessment, the free space field measurement data of an exposure environment is compared with the reference level to preliminarily determine if the peak induced E-field in an exposed object exceeds the basic restriction.



Figure 2.6: (a) A B-field meter and (b) a dual-element E-field and B-field meter, copyright Narda Safety Test Solutions GmbH.

2.4.2 Limitations of Induced Field Measurement

For the measurement of the induced E-field (current density) inside a human body, experimental techniques adopting either an anatomically shaped phantom [21] or non-invasive measurement technique [22] have been investigated. The first approach utilizes a scaled-down human model (see Figure 2.7) filled with a homogeneous conductive solution, e.g., saline. An E-field probe is inserted into the model at various locations to determine the induced E-field and subsequently the current density can be calculated based on the measured E-field and known conductivity value. An advantage of this measurement technique is that the directional characteristics of the induced fields can be captured. On the down side, the field probe might perturb the induced E-fields and contribute to measurement error. In addition, a homogeneous phantom is inadequate to represent the realistic human tissue composition since the human body tissues are highly inhomogeneous from a dielectric property point of view. The second approach can be applied to achieve the measurement of the *short-circuit* current (i.e., the current across the feet of a grounded person) or body surface potential distribution. This type of *ex situ* measurement could yield the maximum current flow occurring at different cross-sections of a human body. However it does not provide information regarding the current distribution within a body. As the human body is composed of biological tissues with various sizes, shapes and dielectric properties, the measurement of the induced E-fields in such a complex environment is limited by the existing phantom modelling and sensor technology. Hence, numerical dosimetry is often employed when detailed induced field distribution and peak magnitude are required.

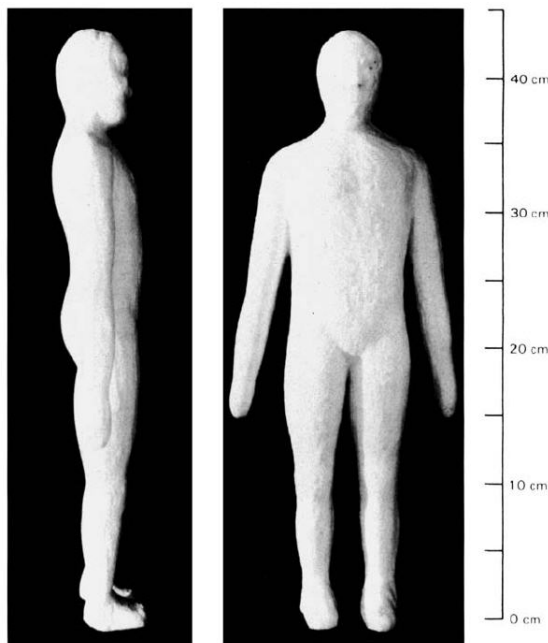


Figure 2.7: A scaled-down human model made of styrofoam cast and filled with saline solution, copyright Kaune and Forsythe 1985 pp.17 [21].

2.5 Anatomical Model and Tissue Dielectric Property

2.5.1 High-Resolution MRI-based Anatomical Models

In the early numerical dosimetry studies, spherical or cubic models were used to represent human bodies [23]. A new class of millimeter-resolution models of the human body emerged in the 1990s, for instance, the “Visible Man Project” [75] by the National Institutes of Health (NIH). Such high resolution anatomical model can be derived from cryosection, Computed Tomography (CT) or Magnetic Resonance Imaging (MRI) data. These models provide detailed geometrical representations of biological tissues and organs. Furthermore the distinct dielectric properties of body tissues can be assigned to the segmented tissue models. In this study, anatomical models [76] from different gender and age groups are employed to provide a broad coverage of body shapes. As shown in Figure 2.8, the models include Roberta, a 5-year-old girl (weight 18 kg, height 1.1 m), Dizzy, an 8-year-old boy (26 kg, 1.4 m), Duke, a 34-year-old male (70 kg, 1.7 m), Ella, a 26-year-old female (58 kg, 1.6 m), Fats, a 37-year-old obese male (120 kg, 1.9 m). These computer-aided-design (CAD) models are derived from high resolution MRI scans and consist of approximately 200 organ parts and 80 tissue types. The CAD format of the objects allows the meshing of the models to be performed at an arbitrary resolution (see Figure 2.9) without the loss of details and small features due to multiple samplings.

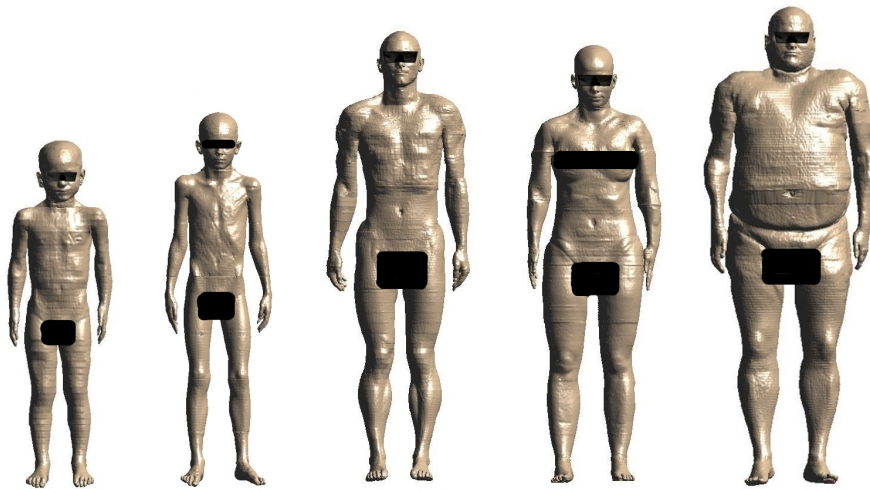


Figure 2.8: The anatomical models employed in this study, from left to right, Roberta, Dizzie, Duke, Ella and Fats.

2.5.2 Posable Anatomical Model

Most of the published literatures [6–17] on LF exposure of the human body are based on fixed-posture body models which are typically in a general standing posture (i.e., body straight with hands on the side). A fixed-posture anatomical CAD model provides general numerical dosimetry results without considering the possible effects of body posture variation on the

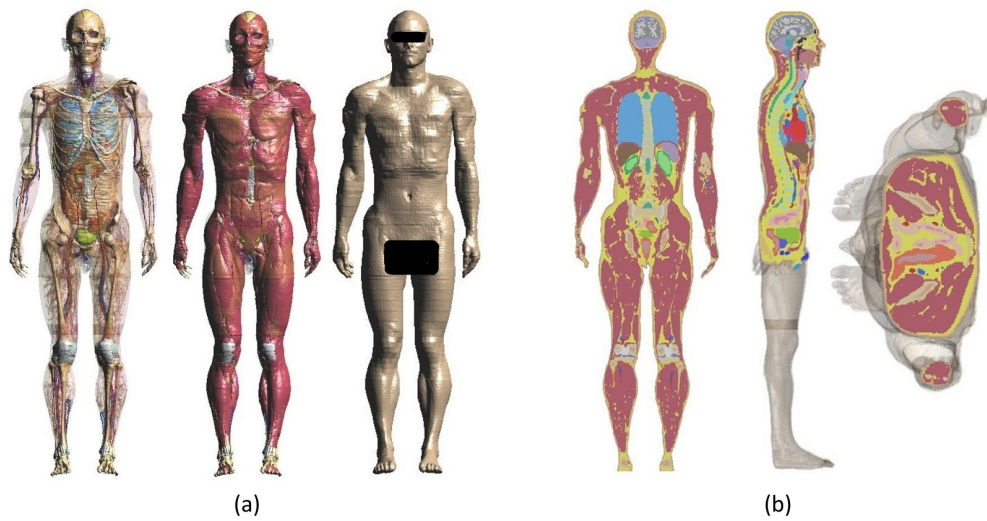


Figure 2.9: The Duke model with (a) detailed skeleton and tissue composition and (b) 2 mm grid resolution voxel slices.

induced E-field distribution and strength. The anatomical models employed in this study belong to a special group of 3D human CAD models known as the *posable human*. The word “posable” implies that the models can be manipulated into different body postures. This is achieved by an approach derived from the dual-quaternion-skinning method, volume-preserving deformations and non-iterative method based on Lagrange multipliers [77]. Theposable human models can assume many realistic body postures, e.g., sitting, squatting and stretching (see Figure 2.10).

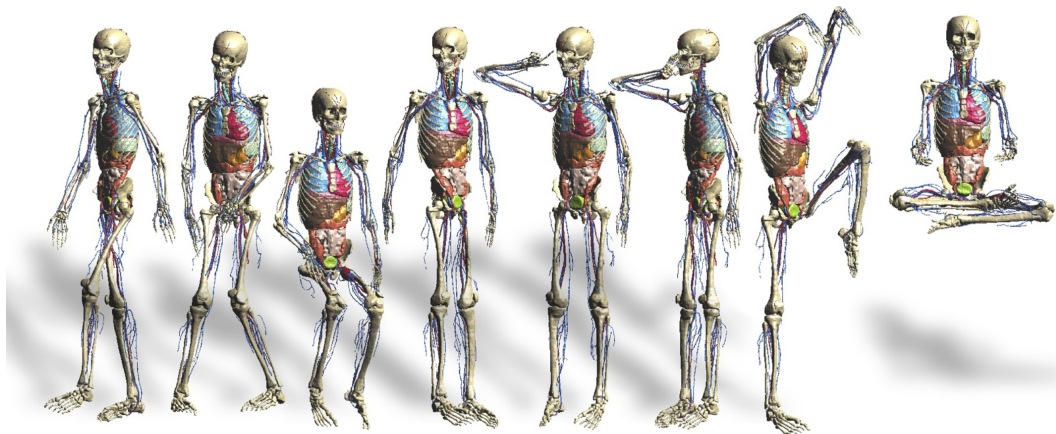


Figure 2.10: Aposable anatomical model manipulated into various postures, copyright IT'IS Foundation, Zurich, Switzerland.

2.5.3 Low Frequency Human Body Tissue Dielectric Property

The dielectric properties of biological tissues vary significantly with respect to frequency. In the low frequency range, human body tissues are mostly diamagnetic, i.e., the permeability of the tissue is equivalent to the free-space permeability (i.e., $\mu = \mu_0$). In addition, most of the tissues exhibit *ohmic-current-dominant* characteristic (i.e., $\sigma \gg \omega\epsilon$). In this study, the human body tissues are assumed to be piecewise-isotropic such that the tensor material parameters, e.g., permittivity (ϵ), conductivity (σ) and permeability (μ), can be treated as scalars. The anisotropy characteristics of the human body tissues are not considered. The tissue conductivity and relative permittivity values used in this work are obtained from [60]. A list of dielectric property values at 50 Hz for selected human body tissues is shown in Table 2.8. As shown, the cerebrospinal fluid exhibits the highest conductivity value and the skin exhibits the lowest conductivity value among all the human body tissues at 50 Hz. At 50 Hz, the relative permittivity of a human body tissue has a dynamic range of 10^2 to 10^7 and the conductivity has a dynamic range of 10^{-4} to 10^0 .

Table 2.8: Dielectric property values of selected human body tissues at 50 Hz.

Tissue	ϵ_r	σ (S/m)
Blood	5260	0.70
Bone	8870	0.02
Brain (Grey Matter)	12100000	0.08
Brain (White Matter)	5290000	0.05
Cartilage	1640000	0.17
Cerebellum	12100000	0.10
Cerebrospinal Fluid	109	2.00
Fat	458000	0.04
Gallbladder	1450	0.90
Heart Muscle	8660000	0.08
Kidney	10100000	0.09
Large intestine	32100000	0.055
Liver	1830000	0.04
Lung	5760000	0.07
Midbrain	12100000	0.10
Muscle	17700000	0.23
Nerve	1610000	0.03
Penis	8100000	0.026
Pineal body	1640000	0.52
Skin	1140	0.0002
Small Intestine	2030000	0.52
Spinal Cord	1610000	0.03
Spleen	10200000	0.09
Stomach	1640000	0.52
Tendon/ligament	17100000	0.27
Uterus	31800000	0.23

2.6 Low Frequency Numerical Dosimetry Techniques

Computational electromagnetics focuses on solving Maxwell's equations by the means of numerical techniques. It benefits from the continuous advancement of computer technology in terms of processing speed, random access memory (RAM) and data storage. For a LF exposure problem, with appropriate assumptions, the full Maxwell's equations can be simplified. This allows an exposure scenario with complex human body geometry and field distribution to be discretized and solved with satisfactory accuracy and efficiency. In this section, various existing computation methods are reviewed and a numerical solver tailored for LF numerical dosimetry is introduced.

2.6.1 Electromagnetic Quasi-Static Approximation

Low frequency computational (analytical and numerical) dosimetry benefits from the electromagnetic quasi-static approximation. This assumption can be applied in a frequency range from 1 Hz up to a few kHz and it allows the analysis of the interactions between biological systems and LF E-field and B-field to be greatly simplified if the following conditions are satisfied [78]:

(a) The size of the exposed object is small when compared to the free-space wavelength of the incident field. This condition ensures that field propagation effects can be neglected, which also implies that the E-field and B-field can be conditionally represented by electro-static or magneto-static fields.

(b) The size of the exposed object is comparable or smaller than the skin depth of the materials inside the object. This condition ensures that the secondary B-field produced by the currents induced in the object will be small and hence the incident B-field is unperturbed by the exposed object. This condition also implies that the secondary B-field will not affect the incident and induced E-fields.

(c) The exposed object is conductive and inside it the conduction currents dominate over the displacement currents (i.e., a large loss tangent). This *ohmic-current-dominant* condition is, strictly speaking, not an essential requirement for the fulfilment of the quasi-static approximation. Its existence is to allow further simplification of the field equations.

Mathematically speaking, the quasi-static approximation can be represented by a set of equations. Maxwell's equations can be expressed in the complex phasor form $\mathbf{X}(r, t) = \Re\{e^{j\omega t}\mathbf{X}(r)\}$ with angular frequency ω :

$$\nabla \times \mathbf{E} = -j\omega\mathbf{B} \tag{2.3}$$

$$\nabla \times \mathbf{H} = j\omega\mathbf{D} + \mathbf{J} \quad (2.4)$$

$$\nabla \cdot \mathbf{D} = \rho \quad (2.5)$$

$$\nabla \cdot \mathbf{B} = 0 \quad (2.6)$$

where \mathbf{E} , \mathbf{D} , \mathbf{B} , \mathbf{H} , \mathbf{J} and ρ are the electric field, displacement current, magnetic flux density, magnetic field, current density and volume charge density, respectively. For linear materials, three constitutive laws govern the electromagnetic theory together with Maxwell's equations:

$$\mathbf{D} = \epsilon\mathbf{E} \quad (2.7)$$

$$\mathbf{B} = \mu\mathbf{H} \quad (2.8)$$

$$\mathbf{J} = \sigma\mathbf{E} + \mathbf{J}_0 \quad (2.9)$$

where σ is the effective conductivity, μ is the permeability, \mathbf{J}_0 is the source current and ϵ is the permittivity given by $\epsilon = \epsilon_r\epsilon_0$ where ϵ_r is the relative permittivity and ϵ_0 is the free space permittivity. A complex permittivity $\tilde{\epsilon}$ is defined as

$$\tilde{\epsilon} = \epsilon + \frac{\sigma}{j\omega} \quad (2.10)$$

The quasi-static approximation is derived from Maxwell's equations by neglecting either the magnetic induction or the electric displacement current. This is equivalent to replacing (2.3) with $\nabla \times \mathbf{E} \simeq 0$ or replacing (2.4) with $\nabla \times \mathbf{H} \simeq \mathbf{J}_0$. A decision as to whether a quasi-static field ought to be classified as Electro-Quasi-Static (EQS) or Magneto-Quasi-Static (MQS) can be

deduced by a simple rule of thumb: lower the frequency of the driving source to zero so that the fields become static, if the B-field vanishes in this limit then the field is EQS; if the E-field vanishes then the field is MQS.

To justify the assumption of quasi-static approximation, one has to ensure that neglecting the magnetic induction in EQS or the displacement current in MQS does not produce significant error. By defining a characteristic length d and a characteristic time τ , the spatial derivatives that make up the curl and divergence operators can be approximated as $\frac{1}{d}$ and the temporal derivative as $\frac{1}{\tau}$. For the EQS approximation, based on (2.3) and (2.4), a quantity E_n given in (2.11) is defined as the E-field term neglected due to the approximation. The quasi-static field and the ratio of the neglected field to the quasi-static field are given in (2.12) and (2.13), respectively. In a similar manner, the ratio for the MQS approximation can be deduced and proven to be the same as that of the EQS case. Both the EQS and MQS approximations are valid by assuming a sufficiently low frequency and small characteristic length, i.e., $\omega^2 \mu \tilde{\epsilon} d^2 \ll 1$ (2.14). This is equivalent to the statement that the quasi-static approximation is valid if an E-field or B-field can propagate through a length d in a time that is short compared to the τ of interest. For a sinusoidal excitation, τ is the reciprocal of the angular frequency ω . The condition (2.14) must be satisfied by all the materials within the computation domain.

$$E_n = \frac{\mu \rho d^3 \tilde{\epsilon}}{\tau^2 \epsilon} \quad (2.11)$$

$$E = \frac{\rho d}{\epsilon} \quad (2.12)$$

$$\frac{E_n}{E} = \frac{H_n}{H} = \frac{\mu \tilde{\epsilon} d^2}{\tau^2} = \omega^2 \mu \tilde{\epsilon} d^2 \quad (2.13)$$

$$\omega^2 \mu \tilde{\epsilon} d^2 \ll 1 \quad (2.14)$$

2.6.2 Existing Low Frequency Numerical Dosimetry Techniques

Finite-Difference Time-Domain (FDTD) Method

The Finite Difference Time Domain (FDTD) [79] method is one of the most widely used computational methods for numerical dosimetry due to its versatility and computational efficiency. The FDTD method solves Maxwell's equations in the time domain for the six vector

Chapter 2. Review of LF Exposure and Dosimetry Techniques

components of electric and magnetic fields arranged in a cubical cell known as Yee cell (see Figure 2.11). The main constraint for the FDTD method is that the cell size (Δd) must be smaller than the smallest wavelength of the materials present in the computation domain. In order to obtain stable solution, the *Courant-Friedrich-Levy* (CFL) criterion must be satisfied. This criterion is stated as $\delta t \leq \Delta d / \sqrt{3}c$, where δt is the time step, Δd is the space step ($\Delta d = \Delta x = \Delta y = \Delta z$) and c is the speed of light. When the FDTD method is applied to a human body exposure simulation, the computation continues until steady state is reached after the incident wave has propagated through the body and back to the source a few times. For a LF exposure simulation, as the human body is much smaller compared to the wavelength, the number of time step which is required to compute the steady-state magnitude and phase is large. This implies that the standard FDTD method is extremely inefficient if it is to be applied directly to a LF problem. As a result, frequency scaling is often employed at low frequency for the FDTD method. This is done by performing a simulation at a slightly higher frequency f' than the actual frequency f . The results are linearly scaled to the desired frequency using (2.15). The tissue dielectric properties at frequency f are assumed to be consistent with the values at frequency f' so that no scaling of the tissue properties is necessary. The drawback of the frequency-scaling approach will be discussed in Section 3.4.

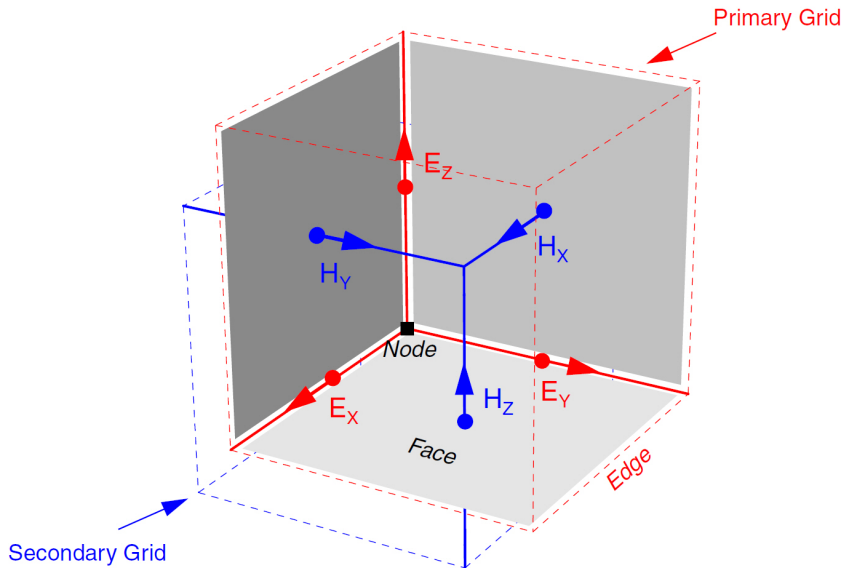


Figure 2.11: 3D Yee cell showing the E- and H-field components in the staggered grid.

$$E(f) = \frac{f}{f'} E(f') \quad (2.15)$$

An alternative approach to apply the FDTD method at low frequency is to take advantage of the fact that the phase of the external and internal fields of a conductive body is known in the quasi-static state. The excitation source can be modelled as a ramped function, e.g.,

the start of a sinusoid with an infinitely long period. A smooth start is used to avoid high-frequency contamination. The amplitude of the external field can be obtained from their rate of change and the amplitude of the internal field from the actual values. The Perfectly-Matched-Layer (PML) technique is valid as an absorbing boundary condition (ABC) for low frequency problems. The quasi-static FDTD approach has been applied to LF numerical dosimetry simulations in [14–16, 80].

Boundary Element Method (BEM)

The Boundary Element Method (BEM) is a combination of the classical boundary integral equation method and the discretization concepts were originated from the Finite Element Method [81]. It is essentially the Method of Moment (MoM) technique when sub-sectional bases and Dirac delta function are used as weighting functions. In a BEM approach, the integral equation formulation of the differential equations governing the electromagnetic problem is derived first. For EQS and MQS problems, the governing differential equation is a Laplace equation for a source-free domain and a Poisson equation if source is present in the domain. Once the integral equation formulation is obtained, the boundaries of a computation domain are discretized into a set of elements. The unknown solution over each element is approximated by an interpolation function which is associated with the values of the functions at the element nodes. Subsequently the corresponding integral equation can be converted into a system of algebraic equations. The solution of the algebraic equation system gives the approximate solution of the original integral equation. The boundary geometry can be discretized into a series of constant, linear or quadratic elements. The geometry of the elements is then expressed in the form of interpolation or shape functions. LF numerical dosimetry examples employing the BEM technique can be found in [41, 82].

Scalar Potential Finite Difference (SPFD) Method

A popular numerical technique for LF numerical dosimetry is the Scalar Potential Finite Difference (SPFD) method [6–12]. It is primarily used for B-field induction and contact current induction problems. The SPFD formulation can be obtained from Maxwell's equations using the concepts of electric scalar potential ϕ_e , magnetic vector potential \mathbf{A} , as well as the electromagnetic quasi-static approximation.

Assuming a magnetic vector potential \mathbf{A} where $\mathbf{B} = \nabla \times \mathbf{A}$ and an electric scalar potential ϕ_e , (2.3) can be written as

$$\nabla \times (\mathbf{E} + j\omega\mathbf{A}) = 0 \tag{2.16}$$

Chapter 2. Review of LF Exposure and Dosimetry Techniques

Using the vector identity $\nabla \times (-\nabla \phi_e) = \vec{0}$, (2.16) can be written as

$$\mathbf{E} = -\nabla \cdot \phi_e - j\omega\mathbf{A} \quad (2.17)$$

From (2.4) and (2.7):

$$\nabla \times \frac{1}{\mu} \nabla \times \mathbf{A} = j\omega\tilde{\epsilon}(-\nabla \cdot \phi_e - j\omega\mathbf{A}) + \mathbf{J} \quad (2.18)$$

Taking $\nabla \cdot$ on both sides of (2.18) and assuming that no charge is generated ($\nabla \cdot \mathbf{J} = 0$ for steady current), (2.18) leads to the scalar potential equation:

$$\nabla \cdot \tilde{\epsilon}(-\nabla \phi_e) = j\omega \nabla \cdot \tilde{\epsilon}\mathbf{A} \quad (2.19)$$

At low frequency, biological tissues in general exhibit *ohmic-current-dominant* characteristic (i.e., $\sigma \gg \omega\epsilon$), hence (2.19) can be further simplified to:

$$\nabla \cdot [\sigma(-\nabla \phi_e - j\omega\mathbf{A})] = 0 \quad (2.20)$$

As suggested by the quasi-static approximation, the excitation terms which account for the impressed E-field and B-field can be considered separately. For the MQS case, the condition $|\omega^2\mu\tilde{\epsilon}d^2| \ll 1$ is introduced in order to neglect the $\omega^2\tilde{\epsilon}\mathbf{A}$ and $j\omega\tilde{\epsilon}\nabla\phi_e$ terms in (2.18). As a result, in addition to the condition $\omega^2\mu\epsilon d^2 \ll 1$, the condition $\omega\mu\sigma d^2 \ll 1$ is imposed to ensure that the ohmic current only negligibly perturb the incident B-field. If $|\omega^2\mu\tilde{\epsilon}d^2| \ll 1$ is satisfied, i.e., the $\nabla \times \nabla \times$ term in (2.18) dominates over the other two terms and (2.18) becomes

$$\nabla \times \frac{1}{\mu} \nabla \times \mathbf{A} = \mathbf{J}_0 \quad (2.21)$$

The magnetic vector potential \mathbf{A} is now equivalent to the magneto-static vector potential \mathbf{A}_0 which is completely decoupled from \mathbf{E} . If the permeability μ is constant over the entire

computation domain Ω , \mathbf{A}_0 can be computed by the Biot-Savart law:

$$\mathbf{A}_0(r) = \frac{\mu}{4\pi} \int_{\Omega} \frac{\mathbf{J}_0(r')}{|r - r'|} d^3 r' \quad (2.22)$$

To establish the discrete form of the SPFD formulation, one could adopt the integral form of (2.20) by applying the divergence theorem. Finite Difference (FD) technique is utilized to define the potential at a node (where cells with dimensions Δ meet) in terms of the potentials at neighbouring nodes. The conductivity values (σ_i) of neighbouring cells are evaluated at half-node points (i.e., half way between nodes), together with the magnetic vector potential values (A_i) at these half-nodes. The three-dimensional segmented SPFD formulation can be expressed as:

$$\phi = \frac{1}{\sum_{i=1}^6 \sigma_i / \Delta_i^2} \cdot \sum_{i=1}^6 \left\langle \frac{\sigma_i}{\Delta_i^2} [\phi_i - (-1)^i j \omega \Delta_i A_i] \right\rangle \quad (2.23)$$

This finite difference problem can be solved using techniques such as the *successive over-relaxation* method [83]. A distinct advantage of the SPFD method is that its computation is only performed within a lossy material volume due to the fact that the scalar potential values in conductive regions (inside the body) are not affected by values in the non-conductive regions (free space) since the average conductivities that link vertexes on the border of the conductive region with the non-conductive vertexes are null. This is only valid with the assumption that the lossy materials exhibit *ohmic-current-dominant* characteristics (i.e., $\sigma \gg \omega \epsilon$).

2.6.3 Scalar Potential Finite Element (SPFE) Method

In this thesis work, an alternative numerical technique is utilized. The adopted approach is similar to the aforementioned SPFD method in the sense that it is also based on the scalar potential equation with electromagnetic quasi-static approximation. The finite element method [81] is employed for the discretization of the problem instead of the finite difference approach utilized in the SPFD method. The finite element discretization approach is only a result of practical implementation choice; it holds no distinct advantage over the finite difference approach. The Scalar Potential Finite Element (SPFE) formulation begins with (2.19), and is expanded into the EQS and MQS cases.

In the EQS case, assuming that no current source is present (i.e., $\mathbf{J}_0 = 0$), (2.19) is reduced to:

$$\nabla \cdot \tilde{\epsilon}(-\nabla \phi_e) = 0 \quad (2.24)$$

With *ohmic-current-dominant* approximation, (2.24) can be written as:

$$\nabla \cdot \sigma(-\nabla \phi_e) = 0 \quad (2.25)$$

Two E-field induction scenarios are described by the aforementioned equations: (2.24) represents the direct E-field induction and (2.25) represents the indirect contact current induction case. When (2.24) is employed, both the external E-field and induced E-field are computed. If (2.25) is utilized, only the E-fields induced in lossy materials (with *ohmic-current-dominant* assumption) due to electric potential difference are computed. During a computation, once ϕ_e is solved, \mathbf{E} can be computed by $\mathbf{E} = -\nabla \cdot \phi_e$. Two boundary conditions, namely Dirichlet (i.e., fixed potential value) and Neumann (i.e., vanishing flux normal to the boundary), are available for the EQS solver.

In the MQS case, the magnetic vector potential \mathbf{A} is first solved by the Biot-Savart law (2.22) and then (2.20) is employed to solve for ϕ_e . Following that, (2.17) is employed for the calculation of \mathbf{E} based on the previously obtained ϕ_e and \mathbf{A} values. (2.20), (2.24) and (2.25) can be discretized using the finite element method and linear nodal basis functions on a structured rectilinear grid. For (2.20) and (2.25), the Neumann boundary condition is imposed for ϕ_e at the tissue-air interface and the value of ϕ_e on one node is fixed (i.e., Dirichlet boundary condition) to remove the degrees of freedom of $\Delta \phi_e$ from the linear system. The resulting linear equation system is solved using the conjugate gradient method [84]. The Scalar Potential Finite Element (SPFE) solver has been implemented in the commercial software package SEMCAD-X [48]. Unless specified otherwise, low frequency dosimetry computations presented in this work are performed using the SPFE solver with a stopping criterion of 8 orders of magnitude reduction for the initial residuum (i.e., the preconditioned residuum drops to 10^{-8} of its initial value).

2.7 Validation of the SPFE Method

2.7.1 Comparison with Analytical Solutions

The validation of the SPFE solver is first conducted by comparing its results to the solutions obtained from analytical methods. An exposure scenario involving an ungrounded ellipsoidal object illuminated by uniform E-field or B-field is chosen for this comparison study. Three orientations of the applied fields along the x , y and z directions are considered. As shown in Figure 2.12, an ellipsoid is defined by three parameters: a , b and c , respectively. To roughly represent the size of an adult human body, the parameters a , b and c are assigned to be 0.9 m,

0.2 m and 0.1 m respectively. The xz plane is considered to be the front of the body while $2a$ is the vertical height of the body. The three field orientations are labelled as TOP (top-to-bottom, z -direction), AP (front-to-back, y -direction) and LAT (side-to-side, x -direction) according to the plane of incidence with respect to the ellipsoid.

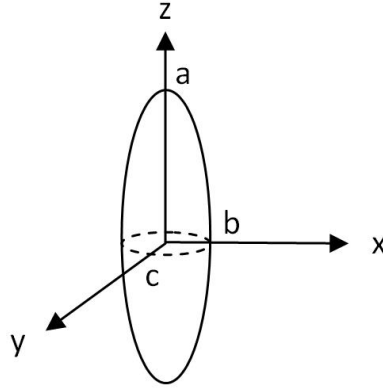


Figure 2.12: The ellipsoidal body employed in the validation study.

The surface of an ellipsoid can be described by the following equation:

$$\frac{x^2}{a^2} + \frac{y^2}{b^2} + \frac{z^2}{c^2} = 1 \quad (2.26)$$

where x, y, z are the rectangular coordinates. The size and shape of an ellipsoid are determined by the values of a, b and c , where $c \geq b \geq a$. Ellipsoidal coordinates (ξ, η, ζ) is used instead of the Cartesian coordinates (x, y, z) to represent such a shape. An analytical approach based on Stevenson's theory [85] is utilized for the calculation of the E-fields induced inside the ellipsoid due to the exposure to an external uniform E-field. To outline the theory, let E_o and E_i denote the incident E-field and the induced E-field, expressed in root mean square form.

The E-field induced inside an ellipsoid (E_i) by an external uniform vertically polarized (i.e., aligned along the z axis) E-field (E_o) is give by:

$$E_i = \frac{\epsilon_0 E_o}{\epsilon} S \quad (2.27)$$

where

$$S = \frac{abc}{2} \int_0^\infty \frac{d\xi}{(\xi + a^2)\sqrt{(\xi + a^2)(\xi + b^2)(\xi + c^2)}} \quad (2.28)$$

The E-field induced by an external uniform B-field (B_o) aligned along the z axis, is given by:

$$E_i = \frac{\omega B_o}{b^2 + c^2} \sqrt{b^4 z^2 + c^4 y^2} \quad (2.29)$$

The maximum induced E-field occurs when $z = c$ and $y = 0$, and is given as:

$$E_{i \max} = \frac{\omega B_o}{b^2 + c^2} b^2 c \quad (2.30)$$

The detailed derivations and solutions of (2.27) and (2.29) can be found in [86] and [87], respectively. The equations can be modified for the other two field orientations by interchanging a and b (or a and c). The ellipsoid is assumed to be homogeneous and has a conductivity value of 0.15 S/m and a relative permittivity value of 7×10^5 . The operating frequency is set to be 100 Hz, at which the requirements for the quasi-static approximation are valid. The intensities of the incident uniform E-field and B-field are set to be 1 V/m and 1 μ T, respectively. Both quantities are expressed in terms of the root-mean-square (rms) values.

A uniform grid size of 1 mm is applied to voxel the ellipsoid with the SPFE solver. The peak induced E-fields calculated by the analytical methods and the SPFE solver are presented in Table 2.9. The peak values obtained from the SPFE solver are extracted at the peak induction locations predicted by the analytical solutions so that numerical artefacts due to stair-casing errors can be avoided to a large extent. For the EQS calculations with the SPFE solver, the preconditioned residual tolerance is set to 10^{-14} to compensate the larger dynamic range between the external E-field and the induced E-field. The solutions obtained from the SPFE solver show good agreement with the analytical solutions ($\Delta \leq 2\%$). The discrepancy between the two solutions is mainly due to the discretization uncertainties which cause the dimensions of the voxelized ellipsoid to be slightly different from the actual values.

2.7.2 Comparison with FDTD Solutions

A uniform LF field exposure scenario with the homogeneous ellipsoid is simulated using a Finite Difference Time Domain (FDTD) full-wave solver from SEMCAD-X [48] and the results are compared to the values obtained from the SPFE solver. The upper bound of the low frequency spectrum, 100 kHz, is selected as the field frequency in this case. The relative permittivity and conductivity of the ellipsoid is assigned to be 1000 and 0.15 S/m, respectively. The incident E-field and B-field strengths are set to be 1 V/m and 1 μ T, respectively. A uniform grid size of 1 mm is applied for both solvers. The stopping criterion for the SPFE solver is 8 orders of magnitude reduction for the initial residual while 20 sinusoidal simulation periods are applied for the FDTD solver. Uniform E-field and B-field are generated in the FDTD

Table 2.9: The peak induced E-field (V/m) at 100 Hz, Δ denotes the difference between the analytical and SPFE solutions in percentage ($\Delta = \frac{|E_{\text{SPFE}} - E_{\text{analytical}}|}{E_{\text{analytical}}} \%$).

Orientation of the external E-field			
V/m	TOP(E_z)	AP(E_y)	LAT(E_x)
analytical	9.6×10^{-7}	5.7×10^{-8}	1.20×10^{-7}
SPFE	9.8×10^{-7}	5.8×10^{-8}	1.22×10^{-7}
Δ	2.0%	1.8%	1.6%
Orientation of the external B-field			
V/m	TOP(B_z)	AP(B_y)	LAT(B_x)
analytical	5.0×10^{-5}	1.20×10^{-4}	6.2×10^{-5}
SPFE	5.1×10^{-5}	1.22×10^{-4}	6.3×10^{-5}
Δ	2.0%	1.6%	1.7%

simulations by utilizing two uniform plane waves oriented with either the electric component or the magnetic component opposite to its counterpart. For the vertically polarized E-field excitation case, the distributions of the perturbed external E-field are shown in Figure 2.13 for both solvers. The field patterns and magnitude agree well between the two solvers. A comparison of the peak induced E-field reveals that $\Delta(\frac{|E_{\text{SPFE}} - E_{\text{FDTD}}|}{E_{\text{average}}} \%) \leq 5\%$ is achieved between the two numerical solvers for both the EQS and MQS exposure scenarios.

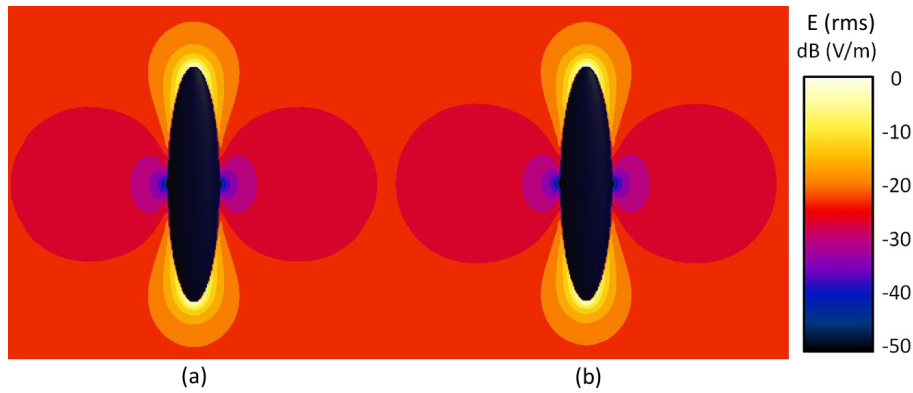


Figure 2.13: The perturbed vertically-polarized external E-field distribution at 100 kHz computed by (a) the SPFE solver and (b) the FDTD solver.

2.8 Quasi-Static Approximation for a Full-Body Exposure

2.8.1 Quasi-Static Frequency Limit

As stated in Section 2.6.1, the quasi-static approximation is valid when an E-field or B-field propagates through a characteristic length d in a time which is short compared to a characteristic time τ of interest. When this condition is satisfied, wave propagation can be neglected,

Chapter 2. Review of LF Exposure and Dosimetry Techniques

i.e., a change in one location implies an immediate change throughout the computational domain. The validity of the quasi-static approximation for the SPFE solver is guaranteed by satisfying the condition $|\omega^2 \mu \tilde{\epsilon} d^2| \ll 1$, this condition can be written as two real-valued criteria:

$$\omega^2 \mu \epsilon d^2 \ll 1 \quad (2.31)$$

$$\omega \mu \sigma d^2 \ll 1 \quad (2.32)$$

In addition, the *ohmic-current-dominant* tissue property condition can be expressed as:

$$\frac{\sigma}{\omega \epsilon} \gg 1 \quad (2.33)$$

For a full human body exposure scenario, the characteristic length d can be approximated by the maximum diagonal length of the body. To assess the valid frequency range for a full-body exposure, (2.31) and (2.32) are computed based on the body height, tissue dielectric property and tissue composition of an adult male and an adult female. The diagonal length of the male adult is assumed to be 2 m and the length of the female adult is assumed to be 1.8 m. The tissue dielectric property values are obtained from [60] and the tissue composition data is obtained from [61]. The tissue composition data is applied to derive a weighted average for the corresponding relative permittivity or conductivity value. As shown in Table 2.10, the mean tissue weights of the skin, fat, muscle, bone and other body tissue are expressed as percentages of the total body weight measured based on 12 male and 13 female cadaver subjects [61]. By assuming equal tissue density and excluding the other body tissues, the weighted average values of the relative permittivity and conductivity can be derived based on the composition of the skin, fat, muscle and bone (which made up approximately 85% of the total body mass). The weighted average dielectric property values based on the adult male tissue composition (see Table 2.10) is presented in Figure 2.14. The left-hand-side values of (2.31), (2.32) and (2.33) are computed based on the weighted average dielectric property values of the adult male body and presented in Figure 2.15. The variations in tissue composition and body height for the adult female case are found to have negligible impact on the left-hand-side values. It is observed that to satisfy the inequality condition for both (2.31) and (2.32), the upper limit of the frequency range is at approximately 200 kHz. The left-hand-side values of (2.33) indicate that the *ohmic-current-dominant* assumption is valid for whole-body exposure in the 1 Hz to 100 kHz frequency range when the weighted average whole-body tissue dielectric properties are considered.

Table 2.10: The tissue composition of adult male and female as a percentage of the total body weight.

Sex	Weight (kg)	Skin	Fat	Muscle	Bone	Other	Total
Male	66.2	5.6%	28.1%	37.4%	14.3%	14.6%	100%
Female	64.3	5.5%	34.6%	32.9%	13.4%	13.6%	100%

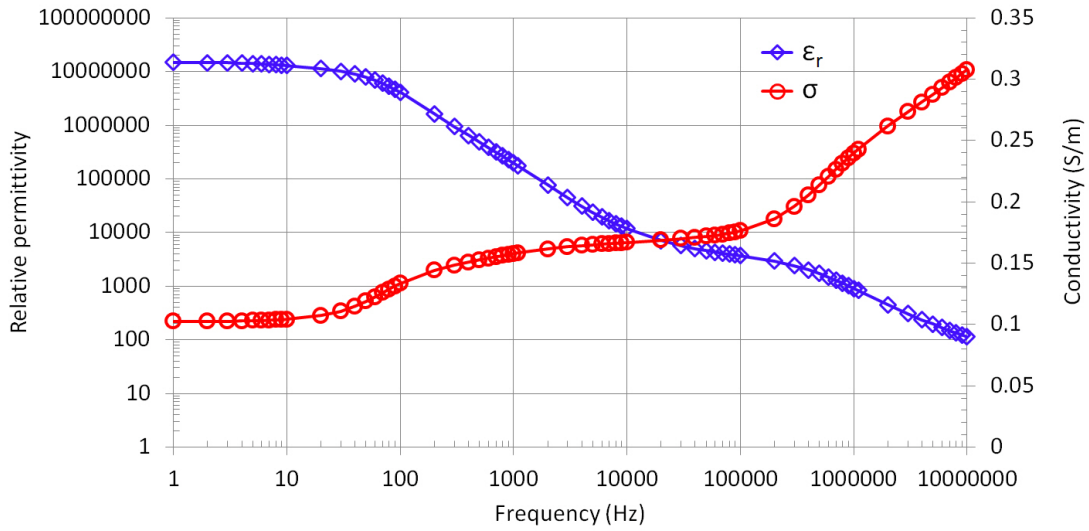


Figure 2.14: The weighted average values of the relative permittivity and conductivity for an adult male body.

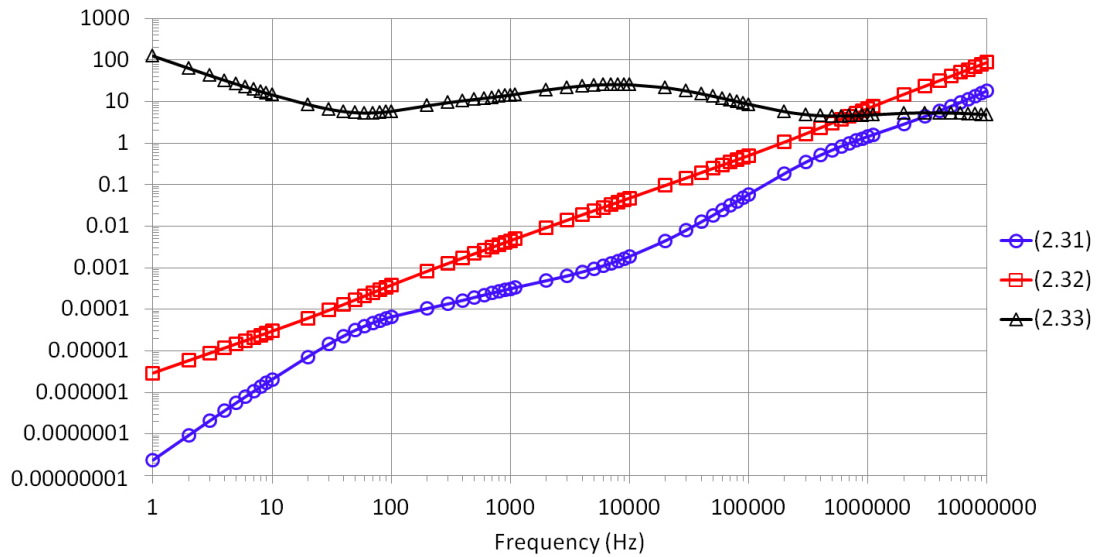


Figure 2.15: The left-hand-side values of (2.31), (2.32) and (2.33) calculated based on the adult male tissue composition data.

2.8.2 Quasi-Static Approximation Uncertainty above 200 kHz

To establish the effect of the electromagnetic quasi-static approximation for a full-body simulation above 100 kHz, a simplified human body model as shown in Figure 2.16 is developed for the simulation of a full-body exposure in uniform E-field or B-field using the SPFE solver and the FDTD solver. The model consists of tissues such as the brain, cerebrospinal fluid (CSF), spinal cord, heart and body shell. Each inner tissue model is represented by a rectangular block. The body shell and inner tissues are constructed based on the dimensions of the adult male anatomical model Duke (see Section 2.5.1). For the inner tissues, the frequency-dependent tissue dielectric properties are obtained from [60]. For the body shell, the weighted average dielectric property values computed based on the adult male tissue composition shown in Table 2.10 are assumed. Uniform vertically polarized 1 V/m E-field and 0.1 mT front-to-back polarized B-field are employed as the incident fields. The computations are performed at three frequency points: 100 kHz, 1 MHz and 10 MHz, respectively. A uniform 2 mm grid resolution is applied for the discretization of the model. For the SPFE solver, the stopping criterion is 10 orders of magnitude reduction for the initial residual. For the FDTD solver, the simulation duration is 20 sinusoidal periods. The peak induced E-fields in the respective tissues are computed and the percentage difference of the computational results ($\Delta = \frac{|E_{\text{SPFE}} - E_{\text{FDTD}}|}{E_{\text{FDTD}}} \%$) from the two solvers are shown in Table 2.11. The deviation between the two sets of computational results is within 6% up to 10 MHz, indicating that the SPFE solver may be applied for a full-body simulation up to a few MHz with small uncertainty due to the violation of the quasi-static approximations.

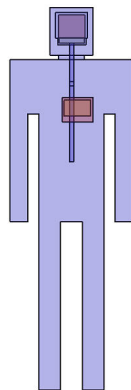


Figure 2.16: A simplified human body model (based on the dimensions of Duke) with brain, cerebrospinal fluid, spinal cord, heart and body shell represented by rectangular blocks.

2.9 Conclusion

In this chapter, a comprehensive literature review of the LF E-field and B-field exposure to the human body is presented. The interaction of biological systems and LF fields is discussed with respect to the associated biological effects to establish the significance of LF exposure limits

Table 2.11: The variation of the computed peak induced E-fields of the simplified body model between the SPFE solver and the FDTD solver ($\Delta = \frac{|E_{SPFE} - E_{FDTD}|}{E_{FDTD}} \%$).

$\Delta\%$ of the peak induced E-field (V/m)					
EQS	Brain	Heart	CSF	Spinal cord	Whole Body
100 kHz	0.8%	0.7%	0.9%	1.1%	0.8%
1 MHz	1.9%	1.6%	1.0%	0.8%	1.4%
10 MHz	3.6%	5.6%	1.6%	2.4%	2.2%

MQS	Brain	Heart	CSF	Spinal cord	Whole Body
100 kHz	1.3%	1.7%	0.8%	1.2%	1.6%
1 MHz	2.1%	2.6%	2.7%	1.8%	2.2%
10 MHz	3.2%	5.3%	2.7%	2.2%	2.5%

and numerical dosimetry. The ambiguity and discrepancy pertaining to the existing exposure guidelines and standards [2, 3, 5] are summarized to establish a core research objective: the derivation of up-to-date conversion factors between the external LF fields and the induced E-fields in the human body. The biological and computational rationales for a LF exposure assessment illustrated in this chapter serves as a basis for the research activities presented in Chapters 3, 4 and 5.

The methods and materials (e.g., high-resolution anatomically realistic model, LF human body tissue dielectric property, existing measurement and numerical techniques) of LF dosimetry are summarized. Based on the concept of an existing LF numerical technique (the scalar potential finite difference method), a Scalar Potential Finite Element (SPFE) solver is introduced as a mean to estimate the induced E-fields in an exposed human body. To validate the SPFE solver, the exposure scenarios of an ellipsoid in uniform E-field and B-field are computed and compared to the corresponding analytical and numerical solutions. Good agreement between the SPFE solutions and the alternative solutions is achieved. Next, the upper frequency limit of a full-body exposure simulation with respect to the validity of the quasi-static approximation is investigated. Based on the weighted average dielectric properties derived from adult male tissue composition, the quasi-static approximation is found to be valid up to 100 kHz for a full-body exposure simulation using the SPFE solver. The validation of the SPFE solver and the assessment of the applicable frequency limit demonstrated its applicability to the complex scenarios outlined in this thesis.

3 LF Magnetic Field Exposure Analysis - Theory and Fundamentals

3.1 Introduction

With the continuous developments of low frequency (LF) magnetic (B) induction technology (e.g., induction cooker, magnetic therapeutic mattress, wireless power transmission) and raising public awareness over the potential adverse health effects [65–67] due to LF B-field induction, particular research interest has been focused on the exposure of the human body to LF B-fields. In this chapter, the numerical dosimetry analysis for LF B-field induction are performed using the SPFE solver [48] described in Section 2.6.3. With high-resolution anatomically realistic models and guideline-compliant spatial averaging algorithms, the peak induced electric (E) fields in the human body are computed. The computational results are employed to examine the validity of the exposure limits and assessment techniques suggested in ICNIRP-2010 [2] and IEEE Std. C95.6-2002 [3].

Numerous studies [6–18] have been published in the field of numerical dosimetry for LF B-field induction. While the effects of spatial averaging algorithms have been investigated in [15], the grid size of the voxelized anatomical models used in [15] is 2 mm. Hence, no averaged field value was reported for the ICNIRP-2010 volume ($2 \times 2 \times 2 \text{ mm}^3$) averaging. To comply with the volume averaging requirement, grid sizes smaller than 2 mm are employed in this study. For the IEEE Std. C95.6-2002 line (5 mm) averaging, the values reported in [15] were obtained by averaging the E-field components along the principal axes and reporting the highest values. This approach does not necessarily estimate the worst-case scenario since the exposed nerve fibres can exhibit random orientations with respect to the principal axes. To achieve a better compliance with the line averaging requirement, the orientation of the line segment in this work is determined by the nodal E-field vector direction. With improved spatial averaging algorithms and adequate grid resolutions, various open issues associated with LF numerical dosimetry (e.g., discretization uncertainty due to grid size variation, potential underestimation of the peak induced E-field due to the use of homogeneous models, the effect of tissue dielectric property and geometrical variations) can be addressed.

The investigations conducted in this chapter are structured as follows: first, the discretization uncertainty associated with grid size variation is analyzed using both canonical models and high-resolution anatomically realistic models to estimate the convergence of the peak spatially averaged and 99th percentile *in situ* E-field values with respect to grid size variation. Next, the effects of tissue conductivity contrast and tissue model geometrical variation are examined using a heterogeneous spherical model. Subsequently, with anatomical models, the worst-case spatially averaged E-fields induced in the human brain and body due to the exposure to a uniform B-field at the ICNIRP-2010 [2] and IEEE Std. C95.6-2002 [3] reference levels are computed at multiple frequency points from 10 Hz to 100 kHz. The computational results are employed to assess the safety margins provided by the IEEE and ICNIRP exposure limits. Furthermore, the impacts of body posture variation and skin layer modelling are addressed to facilitate an in-depth analysis of the whole-body B-field exposure scenario. The research work reported in this chapter leads to a better understanding of the LF B-field induction to the human body in terms of the numerical assessment techniques, the derivation of exposure limits and the identification of critical modelling parameters.

3.2 Post-processing Techniques for the *in situ* E-field

3.2.1 Spatial Averaging

ICNIRP-2010

In ICNIRP-2010 [2], the range of a biologically reasonable averaging distance for the induced E-field is stated to be from 1 to 7 mm. Based on the maximum inter-nodal distance between the nodes of *Ranvier* for myelinated nerve cells, the E-field integration distance is suggested to be 2 mm. The *in situ* E-field is specified as a vector average of the E-fields in a small contiguous tissue volume of $2 \times 2 \times 2 \text{ mm}^3$. In this work, the integration of the E-fields within a cubic volume of $2 \times 2 \times 2 \text{ mm}^3$ is obtained by summing up the contribution of each voxel as follows:

$$\langle \mathbf{E}(r_0) \rangle_V = \frac{1}{V} \sum_n \mathbf{E}(r_n) f_n V_n \quad (3.1)$$

where r_0 is the location of the voxel center, V is the average volume which is fixed at 8 mm^3 , V_n is the volume of the n^{th} voxel within the cube and $0 < f_n \leq 1$ is the filling factor. The filling factor is a coefficient that accounts for the partial volume of the outermost voxels to the averaging cube. The filling factors are determined by the overall cube size (i.e., 8 mm^3) and the grid sizes within the cube. To comply with the $2 \times 2 \times 2 \text{ mm}^3$ average volume, no averaging will be performed at a voxel if the cube is not completely within the tissue of interest, and the E-field value of this voxel will not be considered as a spatially averaged value. In this thesis, the quantity $E_{V,\text{avg}}$ represents the $2 \times 2 \times 2 \text{ mm}^3$ volume-averaged E-field rms value.

While the biological rationale of volume averaging has been questioned in [88], the discussion of the biological significance of spatial averaging is out of the scope of this thesis. Hence, the ICNIRP-recommended spatial averaging algorithm is implemented based on the technical interpretation of the guideline statements without further speculation. In ICNIRP-2010 [2], the exposed tissues are classified as “CNS tissue of the head” and “All tissues of head and body”. The “CNS tissue of the head” is further specified to be the brain and retina. Based on different interpretations of the “brain tissue”, when performing an ICNIRP-recommended volume averaging of the induced E-fields in the brain, one could choose to average the induced E-fields tissue-by-tissue based on the segmented CAD models (e.g., grey matter, white matter, etc.) or average the E-fields over the entire brain (treating the brain as one tissue). It should be noted that the biological rationale of spatial averaging is to determine whether the E-field strength in a specific tissue is sufficient to trigger electro-stimulation. Furthermore, the neurons in the brain are not necessarily confined in one particular brain tissue. Hence, in this thesis, spatial averaging is performed over the entire brain when the brain is chosen as the target tissue. For the whole-body exposure scenario, the induced E-fields in all the body tissues are averaged contiguously.

IEEE Std, C95.6-2002

In IEEE Std. C95.6-2002 [3], the *in situ* E-field is specified as an arithmetic average of E-fields projected onto a straight line segment of 5 mm length oriented in any direction within a tissue. The choice of 5 mm is determined using a non-linear model of a myelinated nerve. Based on a nerve axon with a diameter of 20 μm and an inter-nodal distance of 2 mm, an averaging distance of 5 mm is found to be neither overly conservative nor permissive [89]. To perform the spatial averaging of E-fields along a 5 mm straight in this thesis, a line segment L centred at each voxel r_0 is created in the direction parallel to the E-field vector at that voxel location, i.e., $\hat{l}_0 = \mathbf{E}(r_0)/|\mathbf{E}(r_0)|$. The rationale behind this direction selection is that the E-field at each voxel will provide the maximum contribution to the averaging along this direction. The spatial average is computed as follows:

$$\langle \mathbf{E}(r_0) \rangle_L = \frac{\hat{l}_0}{L} \int_L \mathbf{E}(r) \cdot \hat{l}_0 dl = \frac{K}{L} \hat{l}_0 \quad (3.2)$$

where L is the average distance which is fixed at 5 mm, K is the integral of E-fields along the line segment. For the averaging line segment to be entirely within the tissue, no averaging will be performed at a voxel if the 5 mm line segment extends out of the tissue of interest. In this thesis, the quantity $E_{L,\text{avg}}$ represents the 5 mm line-averaged E-field rms value.

3.2.2 99th Percentile Value

In an attempt to reduce discretization uncertainty due to numerical artefacts such as stair-casing errors, the E-field value exceeded by only 1% of the voxels of a specific tissue, known as the 99th percentile value (E_{99}), is specified as the relevant value to be compared with the basic restriction in ICNIRP-2010 [2]. Several issues associated with the filtering effect of the 99th percentile approach have been reported [17, 18]. For instance, the E_{99} value is dependent on the spatial distribution of the induced E-fields, the size and definition of the tissue of interest and the number of voxels assigned to the tissue. In [17], a 40% underestimation of the maximum induced E-field due to the 99th percentile approach is demonstrated for a layered sphere subjected to localized B-field exposure. Despite the aforementioned issues, the E_{99} E-field rms value is hereby reported for the sake of compliance assessment. In this thesis, the 99th percentile value of a target tissue (e.g., the brain) is obtained by treating the whole tissue group as a single tissue and filtering out the top 1% voxel values. Higher and grid-dependent values are expected if the filtering is to be performed on each segmented tissue model [18].

3.3 Discretization Uncertainty for the Peak Induced E-field

3.3.1 Background

In a LF numerical dosimetry computation, when an anatomically realistic model is discretized with structured grids (i.e., rectilinear grids), the numerical artefacts introduced by stair-casing errors as well as field singularity due to sharp corners render the maximum E-field value of a single voxel unstable with respect to grid size variation. As the prevention of potential nerve stimulation relies on the prediction of the peak induced E-field values in particular organs, large variations in the peak values are undesirable. The 99th percentile value is known to suppress the discretization uncertainty, however the lack of biological rationale and the tendency of potential underestimation diminishes the rationales for the 99th percentile value. The motivation of the subsequent investigations is to characterize the effect of spatial averaging on the discretization uncertainty with respect to grid size variation.

3.3.2 Discretization Uncertainty due to Stair-Casing Error

To assess the discretization uncertainty associated solely with stair-casing errors (due to the approximation of the curvature of surfaces), a spherical model is employed. The exposure scenario of a homogeneous sphere with a diameter of 10 cm and 2 cm in a uniform 50 Hz B-field is computed with uniform grid size from 2 mm to 0.05 mm. The computed peak E-field values are normalized to the respective analytical peak values (see Section 2.7.1). As shown in Figure 3.1, the maximum value in a single voxel, E_{\max} , in general exceeds the analytical peak value due to the stair-casing errors. The $E_{V,\text{avg}}$ and $E_{L,\text{avg}}$ values are much less affected by grid size variation than the E_{\max} value and gradually converge to the analytical peak value, e.g., $\Delta \leq 3\%$ for a grid size of 0.5 mm. This shows that stair-casing errors are successfully

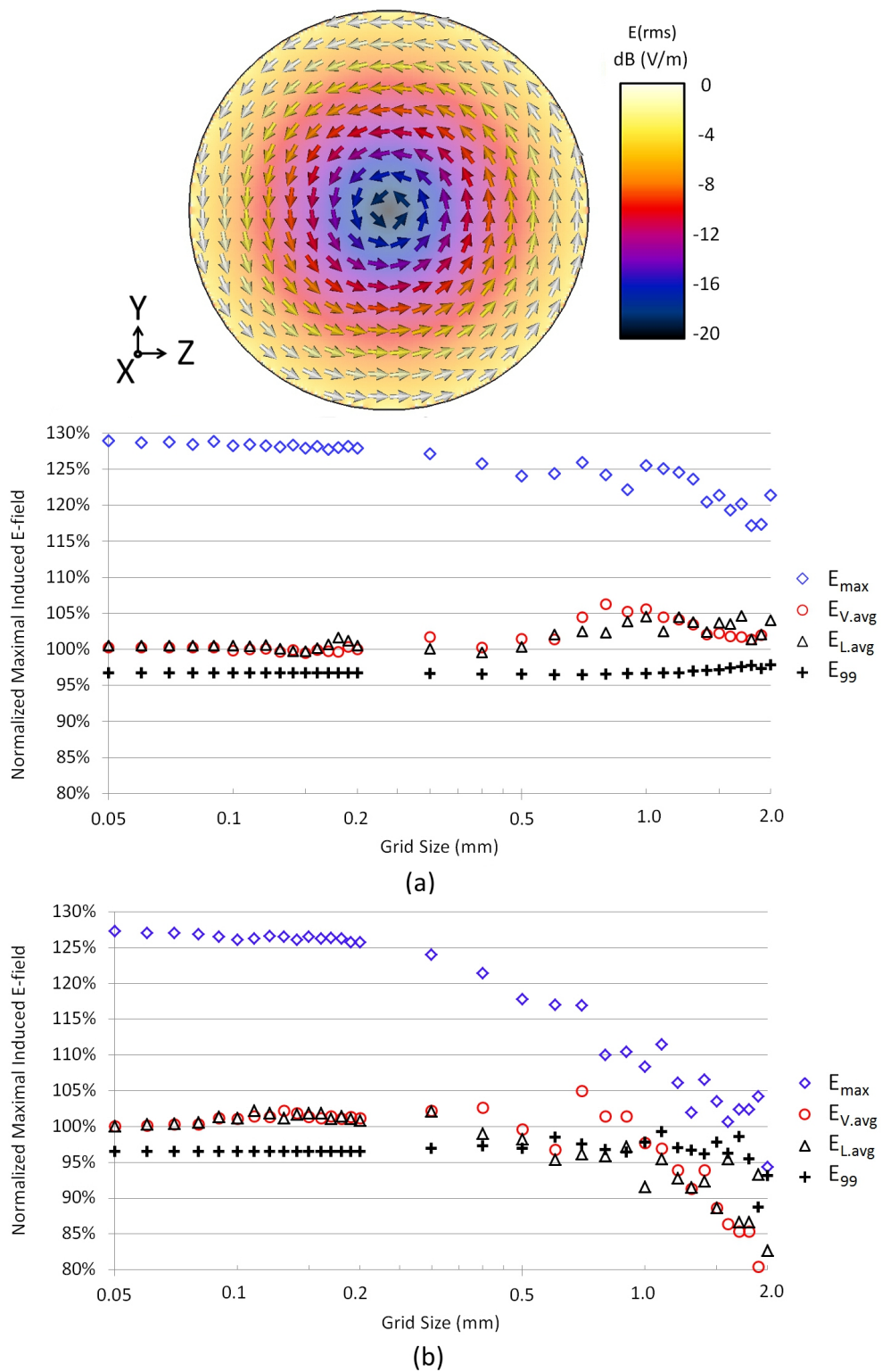


Figure 3.1: The E-field distribution in a sphere with a diameter of (a) 10 cm and (b) 2 cm, exposed to a uniform 50 Hz B-field in the x direction and the peak induced E-field (normalized to the respective analytical value) as a function of grid size.

suppressed by spatial averaging. It is noted that the spatially averaged values could potentially underestimate the peak E-fields when the ratio between the object size and grid size is small (e.g., when a sphere with 2 cm diameter is discretized with a grid size from 2 mm to 1 mm). The E_{99} values are the least affected quantity with respect to grid size variation and stay at 95-100% of the analytical peak value for the investigated grid sizes. As the E_{99} value is both stable and close to the analytical peak value in this particular exposure scenario (i.e., a homogeneous sphere in a uniform B-field), it was often employed as a substitute for the E_{\max} value to obtain a more stable approximation of the peak induced E-field in an anatomical model [10–16]. Issues associated with the prediction of the peak value based on the E_{99} value will be revealed in Sections 3.3.3 and 3.3.4.

To visualize the effect of spatial averaging on the induced E-field distribution in the sphere, the voxel E-field (E_{voxel}), volume-averaged E-field ($E_{V,\text{avg}}$) and line-averaged E-field ($E_{L,\text{avg}}$) distributions are presented in Figure 3.2. The stair-casing errors are prominent in the E_{voxel} case; bright spots are observed along the peripheral of the sphere (see Figure 3.2(a)). The $E_{V,\text{avg}}$ field distribution shown in Figure 3.2(b) indicates that the $2 \times 2 \times 2 \text{ mm}^3$ volume averaging truncates the outermost 1 mm layer of the sphere. This is due to the specification of the volume averaging algorithm which allows the exclusion of voxels that do not fit in the $2 \times 2 \times 2 \text{ mm}^3$ cube. The stair-casing bright spots are removed from the $E_{V,\text{avg}}$ field due to this volume truncation; it should be noted that this truncation only occurs on the outermost layer of a target tissue. For the induced E-fields in inner tissues, the volume averaging will merely smooth out the high values due to stair-casing errors. In Figure 3.2(c), the $E_{L,\text{avg}}$ field distribution shows that very little truncation of the sphere is caused by the line averaging. This is due to the fact that the vectorial E-fields circulate the sphere tangentially, hence the averaging line is projected also tangentially along the sphere surface. The stair-casing errors are effectively suppressed in the $E_{L,\text{avg}}$ case while maintaining the *in situ* E-field distribution with minimum truncation. The presented E-field distributions depict the scenario of a homogeneous spherical body which demonstrates visually the stair-casing error suppression capability of spatial averaging.

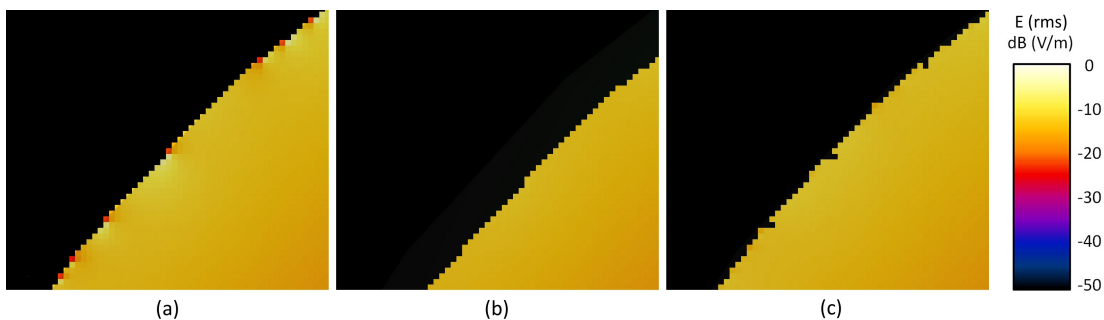


Figure 3.2: The induced E-field distribution on the upper left corner of the sphere (with 10 cm diameter) for (a) E_{voxel} , (b) $E_{V,\text{avg}}$ and (c) $E_{L,\text{avg}}$, the E-field values are normalized to the peak induced E_{\max} value.

3.3.3 Discretization Uncertainty due to Field Singularity

While stair-casing errors must be suppressed, local peak induced E-fields should be preserved to reflect the actual induction scenario. To assess the discretization uncertainty associated solely with field singularity, the exposure scenario of a homogeneous $10 \times 10 \times 10 \text{ cm}^3$ cube with a missing octant in a uniform 50 Hz B-field is computed with grid size from 2 mm to 0.05 mm. As shown in Figure 3.3, field singularities arise when the induced E-fields are forced to “squeeze” into sharp concave corners carved out by the missing octant. The E-field values at such singularity points are expected to approach infinity if the grid size is allowed to shrink indefinitely (i.e., approach a physical singularity). The E-field values are normalized to the $E_{V,avg}$ value computed at 0.05 mm grid size and presented in Figure 3.3 as a function of grid

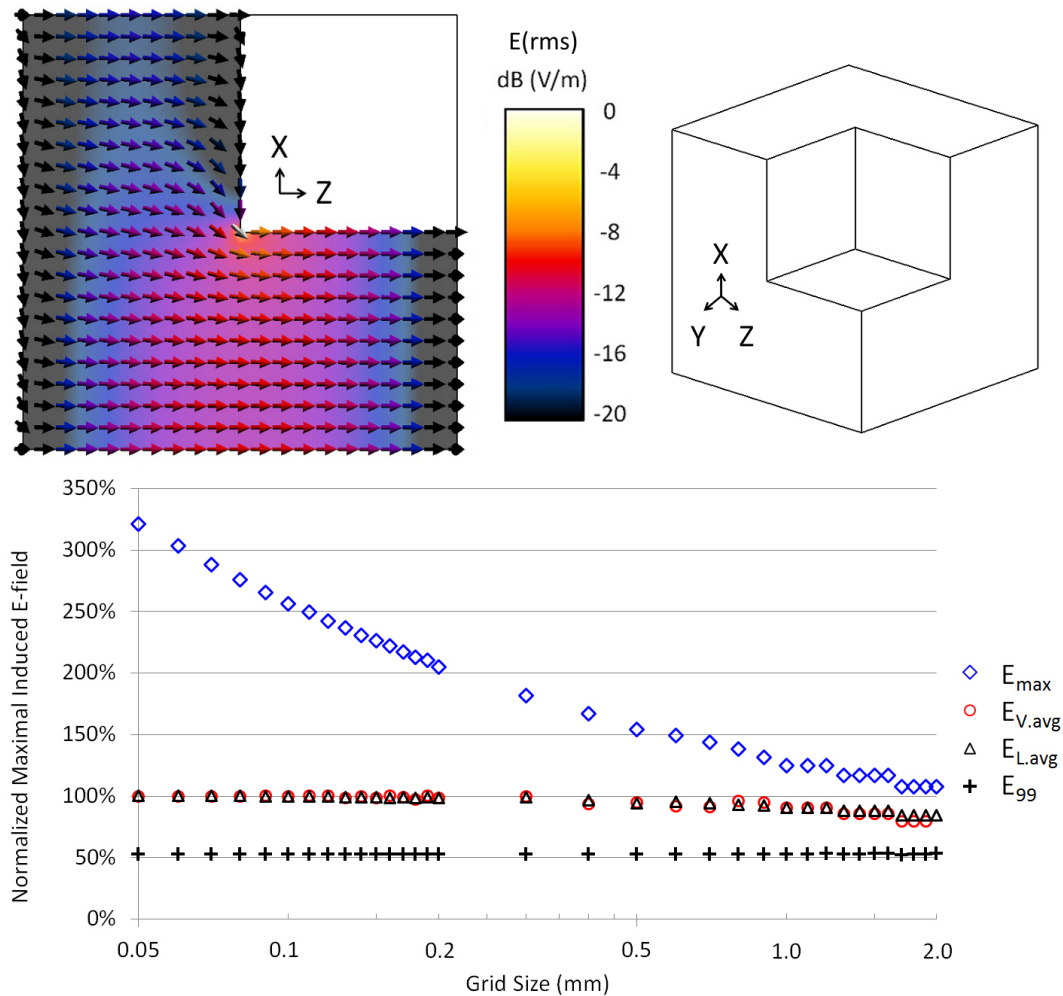


Figure 3.3: The E-field distribution (on the xz plane, at $y = +5 \text{ cm}$, $y = 0 \text{ mm}$ at the cubic center) in a $10 \times 10 \times 10 \text{ cm}^3$ cube with a missing octant exposed to a uniform 50 Hz B-field in the x direction and the peak induced E-field value (normalized to the $E_{V,avg}$ value at the grid size of 0.05 mm) as a function of grid size.

size. As expected, the E_{\max} value increases with decreasing grid size. Instead, the $E_{V,\text{avg}}$ and $E_{L,\text{avg}}$ values are found to gradually converge to a stable value, e.g., $\Delta \leq 5\%$ for a grid size of 0.5 mm. This indicates that the edge singularities are preserved by the spatially-averaged value while numerical stability is progressively achieved. The E_{99} values are approximately 50% lower than the spatially averaged values due to the arbitrary exclusion of peak values. This serves as a clear indication that the 99th percentile approach can potentially lead to an underestimation of the peak induced E-field.

3.3.4 Discretization Uncertainty for an Anatomical Model

To analyze the discretization uncertainty (due to both stair-casing errors and field singularities) associated with an anatomically realistic model, the exposure scenario of Duke in a uniform LAT (side-to-side) 50 Hz B-field is computed. Uniform grid sizes from 2 mm down to 1 mm, with a step change of 0.1 mm, are employed for the discretization. In addition, 0.9 to 0.5 mm uniform grid sizes are applied to discretize the head while a 2 mm grid size is applied to the rest of the body with a fixed grading ratio (i.e., the spatial step ratio of adjacent cells) of 1.2. The variation in the computed peak E-fields due to the change of grid size from 2 mm to 1 mm for the rest of the body (with the grid size for the head fixed at 0.5 mm) is investigated. The variations in the peak E-field values ($E_{V,\text{avg}}$, E_{99} and $E_{L,\text{avg}}$) in the brain are found to be within 3%. This indicates that the computational results of the induced E-field in the brain are not significantly affected by the grid resolutions of the body trunk for a uniform B-field exposure. The peak E-field values in the brain are normalized to the peak $E_{V,\text{avg}}$ value computed with 0.5 mm grid size and presented in Figure 3.4. The E_{\max} values of the anatomical model are

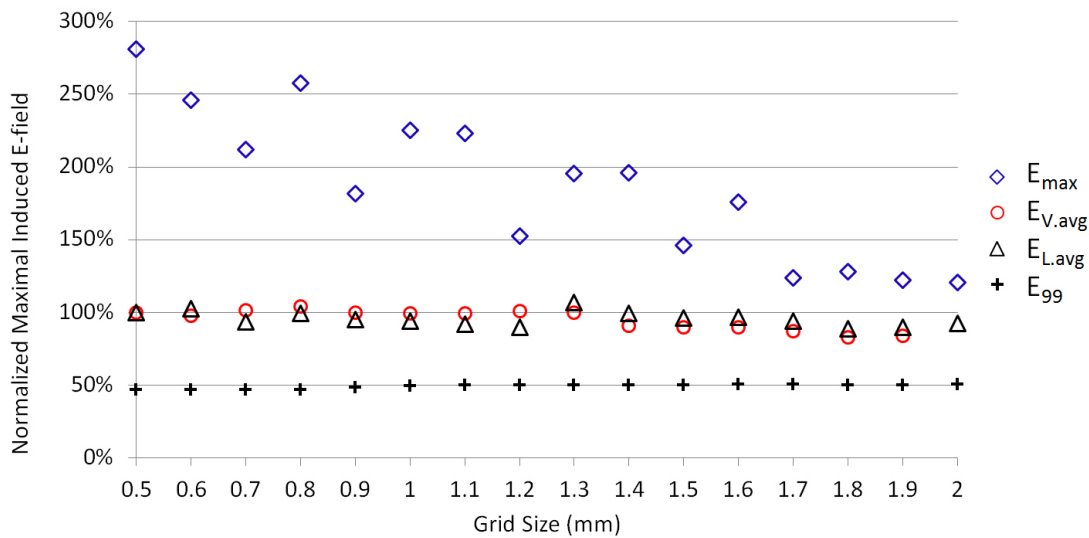


Figure 3.4: The peak induced E-field values (normalized to the $E_{V,\text{avg}}$ value at 0.5 mm) in the brain of Duke as a function of grid size due to 50 Hz LAT (side-to-side) uniform B-field exposure.

found to be significantly influenced by the numerical artefacts. Owing to the spatial averaging, the $E_{V,avg}$ and $E_{L,avg}$ values are much less affected by grid size variation. The variations of the peak spatially averaged values are within 10% between the grid sizes of 1 mm to 0.5 mm. Similar to the field singularity case (see Section 3.3.3), the E_{99} values of the anatomical brain model are found to be approximately 50% below the spatially averaged values. Based on the discretization uncertainty behaviour of the canonical models, the peak spatially averaged E-field value computed in the brain of an anatomical model at a grid size of 0.5 mm can be regarded as a stable peak approximation. To achieve absolute numerical convergence with respect to grid variation for an anatomical model, grid size smaller than 0.5 mm should be investigated. However, based on the computation hardware and the segmentation quality of anatomical models (i.e., based on MRI scans with minimum 0.5 mm resolution) employed in this study, the minimum grid size applied for a dosimetry computation with anatomically realistic models is limited to 0.5 mm.

3.3.5 Summary of the Discretization Uncertainty Analysis

The discretization uncertainty associated with a rectilinear-voxellized model has always been an obstacle for numerical dosimetry in the past. The prediction of the peak induced E-field suffered from high uncertainty due to the numerical artefacts introduced by stair-casing errors and field singularities. To address this issue, percentile filtering approach such as the 99th percentile value has been introduced. However, it is revealed in this section that a filtering technique without reliable biological basis can lead to a gross underestimation of the actual peak induced E-field. The computational results of this study indicate that a well-implemented spatial averaging algorithm and a suitable grid resolution can provide discretization uncertainty suppression and at the same time preserve the biologically significant peak E-field values. Through the analysis of canonical and anatomical models, the effect of guideline-compliant volume and line spatial averaging on the numerical convergence with respect to grid size variation is disclosed. It is observed that with sufficiently refined grids, the peak spatially averaged E-field value serves as a more suitable peak approximation than the 99th percentile value. The practice of percentile filtering in an exposure guideline is therefore discouraged based on the analysis results shown in this section.

3.4 Analysis of Human Brain Exposure

3.4.1 Background

The peak E-field induced in the human brain due to the exposure to LF B-field has been numerically computed and reported in [6–18]. To provide an up-to-date estimation of the peak spatially averaged E-field induced in the human brain due to uniform B-field exposure, numerical computations are performed in this section with canonical and anatomically realistic models using the SPFE solver [48] and the spatial averaging algorithms described in Section 3.2.1. The computed peak E-fields in an anatomical brain model are scaled with respect to the relevant reference levels (RL) suggested in IEEE Std. C95.6-2002 [3] and ICNIRP-2010 [2]. These values are then compared with the corresponding basic restrictions (BR) to assess the safety margins provided by the aforementioned exposure guidelines and standards for the prevention of brain stimulation due to the exposure to a LF B-field.

3.4.2 Canonical Head Model

Prior to the availability of anatomically realistic models, homogeneous ellipsoidal and spherical models were often employed to estimate the peak induced E-field in the human brain and body. Although analytical solutions can be derived using these simplified homogeneous models, details such as inner tissue geometry, tissue-to-tissue conductivity contrast and variation in tissue conductivity with respect to frequency are completely neglected. As a result, the peak induced E-field value calculated in a homogeneous model does not necessarily represent a conservative worst-case estimation. The research objective in this section is to characterize the effect of tissue conductivity contrast and model geometrical variation on the induced E-fields in the human brain.

Based on the overall size of Duke's head, a spherical model is constructed. This canonical model is comprised of a sphere and a circular dish layer with the horizontal edge conform to the sphere as shown in Figure 3.5(a). The sphere represents a larger organ (e.g., the head) while the dish layer represents a potential tissue-to-tissue interface with conductivity contrast within the head (e.g., between the brain tissues with lower conductivity and the cerebrospinal fluid with higher conductivity). Uniform x -direction-oriented B-field exposure scenario is simulated with a uniform grid size of 0.5 mm for the canonical model. In this case, the induced E-fields are forced to circulate the sphere and pass through the tissue interface normally (i.e., the E-field vectors pass the horizontal surfaces of the dish vertically). The sphere has a fixed radius of 11 cm. Two thickness values (2 mm and 10 mm) for the dish layer are investigated. Conductivity values σ_1 and σ_2 are assigned to the sphere and dish layer, respectively. In addition to the homogeneous case (i.e., $\sigma_1 = \sigma_2$), four conductivity contrast ratios are considered: $\sigma_1:\sigma_2 = 10:1$, $100:1$, $1:10$ and $1:100$. The $E_{V,avg}$ field distributions are presented in Figure 3.5 for the configuration of $\sigma_1:\sigma_2 = 100:1$. It is observed that when compared to a homogeneous model, the induced E-fields are significantly higher in a heterogeneous model. The peak induced

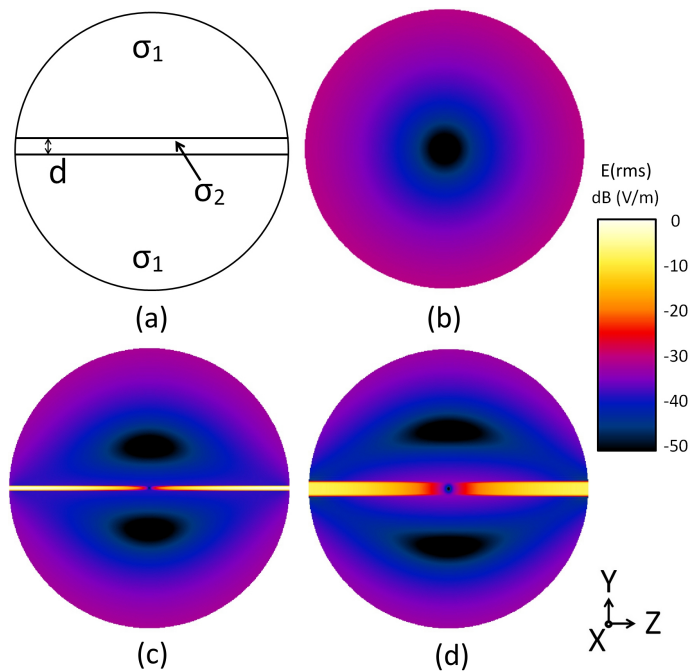


Figure 3.5: (a) A canonical head model with a dish layer of thickness d , for a conductivity ratio of $\sigma_1:\sigma_2 = 100:1$, the $E_{V,avg}$ field distributions in (b) a homogeneous model, (c) $d = 2$ mm and (d) $d = 10$ mm.

E-field is observed to be inversely proportional to the thickness of the tissue transition layer. High concentration of induced E-fields are found within the σ_2 layer. When compared with the homogeneous case, the E-field distribution in the sphere is significantly altered due to the presence of the tissue contrast layer.

The peak $E_{V,avg}$ values of the investigated conductivity contrast ratios and model configurations are normalized to the peak $E_{V,avg}$ value of the homogeneous sphere case and presented in Figure 3.6. This normalized quantity is referred to as the enhancement factor for the peak $E_{V,avg}$ value. No variation in the peak induced E-field is observed when σ_1 is smaller or equal to σ_2 . However, when σ_1 is greater than σ_2 , significantly higher peak E-field is observed in the less conductive tissue region (i.e., the σ_2 layer). This indicates that a high-low-high tissue conductivity distribution will result in higher induced E-field in the less conductive tissue. A narrower transition region will cause greater E-field enhancement due to the reduced distance between the opposite surface charges. It should be noted that the induced E-field orientation in this example is configured to be normal to the tissue contrast layer on purpose. If the tissue contrast interface is tangential to the E-field vectors, no variation in the E-field intensity is expected. An inspection of Figures 3.5 and 3.6 reveals that the peak induced E-field is a function of the conductivity contrast and tissue model geometry. This investigation indicates that, without considering tissue conductivity contrast and tissue geometry, a homogeneous head model is likely to significantly underestimate the peak induced E-field in the brain.

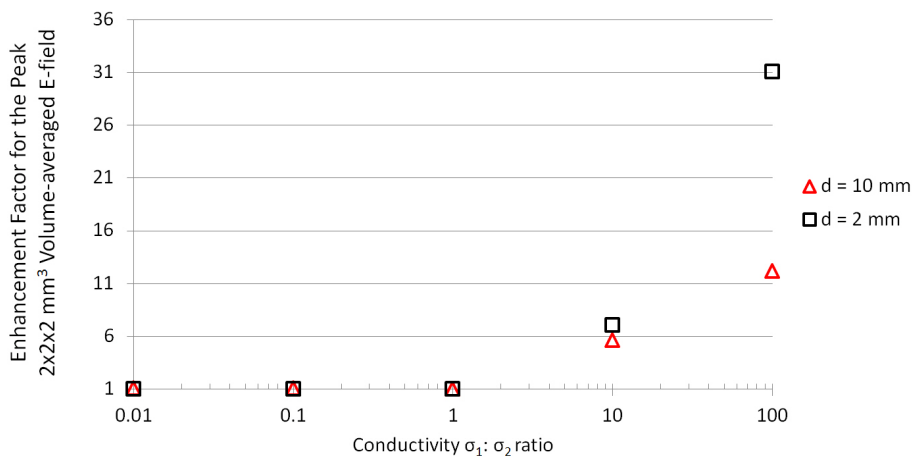


Figure 3.6: The enhancement factor for the peak $E_{V,avg}$ value in the heterogeneous spherical model due to tissue conductivity contrast and model variation (when compared to the homogeneous sphere case) as a function of conductivity contrast ratio and layer thickness (d).

3.4.3 Computational Results of Anatomical Models

Peak induced E-fields at ICNIRP and IEEE Reference Levels

A uniform B-field is applied as the source of exposure at twelve frequency points from 10 Hz to 100 kHz. Three field orientations, namely TOP (top-to-bottom), AP (front-to-back) and LAT (side-to-side) are considered. The five anatomical models described in Section 2.5.1 are investigated. Based on the discretization uncertainty analysis reported in Section 3.3, a uniform grid size of 0.5 mm is applied to discretize the head while a 2 mm grid size is applied to the rest of the body with a fixed grading ratio of 1.2. Three E-field quantities are computed: the $2 \times 2 \times 2 \text{ mm}^3$ volume-averaged E-field ($E_{V,avg}$), the 5 mm line-averaged E-field ($E_{L,avg}$) and the 99th percentile value (E_{99}). The LAT B-field orientation is found to produce the highest induced E-fields in the brain for the investigated anatomical models. This finding is consistent with the previously published results, e.g., the E_{99} values reported in [11] and [16]. This is likely due to the fact that the brain exhibits the largest cross-sectional area in the sagittal plane. Among the five anatomical models, the Duke model produces the highest induced E-field in the brain at all the investigated frequencies. The peak E-field ($E_{V,avg}$, E_{99} and $E_{L,avg}$) values computed in the brain of Duke, scaled to the reference levels suggested in the ICNIRP-2010 [2] and IEEE Std. C95.6-2002 [3], are presented in Figure 3.7 with the respective basic restrictions.

As shown in Figure 3.7(a) and Figure 3.7(b), the E_{99} values are compliant with the ICNIRP-2010 basic restrictions. This is expected since the ICNIRP-2010 reference levels were derived based on the E_{99} values [11, 12] with additional safety factors to account for dosimetry uncertainties. However, it should be noted that the 99th percentile value has been shown to potentially underestimate the peak induced E-field in the brain by approximately 50% when compared to the $E_{V,avg}$ and $E_{L,avg}$ values (see Sections 3.3.3 and 3.3.4). The $E_{V,avg}$ values are found to be

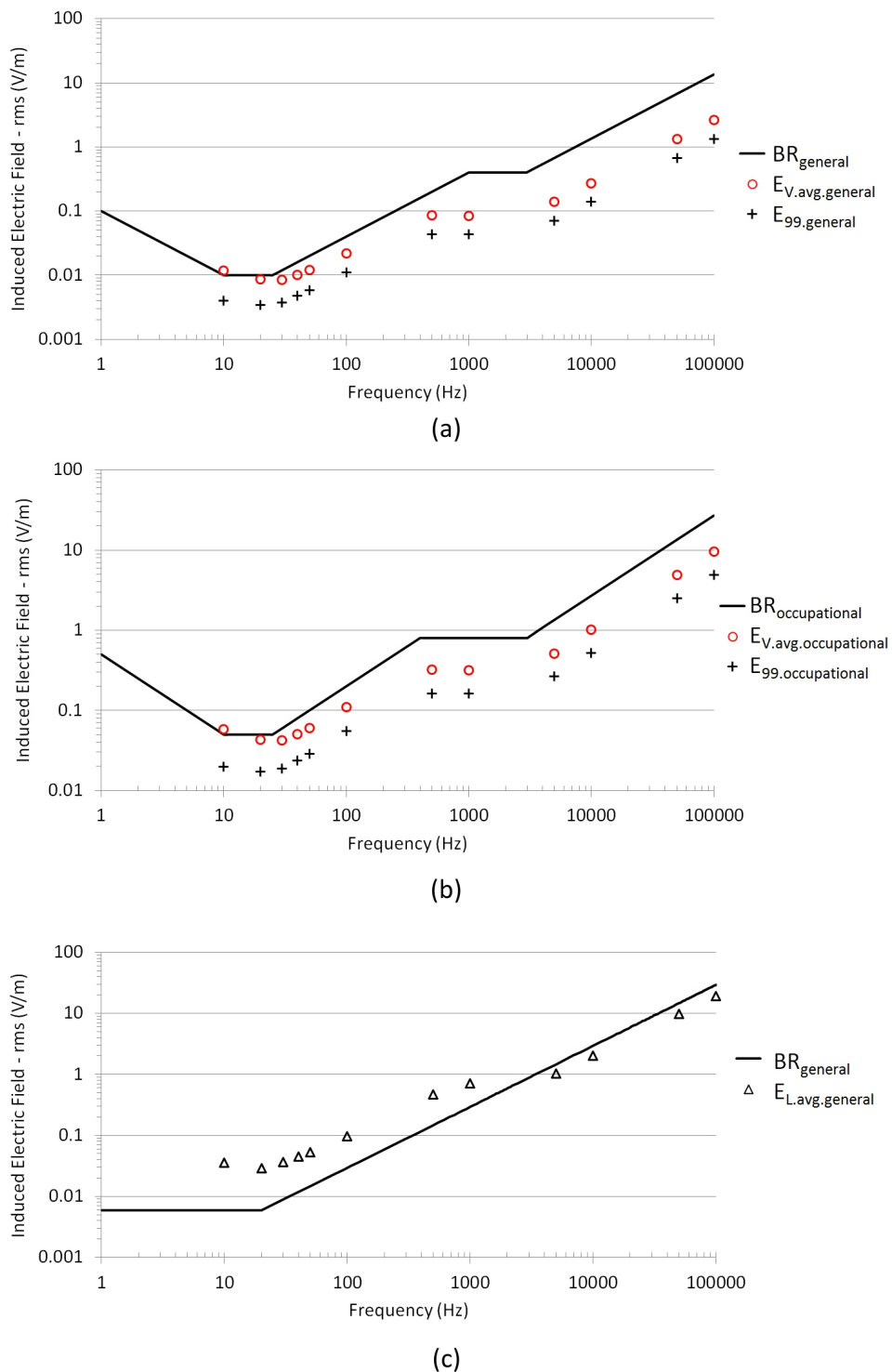


Figure 3.7: The ICNIRP-2010 BR levels for the CNS tissues and the peak $E_{V,avg}$, E_{99} values for (a) general public and (b) occupational exposure, and (c) the IEEE.Std.C95.6-2002 BR levels for the brain and the peak $E_{L,avg}$ values for general public exposure, in the brain of Duke exposed to a uniform LAT (side-to-side) B-field at the respective reference level.

compliant with the ICNIRP-2010 basic restrictions except at 10 Hz. As shown in Figure 3.7(c), the $E_{L,avg}$ values exceed the IEEE Std. C95.6-2002 basic restriction levels (e.g., by a factor of 6 at 10 Hz) in the frequency range of 10 Hz to 1 kHz. A similar finding is reported in [16] in which the E_{99} values in the brains of anatomically realistic models at 20 Hz were found to be 10-70% higher than the IEEE Std. C95.6-2002 basic restrictions. To investigate the root cause of this discrepancy, numerical computation is performed for the 50 Hz LAT B-field exposure case by applying 0.085 S/m as a weighted average conductivity value to the grey matter ($\sigma_{50Hz} = 0.075$ S/m), white matter (0.053 S/m) and cerebrospinal fluid (2 S/m). As a result, a reduction factor of 3 is observed for the peak $E_{V,avg}$ and $E_{L,avg}$ values of the brain tissues, compared to the heterogeneous case. Recall the finding in Section 3.4.2: the peak spatially averaged E-field value estimated in a heterogeneous model can be significantly higher than the value derived from a homogeneous model. The computational results reported in this study evidently suggest that the IEEE Std. C95.6-2002 B-field exposure limits, which were derived from homogeneous ellipsoidal models, are most likely not conservative enough to represent the worst-case peak induced E-field in the human brain.

Conversion factor

A conversion factor (CF) between the external B-field (or E-field) and the induced E-field can be defined as:

$$CF_f = \frac{E_{ind}}{B_{ext} \times f} \quad (3.3)$$

where f is the frequency of interest, E_{ind} is the induced E-field and B_{ext} is the external B-field (or E-field). For a biological system which exhibits tissue composition with frequency-independent tissue-to-tissue dielectric property contrast (i.e., the dielectric property value of an individual tissue might be different in frequency but the tissue-to-tissue dielectric property contrast remains the same), the conversion factor of a LF B-field exposure scenario should be frequency-independent. The conversion factors between a 1 T uniform LAT (side-to-side) B-field and the computed peak induced E-field in the brain of Duke are presented in Table 3.1. It is observed that the conversion factor for a human brain model is in fact frequency-dependent (e.g., between 10 Hz and 50 Hz); this in term suggests that frequency scaling should not be applied directly for the conversion of the external B-field to the *in situ* E-field. The conversion factors provided in this section serve as an up-to-date numerical dosimetry reference. Together with a set of known BR or RL levels (i.e., obtained from nerve stimulation models or experimental data), the reported conversion factors can be applied to derive the corresponding exposure limits for the exposure of human brain in LF B-field.

Table 3.1: The conversion factors between a 1 T uniform LAT (side-to-side) B-field and the computed peak induced E-field in the brain of Duke.

(V/m)/T/Hz	Frequency (Hz)								
	10	50	100	500	1000	5000	10000	50000	100000
$E_{V,avg}$	2.34	1.20	1.10	1.07	1.06	1.03	1.01	0.98	0.96
E_{99}	0.79	0.58	0.55	0.54	0.54	0.53	0.52	0.50	0.49
$E_{L,avg}$	1.99	1.17	1.07	1.05	1.04	1.00	0.99	0.95	0.94

Compliance level

A compliance level (CL) with respect to the basic restriction at a fixed frequency point can be defined as:

$$CL_f = \frac{E_{ind,RLf}}{E_{BRf}} \quad (3.4)$$

where f is the frequency of interest, $E_{ind,RLf}$ is the worst-case peak induced E-field value scaled to the reference level (RL) at f and E_{BRf} is the basic restriction (BR) level at f . A compliance level value greater than 1 implies that compliance with the reference level does not ensure compliance of the basic restriction at the frequency of interest. Hence, the compliance level quantity (CL) is employed in this study to examine the validity of the claim: *compliance with the reference level will ensure compliance with the relevant basic restriction* stated in ICNIRP-2010 [2] and the claim: *the MPEs incorporate conservative assumptions such that adherence to them insures that the basic restrictions are not exceeded* stated in IEEE Std. C95.6-2002 [3].

The compliance levels for the investigated anatomical models at 10 Hz and 50 Hz for the general public exposure limits are presented in Figure 3.8. For Duke, the CL_{10Hz} value is twice of the CL_{50Hz} value for the volume-averaged E-field. This discrepancy can also be observed in the data presented in Table 3.1. As a result, the $E_{V,avg}$ value exceeds the ICNIRP-2010 basic restriction at 10 Hz as shown in Figure 3.7(a) and Figure 3.7(b). Based on the conversion factors provided by ICNIRP and IEEE (see Section 2.3.2), frequency scaling which assumes invariant tissue conductivity contrast ratio with respect to frequency variation was evidently employed. However, the computational results of this study indicate that the conversion factors can be strongly frequency-dependent, i.e., frequency scaling would not be valid throughout the entire low frequency range. To verify this claim, the low frequency conductivity values [60] and the contrast ratios with respect to the cerebrospinal fluid (CSF) for several biological tissues in the human head are presented in Figure 3.9. An apparent increase of the conductivity contrast ratio from 50 Hz to 10 Hz can be observed for the brain grey matter, brain white matter and cerebellum (e.g., $\sigma_{CSF} : \sigma_{grey} \approx 70$ at 10 Hz and $\sigma_{CSF} : \sigma_{grey} \approx 40$ at 50 Hz). As discussed in Section 3.4.2 and demonstrated in Figure 3.6, an increase in conductivity contrast ratio could lead to higher induced E-field in a heterogeneous head model and the amount of E-field

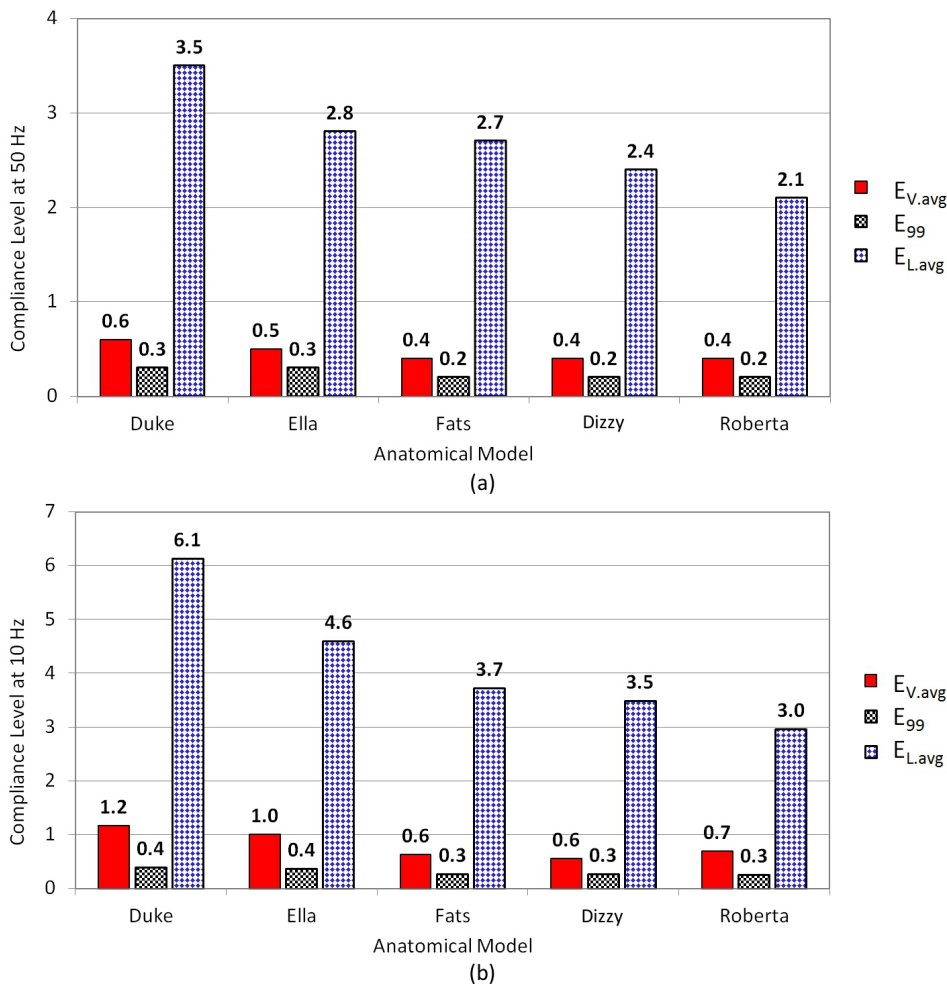


Figure 3.8: The compliance levels for the peak induced $E_{V.avg}$, E_{99} for ICNIRP-2010 and $E_{L.avg}$ for IEEE Std. C95.6-2002, in the brains of the five anatomical models due to uniform LAT B-field exposure at (a) 50 Hz and (b) 10 Hz for general public exposure.

enhancement is subjected to the tissue geometry at the peak induction location. Hence, the variation of the compliance levels between 50 and 10 Hz can be attributed to the variation of the frequency-dependent tissue conductivity contrast ratio.

To explain why the compliance levels of different anatomical models do not scale linearly between 10 Hz and 50 Hz, a comparison of the induced $E_{V.avg}$ distributions at 50 Hz between Duke and Roberta is presented in Figure 3.10. In the 0.5 mm voxel slice views, the dark color tissue represents the CSF while the lighter color tissues enclosed by the CSF represent the brain tissues. The induced E-field distributions demonstrate that due to the difference in tissue geometry between the two investigated anatomical models, the peak induced E-field occurs at different locations (marked by circles). It is observed that while the peak induction location stays the same for the two anatomical models between 10 Hz and 50 Hz, the conversion factor becomes different. This agrees with the finding in Section 3.4.2: a change in the conductivity

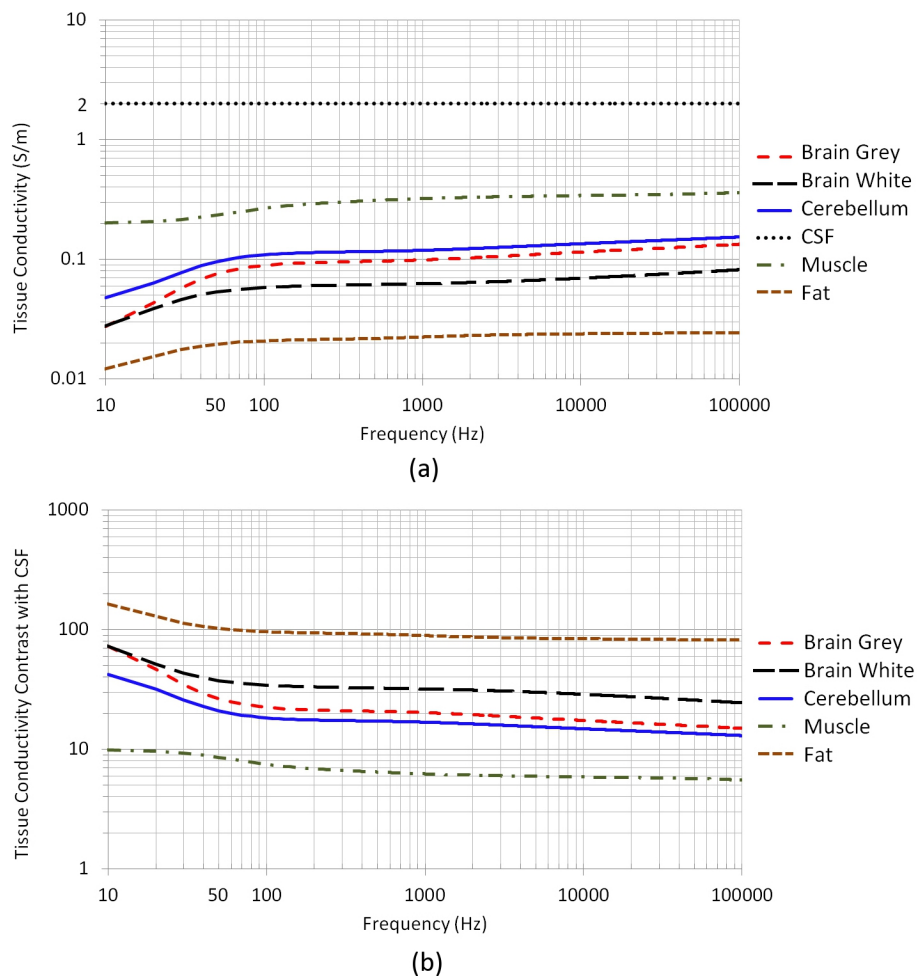


Figure 3.9: (a) Tissue conductivity value and (b) conductivity contrast ratio ($\sigma_{CSF} : \sigma_{Tissue}$) with respect to the cerebrospinal fluid (CSF) for selected biological tissues at low frequency.

contrast ratio is expected to produce different effects on the induced E-field in two distinct models (as demonstrated by the spherical heterogeneous model with different dish layer thickness). The exact amount of variation depends the tissue conductivity contrast ratio and the tissue model geometry at the peak induction location (see Figure 3.6).

3.4.4 Summary of the Human Brain Exposure Analysis

In this section, several critical open issues pertaining to LF numerical dosimetry are addressed. With canonical models and an anatomically realistic model, the effect of spatial averaging on the discretization uncertainty associated with grid size variation is investigated. The computational results indicate that stable peak spatially averaged E-field value can be achieved when the applied grid size is sufficiently small compared to the averaging dimension (e.g., a grid size of 0.5 mm for the ICNIRP-2010 $2 \times 2 \times 2 \text{ mm}^3$ volume averaging or the IEEE Std. C95.6-2002 5 mm line averaging). The 99th percentile value would allow larger grid size and can

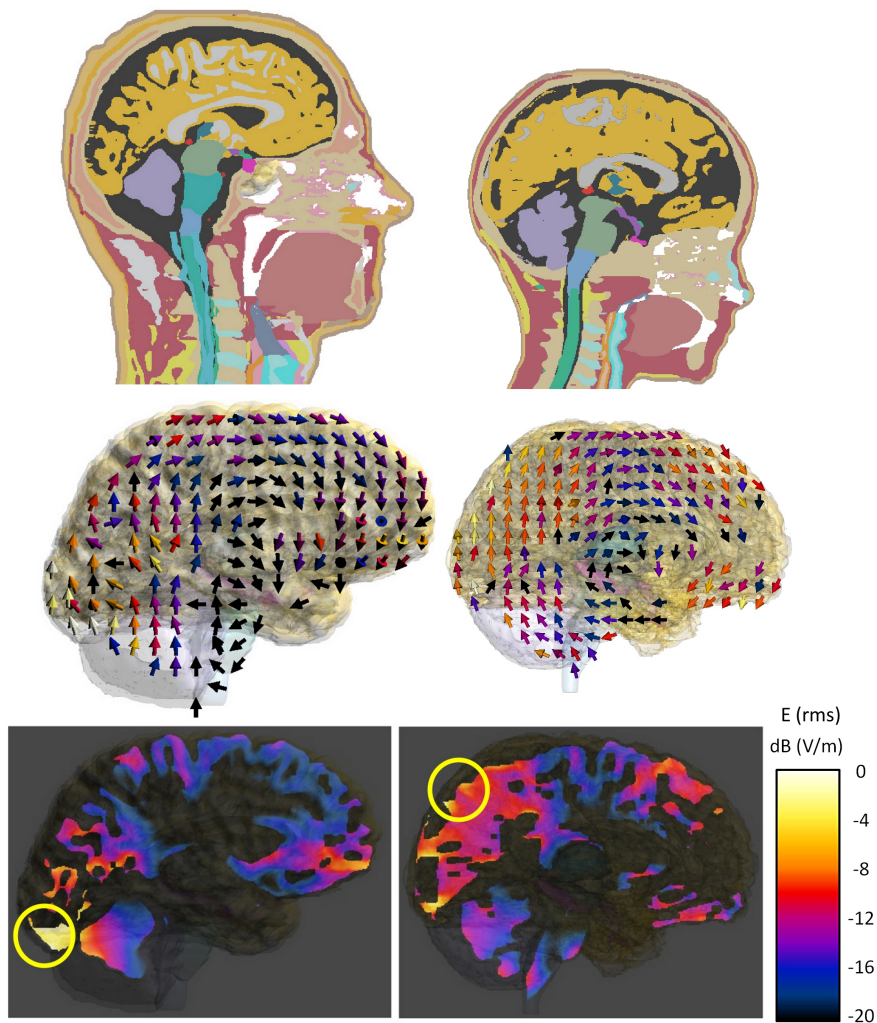


Figure 3.10: The sagittal 0.5 mm voxel slice views (at the peak induction location) of Duke and Roberta and the $E_{V,avg}$ field distributions at 50 Hz due to uniform LAT (side-to-side) B-fields.

conveniently achieve numerical convergence, however it may also significantly underestimate the peak induced E-field. The computational results of high-resolution anatomically realistic models lead to three conclusions: (1) frequency scaling should not be applied if frequency-dependent tissue conductivity contrast ratios are expected; (2) the peak induced E-field derived in a homogeneous head model is most likely not conservative enough to represent the worst-case peak induced E-field in the human brain; (3) the B-field reference levels of IEEE Std. C95.6-2002 [3] can be in contradiction with the basic restrictions by a factor of more than 5 (e.g., at 10 Hz). Based the aforementioned research findings, a revision of the IEEE exposure limits is recommended to achieve a technically sound exposure standard without ambiguity. A list of conversion factors are provided for the human brain exposure in uniform LAT (side-to-side) B-field (from 10 Hz to 100 kHz). These conversion factors serve as an up-to-date reference for the derivations of LF B-field induction exposure limits.

3.5 Analysis of Human Body Exposure

3.5.1 Background

While a detailed analysis of the exposure of human brain tissues to a LF uniform B-field is provided in the previous section, the current section focuses on the exposure of the peripheral nerve system (PNS). A peripheral nerve is defined as the nerve found outside the central nervous system (CNS) and leading to and from the CNS. It is stated in ICNIRP-2010 [2] that the skin can be treated as a worst-case target tissue as it is the outermost anatomical site where sensory nerve endings first emerge. Although the choice of a worst-case target tissue is not specified in IEEE Std. C95.6-2002 [3], the same rationale could be applied. Hence, the modelling of the skin plays a critical role in a LF numerical dosimetry assessment. Despite its importance, the modelling of skin layers was inadequately addressed in past literatures. In [11], a conductivity value of 0.1 S/m (at 50 Hz) was proposed to represent the skin of an anatomical model. This value was described as the value to represent a composite tissue consisting of the skin and the subcutaneous fat. However, it was unclear if the skin layers can in fact be treated as a single composite tissue without compromising the estimation of the peak induced E-field. Also, the derivation of the value 0.1 S/m is not clarified in [11], leading to further ambiguity. Most importantly, the effects of the conductivity contrast among skin layers and the influence of the thickness of skin layers were not characterized prior to this study.

To address the aforementioned open issues, an in-depth investigation is conducted in this section. A multi-layer sub-millimeter skin structure is modelled to represent the actual biological composition of the human skin. By analyzing the impact of the conductivity and thickness of various skin layers on the peak induced E-field in the *dermis* layer (i.e., where sensory nerve endings emerge), an equivalent single layer skin model is derived for a limb-non-touching body posture (e.g., a general standing posture). The research objective of this section is to establish the biological and numerical basis for the modelling of skin in a numerical dosimetry assessment for LF B-field induction.

3.5.2 Skin Anatomy and Tissue Dielectric Property

In this section, a literature review of the skin anatomy and tissue dielectric property is provided to establish a biological basis for the numerical skin model. As shown in Figure 3.11, the human skin consists of mainly two structural layers: the *epidermis* and *dermis* [90]. The fatty layer below the dermis is known as the *hypodermis* (i.e., subcutaneous fat). The hypodermis layer is often not considered as part of the skin. The epidermis layer can be further classified into several layers based on biological composition and function. The outermost epidermis layer is known as the *stratum corneum* (i.e., the keratin layer). This layer is made up mainly by corneocytes (dead, anucleate cells) and contributes significantly to the impedance of the skin (i.e., poorly conductive). The epidermis layers beneath the stratum corneum are often referred to as the *cellular epidermis* in order to differentiate them from the keratin layer. The innermost

Chapter 3. LF Magnetic Field Exposure Analysis - Theory and Fundamentals

epidermis layer is a basale layer known as the *stratum basale* and this layer is usually only one cell thick. Within the basale layer, Merkel nerve endings start to emerge. During keratinization, live cells are generated in the basale layer and gradually migrate towards the keratin layer where they are flattened out. The skin layer below the epidermis is the dermis which mainly consists of connectivity tissue, blood vessels and sensory nerve endings. The hairs and hair follicles associated with hairy skin are not considered in this study. From a nerve stimulation point of view, the Merkel nerve endings in the stratum basale layer signify the outermost site of potential electro-stimulation. As the extremely thin basale layer resides on top of the dermis, the peak E-field induced in the dermis can be regarded as the field quantity which is relevant to peripheral nerve stimulation.

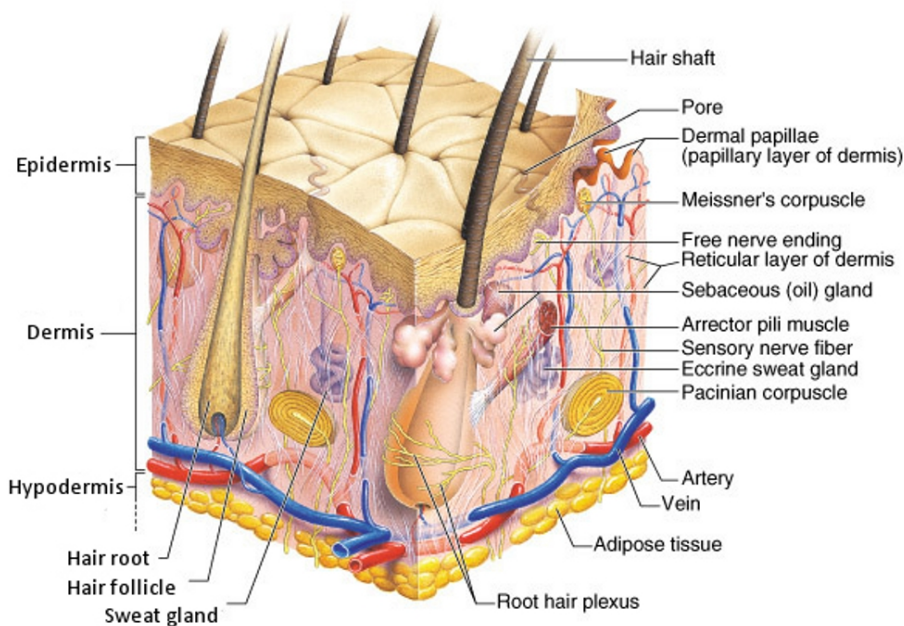


Figure 3.11: Skin anatomy and layer structure (copyright 2009 Pearson Education, Inc., publishing as Benjamin Cummings).

The thickness of the skin varies with respect to anatomical site, gender and age, ranges approximately from 0.5 mm (e.g., on the eyelids) to 3 mm (e.g., on the soles of the feet). According to the reported skin thickness measurement data [91–93], the thickness of a skin layer is approximately 0.02 mm to 0.04 mm for the stratum corneum, 0.08 mm to 1.0 mm for the cellular epidermis, 0.5 mm to 2 mm for the dermis and 5 mm to 10 mm for the hypodermis. The dielectric property of the skin has been investigated in various studies [94–99]. The conductivity values of both dry and moistened skin were reported based on *in vivo* measurements. It is stated in [95] that the effect of the stratum corneum is dominant at frequencies below 10 kHz and the conductivity value is affected by the degree of hydration and the type of moistening agent used. To the authors' best knowledge, no existing literature provides conductivity measurement data for the distinct layers of the skin. The reported values were obtained by

treating the skin layers as a whole. In this study, the skin conductivity values reported in [95] is employed as a basis for the conductivity of the stratum corneum. The conductivity values of the cellular epidermis, dermis and hypodermis layers are postulated based on the respective biological tissue composition. The conductivity value of the muscle is employed as a basis for the dermis and the conductivity value of the fat is employed for the hypodermis. The tissue transition characteristics (live to dead cells) of the cellular epidermis is considered by assuming either linear or non-linear conductivity variation from the conductivity value of the stratum corneum to the conductivity value of the dermis.

3.5.3 Multi-layer Skin Modelling

Based on the skin anatomy illustrated in Figure 3.11, a multi-layer skin model is established to assess the effect of skin layer thickness and skin tissue conductivity on the peak induced E-field in the dermis for a limb-non-touching body posture. Subsequently, the possibility of estimating the peak induced E-field in a multi-layer skin model with an equivalent single-layer skin model is investigated.

Multi-layer Skin Model Configuration

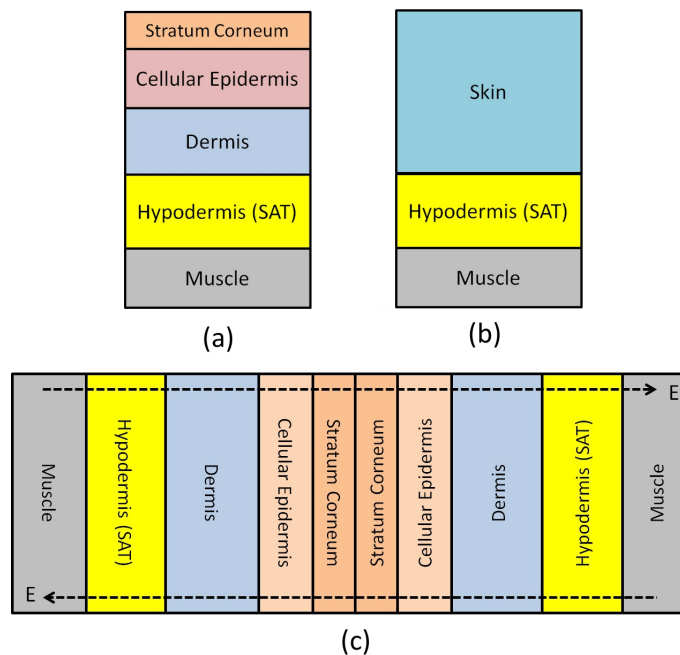


Figure 3.12: (a) A multi-layer skin structure, (b) a single-layer skin structure and (c) an overlapped skin model (note that the skin layer dimensions are not drawn to scale).

To investigate the effect of skin layer thickness and heterogeneous conductivity on the peak induced E-field in the skin, a multi-layer skin model is constructed as shown in Figure 3.12(a). A corresponding single-layer skin model is obtained by replacing the multiple layers with a

homogeneous single layer skin model (see Figure 3.12(b)). As only the E-field component which is normal to the skin layer transition interface is affected by the conductivity contrast, the uneven structure of an actual skin layer can be approximated with a flattened smooth surface as a worst-case scenario. To simulate the overlapped skin structure for a limb-non-touching posture, two blocks of the multi-layer skin models are joined to form an overlapped skin model as shown in Figure 3.12(c). As no modification of the induced E-field distribution due to body posture is considered in this overlapped skin model, the investigation in this section focuses solely on the skin contact scenario for a limb-non-touching posture.

In the overlapped skin model (see Figure 3.12(c)), E-fields which are normal to the skin layer interfaces are induced by exposing the overlapped skin model in a uniform B-field which is aligned tangentially to the interface surface of the skin layers, i.e., perpendicularly in or out of the paper in Figure 3.12(c). The two skin blocks are assumed to be identical in terms of thickness and conductivity distribution. The stratum corneum layer interface is assumed to exhibit perfect contact, i.e., no substances such as dirt and hairs exist at the interface. This ensures the induced E-fields to transit normally across the skin layers. In the case of an imperfect skin-to-skin contact, the induced E-fields will be perturbed whenever a non-conductive obstacle is encountered. As both the thickness and conductivity values of the skin layers are variables, a set of typical values is proposed as the initial simulation parameters based on the reported skin measurement data. The typical thickness value is 0.02 mm for the stratum corneum, 0.08 mm for the cellular epidermis, 1 mm for the dermis and 5 mm for the hypodermis. The conductivity value at 50 Hz is selected to be 0.0002 S/m (i.e., the value of dry skin) for the stratum corneum, 0.23 S/m (i.e., the value of muscle) for the dermis and 0.04 S/m (i.e., the value of fat) for the hypodermis. The aforementioned thickness and conductivity values serve as the initial configuration of the skin model simulations. A uniform grid step size of 0.005 mm is employed to resolve the layer thickness and a uniform 50 Hz B-field is considered. The range of the investigated skin layer conductivity and thickness values is presented in Table 3.2.

Table 3.2: The range of the investigated skin layer conductivity values and thickness values, the typical values are shown in the parenthesis.

	Conductivity (S/m)	Thickness (mm)
Stratum Corneum	0.0002 - 0.002 (0.0002)	0.01 - 0.05 (0.02)
Cellular Epidermis	0.0002 - 0.3 (0.23)	0.08 - 1 (0.08)
Dermis	0.1 - 0.7 (0.23)	0.5 - 2.5 (1)
Hypodermis	0.01 - 0.1 (0.04)	5 - 20 (5)

Sensitivity Analysis of Skin Layer Thickness and Conductivity

To analyze the influence of skin layer thickness and conductivity variation on the peak induced E-field in the dermis, the E-fields in the multi-layer skin model are computed with the parameter range shown in Table 3.2. The computations are performed by sweeping the

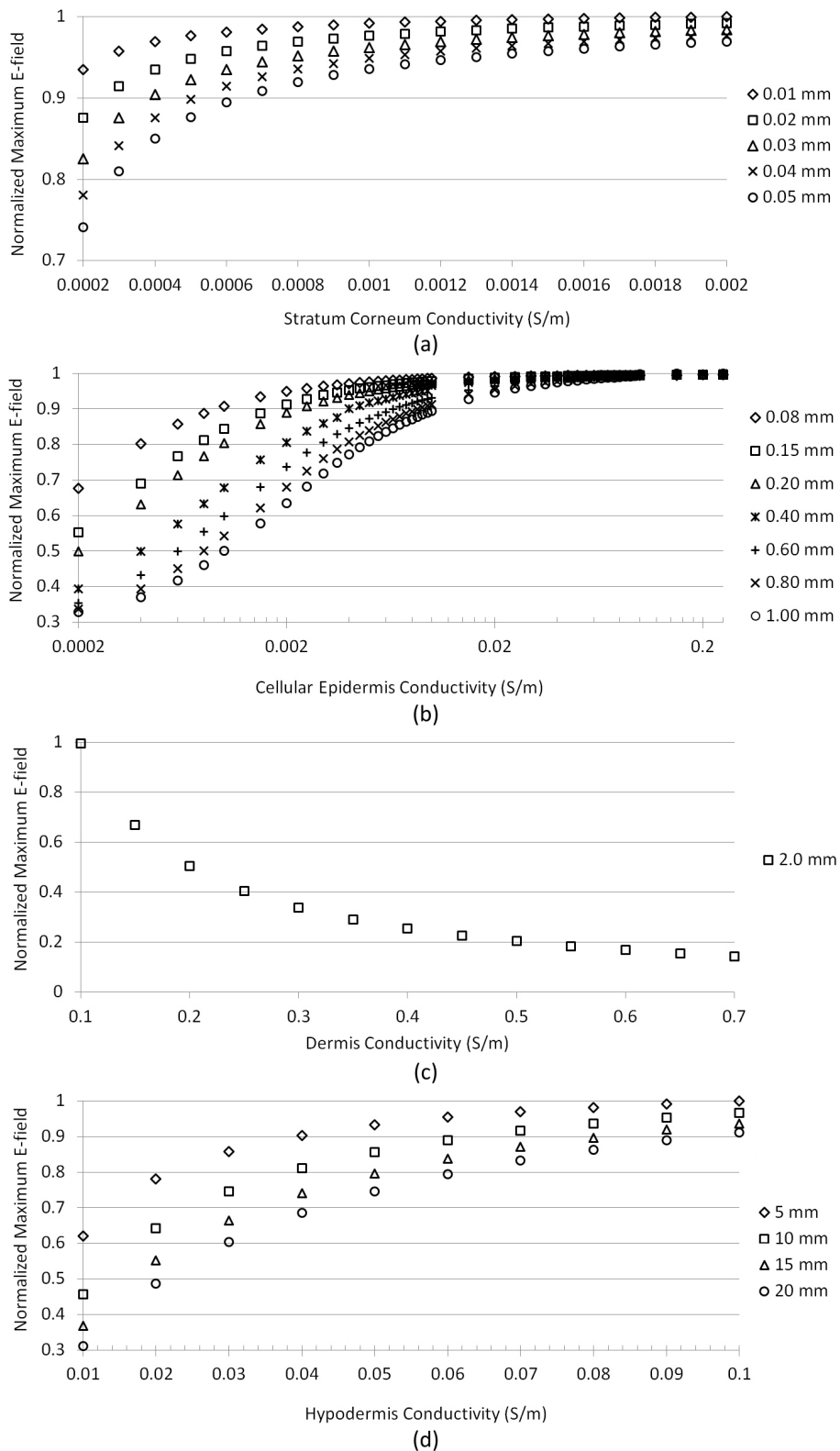


Figure 3.13: The normalized peak induced E-field in the dermis layer as a function of the conductivity (S/m) and thickness (mm) of (a) stratum corneum, (b) cellular epidermis, (c) dermis and (d) hypodermis.

parameters (i.e., the thickness and conductivity values) of a selected skin layer while keeping the parameters of the other layers constant at the typical values. The computational results of the peak induced E-fields in the dermis are shown in Figure 3.13. The values are normalized to the highest value obtained within the investigated parameter range. As shown in Figure 3.13(a), a thicker and less conductive stratum corneum layer leads to lower peak induced E-fields in the dermis. The stratum corneum thickness becomes less influential with ascending conductivity value. A similar trend is observed with the cellular epidermis and hypodermis layers (see Figure 3.13(b) and (d)). The thickness of the dermis is found to exert little impact on the peak induced E-field, hence only the E-field values of 2 mm thickness are shown in Figure 3.13(c). On the other hand, the conductivity of the dermis is found to cause significant variation of the peak value. The higher the dermis conductivity, the lower the peak induced E-field in the dermis. This is due to the increasing high-low-high (dermis-epidermis-dermis) conductivity contrast, more E-fields are accumulated within the epidermis layers and less in the dermis. The result of the sensitivity analysis indicates that the conductivity value of the dermis is a dominant tissue parameter which has strong influence on the peak induced E-field in the dermis. Within the investigated conductivity range, the worst-case peak E-field value in the dermis occurs when the conductivity values of the stratum corneum, cellular epidermis and hypodermis are at the respective upper limit while the conductivity value of the dermis is at its lower limit.

Equivalent Single-layer Skin Model

To evaluate the possibility of estimating the peak induced E-field in the dermis of a multi-layer model with an equivalent single-layer skin model, an overlapped single-layer model is simulated with skin thickness values ranging from 1 mm to 4 mm and conductivity value from 0.0002 S/m to 0.7 S/m. The computed peak E-field values are normalized to the maximum value obtained within the investigated parameter range and presented in Figure 3.14. As shown in Figure 3.14(a), the peak induced E-field value in the single-layer skin model is highly sensitive to the layer thickness for low conductivity values. The dependency of layer thickness reduces significantly with ascending conductivity value. In Figure 3.14(b), the peak E-field values in the single-layer skin are displayed together with the peak E-field values (i.e., the horizontal lines) computed in the dermis (with conductivity values from 0.1 S/m to 0.7 S/m) of the multi-layer skin model in the worst-case scenario within the investigated skin parameter range (see Table 3.2). The parameter σ_S represents the conductivity value of the single-layer skin model and σ_M refers to the conductivity value of the dermis in the multi-layer skin model. It is observed that when the same conductivity value (in the range of 0.1 S/m to 0.7 S/m) is applied for σ_S and σ_M , the peak E-field value found in the single-layer skin model (i.e., marked as black dots in Figure 3.14(b)) is consistently higher than the peak value found in the dermis of the multi-layer model. A comparison between the computational results of the single-layer skin model and the multi-layer skin model reveals that a single-layer skin model with the same conductivity as the dermis of a multi-layer model can provide a conservative estimation of the peak induced E-field in the dermis.

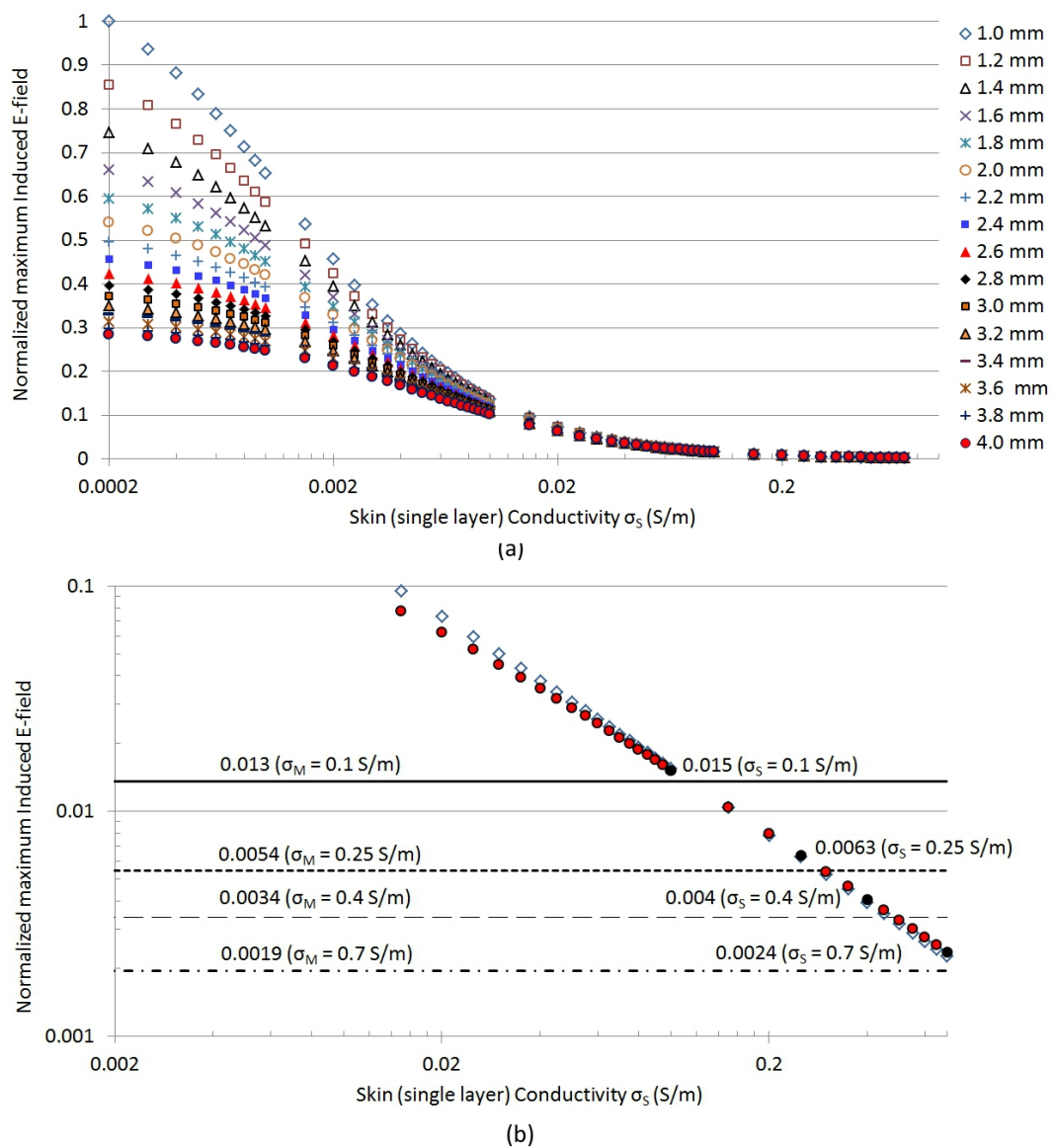


Figure 3.14: (a) The normalized peak induced E-field in the single-layer skin model as a function of the skin conductivity (S/m) and layer thickness (mm), and (b) a comparison with the peak E-field values (horizontal lines) computed in the dermis of the multi-layer skin model.

3.5.4 Computational Results of an Anatomical Model

In this section, the anatomical model Duke is employed for the computations of the induced E-fields in the human body. The skin layer of Duke was segmented as a single-layer CAD model (approximately 2 mm to 4 mm thick) which completely covers the body surface. As a separate CAD model was segmented for the hypodermis, the anatomical skin model hereby represents a composite single-layer tissue consisting of the epidermis and dermis. The subsequent investigations focus on assessing the skin modelling characteristics derived in Sections 3.5.3 on an anatomically realistic model.

Chapter 3. LF Magnetic Field Exposure Analysis - Theory and Fundamentals

Based on the canonical skin model investigated in Section 3.5.3, the anatomical skin model can be considered as an equivalent single-layer skin for a limb-non-touching body posture. To assess the impact of conductivity and grid size variation on the peak induced E-field in the skin of an anatomical model, the scenario of Duke exposed to a uniform 50 Hz AP (front-to-back) 0.1 mT B-field is investigated (i.e., corresponds to the maximum circumference of the body). The model is posed in a general standing posture with arms to the side of the body and legs slightly split from each other (see Figure 2.9). The computations are performed with uniform grid size ranging from 2 mm to 1 mm (with a step change of 0.1 mm) and skin layer conductivity at either 0.0002 S/m (i.e., the value of dry skin) or 0.23 S/m (i.e., the value of muscle).

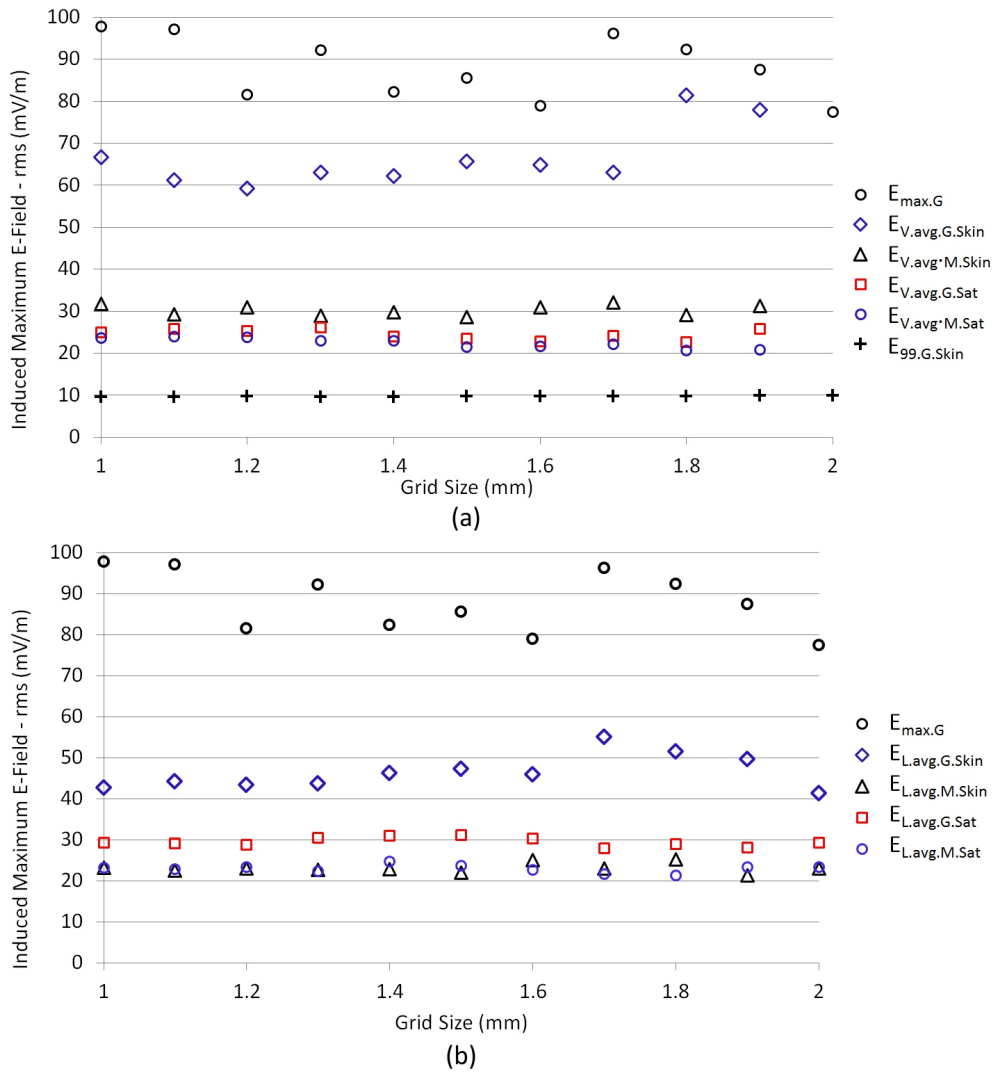


Figure 3.15: The peak E-field induced in Duke due to 0.1 mT 50 Hz uniform front-to-back B-field as a function of grid size with two skin conductivity values, “G” stands for a conductivity of 0.0002 S/m and “M” stands for 0.23 S/m, “Skin” stands for E-field in the skin and “Sat” stands for E-field in the hypodermis.

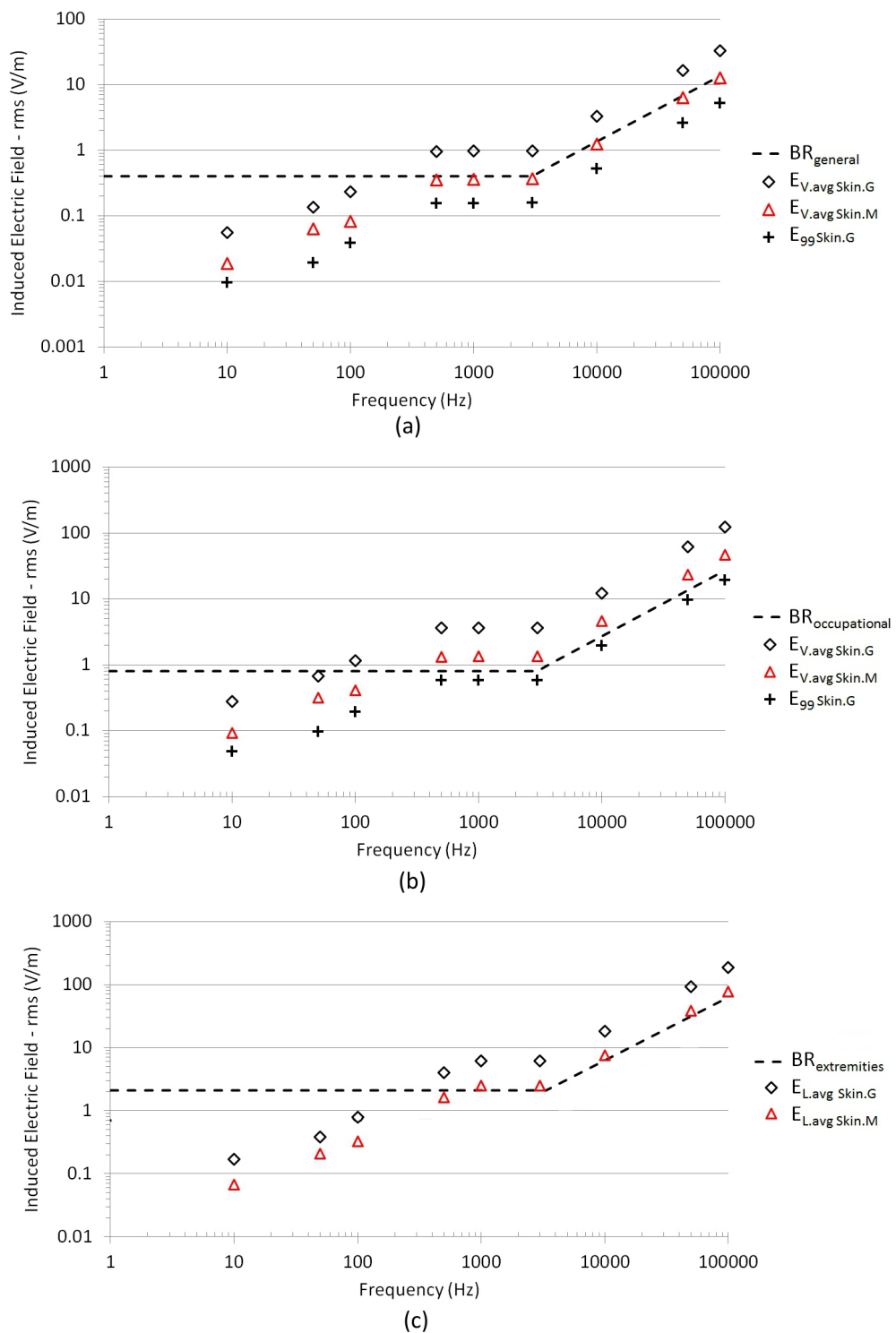


Figure 3.16: The ICNIRP-2010 BR levels for the PNS tissue and the peak $E_{V,\text{avg}}$, E_{99} values for (a) general public and (b) occupational exposure, and (c) the IEEE.Std.C95.6-2002 BR levels for the extremities and the peak $E_{L,\text{avg}}$ values for general public exposure, in the skin of Duke exposed to a uniform AP (front-to-back) B-field at the respective reference level, “G” stands for a skin conductivity of 0.0002 S/m and “M” stands for 0.23 S/m.

The peak induced E-fields computed in the skin and the hypodermis are presented as a function of grid size in Figure 3.15. As expected, the voxel maximum value (E_{\max}) varies significantly with respect to grid size variation. Since the variation of grid size could potentially change the discretized skin layer thickness, the voxelized model exhibits slightly variable skin thickness with respect to the applied grid size. The spatially averaged peak induced E-field in the skin with 0.0002 S/m conductivity is the highest among the spatially averaged values (i.e., due to lower skin conductivity) and exhibits moderate dependency to grid size variation. The fluctuation of the E-field values can be explained by Figure 3.14(a) which demonstrates that the induced E-field in a single-layer skin model is significantly influenced by the skin thickness for low skin conductivity values (e.g., at 0.0002 S/m). The remaining spatially averaged and 99th percentile E-field values are much less affected by grid size variation (i.e., due to higher skin conductivity). When the skin conductivity value is at 0.23 S/m, the peak E-field in the hypodermis closely resembles the peak value in the skin. This agrees with the finding in Section 3.5.3 that the peak E-field in the hypodermis can be the dominant peak value due to its lower conductivity compared to the conductivity value of muscle. As shown in Figure 3.15(a), the 99th percentile value underestimates the peak E-field significantly when compared to the volume-averaged value. The computational results in this section indicate that for a limb-non-touching anatomical model with a single-layer skin, the dermis conductivity should be applied to the skin layer to avoid overestimation and grid dependency. The spatially averaged peak induced E-field in the skin (which also includes the values in the hypodermis due to contiguous averaging) can be considered as the relevant field quantity to be compared with the basic resections.

Subsequently, the same exposure scenario is computed with a uniform 1 mm grid size and two skin conductivity values (i.e., the values of dry skin and muscle) at nine frequency points from 10 Hz to 100 kHz. The peak E-field ($E_{V,avg}$, E_{99} and $E_{L,avg}$) values found in the skin of Duke, scaled to the reference levels suggested in ICNIRP-2010 [2] and IEEE Std. C95.6-2002 [3] are presented in Figure 3.16 with the respective basic restrictions. The peak E-field values due to the dry skin conductivity is provided as a reference to indicate the amount of potential overestimation due to the erroneous conductivity value assumption. As shown in Figure 3.16(a) and (b), the E_{99} values are compliant with the ICNIRP-2010 basic restrictions. This is expected since the ICNIRP-2010 reference levels were derived based on the E_{99} values [11, 12]. However, it should be noted that the 99th percentile value has been shown to potentially underestimate the peak induced E-field when compared to the $E_{V,avg}$ value (see Figure 3.15(a)). The volume-averaged E-field values are marginally compliant for the ICNIRP-2010 general public exposure limits and non-compliance is demonstrated for the occupational exposure limits for frequencies above 100 Hz. This is due to the fact that a less stringent safety factor is applied for the ICNIRP-2010 occupational exposure limits. As shown in Figure 3.16(c), for the comparison between the line-averaged E-field values and the IEEE exposure limits, marginal compliance is demonstrated for frequencies above 100 Hz. In summary, the computational results of the limb-non-touching Duke model suggest that the exposure limits [2, 3] should be revised to provide adequate safety margins. The conversion factors between a 1 T uniform AP

(front-to-back) B-field and the computed peak induced E-field in the skin (with the conductivity value of muscle) and hypodermis (with the conductivity value of fat) of Duke is presented in Table 3.3. It is observed that the conversion factors for the whole-body B-field exposure are relatively invariant with respect to frequency shift.

Table 3.3: The conversion factors between a 1 T uniform AP (front-to-back) B-field and the computed peak induced E-field in the skin of Duke when the conductivity value of muscle is applied to the skin layer.

(V/m)/T/Hz	Frequency (Hz)								
	10	50	100	500	1000	3000	10000	50000	100000
$E_{V,avg}$	4.70	4.96	4.09	4.40	4.45	4.51	4.56	4.62	4.67
E_{99}	1.83	1.92	1.87	1.84	1.85	1.93	1.89	1.96	1.86
$E_{L,avg}$	4.51	4.78	4.63	4.72	4.76	4.79	4.82	4.85	4.88

3.5.5 Summary of the Human Body Exposure Analysis

In this section, open issues pertaining to the modelling of skin layer (i.e., a potential worst-case target tissue for a LF B-field full-body exposure) are addressed. By developing and simulating a multi-layer skin structure, the impact of the conductivity and thickness of various skin layers on the peak induced E-field in the dermis (i.e., where sensory nerve endings emerge) is investigated. It is revealed that the peak E-field in the dermis can be conservatively approximated by an equivalent single-layer skin model for a limb-non-touching body posture (e.g., a general standing posture). The computational results of an anatomical model indicate that the reference levels recommended by ICNIRP-2010 [2] and IEEE Std. C95.6-2002 [3] provide inadequate safety margins for a limb-non-touching human body exposed to a LF uniform B-field.

3.6 Conclusion

In summary, the research work presented in this chapter illustrates the applications of the SPFE solver in the exposure analysis of LF B-field induction. The core research objective is to improve on the existing knowledge of the peak induced E-field in the brain tissues (CNS) and peripheral tissues (PNS) of a human body exposed to LF B-field. To this aim, the spatial averaging and percentile filtering techniques recommended in ICNIRP-2010 [2] and IEEE Std. C95.6-2002 [3] are implemented based on a sound interpretation of the associated biological and numerical rationales. Next, to quantify the effects of spatial averaging and 99th percentile filtering algorithms on the discretization uncertainties with respect to stair-casing errors, field singularities and grid size variations, the simulations of canonical and anatomical models are investigated. The computational results indicate that the guideline-recommended spatial averaging is capable of suppressing the discretization uncertainties, provided that a suitable grid resolution is applied (e.g., 0.5 mm grid size for the $2 \times 2 \times 2 \text{mm}^3$ volume averaging

and the 5 mm line averaging). The 99th percentile filtering, as suggested in ICNIRP-2010 [2], is discouraged by the research outcome of this study because it is shown to potentially underestimate the peak induced E-field. The research findings reported in this chapter have established a sound basis for further investigations with high-resolution anatomically realistic models.

The subsequent research work leads to a detailed analysis of the human brain and whole body exposure in a LF uniform B-field. For the first time, the conversion factors between the external uniform B-field and the peak induced E-field in the human brain and human body are derived based on the computational results of the spatially averaged peak E-field values. Compliance assessments with the published LF exposure limits [1–3, 5] are conducted to assess the validity of these exposure limits. In the human brain exposure analysis, it is observed that the ICNIRP-2010 reference level at 10 Hz is non-conservative due to the erroneous assumption of frequency scaling and the IEEE Std. C95.6-2002 reference levels below 1 kHz are non-conservative due to the assumption of tissue conductivity homogeneity. These findings are verified by the computational results of a canonical heterogeneous model which demonstrate the potential underestimation due to the neglect of tissue-to-tissue conductivity contrast and frequency-dependent tissue conductivity variation. In the whole body exposure analysis, the modelling of a multi-layer skin is addressed for the first time. The computational results indicate that for a limb-non-touching body posture, a multi-layer heterogeneous skin structure can be conservatively approximated by a single-layer homogeneous model.

4 LF Magnetic Field Exposure Analysis - Practical Investigations

4.1 Introduction

Wireless power transfer (WPT) via magnetic resonant coupling has been a popular research topic in recent years [100–102]. Both mid-range and close-range WPT system designs have been experimentally explored for practical wireless charging applications [103–105]. Besides achieving adequate power transfer efficiency and link range, another critical design requirement for a practical WPT system is the electromagnetic exposure safety compliance for a human body in close vicinity of the system. The evaluations of mid-range high-power WPT system exposure to the human body at MHz range have been reported in [106] and [107]. In this section, the exposure of a human body to a close-range low-power (5 W) 4-link WPT system is numerically examined with respect to the peak induced spatially averaged electric field (E-field) and specific absorption rate (SAR). The exposure limits of the peak induced E-field and SAR (i.e., the basic restrictions) recommended by the International Commission on Non-Ionizing Radiation Protection (ICNIRP-1998 [1] and ICNIRP-2010 [2]) and the Institute of Electrical and Electronics Engineers (IEEE C95.1-1991 [4] and IEEE C95.1-2005 [5]) are employed as the basis of compliance assessment.

The distinct differences between the currently investigated WPT system and the systems examined in [106–108] lie in the operating frequency (i.e., at kHz range for the current WPT system and MHz range for the previously reported systems) and the overall system dimensions (i.e., a maximum coil dimension of 125 mm compared to 580 to 600 mm in [106, 107]). Another distinguishing feature of the investigated WPT system is the inability of one subsystem to work independent of the others, due to proprietary algorithms and control circuitry. This makes the study of a complete 4-link system the only configuration necessary for the exposure assessment during a normal operation.

In addition to the exposure assessment of a practical close-range low-power resonant WPT system, a theoretical assessment of the effects of coil dimension, coil-to-body distance and WPT operating frequency on the induced peak field intensity is also conducted to systematically reveal the impacts of system design parameters on exposure compliance. To this aim,

this section is structured as follows: first, the employed anatomical models, exposure limits and numerical techniques are described to provide a basis for the forthcoming investigations. Next, the exposure assessment of a practical 4-link WPT system is conducted to determine the exposure compliance with respect to the published exposure limits. Subsequently, the induction characteristics of generic coils are analyzed using homogeneous phantom and high-resolution anatomical models to establish the dependence of induced peak field intensity on WPT system parameters (e.g., coil dimension and operating frequency). A semi-analytical estimation approach is proposed to be applied during the key design phase of a practical close-range WPT system to conservatively predict the worst-case induced field intensity in a human body.

4.2 Exposure to Close-Range Wireless Power Transfer System

4.2.1 Methods and Materials

Anatomical Models and Exposure Locations

Four anatomically realistic human models (Duke, Ella, Fats and Dizzie) and one homogeneous torso phantom are used for the numerical simulations in this study. As a homogeneous model leads to induced E-fields which are independent of tissue dielectric properties at low frequency (i.e., when the body dimension is significantly smaller than the wavelength),

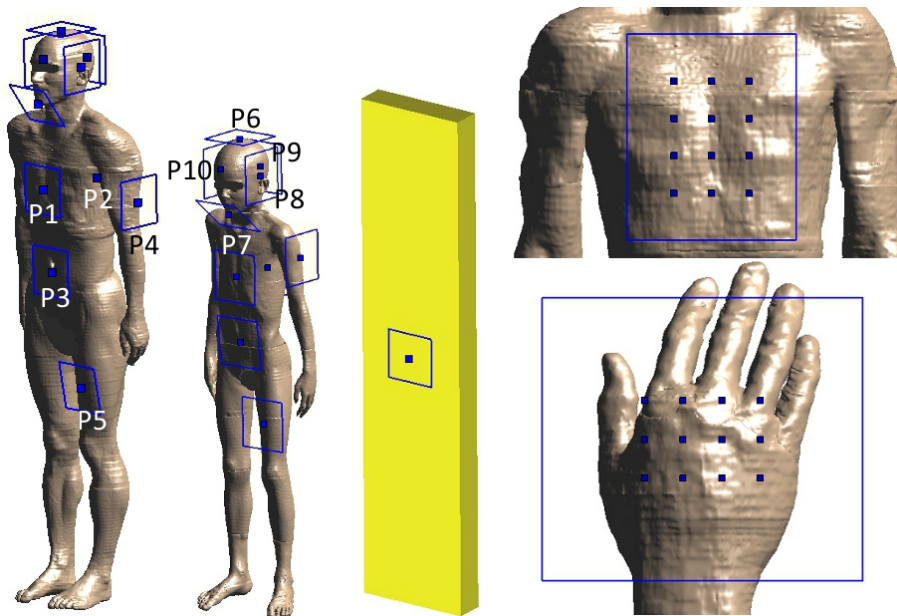


Figure 4.1: Human body models (Duke and Dizzie) with the investigated sites of exposure and system positions (torso and hand) for location sensitivity analysis, the encircled area indicates the region exposed to the WPT system.

the induced peak E-field based on a homogeneous model can be non-conservative (i.e., potential underestimation) compared to the peak intensity estimated by a heterogeneous anatomical model (see Section 3.4). Hence, a $1.54 \times 0.34 \times 0.09 \text{ m}^3$ homogeneous phantom is considered in this study solely for the derivation of induced peak E-field characteristics, instead of compliance assessment. As indicated in Figure 4.1, ten exposure locations are selected for investigation. These anatomical sites are identified as : P1: center chest, P2: center back, P3: center tummy, P4: left arm, P5: left leg, P6: top of the head, P7: chin, P8: left head, P9: back of the head and P10: right head. The coils in Figure 4.1 represent the potential locations of the closest current-carrying element of a WPT system to a human body. The coil-to-body distance will be specified according to the investigated exposure scenarios in the subsequent sections. The coil surface is orientated tangential to the body surface at the coil center. It should be noted that some of the selected exposure locations, e.g., P6 (top of the head), are unlikely to occur in a practical exposure scenario. They are included only as a pre-cautious measure. The Duke and Dizzie models are employed for the analysis of P1 to P10 sites of exposure. In addition, a location sensitivity analysis is performed with all four anatomical models by shifting the center of the WPT system within a 3×4 grid array by a uniform step of 50 mm as shown in Figure 4.1 on the front and back (i.e., the largest flat torso region) of the four anatomical models. The sensitivity analysis is performed to assess the worst-case exposure corresponding to a flat body region which could potentially be exposed to the magnetic flux generated by the WPT system. Furthermore, to depict the most frequently encountered exposure scenario, an user hand exposure case is also considered by employing a 4×3 location grid array with a uniform step of 20 mm.

Table 4.1: The ICNIRP and IEEE exposure limits relevant for WPT operating between 0.1–10 MHz, f in Hz.

Quantity	Spatial Average	Value
ICNIRP 1998 (psSAR _{10g}) and ICNIRP 2010 (E, B)		
$B_{inc-limit}$	point	27 μT
$E_{ind-limit}$	8 mm ³ (cubic)	$e_{limit} \cdot f$ ($e_{limit} = 13.5 \text{ mV/m/Hz}$)
psSAR _{limit}	10g (cubic)	2 W/kg (head&body) 4 W/kg (extremities)
IEEE C95.1-1992 (psSAR _{1g}) and IEEE C95.1-2005 (E, B, psSAR _{10g})		
$B_{inc-limit}$	point	205 μT
$E_{ind-limit}$	5 mm (line)	$e_{limit} \cdot f$ ($e_{limit} = 20.9 \text{ mV/m/Hz}$)
psSAR _{limit}	10g (cubic)	2 W/kg (head&body) 4 W/kg (limbs)
psSAR _{limit}	1g (cubic)	1.6 W/kg (head&body) 4 W/kg (limbs)

Relevant ICNIRP and IEEE Exposure Limits

The general public basic restrictions (i.e., the maximum value of the induced E-field and SAR allowed in an exposed human body) are considered in this study. The following international exposure guidelines are considered: ICNIRP 1998 [1], ICNIRP 2010 [2], IEEE C95.1-1999 [4] and IEEE C95.1-2005 [5]. As shown in Table 4.1, the basic restriction values for body tissues in the frequency range between 100 kHz and 10 MHz are the relevant exposure limits for this investigation. It should be noted that ICNIRP 1998 [1] which employs current density (J) for low frequency exposure is referred only for the SAR limit in this study. The maximum permissible external field intensity, known as the reference level (for ICNIRP) and maximum permissible exposure (for IEEE), are provided by the respective exposure guidelines based on worst-case uniform field exposure scenarios. As a human body can be a few millimeters away from the current-carrying elements of the investigated WPT system during normal operation, the exposure will be largely localized. Hence, the reference level based on worst-case uniform exposure is not representative of the exposure threshold for the investigated WPT system.

Relevant Basic Restriction Field Quantities

For the induced peak E-field, a vector average of the E-fields within a contiguous tissue volume of $2 \times 2 \times 2 \text{ mm}^3$ is specified in ICNIRP 2010 [2] while an arithmetic average determined over a straight line segment of 5 mm length oriented in any direction within the tissue is recommended in IEEE C95.1-2005 [5]. It is stated in the ICNIRP 2010 guidelines that for a specific tissue, the 99th percentile value (i.e., the value exceeded by 1% of the total voxel elements) of the E-fields is the relevant value to be compared with the basic restriction. Several drawbacks of the 99th percentile filtering, e.g., underestimation of the peak value for localized exposure, have been reported in [15] and [18] and Sections 3.4, 3.5. As only localized exposure scenarios are investigated in this study, the non-filtered peak spatially averaged E-field serves as a conservative quantity to be compared with the basic restriction. For the localized peak spatial specific absorption rate (SAR), spatial averaging in a 10 gram or 1 gram tissue mass is specified in ICNIRP 1998 [1] and IEEE C95.1-1991 [4]. The frequency range in which both the induced peak E-field and SAR are required to be assessed concurrently is 100 kHz to 10 MHz for the ICNIRP guidelines and 100 kHz to 5 MHz for the IEEE standards.

Quasi-Static Approximation Frequency Limit

In this work, low frequency exposure simulations are performed using the Scalar Potential Finite Element (SPFE) solver [48]. A stopping criterion of 10 orders of magnitude reduction for the initial residual is applied for all the low frequency simulations. The validity of quasi-static approximation for the SPFE solver is guaranteed by satisfying the condition $|\omega^2 \mu \tilde{\epsilon} d^2| \ll 1$, where μ is the permeability, $\tilde{\epsilon}$ is the complex permittivity and d is the characteristic length (i.e., the maximum dimension of an exposed object). This condition and the ohmic-current-dominant tissue property condition have been described in 2.31, 2.32 and 2.33. As local-

ized exposure scenario is investigated in this study, an exposed body region with the size of $230 \times 230 \times 80 \text{ mm}^3$ is assumed based on the 0 dB to -30 dB B-field distribution region (on one side of the coil) by a $150 \times 150 \text{ mm}^2$ current-carrying coil (i.e., the maximum dimension of the investigated coil sizes). The diagonal distance of this exposure region, 335 mm, is employed as the characteristic length d . The tissue dielectric properties (μ and ϵ) are approximated by the weighted averaged values based on measured percentage tissue compositions of male adults [61] and individual tissue dielectric properties [60]. The left-hand-sides of 2.31, 2.32 and 2.33 are computed and presented in Figure 4.2. Based on the plots, numerical simulations at frequencies below 1 MHz are performed with the SPFE solver. For frequencies above 1 MHz, exposure simulations are performed with a full-wave finite-difference time-domain (FDTD) solver provided in SEMCAD-X V.14.8 [48]. The anatomical models are discretized without truncation for all the simulations.

To ensure that the E-fields produced by the system components (e.g., the tuning capacitors) do not impair the assumption of magnetic induction dominance, an electro-quasi-static (EQS) simulation is performed using the EQS SPFE solver provided in the same software package. The homogeneous flat body phantom as shown in Figure 4.1 is employed. A $1 \times 1 \text{ cm}^2$ capacitor plate with a 2 mm gap is placed 5 mm away from the front center of the phantom. The dielectric properties of the phantom is assumed to be 0.18 S/m for the conductivity (σ) and 3600 for the relative permittivity (ϵ_r) based on the weighted averaged tissue properties at 100 kHz. The simulation result indicates that to induce 20.9 V/m (IEEE-C95.1-2005 basic restriction) of E-field in the body at 100 kHz, an external E-field of 760 kV/m immediately outside of the body is required, equivalent to a voltage of 9.8 kV in the capacitor. This voltage level is significantly higher (by a factor of 100) than the maximum voltage across the tuning capacitors in the investigated system. Based on the results, the contribution of E-field induction at 100 kHz is assumed to be negligible in this study.

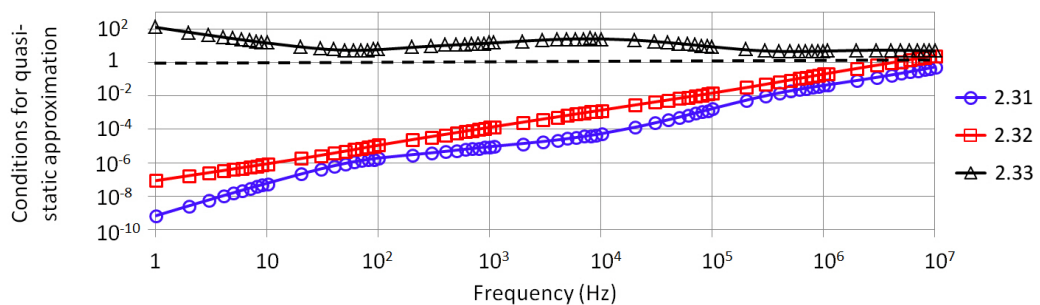


Figure 4.2: The quasi-static approximation validity conditions computed by 2.31, 2.32 and 2.33, based on weighted average tissue dielectric properties and a characteristic length of 335 mm.

4.2.2 Investigation of a Practical WPT System

In this section, the exposure of a practical 100 kHz WPT system is investigated with anatomically realistic human body models and a validated numerical WPT model. The peak induced field quantities are compared with the associated exposure limits to determine the compliance of the investigated WPT design with respect to the ICNIRP and IEEE exposure guidelines.

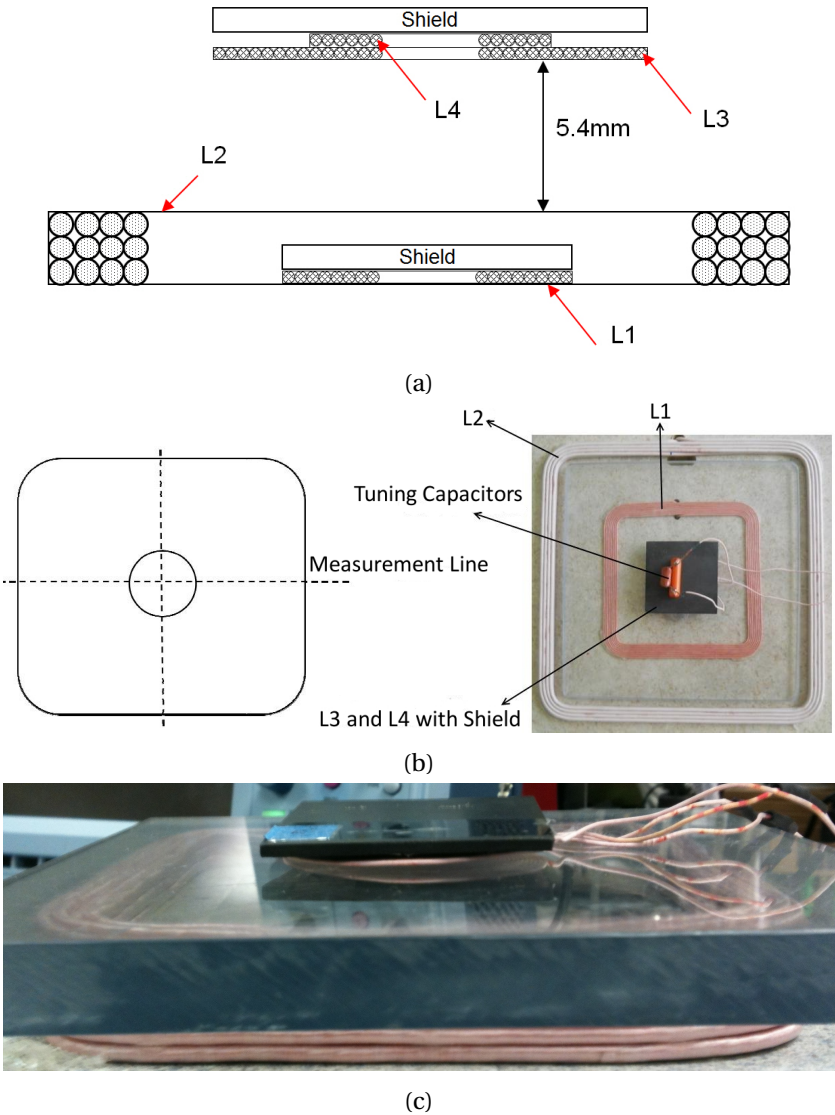


Figure 4.3: The structure of the investigated WPT system (not drawn to scale): (a) L1 to L4 coil positions, (b) top view of the system with B-field measurement line and (c) side view of the system.

Description of the Investigated WPT System

The WPT system under investigation is a 5 W 4-link power transfer unit which operates at 100 kHz with dimensions and inductances optimized for magnetic resonant wireless power transfer. The coils, L1 to L4, are separated into the Tx (co-axial L1 and L2) and Rx (co-axial L3 and L4) subsystems as shown in Figure 4.3. A Tx-to-Rx subsystem separation of 5.4 mm is considered in this study. L1 is an 8-turn single-layer square coil of 66/38 Litz wire with inductance of 12.49 μH , equivalent series resistance (ESR) of 106 $\text{m}\Omega$ and outer dimension of $74 \times 74 \text{ mm}^2$. A $76 \times 76 \times 2.5 \text{ mm}^3$ ferrite disc is attached on the top of L1 to limit the non-adjacent coil coupling and to increase coil inductance. L2 is a 4-turn 3-layer square coil of 420/38 Litz wire with outer dimension of $125 \times 125 \text{ mm}^2$, inductance of 34.78 μH and ESR of 47 $\text{m}\Omega$. L3 is a 14-turn single-layer spiral coil of 75/41 Litz wire with inductance of 17.8 μH , ESR of 138 $\text{m}\Omega$, inner diameter of 27.8 mm and outer diameter of 52.8 mm. L4 is a 6-turn single-layer spiral coil of 75/41 Litz wire with inductance of 4.44 μH , ESR of 61.5 $\text{m}\Omega$, inner diameter of 27.8 mm and outer diameter of 38.4 mm. A $50 \times 50 \times 2.5 \text{ mm}^3$ ferrite disc is attached above L3 and L4 to act as both flux guide and shielding of device electronics. The investigated WPT system is designed towards conforming to the interoperability and compatibility standards of the international wireless power standard, the Qi-standard, by the Wireless Power Consortium (WPC) [109].

Numerical Modelling and Experimental Validation

The incident B-fields generated by the WPT system with one Rx subsystem in active charging operation (aligned center-to-center with respect to the Tx subsystem) were measured along the central horizontal axis on the plane 9.7 mm above the top of the Rx subsystem with a Narda ELT-400 Exposure Level Tester (see Figure 4.3(b)). The measurements were performed at 100 kHz with the Rx subsystem attached to a 5 Ω load, drawing 5 W power from the L1 source coil. The uncertainty of the instruments is $\pm 6\%$, the integration results in an error of 5% and the repeatability is $< 2.5\%$, i.e., the combined uncertainty (*root sum square*) for $k = 2$ was less than 8%. At the surface of the enclosure the peak B-field is approximately 7 times above the $B_{inc-limit}$ of ICNIRP 2010 and approaching the $B_{inc-limit}$ of IEEE C95.1-2005 (see Table 4.1). A numerical model consisting of Tx and Rx coils is constructed to simulate the exposure of the actual system (see Figure 4.4).

Exposure Assessment using Anatomical Models

A grid analysis is initiated to assess the influence of discretization variation on the computed induced peak E-field in an anatomical model. The scenario of the adult model exposed to the WPT system at P2 (center back) is computed with a uniform grid size from 2 mm to 0.5 mm, with a step change of 0.1 mm. The computed induced peak E-field values are presented in Figure 4.5. As shown, the spatially averaged E-field value is relatively stable with respect to discretization variation for a grid size $\leq 1 \text{ mm}$, with a maximum deviation of 7% among the

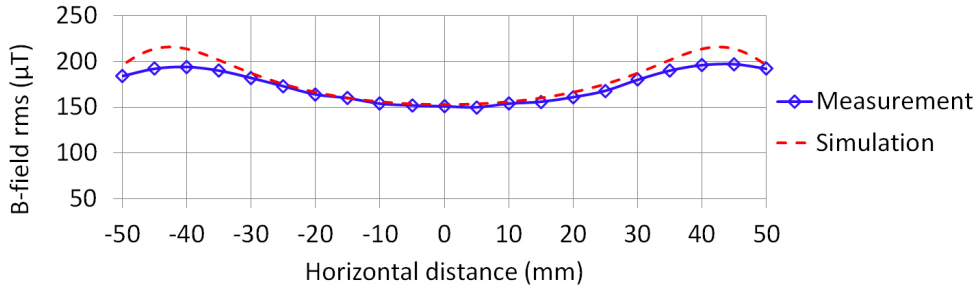


Figure 4.4: The measured and simulated B-field along the central horizontal axis, 9.7 mm above the top of the Rx subsystem.

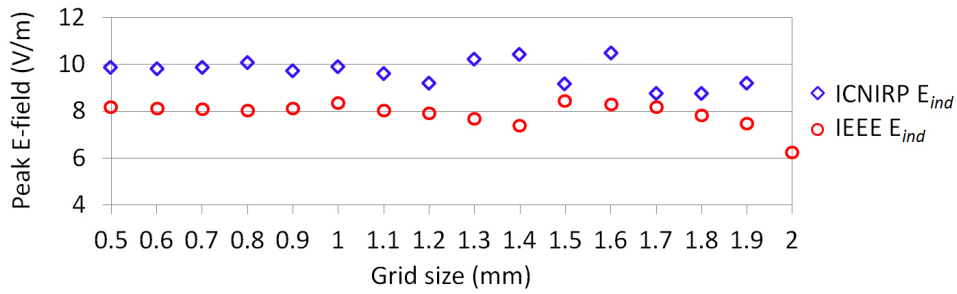


Figure 4.5: The peak $E_{V,avg}$ and $E_{L,avg}$ values (V/m) for the Duke model at P2 exposure location as a function of grid size.

peak values. Hence, a computed $E_{V,avg}$ or $E_{L,avg}$ value based on a uniform 1 mm grid resolution can be considered as a stable numerical quantity to be compared with the respective exposure limit for compliance assessment.

To facilitate a convenient assessment metric with respect to the basic restrictions for the investigated WPT system, a compliance factor C_E for the induced peak E-field, which compares the peak value with the relevant basic restriction, is defined in this study as:

$$C_E = \frac{E_{ind}}{E_{ind-limit}} \quad (4.1)$$

where E_{ind} is the computed induced peak E-field in a human body due to the exposure to a WPT system at its operating frequency f and $E_{ind-limit}$ is the guideline-specified basic restriction at f . A C_E value greater than 1 indicates that the basic restriction is exceeded, while a value lower than 1 serves as an indication of the available margin (below exposure threshold) for the external B-field. A similar compliance factor is defined for the SAR:

$$C_{psSAR} = \frac{psSAR_{ind}}{psSAR_{Limit}} \quad (4.2)$$

Chapter 4. LF Magnetic Field Exposure Analysis - Practical Investigations

The exposure scenario of the WPT system located at P1 to P10 positions for Duke and Dizzie are computed with the validated numerical WPT model at 100 kHz. A uniform 1 mm grid resolution is employed to discretize the anatomical models. The WPT system is orientated

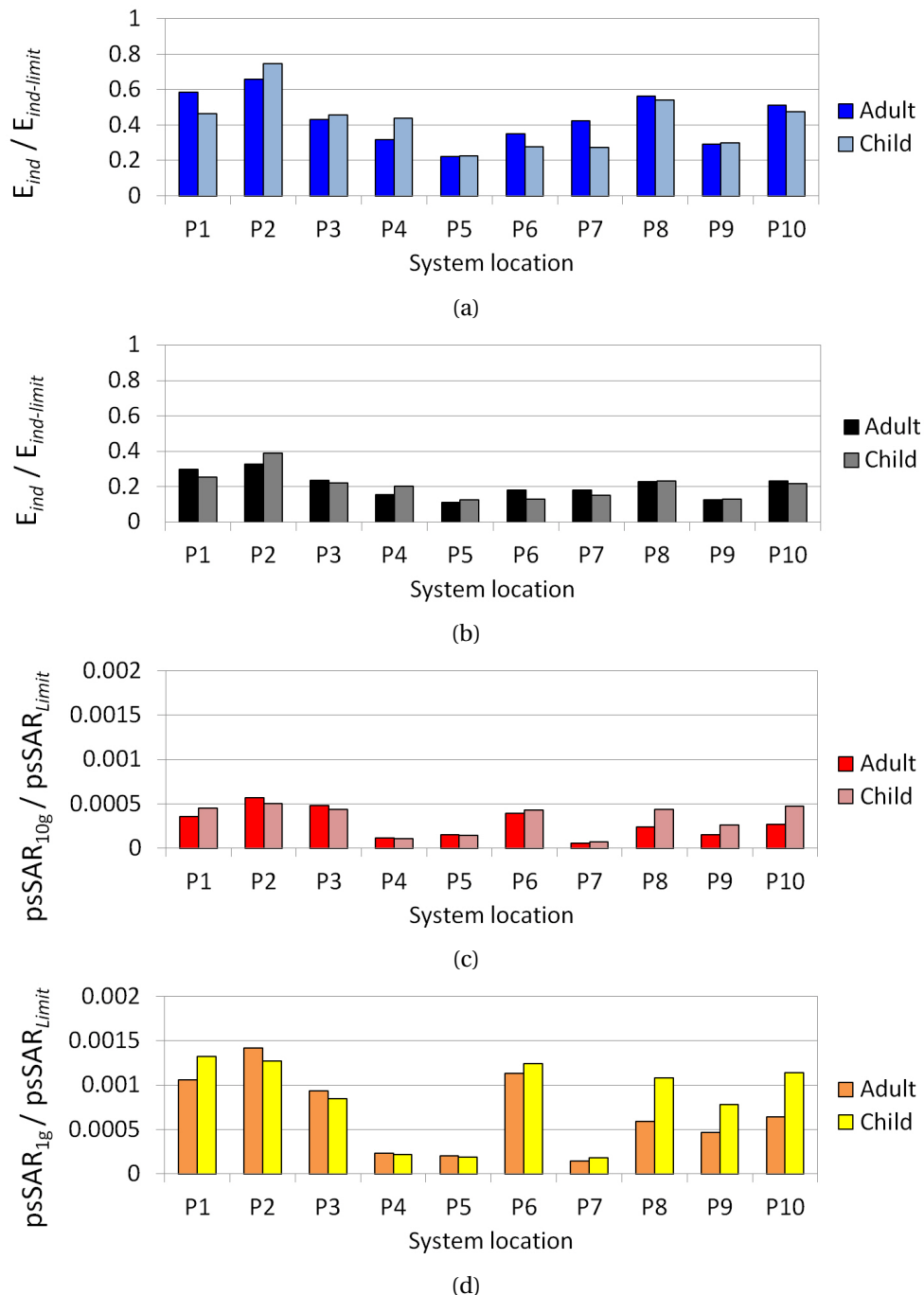


Figure 4.6: The compliance factors for (a) the peak $E_{V,avg}$ (ICNIRP 2010), (b) the peak $E_{L,avg}$ (IEEE C95.1-2005), (c) the peak SAR_{10g} (ICNIRP 1998) and (d) the peak SAR_{1g} (IEEE C95.1-1991).

with the measurement plane on top of the Rx subsystem touching the body and centered on the exposure location. The computed C_E and C_{psSAR} values at 100 kHz are presented in Figure 4.6. It is observed that the two anatomical models lead to higher induced field intensity levels at flat torso regions (e.g., P1 and P2). At P2, the peak $E_{V,avg}$ is 1.4 times lower than the ICNIRP 2010 basic restriction, the peak $E_{L,avg}$ is 2.5 times lower than the IEEE C95.1-2005 basic restriction, the peak SAR_{10g} is 1760 times lower than the ICNIRP 1998 basic restriction and the peak SAR_{1g} is 730 times lower than the IEEE C95.1-1991 basic restriction. Therefore, the induced E-field restriction of ICNIRP 2010 is the most stringent exposure limit for the evaluated WPT system.

To assess the sensitivity of the peak E-field intensity on the system location variation around the location of highest exposure, i.e., front and back of the torso, the induced peak E_{ind} values for the 12 torso positions depicted in Figure 4.1 are computed on the front and back of the four anatomical models. The analysis of the induced E-fields normalised to the limit of ICNIRP 2010 for the 96 exposure scenarios resulted in a mean value of 0.45, a maximum value of 0.85 and a standard deviation value (σ_{sd}) of 0.15, based on a sample size of 96. The mean, maximum and standard deviation values for the IEEE C95.1-2005 E-field compliance factor were 0.27, 0.48 and 0.07, respectively. These values are conservative estimations for any potential location of the WPT system. It should be noted that the ICNIRP 2010 E-field compliance factor will be significantly lower than the presented values if the 99th percentile E-field is to be employed as dosimetric quantity.

In addition, we also have evaluated the most common scenario, namely the exposure of the hand picking up a power receiving device. As shown in Figure 4.7a, a possible anatomical adult hand model is positioned on top of the WPT system with fingers touching the top of the Tx subsystem and palm facing the top of the Rx subsystem. For the 12 investigated system location, the mean, maximum and standard deviation values of the compliance factor are found to be 0.26, 0.33, 0.04 for ICNIRP 2010 and 0.15, 0.19, 0.02 for IEEE C95.1-2005. In conclusion, the investigated WPT system is in compliance with the considered exposure guidelines for all the investigated potential exposure scenarios provided that the assessment uncertainties are not considered in the evaluations.

4.2.3 Characterization of Generic Coils

In this section, the exposure characteristics of a generic circular single-turn coil are analyzed with respect to coil dimension and operating frequency using flat body phantom and anatomical models. The purpose of this investigation is to reveal the impact of WPT system design parameters on the induced peak field intensity. Coils with diameter ranging from 20 to 150 mm are considered. This dimensional range is selected as it encompasses the typical coil sizes for low and medium power devices such as mobile phones and tablet computers. By considering housing thickness and Tx-to-Rx subsystem distance, the coil is assumed to be located at either 5 mm or 10 mm away from the exposed body, with the coil surface oriented

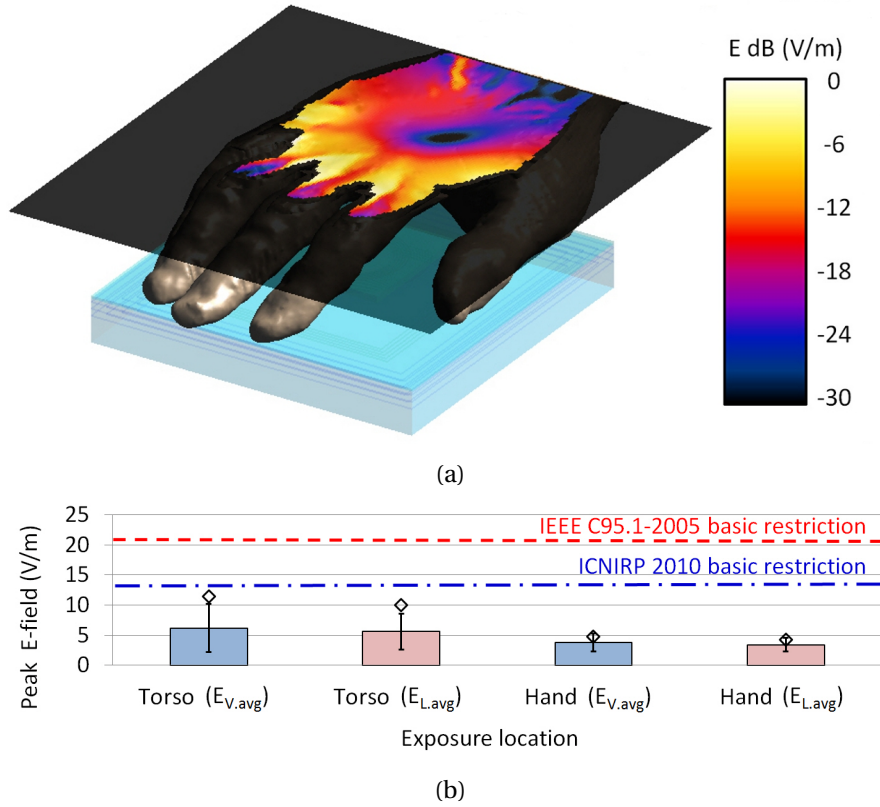


Figure 4.7: (a) The E-field distribution in an adult hand due to the exposure to the WPT system operating at 100 kHz with 5 W received power, and (b) the peak E-field values (maximum and mean $\pm 2\sigma_{sd}$) in the torso and hand with respect to the relevant basic restrictions.

tangential to the surface of the body.

Approximation

The $1.54 \times 0.34 \times 0.09 \text{ m}^3$ homogeneous flat body phantom shown in Figure 4.1 is employed to represent the human body. A uniform 1 mm grid resolution is employed to discretize the phantom. In addition to the numerical simulation results, an analytical approach is employed to calculate the induced peak E-field in the phantom. The coupling between two coils can be estimated from the mutual inductance between them using Neumann's formula:

$$M_{ij} = \frac{\mu}{4\pi} \oint_{C_i} \oint_{C_j} \frac{d\vec{l}_i \cdot d\vec{l}_j}{|\vec{D}_{ij}|} \quad (4.3)$$

where M_{ij} is the mutual inductance between coils C_i and C_j , $d\vec{l}_i$ and $d\vec{l}_j$ are the differential elements of the coils in the direction of the current, and D_{ij} is the distance between these differential elements. In this case, one of the coils represents the currents induced in the body.

Chapter 4. LF Magnetic Field Exposure Analysis - Practical Investigations

For two co-axial parallel circular single-turn coils, the mutual inductance M can be simplified to [110]:

$$M = \mu\sqrt{Rr} \left[\left(\frac{2}{k} - k \right) F - \frac{2}{k} E \right] \quad (4.4)$$

where R is the radius of the induced currents in the body which leads to the peak E-field, r is the excitation coil radius, and k is given by:

$$k = \frac{2\sqrt{Rr}}{\sqrt{(R+r)^2 + D^2}} \quad (4.5)$$

with F and E being the complete elliptical integrals of the first and second kind to the modulus k , and D as the distance between the two coils. The peak induced rms E-field can then be expressed as:

$$E_{ind} = \frac{NM\omega I}{2\pi R} \quad (4.6)$$

where N is the number of turns of the coil and I is the rms current in the coil. Subsequently, the SAR can be computed by:

$$SAR = \frac{\sigma E_{ind}^2}{\rho} \quad (4.7)$$

where σ and ρ are the conductivity and density of the medium, respectively. The numerically and analytically calculated peak rms E-field values are normalized to 1 A peak current values and presented in Figure 4.8. The maximum deviation of the numerical results from the analytical results is found to be within 5%, indicating good agreement between the numerical and analytical solutions. The discrepancy is the result of discretization uncertainty and spatial averaging. As shown in Figure 4.8, the peak E-field value increases logarithmically with ascending coil dimension.

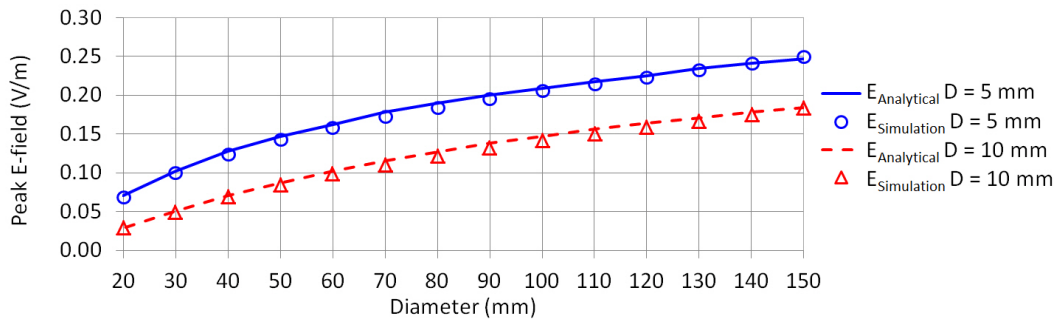


Figure 4.8: The peak rms E-field values normalized to 1 A peak current for the homogeneous phantom at 100 kHz as a function of coil dimension and coil-to-body distance (D), $E_{Analytical}$ is the analytically calculated E-field and $E_{Simulation}$ is the result of the SPFE solver.

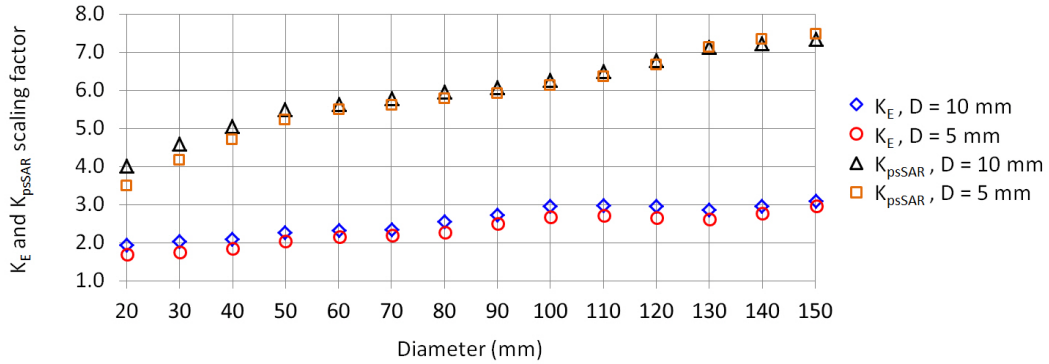


Figure 4.9: The K_E and K_{psSAR} factors at 100 kHz to convert the peak field values in a homogeneous Duke model to values of a heterogeneous Duke model as a function of coil diameter (d) for two coil-to-body distances ($D = 5$ and 10 mm) at P2.

Scaling Factors Based on Anatomical Models

Since a homogeneous phantom does not account for field enhancements due to tissue contrasts, a scaling factor which is determined statistically is introduced. An E-field scaling factor is defined in this study as $K_E = E_{hetero}/E_{homo}$ where E_{hetero} and E_{homo} are the peak E-field in a heterogeneous anatomical model and a homogeneous anatomical model, respectively. The homogeneous flat phantom is found to produce higher induced peak E-field compared to a homogeneous anatomical model at the same coil-to-body distance (i.e., the minimum coil-to-body distance in the case of an anatomical model). Hence, the scaling factor in this study is computed conservatively by applying the peak E-field of a homogeneous anatomical model as E_{homo} . A similar SAR scaling factor is defined as $K_{psSAR} = SAR_{hetero} / SAR_{homo}$. Subsequently, an approximated E-field compliance factor of a WPT system can be formulated as:

$$C_{E,approx.} = \frac{K_E N M}{e_{limit} R} I \quad (4.8)$$

where N , M , I and R are the number of coil turns, mutual inductance, coil current and coil radius defined by a WPT system and e_{limit} is a constant value defined by the basic restrictions (see Table 4.1). In a similar manner, the SAR compliance factor can be approximated by using a low σ value of 0.05 S/m and a ρ value of 1000 kg/m³:

$$C_{psSAR,approx.} = \frac{\sigma K_{psSAR} (NM)^2}{\rho psSAR_{limit} R^2} f^2 I^2 \quad (4.9)$$

The scaling factors were determined for the anatomical versus the homogeneous Duke model composed of low conductivity medium ($\sigma = 0.05$ S/m). In the first approximation, the scaling factor is assumed to be frequency independent as the contrast between the different tissues in the frequency range hardly changes, e.g., for muscle versus bone from 17 at 100 kHz to 15 at 10 MHz and for muscle versus fat from 10 to 12, respectively. The scaling factors due to coil

Chapter 4. LF Magnetic Field Exposure Analysis - Practical Investigations

with variable diameter at the P2 location are presented in Figure 4.9. Based on these results, the scaling factor of a $d = 150$ mm coil serves as a conservative value for the investigated coil dimensions. To analyze the sensitivity of the scaling factor with respect to body model and coil position, the scaling factors of a 150 mm coil at 5 mm and 10 mm coil-to-body distances are computed for the front and back of the four anatomical models. The mean, maximum and standard deviation values for the E-field and SAR scaling factors are presented in Table 4.2 based on a sample size of 192. The validity of the compliance approximation is checked against the system investigated in this study as well as the system analysed in [108]. For the system in [108], the coil dimensions of 170×280 mm³ is approximated by a $d = 123$ mm coil. The compliance factors are compared in Table 4.3, demonstrating the validity and conservativeness of the approximation when applying the mean $+ 2\sigma_{sd}$ K_E and K_{psSAR} scaling factors.

Frequency Dependence of the Peak E-field and SAR

An examination of 4.8 and 4.9 suggests that the E-field compliance factor is independent of frequency while the SAR compliance factor varies with the square of frequency. This is due to the fact that the E-field basic restriction level increases linearly with frequency as the stimulation threshold of nerve fibres rises with frequency; while the SAR basic restriction is a constant value to prevent harmful thermal effects at any frequency. As the reactive power stored in a WPT system can be approximated by $P = \frac{1}{2}\omega LI^2$ where L is the coil inductance and

Table 4.2: The mean, maximum and standard deviation values of the K_E and K_{psSAR} scaling factors based on the sensitivity analysis of a 150 mm coil placed at 24 locations on the body with 5 and 10 mm coil-to-body distances at 100 kHz.

Scaling Factor	Mean	Maximum	StdDev
K_E (ICNIRP 2012)	2.9	4.8	0.73
K_E (IEEE C95.1-2005)	2.6	4.4	0.65
K_{psSAR} (IEEE C95.1-1992)	7.2	15.7	2.8
K_{psSAR} (ICNIRP 1998)	5.4	8.9	1.3

Table 4.3: Compliance factors versus approximations, d is coil diameter and D is coil-to-body distance.

$C_{E(ICNIRP)}$		$C_{E(IEEE)}$		$C_{psSAR_{10g}}$		$C_{psSAR_{1g}}$	
test	4.8	test	4.8	test	4.9	test	4.9
System I, $f = 100$ kHz, $D = 20$ mm, $d = 125$ mm, $NI = 17.5 A_{rms}$							
0.85	1.28	0.48	0.74	8.7×10^{-4}	1.6×10^{-3}	1.8×10^{-3}	3.2×10^{-3}
System II [108], $f = 6.78$ MHz, $D = 50$ mm, $d \approx 123$ mm, $NI = 5.36 A_{rms}$							
0.14	0.24	N.A.	N.A.	0.15	0.48	0.42	0.86

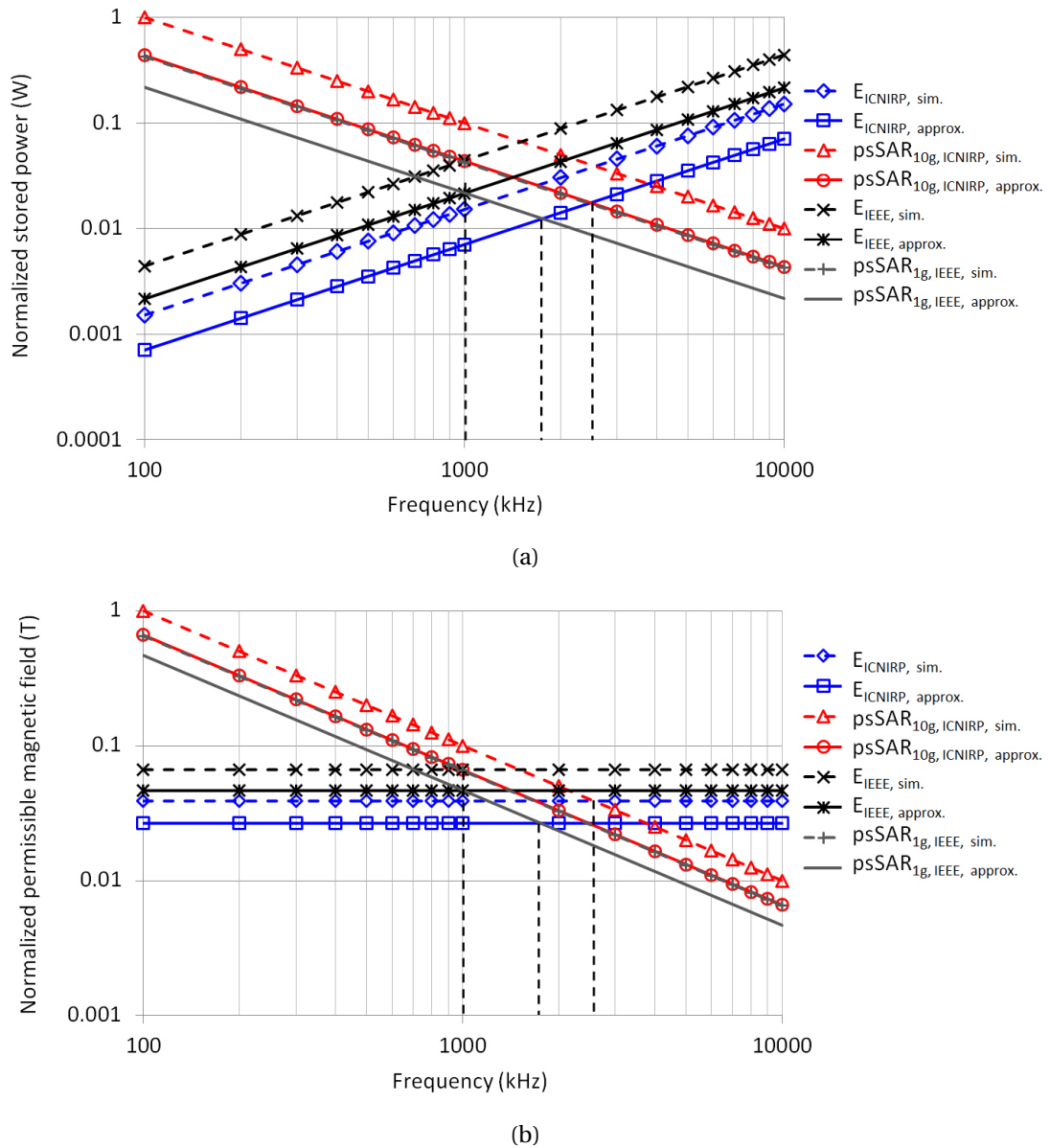


Figure 4.10: (a) The normalized source power (W) and (b) the normalized permissible B-field (T) with respect to the basic restrictions ($E_{ind-limit}$, $psSAR_{limit}$) based on the simulation results ($E_{sim.}$ and $psSAR_{sim.}$) and approximation results ($E_{approx.}$ and $psSAR_{approx.}$) of a 150 mm coil at 5 mm coil-to-body distance for the Duke model at P2, the vertical dashed lines indicate the frequencies to achieve the maximum WPT source power and permissible B-field.

I is the coil current, this implies that there exists an optimal frequency at which a WPT system could operate with a maximum source power without exceeding both the E-field and SAR basic restrictions.

Chapter 4. LF Magnetic Field Exposure Analysis - Practical Investigations

To determine the frequency point, above which the SAR becomes dominant over the E-field for exposure compliance, the WPT source powers and permissible B-field intensity subjected to the ICNIRP and IEEE exposure limits are computed for the Duke model with a 150 mm coil positioned 5 mm away from the body at P2 exposure location in the frequency range from 100 kHz to 10 MHz. In addition to the anatomical model results, the approximation results based on 4.8 and 4.9 are also calculated by applying the mean + 2StdDev of K_E and K_{psSAR} values. The computed power and B-field results are normalized to the maximum value and presented in Figure 4.10. As shown, both the simulation and approximation results, for stored power and permissible B-field, lead to the same optimal frequency (i.e., where the SAR-related power curve intersects the E-related power curve). Based on the approximation results, the WPT operating frequency to achieve the maximum permissible source power is 2.5 MHz for the ICNIRP exposure guidelines, 1 MHz for the IEEE exposure standards and 1.8 MHz for the both of them. As the system stored power and incident B-field can deviate from the simple $P \propto B^2$ relationship based on the applied WPT technologies (e.g., link range, shielding), the optimal frequency for a specific design should fall within the derived range, i.e., 1 MHz to 2.5 MHz.

4.2.4 Summary of the Short-range Wireless Power Transfer System Analysis

In this section, the exposure assessment of a practical 100 kHz close-range low-power wireless power transfer (WPT) unit is conducted with a novel and simple comparison metric based on practical system measurements and numerical dosimetry. A generic coil study estimates that the optimum WPT operating frequency range to achieve exposure compliance is at 2.5 MHz for the ICNIRP guidelines and at 1 MHz for the IEEE standards. Furthermore, the generic coil study establishes a convenient method for the exposure estimation of a practical WPT system with known B-field intensity and distribution. The investigated WPT system is employed to validate the accuracy and viability of this formula. The proposed approach provides an easy-to-adapt assessment routine in achieving an initial exposure estimation, in the low and medium power regime, for close-range magnetic resonant WPT systems.

4.3 Theoretical Assessment of the Maximum Obtainable Power for Mid-range Wireless Power Transfer Based on Exposure Limits

4.3.1 Background

As discussed in the Section 4.2, besides achieving adequate power transfer efficiency and link range, a critical requirement for a practical WPT system is the electromagnetic exposure safety compliance for a human body exposed to the low frequency magnetic field (B-field) generated by such a system. The transmit (Tx) and receive (Rx) coil diameters in previous reported studies ([106], [107], [108] and Section 4.2) are in the range of 0.2 to 0.6 m, which lead to more localized exposure for a close-by human body. In this section, the whole-body exposure scenario in a room-size WPT environment (i.e., Tx coil diameter of 2.5 m) is numerically examined with respect to the peak induced electric field (E-field) and specific absorption rate (SAR) induced in a human body.

The same exposure limits mentioned in Section 4.2 are employed as the basis of compliance assessment. Once again, the exposure limits for the external E-field and B-field, known as the reference level (ICNIRP) or maximum permissible exposure (IEEE), are not representative for a room-size WPT environment since they were established conservatively based on the scenario of whole-body exposure to uniform field. To determine the exposure characteristics of a human body in a non-uniform exposure scenario, the source field and the potential exposure conditions (e.g., body orientation and location with respect to the source) should be considered. In this section, the exposure of a human body in the B-fields generated by the Tx coil of a room-size WPT system is investigated. The research objective is to determine the maximum power that can be obtained by a Rx coil (i.e., embedded in a wireless device which is much smaller than the Tx coil) in the presence of a human body without exceeding the exposure limits. To this aim, numerical dosimetry techniques and high-resolution anatomically realistic models are employed to derive the exposure characteristics of a human body in a full-room WPT scenario with respect to the body orientation/position in the room, Tx coil shape/location, WPT operating frequency and room size variation. This section is structured as follows: first, the incident B-fields generated by a Tx coil is analyzed. Next, the exposure assessment in a room-size environment is conducted to determine the maximum permissible B-field intensity at the threshold of exposure limit and validate the optimum operating frequencies derived in Section 4.2. Lastly, based on the computed dosimetry data and B-field distribution, the maximum power obtainable by a Rx coil with pre-defined parameters is estimated to assess the feasibility of a room-size WPT system with respect to the human body exposure limits.

4.3.2 Methods and Materials

Anatomical Models

The same high-resolution anatomically realistic human models (Duke, Ella, Fats, Dizzie as shown in Figure 2.8) in Section 4.2 were employed for the numerical simulations in this section. Only general standing and lying-down body postures (with arms on the side of the body and legs slightly apart) are investigated in this work. The skin layer of an anatomical model is considered as a single-layer tissue which represents the composition of cellular epidermis and dermis instead of the stratum corneum (i.e., the low conductive outermost skin layer) which contains no excitable nerve endings.

Investigated Basic Restriction Quantities

In addition to the basic restriction quantities described in Table 4.1. The 99th percentile volume averaged E-field taken over the whole body, which is expected to be the lower bound of a 99th percentile peak estimation, is also reported in this section. Alternative 99th percentile filtering (e.g, tissue-by-tissue) is expected to produce peak estimation in between this value and the non-filtered volume averaged value. For a whole-body exposure scenario above 100 kHz, in addition to the 10 gram tissue mass averaged peak spatial SAR which is established mainly for localized exposure, the whole-body average SAR is also specified as the relevant dosimetric quantity by ICNIRP and IEEE with a limit of 0.08 W/kg at any frequency. In this section, wbSAR refers to the whole-body averaged SAR, psSAR_{1g} and psSAR_{10g} refer to the 1 gram and 10 gram averaged peak spatial SAR, $E_{V,avg}$ refers to the peak $2 \times 2 \times 2$ mm³ volume-averaged root-mean-square (rms) E-field, $E_{L,avg}$ refers to the peak 5 mm line-averaged rms E-field and E_{99} refers to the 99th percentile of the $2 \times 2 \times 2$ mm³ volume-averaged E-field taken over the entire body.

Computational Techniques

According to Figure 2.15, the left-hand-sides of 2.31, 2.32 and 2.33 indicate that the quasi-static approximation is valid up to 100 kHz for a whole body exposure scenario. For frequencies above 100 kHz, a full-wave finite-difference time-domain (FDTD) solver with Huygens box approach [106], is employed to assess the deviation between a full-wave method and the quasi-static method. The whole-body exposure of the Duke and Dizzie model in a uniform front-to-back B-field are computed at 1 MHz, 5 MHz and 10 MHz, respectively, with the SPFE and FDTD solvers. The maximum deviation is found to be 8.2% for $E_{V,avg}$, 10% for psSAR_{1g} and 18% for wbSAR, respectively. The findings in this study are consistent with the results reported in [107] which suggest that a quasi-static approach can be applied for a whole-body dosimetry computation up to 10 MHz with acceptable tolerance. Hence, all the simulations in this study (from 100 kHz to 10 MHz) are computed using the SPFE solver [48] with a 1 mm uniform grid resolution for the discretization of the anatomical models.

4.3.3 Incident B-field based on Tx Coil Size

To cover a room space with wireless power, two types of Tx coil set-ups can be considered: 1) a single Tx coil and 2) a Tx coil array. To decide an initial approximation of suitable Tx coil dimensions, a room size dimension of $5 \times 5 \times 2.6 \text{ m}^3$ is considered. The incident B-fields generated by a Tx coil is calculated by the Biot-Savart equation.

A Tx coil with radius R varying from 0.5 m to 2.5 m is considered. The incident B-fields at 0.1 and 1 m away from the coil with various dimensions are normalized to the same stored power at 200 kHz and presented in Figure 4.11. As shown, for the same broadcast power, a smaller coil leads to higher incident B-field at close range (e.g., 0.1 m) but lower power coverage at a further distance (e.g., 1 m). At higher frequency, the rate of decay for B-field further away from the coil decreases due to the transition from near field to far field regime. Hence, from an exposure and power coverage point of view, a larger coil is a suitable choice. As the practical issues with regard to the choice of Tx coil dimension (e.g., cost, windings, power handling capacity) is not considered in this study, a large Tx coil is selected for investigation. The actual size of the considered Tx coil is $5.2 \times 5.2 \text{ m}^2$, a 0.1 m isolation distance is assumed to account for wall embedment and coil housing.

Investigated Exposure Scenarios

The B-fields generated by a single-turn coil are employed to approximate the B-fields produced by a multi-turn Tx coil which encircles an entire room. When the turns of the Tx coil are concentrated at the outer diameter with close spacing, the approximation is valid when the currents in a multi-turn coil can be considered to be in-phase (i.e., one tenth of the free-space wavelength $0.1\lambda_{fs} \gg \text{room size}$). At higher frequency (e.g., 10 MHz), series capacitive compensation can be introduced along the coil to balance the current phase shifts. Hence, by multiplying the peak B-field intensity of a single-turn coil with N^2 , the peak B-field of a N -turn coil can be calculated with the assumptions of negligible ohmic and magnetic losses. In this study, the B-field perturbation due to any electric and magnetic objects in the room or in the human body (e.g., medical implants) are not considered. In addition, only the exposure due to the Tx coil is analyzed in this study, i.e., the simultaneous localized exposure from a Rx coil is considered as a separate topic for future investigation.

Two Tx coil shapes: square and circular; and three Tx coil positions: ceiling level, quarter level (i.e., 0.65 m above the floor to represent table level) and floor level, are considered as shown in Figure 4.12. In a full-room exposure environment, the freedom of body location and orientation in the room should be taken into consideration. To this aim, 9 body locations (P1 to P9, P* for a circular Tx coil) which represent the potential worst-case exposure locations are investigated. Two body orientations: standing straight and face-up lying down, are considered. The body locations are selected based on the typical scenarios which lead to the smallest spatial distance between a Tx coil and a human body.

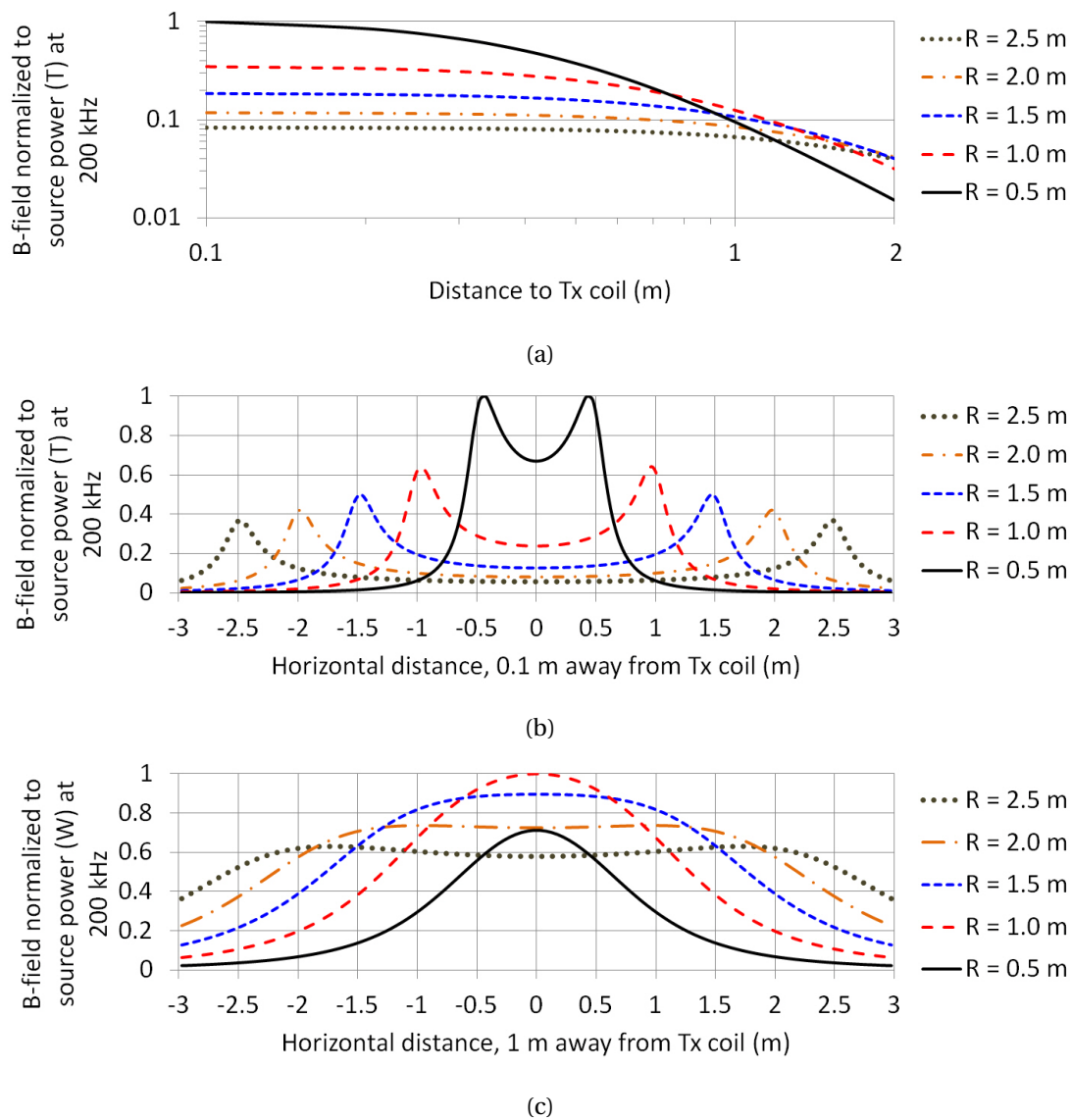


Figure 4.11: The analytically calculated normalized B-field at 200 kHz along: (a) the central vertical axis, (b) the central horizontal axis 0.1 m away from a Tx coil and (c) the central horizontal axis 1 m away from a Tx coil, for Tx coils with radius in the range of 0.5 to 2.5 m.

As shown in Figure 4.12, the child (Dizzie) model is employed to illustrate some of the investigated body locations with respect to the Tx coil positions. With reference to a plane tangential to the floor surface, the center or corner of a rectangular bounding box which encloses the entire body model is aligned with the predefined locations (P1 to P9). The following body-coil configurations are investigated: (1) ceiling-level Tx coil with (i) elevated standing body (e.g., stands on a bookshelf) and (ii) face-up lying-down body at quarter level (represents bed level), (2) quarter-level Tx coil with (i) floor-bound standing body and (ii) face-up lying-down body at quarter level, and (3) floor-level Tx coil with (i) floor-bound standing body and (ii)

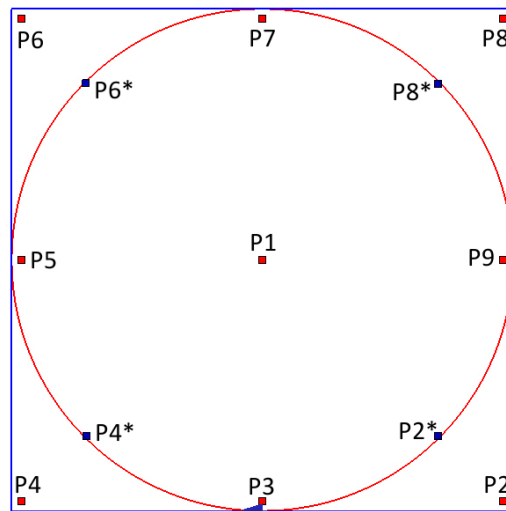
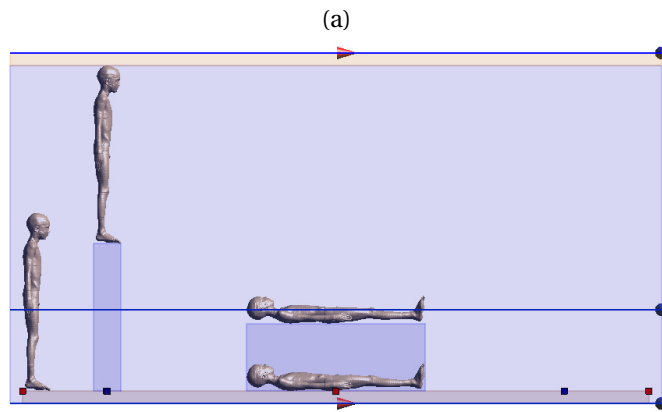
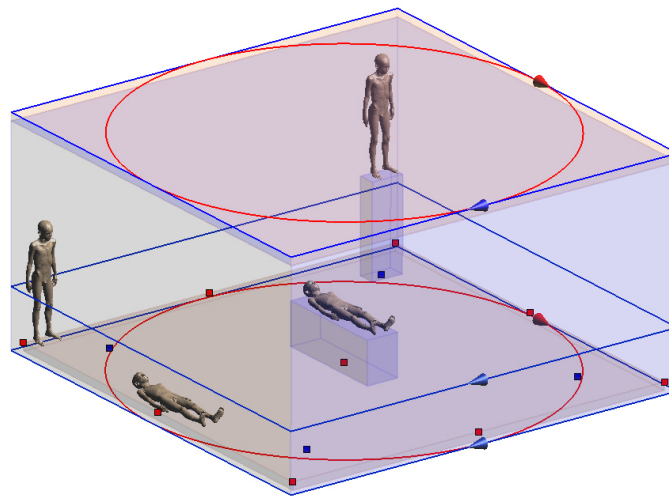


Figure 4.12: The Tx coil locations with body positions and orientations: (a) 3D-view, (b) side-view and (c) top-view with labelled body positions (P1 to P9).

face-up lying-down body on the floor. The included Tx coil placements, body locations and orientations provide a thorough coverage of the potential worst-case exposure scenarios in a full-room WPT exposure environment.

Investigated Operating Frequency Range

To decide the frequency points which should be considered in this study, the preferences of practical WPT implementations are taken into account. The frequencies in the lower kHz range, e.g., 200 to 500 kHz, are the frequencies of choice for most of the wireless-charging products in the market today. The Consumer Electronics Association (CEA) [111] and Wireless Power Consortium (WPC) [109] standards fall in this frequency range. The frequency 6.78 MHz is an alternate choice which has been considered by the wireless power community with the advantage that it is in the Industrial, Scientific and Medical (ISM) band, and hence leads to less restriction on the electromagnetic compatibility (EMC) issue than the other competing standards in the frequency spectrum. Based on the aforementioned rationales, two frequency points: 200 kHz and 6.78 MHz, are selected as the primary frequencies of investigation in this study. The frequency range from 100 kHz to 10 MHz is also considered for the worst-case exposure scenarios to analyze the frequency-dependent characteristics of the induced field intensity with respect to the research findings in Section 4.2.

4.3.4 Maximum Permissible B-field Intensity

B-field Intensity based on Exposure Limits

The induced peak E-field (i.e., $E_{V,avg}$, E_{99V} , and $E_{L,avg}$) and SAR (wbSAR, psSAR_{1g} and psSAR_{10g}) are computed with the four anatomical models positioned at the predefined locations (P1 to P9) for the investigated coil-body orientations at 200 kHz and 6.78 MHz, respectively. According to the B-field intensity at which the induced field value exceeds the relevant exposure limit, the peak induced E-field leads to lower source B-field than the wbSAR at 200 kHz, i.e., the peak E-field is the determinant factor for the compliance of exposure limit at 200 kHz. This agrees well with the findings in Section 4.2. Based on the computational results, a square Tx coil results in lower induced peak E-field and SAR than a circular coil due to the avoidance of small coil-to-body proximity scenarios such as P2* to P8*, especially for the lying-down body position. This suggests that a larger keep-out distance should be considered for practical implementation of the Tx coil. The Duke model and the Fats model are responsible for the majority of low B_z values among the investigated anatomical models. This is likely due to the larger body cross-sectional areas exhibited by these two models. A quarter-level Tx coil is found to produce the lowest maximum permissible B_z in the center of the room among the three investigated Tx coil locations. This indicates that the increase in the peak induced field intensity outweighs the gain in the B_z intensity for a quarter-level Tx coil. Hence, only the results of a square Tx coil at the ceiling and floor levels are presented. The mean, maximum and standard deviation of the maximum permissible B_z in the center of the room by a square Tx

Chapter 4. LF Magnetic Field Exposure Analysis - Practical Investigations

Table 4.4: The mean (μ), maximum (max) and standard deviation (σ_{sd}) of the B-field intensity in the center of the room at the middle and quarter levels before the induced E-field exceeds the ICNIRP 2010 and IEEE C95.1-2005 basic restrictions at 200 kHz.

B-field (μ T) at the middle vertical room level			
BR	ICNIRP (E_{99})	ICNIRP ($E_{V,avg}$)	IEEE ($E_{L,avg}$)
	μ , max, σ_{sd}	μ , max, σ_{sd}	μ , max, σ_{sd}
Ceiling ^a	22, 54, 13	4.5, 11, 2.7	11, 24, 6.2
Ceiling ^b	75, 122, 27	15, 27, 5.4	24, 46, 9.3
Floor ^c	8.7, 25, 4.8	1.8, 5.6, 1.2	2.7, 7.7, 1.7
B-field (μ T) at the quarter vertical room level			
BR	ICNIRP (E_{99})	ICNIRP ($E_{V,avg}$)	IEEE ($E_{L,avg}$)
	μ , max, σ_{sd}	μ , max, σ_{sd}	μ , max, σ_{sd}
Ceiling ^a	16, 40, 9.3	3.2, 7.8, 1.9	8.2, 18, 4.6
Ceiling ^b	55, 90, 20	11, 20, 4.2	18, 34, 6.8
Floor ^c	11, 31, 5.9	2.3, 7.0, 1.2	3.5, 10, 1.7

^a Ceiling-level square Tx coil with elevated body

^b Ceiling-level square Tx coil with floor-bound body

^c Floor-level square Tx coil

coil are presented in Tables 4.4 and 4.5, for 200 kHz and 6.78 MHz, respectively. It is observed that a ceiling Tx coil, when excluding the elevated body scenario (i.e., assuming that the power of a Tx coil can be deactivated upon the detection of a human body by a proximity sensor), leads to the highest B_z among the investigated coil-body configurations.

Optimum Operating Frequency based on Exposure Limits

To investigate the frequency-dependent characteristics of the maximum permissible B-field for whole body exposure, two exposure scenarios are considered: (1) the worst-case scenario of a standing model; and (2) the worst-case scenario of a lying-down model. The maximum permissible B_z in the center of the room at the middle vertical level, with respect to the peak E-field and SAR, are converted to the normalized source power and presented in Figure 4.13 as functions of frequency. The intersection points between the E-field related curves and the SAR related curve are marked by the vertical dotted lines in Figure 4.13. According to Figure 4.13(a) the optimum operating frequencies, i.e., 1 and 2.5 MHz, agree well with the results in Section 4.2 for a standing model. The E_{99} value leads to lower optimal frequency as it allows higher incident B-field. As shown in Figure 4.13(b), the optimal frequencies are shifted when the lying down body is considered. This is due to the change of exposure quantity from psSAR to wbSAR (i.e., the worst-case quantity for a lying-down model). It can therefore be concluded that the optimal WPT frequency for both close-range and mid-range operation lies in the range from 500 kHz to 2.5 MHz, depending on the investigated exposure quantities.

Chapter 4. LF Magnetic Field Exposure Analysis - Practical Investigations

Table 4.5: The mean (μ), maximum (max) and standard deviation (σ_{sd}) of the B-field intensity in the center of the room at the middle and quarter levels before the induced SAR exceeds the ICNIRP 1998, IEEE C95.1-1991 and IEEE C95.1-2005 basic restrictions at 6.78 MHz.

B-field (μ T) at the middle vertical room level			
BR	ICNIRP (wbSAR)	IEEE (psSAR _{10g})	IEEE (psSAR _{1g})
	μ , max, σ_{sd}	μ , max, σ_{sd}	μ , max, σ_{sd}
Ceiling ^a	1.5, 3.3, 0.8	1.3, 2.9, 0.5	0.7, 1.5*, 0.3
Ceiling ^b	5.3, 7.9, 1.6	4.5, 6.0, 1.1	2.3, 3.3*, 0.6
Floor ^c	0.6, 1.6*, 0.4	1.3, 4.5, 1.2	0.7, 2.6, 0.6
B-field (μ T) at the quarter vertical room level			
BR	ICNIRP (wbSAR)	IEEE (psSAR _{10g})	IEEE (psSAR _{1g})
	μ , max, σ_{sd}	μ , max, σ_{sd}	μ , max, σ_{sd}
Ceiling ^a	1.1, 2.5, 0.6	0.9, 2.1, 0.4	0.5, 1.1*, 0.2
Ceiling ^b	3.9, 5.8, 1.2	3.7, 5.0, 0.9	1.8, 2.6*, 0.5
Floor ^c	0.7, 2.0*, 0.4	1.4, 4.7, 1.2	0.7, 2.4, 0.6

^a Ceiling-level square Tx coil with elevated body

^b Ceiling-level square Tx coil with floor-bound body

^c Floor-level square Tx coil

* The lowest maximum B_z value among wbSAR, psSAR_{1g} and psSAR_{10g}

4.3.5 Estimation of the Maximum Obtainable Power

When a Rx coil is immersed in the B-fields generated by a Tx coil (B_{Tx}), assuming that the Rx coil turns are concentrated at its outer diameter and B_{Tx} is homogeneous over the Rx coil surface area, the output voltage V_{out} of the Rx coil is equivalent to the induced voltage V_{ind} :

$$V_{ind} = N \cdot A \cdot j\omega \cdot B_{Tx} \quad (4.10)$$

where N is the number of coil turns and A is the coil surface area. In the case of series resonance, maximum power (P_{max}) can be achieved when the Rx coil resistance R_S equals the load resistance R_L :

$$P_{max} = Q \cdot \frac{|V_{ind}|^2}{4\omega \cdot L_{Rx}} \quad (4.11)$$

where Q is the quality factor of the Rx coil inductor and L_{Rx} is the Rx coil inductance. Assuming a perfectly lossless capacitor component, Q can be expressed as $Q = \omega L_{Rx} / R_S$. With a known operating frequency, B_{Tx} intensity and Rx coil parameters (e.g., Q factor, inductance and coil size), the maximum obtainable output power can be estimated based on (5). By defining a

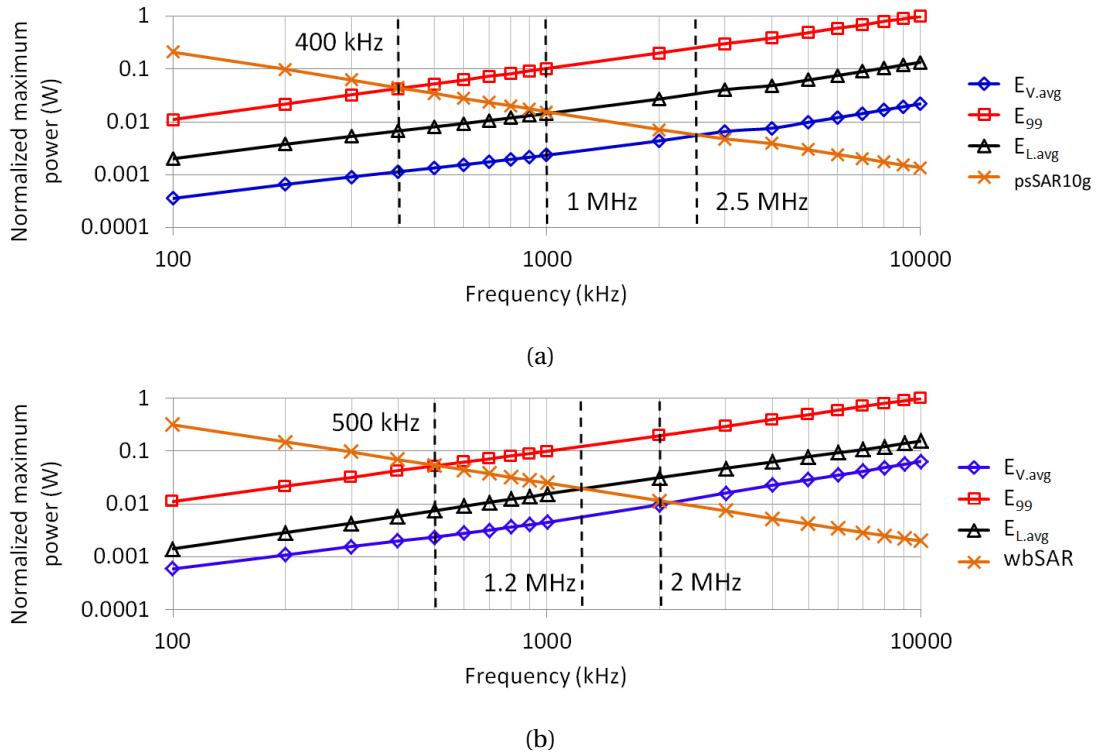


Figure 4.13: The normalized maximum permissible power (W) at the middle vertical level for (a) a ceiling-level Tx coil with a ground-level standing body and (b) a floor-level Tx coil with a lying-down body, as a function of frequency.

term L^* to be the inductance normalized to per coil turn with $L^* = L_{Rx}/N^2$, the maximum output power with normalized inductance can be expressed as [112]:

$$P_{max}^* = Q \cdot \frac{\omega \cdot (A \cdot |B_{Tx}|)^2}{4L^*} \quad (4.12)$$

While the shape and size of a Rx coil vary with respect to a specific electronic device design, Rx coil dimensions of $50 \times 100 \text{ mm}^2$ and $200 \times 300 \text{ mm}^2$ are considered in this work based on the typical dimensions of mobile phone and laptop computer. The inductance of a single-turn rectangular coil with 0.3 mm wire diameter is estimated to be about 0.32 μH and 1.32 μH , for a $50 \times 100 \text{ mm}^2$ coil and a $200 \times 300 \text{ mm}^2$ coil, respectively [110]. Based on the aforementioned parameters, the maximum obtainable power P_{max}^* at 1.3 m above the floor (e.g., center vertical level) in a $5 \times 5 \times 2.6 \text{ m}^3$ room, delivered by a square Tx coil and received by a small ($50 \times 100 \text{ mm}^2$) or large ($200 \times 300 \text{ mm}^2$) Rx coil, is estimated based on the respective mean + $2\sigma_{sd}$ permissible B_z intensity (see Tables 4.4 and 4.5). The P_{max}^* value is presented in Table 4.6 for $Q = 100$, small and large Rx coil sizes, with ceiling-mount and floor-mount Tx coils, at 200 kHz and 6.78 MHz, respectively.

Chapter 4. LF Magnetic Field Exposure Analysis - Practical Investigations

Table 4.6: The maximum power (W) obtainable by a small ($50 \times 100 \text{ mm}^2$) and large ($200 \times 300 \text{ mm}^2$) Rx coil ($Q = 100$) 1.3 m above the floor tangential to a $5.2 \times 5.2 \text{ m}^2$ Tx coil (a) 2.7 m above the floor (assume floor-bound body), (b) 0.1 m below the floor, at 200 kHz and 6.78 MHz, based on the $\mu \pm 2\sigma_{sd}$ of the calculated maximum permissible B_{Tx} , while maintaining compliance with the ICNIRP and IEEE basic restrictions.

(a) Ceiling-mount Tx Coil		
ICNIRP 1998 ($psSAR_{10g}$) and ICNIRP 2010 ($E_{V,avg}$)		
	Small Coil	Large Coil
200 kHz	1.7	56
6.78 MHz	3.7	130
IEEE C95.1-1992 ($psSAR_{1g}$) and IEEE C95.1-2005 ($E_{L,avg}$)		
	Small Coil	Large Coil
200 kHz	4.5	158
6.78 MHz	0.65	22.8

(b) Floor-mount Tx Coil		
ICNIRP 1998 ($wbSAR$) and ICNIRP 2010 ($E_{V,avg}$)		
	Small Coil	Large Coil
200 kHz	0.04	1.5
6.78 MHz	0.16	5.7
IEEE C95.1-1992 ($wbSAR$) and IEEE C95.1-2005 ($E_{L,avg}$)		
	Small Coil	Large Coil
200 kHz	0.09	3.2
6.78 MHz	0.16	5.7

As shown, the maximum obtainable power varies according to Tx coil location and investigated exposure guidelines. In this section, the achievable power ranges from 0.04 to 158 W, depending on the considered parameters. These estimated value serves as the theoretical upper and lower bounds of the received power limit, the practically achievable power is determined by system parameters such as component loss, link range, power transfer efficiency and actual operating frequency.

4.3.6 Summary of the Mid-range Wireless Power Transfer Analysis

This study provides a systematic analysis of the maximum obtainable power by a mobile phone or laptop-size electronic device in a wireless-powered room-size environment with respect to the ICNIRP and IEEE exposure limits. Based on the computational results of the peak spatially averaged E-field, 1 gram, 10 gram averaged peak spatial SAR and whole-body SAR in high-resolution anatomical models, the maximum permissible B-field intensities, at 200 kHz and 6.78 MHz, with respect to various wireless power transmit configurations are derived.

In addition, the optimum WPT operating frequency, i.e., the highest frequency to achieve maximum permissible B-field intensity in the investigated frequency range (100 kHz to 10 MHz), is determined by examining the frequency-dependent characteristics of the induced field quantities. With known maximum permissible B-field intensity and predefined Tx/Rx coil parameters, the estimation of the maximum power obtainable by a small receiver is presented. The assessment results suggest that in theory, low to medium received power (e.g., 0.04 to 158 W) can be achieved in a room-size wireless power transfer environment while maintaining compliance to the ICNIRP and IEEE human body exposure limits.

4.4 Conclusion

The investigation of both close-range and mid-range wireless power transfer leads to several important design guidelines for exposure-compliant WPT system designs. Most importantly, the optimal frequency range, i.e., 1 – 2.5 MHz, to achieve maximum stored power and exposure compliance is determined by both numerical and analytical methods. In addition, the effect of Tx coil dimensions is analyzed to provide system designers with guidelines to estimate the maximum obtainable power in a mid-range WPT set up.

5 LF Electric Field Exposure Analysis

5.1 Introduction

In this chapter, the electric (E) field and contact current (I) induced in a human body due to the exposure to low frequency (LF) external E-field and the contact with a conductive object are numerically investigated with a high-resolution anatomically realistic model (Duke) and the SPFE solver described in Chapter 2. In general, there are less man-made and natural high-intensity E-field environments than high-intensity magnetic (B) field environments. Highly intensive LF E-fields are commonly encountered near high-voltage facilities (e.g., a pylon carrying power lines). As the human body exhibits high relative permittivity and conductivity values at low frequency, the induced E-fields are significantly lower than the external E-fields (e.g., 5 to 6 orders of magnitude reduction at 50–60 Hz). Furthermore, protective measures (e.g., the *Faraday* suit) against LF E-field exposure has been well established for professional workers operating near high-voltage facilities. As a result, the human body exposure to LF E-field has received less research attention than the exposure to LF B-field. Nevertheless, the availability of state-of-art anatomical model and numerical techniques allows a research update to the existing knowledge of the peak induced E-field in the human body due to the exposure to a LF E-field.

5.2 Analysis of the Exposure to Uniform E-field

5.2.1 Background

The computational results of the induced E-field and current density (J) in the human body due to the exposure to a LF uniform E-field have been reported in [11–13]. In a LF E-field induction case, two scenarios are considered: the *direct* induction of E-fields in the human body due to the oscillating surface charges introduced by an external E-field and the *indirect* induction due to the contact currents induced in the body when it is in contact with a conductive object which is at a different electric potential than the body. Some of the characteristics of E-field

induction are summarized here based on published literatures [11–13]: (1) the maximum induced E-field occurs when the human body is aligned with the external E-field lines (i.e., due to the greater potential difference induced between the head and the feet), (2) higher induced E-field occurs when the feet are grounded instead of floating, and (3) the induced E-fields due to the direct induction are in general weaker than the indirect induction due to the high permittivity and conductivity nature of the human body tissues at low frequency. In this section, an up-to-date database of the computational peak induced E-field and short-circuit current (i.e., current which flows through the body to the ground) is provided to assess the safety margins provided by the ICNIRP-2010 [2] and IEEE Std. C95.6-2002 [3] reference levels.

5.2.2 Computational Results of an Anatomical Model

In this section, the Duke model in its general standing posture as shown in Figure 2.9 is numerically investigated for the exposure to a uniform vertically polarized E-field. The model is grounded on both feet at zero potential for all the simulations. The skin layer is treated as the *stratum corneum* (i.e., poorly conductive). To ensure a proper ground-to-sole contact, two 5-mm-thick slabs (with the same dielectric properties as the skin layer) are inserted between the sole and the ground as shown in Figure 5.1(e). A uniform grid size of 1.5 mm is applied for the discretization of the body and a grid size of 1 cm with a grading ratio of 1.2 is applied for the space around the body. The exposure scenario is computed at nine frequency points from 10 Hz to 100 kHz. Residual tolerance (i.e., the stopping criterion for the SPFE solver) in the range of 10^{-16} to 10^{-10} are applied with respect to the frequency-dependent tissue relative permittivity values. The peak induced E-field values ($E_{V,avg}$, E_{99} and $E_{L,avg}$) are computed with the post-processing techniques described in Section 3.2. As shown in Figure 5.1, highly intensive external perturbed E-field is observed around the top of the head and close to the nose (i.e., due to its protruding shape). The induced E-field distribution shown in Figure 5.1(d) indicates a significant concentration of E-field in the ankle regions (due to the smaller cross-sectional areas).

The conversion factors between a 1 kV/m vertically polarized external E-field and the peak induced E-field in the brain and body (excluding the skin layer) are presented in Tables 5.1 and 5.2. The induced E-field in the skin layer is omitted since no nerve-stimulation can occur in the *stratum corneum*. The conversion factors for the peak induced E-field in the heart and the short-circuit current across the ankles are shown in Table 5.3. It is observed that the conversion factors for the induced E-field in the body are less frequency-dependent than those for the brain and heart. This is due to the fact that the total body resistance varies linearly with respect to frequency. The trend is also verified by observing the frequency-independent short-circuit current conversion factor presented in Table 5.3(b). An additional simulations is performed by treating the skin layer as muscle (more conductive and capacitive) instead of stratum corneum (i.e., dry skin). It is observed that due to this variation, the peak induced E-fields in the brain and heart are reduced by approximately 8% while the peak value in the body tissues drops by about 30-40%.

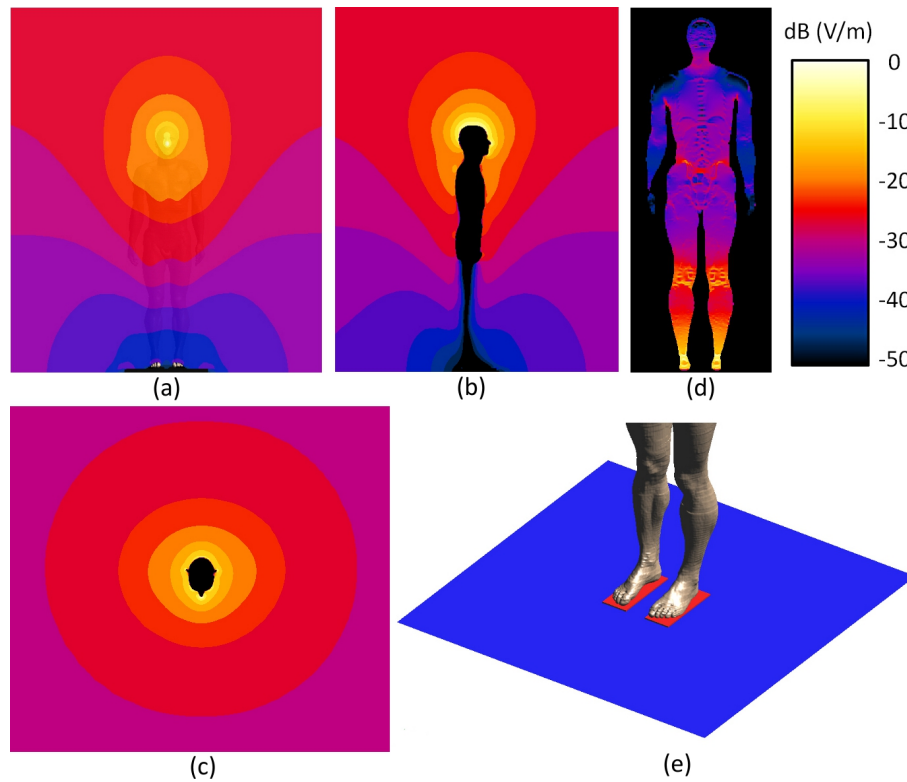


Figure 5.1: The external E-field distribution (a) front view, (b) side view, (c) top view, and (d) the induced E-field ($E_{V.avg}$) distribution, (e) the configuration of ground-to-sole contact.

The computed peak induced E-field and short-circuit current values are scaled by the respective reference levels (maximum permissible exposure) and compared to the associated

Table 5.1: The conversion factors between a 1 kV/m uniform vertically polarized E-field and the computed peak induced E-fields in the brain of Duke.

(mV/m)/(kV/m)/Hz	Frequency (Hz)								
	10	50	100	500	1000	3000	10000	50000	100000
$E_{V.avg}$	0.09	0.07	0.06	0.06	0.05	0.05	0.05	0.04	0.04
E_{99}	0.06	0.04	0.04	0.04	0.03	0.03	0.03	0.03	0.03
$E_{L.avg}$	0.10	0.08	0.06	0.06	0.06	0.05	0.05	0.05	0.04

Table 5.2: The conversion factors between a 1 kV/m uniform vertically polarized E-field and the computed peak induced E-fields in the body of Duke (excluding the skin layer).

(mV/m)/(kV/m)/Hz	Frequency (Hz)								
	10	50	100	500	1000	3000	10000	50000	100000
$E_{V.avg}$	1.20	1.28	1.21	1.15	1.14	1.13	1.15	1.21	1.21
E_{99}	0.82	0.74	0.69	0.72	0.74	0.78	0.82	0.75	0.79
$E_{L.avg}$	1.27	1.38	1.36	1.22	1.31	1.27	1.25	1.28	1.26

Chapter 5. LF Electric Field Exposure Analysis

Table 5.3: The conversion factors between a 1 kV/m uniform vertically polarized E-field and (a) the computed peak induced E-field in the heart of Duke and (b) the short-circuit current (I_{SC}) across the ankles of Duke.

	Frequency (Hz)								
	10	50	100	500	1000	3000	10000	50000	100000
(mV/m)/(kV/m)/Hz	(a)								
$E_{L,avg}$	0.17	0.10	0.09	0.08	0.08	0.07	0.05	0.04	0.04
mA/(kV/m)/Hz	(b)								
I_{SC}	3.0×10^{-4}								

basic restrictions in Figures 5.2, 5.3 and 5.4, respectively. In Figure 5.2(a) and 5.2(b), it is observed that the ICNIRP-2010 external E-field reference levels are in general conservative for the induced E-field in the brain for both general public and occupational exposure. The only exception occurs at 50 Hz when the $E_{V,avg}$ value approach the general public threshold limit ($E_{V,avg} = 0.017$ V/m, BR = 0.02 V/m). This is due to the variation in the RL-to-BR conversion factors between the general public exposure and the occupational exposure in ICNIRP-2010 at 50 Hz (i.e., 5 kV/m to 0.02 V/m for the general public exposure and 10 kV/m to 0.1 V/m for the occupational exposure). The IEEE Std. C95.6-2002 reference level is found to be marginally conservative for the peak induced E-field in the brain (see Figure 5.2(c)).

For the peak induced E-field in body tissues, the ICNIRP-2010 reference levels are found to be conservative throughout the investigated frequency range as shown in Figure 5.3(a) and Figure 5.3(b). The IEEE Std. C95.6-2002 reference levels for the controlled environment are found to be non-conservative for frequencies above 100 Hz as shown in Figure 5.3(c). This is due to the fact that while the basic restrictions for the body extremities (i.e., hands, wrists, feet and ankles) are invariant between the general public and controlled environment, the reference levels of the controlled environment are given relaxation factors of 3 and 4. The rationale given in IEEE Std. C95.6-2002 for this relaxation is that the exposed person (e.g., a power-line worker) in a controlled environment can consciously take preventive measures such as wearing a conductive suit, hence higher external E-field is allowed. For the peak induced E-field in the heart and the short-circuit current across the ankles, a comparison to the basic restrictions reveals that both ICNIRP and IEEE exposure limits are conservative (see Figure 5.4). This is due to the fact that the external E-field threshold limits are mainly derived based on the scenario of indirect contact current, instead of direct induction from external E-field. In general, higher induced current is expected in an indirect induction case (i.e., due to the contact with a conductive object).

5.2.3 Summary of the Uniform E-field Exposure Analysis

In summary, the computational results of an anatomical model in a general standing posture suggest that the external E-field reference levels provided in ICNIRP-2010 are in general ca-

pable of preventing the induced E-field from exceeding the basic restrictions for a grounded person exposed to a uniform E-field. A larger safety factor is recommended for the IEEE standard based on the brain and body exposure results. It is noted that the RL-to-BR conversion is not consistent between the IEEE Std. C95.6-2002 general public and controlled environment body extremities exposure scenarios. This could give rise to confusion during the interpretation of the exposure limits since the assumption of conductive suit shielding is not stated in the definition of controlled environment in IEEE Std. C95.6-2002. To maintain a coherent conversion factor between the external E-field and the induced E-field for body extremities, one recommendation for the IEEE standard is to provide a separate reference level for an exposed person without protective gears in a controlled environment or state clearly in the standard that the reference level for the controlled environment applies with the assumption that the exposed person is protected by a conductive suit.

The computational results of an anatomically realistic model provide the estimation of the spatially averaged peak induced E-field in the human brain and body due to LF E-field induction. Through a comparison with the basic restrictions provided in ICNIRP-2010 and IEEE Std. C95.6-2002, the ICNIRP-2010 reference levels are found to be in general conservative while larger safety factor is recommended for the IEEE reference levels. The investigation of the impact of skin layer dielectric property indicates that a less conductive skin layer represents a more conservative set-up for the E-field induction assessment of a grounded body.

Chapter 5. LF Electric Field Exposure Analysis

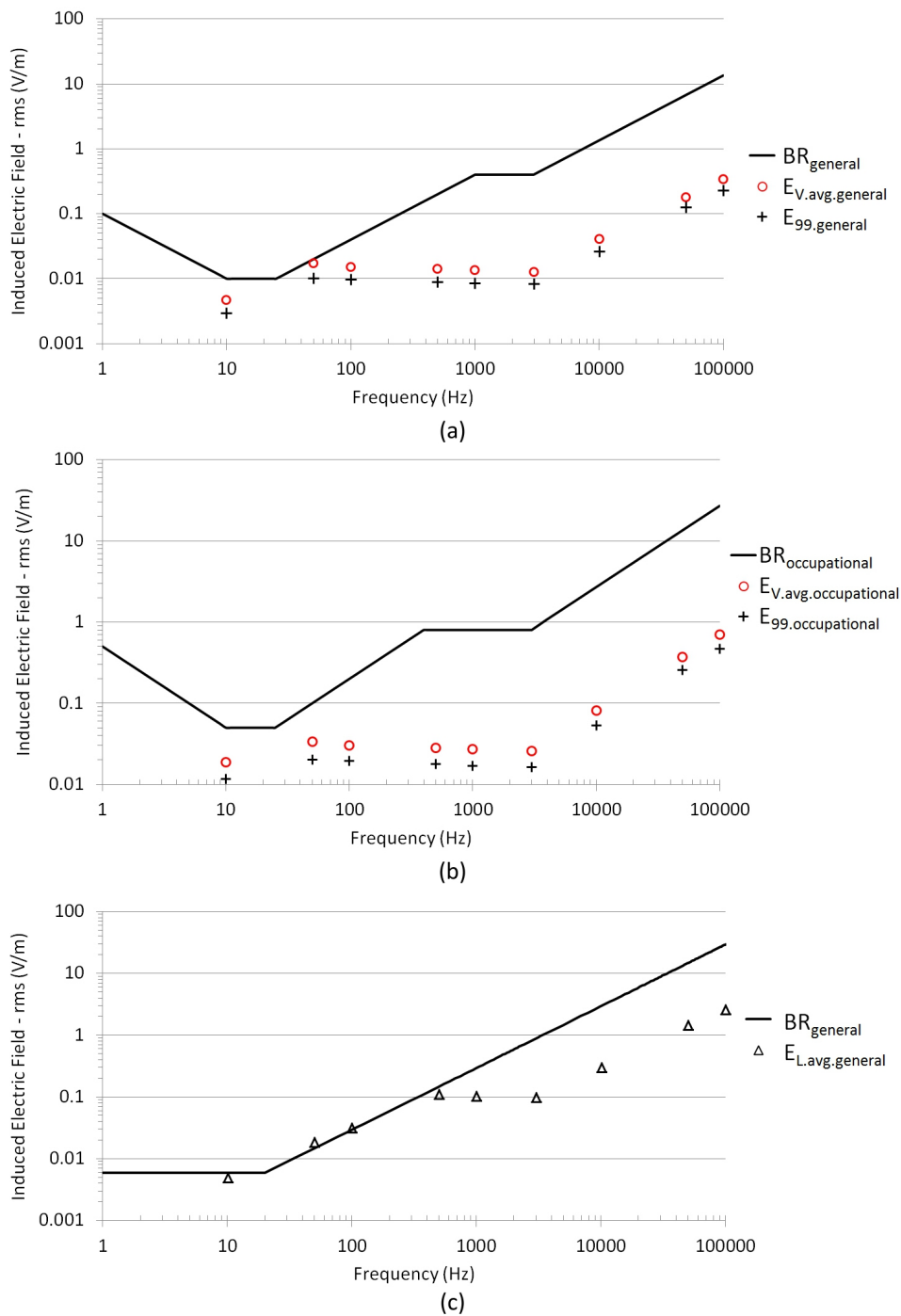


Figure 5.2: The ICNIRP-2010 BR levels for the CNS tissues and the peak $E_{V,avg}$, E_{99} values for (a) general public and (b) occupational exposure, and (c) the IEEE Std. C95.6-2002 BR levels for the brain and the peak $E_{L,avg}$ values for general public exposure, in Duke exposed to a uniform vertically polarized E-field at the respective reference level.

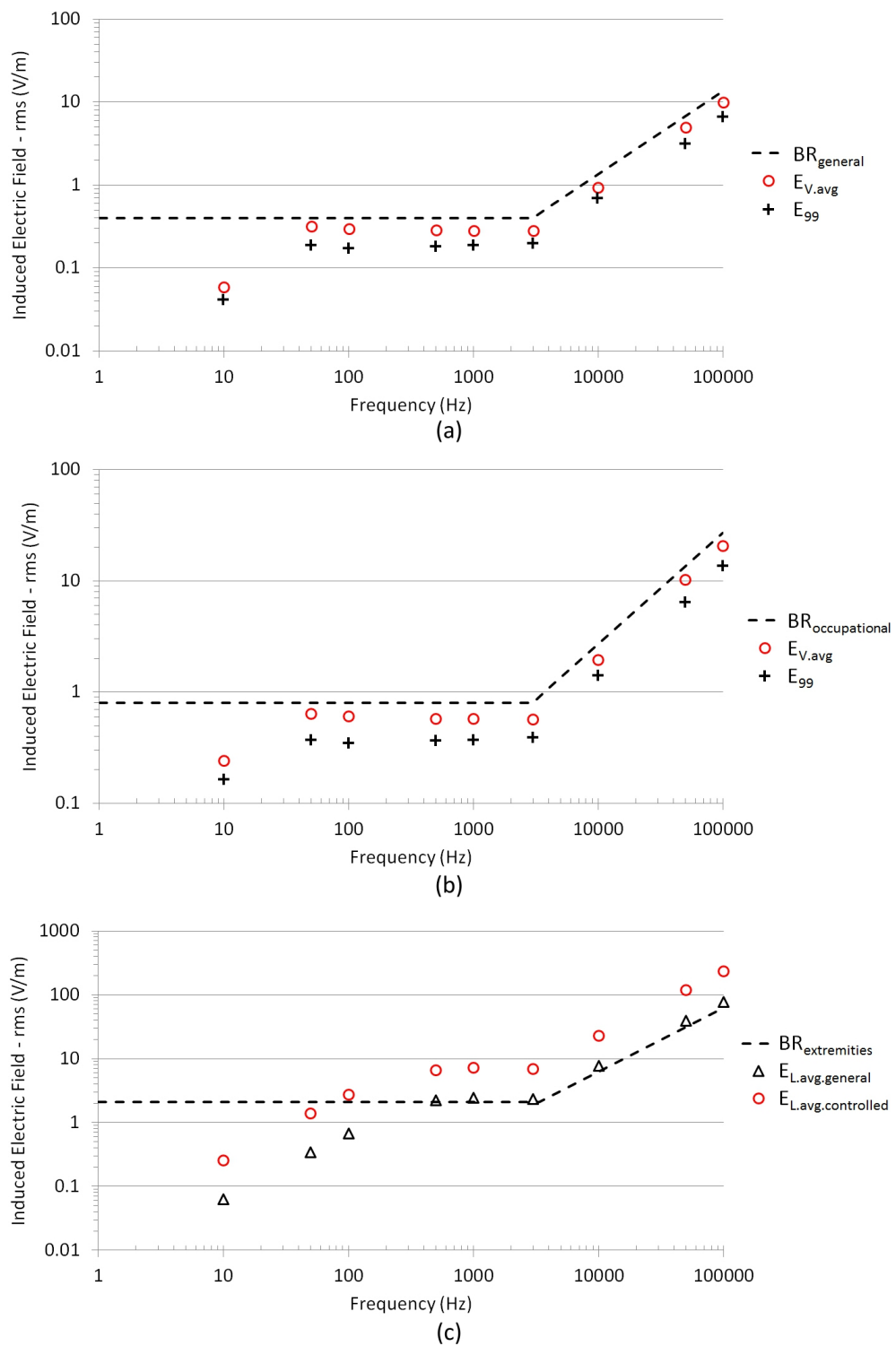


Figure 5.3: The ICNIRP-2010 BR levels for the PNS tissues and the peak $E_{V,\text{avg}}$, E_{99} values for (a) general public and (b) occupational exposure, and (c) the IEEE Std. C95.6-2002 BR levels for the extremities and the peak $E_{L,\text{avg}}$ values, in Duke (excluding skin) exposed to a uniform vertically polarized E-field at the respective reference level.

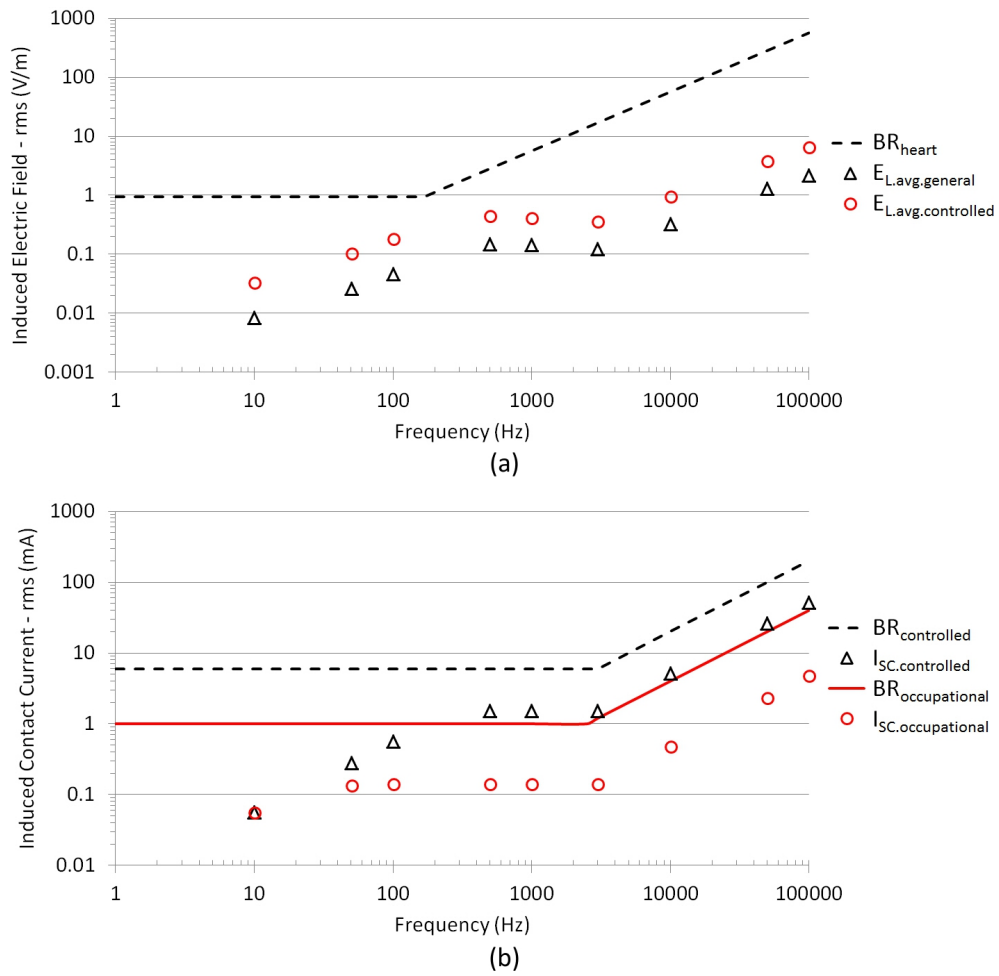


Figure 5.4: (a) The IEEE Std. C95.6-2002 BR levels and the peak $E_{L,avg}$ values for the heart, and (b) the ICNIRP-2010 (occupational), IEEE.Std.C95.6-2002 (controlled environment) threshold limits for contact current and the computed short-circuit current (I_{SC}) in Duke exposed to a uniform vertically polarized E-field at the respective reference level.

5.3 Analysis of Contact Current

5.3.1 Background

Besides the direct E-field induction due to the exposure to an external E-field, certain exposure scenario includes an additional source of induced E-field: physical contact with a conductive object at a different potential. The conductive object may be charged due to a physical connection to a voltage source or through the exposure to an external E-field. Alternatively, the conductive object may be grounded while the human body is charged at a different potential. These two induction types could occur simultaneously when both induction sources are present. In this section, a “hot stick” live-line working scenario is investigated by simulating a person operating a voltage detector underneath a high voltage distribution line. In this case, two mechanisms are responsible for the induced E-field in the worker’s body: physical contact with the voltage detector and exposure to the E-field generated by the power line. The exposure to external E-field has been investigated in the previous section, hence only the indirect induction case is investigated in this section. Three body postures with respect to the handling of voltage detector are employed to assess the impact of posture variation on the induced contact current. In a contact current induction scenario, the induced E-field in the human body is generated due to the electric potential difference between two physical contact points. In general, one of the possible contact is the feet-to-ground contact and the other contact is between the body (e.g., the hand) and a charged object. With the *ohmic-current-dominant* approximation for biological tissues, (2.25) can be applied to solve for the induced E-field within the lossy tissue materials by neglecting the displacement current (see Section 2.6.3). A human body can be treated as a cascaded resistor network with the body tissues modelled as resistor segments. The induced ohmic current is expected to flow in a path defined by the tissue resistance between the contact points.

5.3.2 High Voltage Detector

A single-pole high voltage detector is often utilized for overhead contact systems in electric railways and substations. It is designed to determine the presence of high voltage on a power distribution line. A high voltage detector consists of the following components: contact electrodes, indicator, insulating elements and a elongated handle with a specific length. During the operation of a high voltage detector, a person standing on the ground holds the detector at one end and touches a power line with the other end. A conducting path is formed between the power line and the ground through the voltage detector and the person operating it. As a result, a small amount of current can be detected if the power line is energized. As shown in Figure 5.5, the contact current is a ratio of the power line voltage to the sum of voltage detector resistance R_i and body resistance R_b . R_i must be large enough to limit the amount of current which is allowed to flow through the human body. Note that additional resistance introduced by footwear or gloves will further reduce the strength of the contact current.

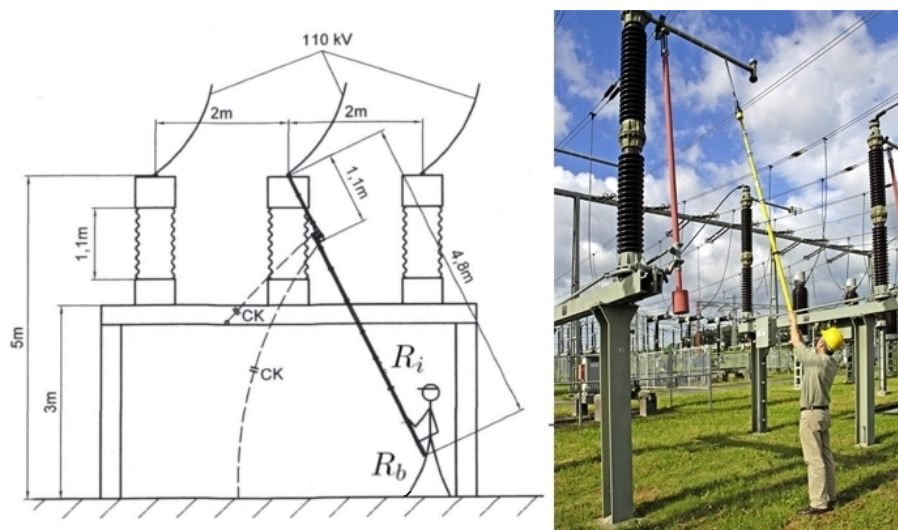


Figure 5.5: The outline of a person operating a voltage detector (left) and a photograph depicting a realistic operation (right), copyright Pfisterer AG.

5.3.3 Analysis of the Contact Current due to a High Voltage Detector

Based on the details of an actual exposure environment provided by the power facility company (Pfisterer International AG), numerical computations are performed with the SPFE solver and a possible anatomical model (Duke) to investigate the induced E-field and short-circuit current in a human body during the operation of a voltage detector. The voltage detector employed in this study exhibits an operational resistance of $300\text{ M}\Omega$ or $3000\text{ M}\Omega$, respectively, depending on whether it is wet and dirty or dry and clean. A resistance of $300\text{ M}\Omega$ is assumed to be the worst-case scenario within the manufacturing tolerance of the voltage detector. The computational model is constructed with the Duke holding a conductive stub which represents the handle of the voltage detector and standing on a ground plane with both of his feet grounded (represents the worst-case short-circuit scenario). A three-phase 50 Hz power line system located 5 meters above the human body as shown in Figure 5.5 is considered as the electric potential source. The power lines exhibit a peak voltage of 110 kV and a peak load current of 600 A. A uniform grid resolution of 1 mm is employed for the discretization of the anatomical model.

Three body postures are modelled as shown in Figure 5.6. The selected body postures represent some of the typical worker's postures during a voltage detector operation based on the survey result provided by the associated organization. In the first posture scenario, the Duke model holds the stub in his right hand and positions it close to his waist level. This body posture is noted as P_1 . In the second posture scenario (P_2), Duke's right arm is rotated by 90° and the stub is raised to his eye level. In the third posture scenario (P_3), the Duke model grabs the conductive stub with both of his hands and holds it at his chest level. As the contact area between the hand and the stub serves as an entry point for the current flow, the possible human body is modelled to offer hand grip that bears resemblance to real-life hand grip

scenario as shown in Figure 5.7. Uncertainty is expected due to the resistance difference between the homogeneous skin model employed in this study and the realistic multi-layer skin structure. Based on the tissue *ohmic-current-dominant* approximation, the current flow through the body due to the potential difference between the voltage detector and the ground can be computed with the assumption that the external E-field generated by this potential difference and the displacement current in the lossy tissues are negligible.

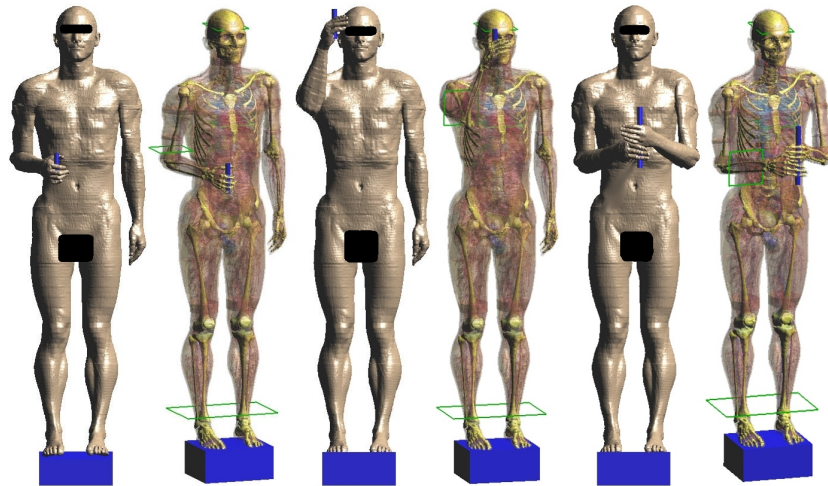


Figure 5.6: Three body postures for the simulation of a person operating a voltage detector, from left to right, body posture P₁, P₂ and P₃.

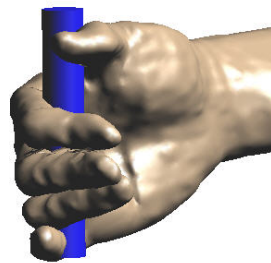


Figure 5.7: The possible hand grip of the voltage detector handle.

The ground plane is set to zero potential while the conductive stub is set to an arbitrary positive non-zero potential. The body resistance R_b during the operation of a voltage detector is derived based on the computed short-circuit current I_{SC} . The body resistance is found to be in the range of 3-5 k Ω for the investigated body postures. Compared to the measured resistance of a dry skin hand-to-hand configuration presented in Table 5.4 [70], the computed hand-to-feet body resistance is within a reasonable range. In the case when R_i is at 300 M Ω , the electric potential value at the detector handle is found to be 1.9 V, 1.8 V and 1.1 V, respectively, for P₁, P₂ and P₃. At these potentials, the volume-averaged peak induced E-fields in various body tissues are presented in Table 5.5. In accordance with *Kirchhoff's current law*, the currents which flow through the trunk, ankles and the arm/arms are found to be consistent.

Chapter 5. LF Electric Field Exposure Analysis

Table 5.4: The measured resistance of a hand-to-hand configuration for dry skin and large contact areas, with respect to the contact voltage (V) and population percentile (%) at 50 Hz.

Voltage (V)	5%	50%	95%
25	1.75 k Ω	3.25 k Ω	6.10 k Ω
100	1.20 k Ω	1.88 k Ω	3.20 k Ω
220	1.00 k Ω	1.35 k Ω	2.13 k Ω
1000	0.70 k Ω	1.05 k Ω	1.50 k Ω

Table 5.5: The computed body resistance R_b with respect to posture variation, the corresponding peak induced E-field ($E_{V,avg}$) and the short-circuit current (I_{SC}), for R_i of 300 M Ω and V_{source} of 110 kV at 50 Hz.

Posture	R_b (k Ω)	E (V/m)			I_{SC} (mA)
		Brain	Heart	Ankle	
P_1	5.2	4.5×10^{-3}	0.23	0.72	0.37
P_2	4.9	3.5×10^{-3}	0.22	0.74	0.37
P_3	3.1	1.1×10^{-3}	0.16	0.78	0.37

It is observed that the variation of body posture from P_1 to P_2 alters the body resistance slightly without affecting the corresponding short-circuit current. The change in body resistance can be explained with the compression of body tissues caused by, e.g., bending of the arm, which leads to different cross-sectional areas for the current path. The change in body posture from P_1 to P_3 results in a greater variation in the body resistance. However, the short-circuit current remains invariant. This is due to the fact that the detector resistance is much larger than the body resistance, therefore the range of the body resistance variation is not big enough to significantly alter the total resistance ($R_i + R_b$). The greater body resistance variation from P_1 to P_3 can be explained as follows: grabbing the detector handle with both hands instead of a single hand is equivalent to adding a shunt resistor in the current path, which effectively lower the body resistance. Based on the given power line voltage of 110 kV and the minimum detector resistance of 300 M Ω , the variation in the posture-related body resistance is found to have negligible effect on the short-circuit current. The contact current threshold limit is given as 1 mA for ICNIRP-2010 [2] occupational environment and 6 mA for IEEE Std. C95.6-2002 [3] controlled environment at 50 Hz. The contact currents computed in this case study are well below these limits due to the presence of a large voltage detector resistance. The contact current of 6 mA [3] requires a faulty detector resistance at or below 18 M Ω . The current density distributions for the investigated body postures are presented in Figure 5.8. Higher current density is observed in the wrist and ankle regions due to their relatively smaller cross-sectional areas. Significantly higher currents are found in the heart than in the head because the head does not lie in the current flow path as observed in Figure 5.8. The peak E-fields induced in the brain, heart and ankle are found to be within the exposure limits.

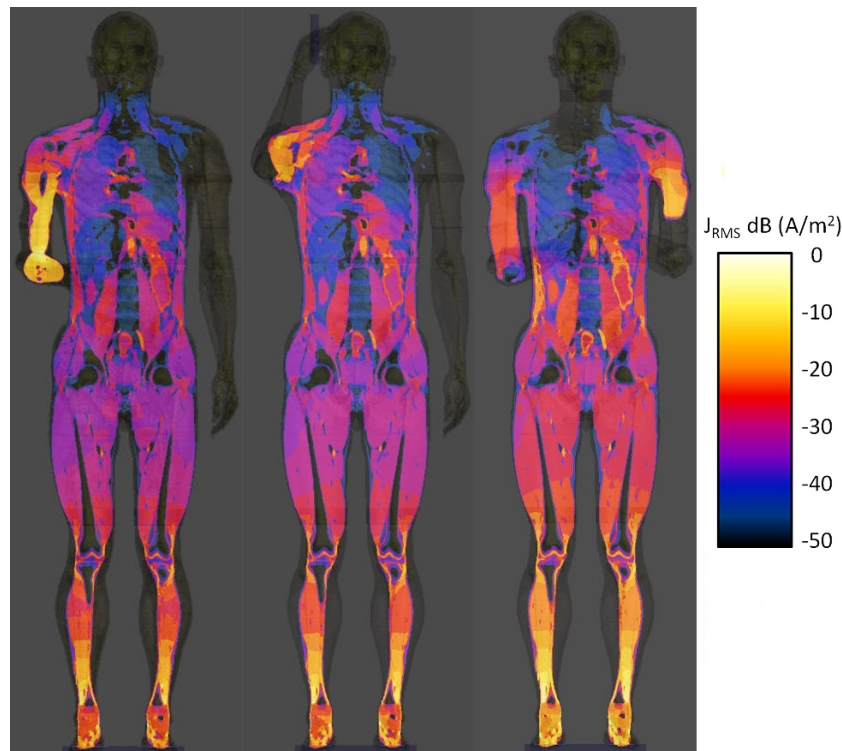


Figure 5.8: The induced current density distribution for the three investigated body postures, from left to right, body posture P_1 , P_2 and P_3 .

5.3.4 Summary of the Contact Current Analysis

In this study, the contact current induced in a human body due to the operation of a voltage detector is numerically investigated with a possible anatomical model and the SPFE solver. It is demonstrated that the body resistance and contact current can be estimated with respect to different body postures and contact configurations. Based on a practical exposure environment with a known voltage source and detector resistance, three body postures which represent typical operation scenarios are employed to investigate the effect of posture variation on the body resistance and short-circuit current.

The investigated body postures are found to have negligible effect on the total short-circuit current due to the large ratio between the voltage detector resistance and the body resistance. The computational results indicate that as long as the voltage detector resistance is high enough (i.e., ≥ 18 M Ω), the contact current induced in the operator will be lower than the IEEE Std. C95.6-2002 exposure limit (i.e., 6 mA at 50 Hz). The investigation performed in this study assumes the scenario of a grounded person in contact with a voltage detector as the worst-case scenario for a voltage detection operation. To cover all the possible exposure scenarios, e.g., when the person is touching an additional conductive object while operating the voltage detector, further analysis is required.

5.4 Conclusion

The research work presented in this chapter not only leads to the validation of several known induction characteristics for a grounded body exposed to a vertically polarized uniform E-field, it also addresses some of the practical open issues for LF E-field induction numerical dosimetry. The conversion factors between the external E-field and the peak induced E-field (and short-circuit current) are derived based on the computational results of the anatomical model. In the second part of this chapter, a realistic exposure scenario of a person operating a high voltage detector below a power distribution line is numerically investigated with a possible anatomical model. The induced contact currents in a human body estimated based on the computational results of several body postures reveal no tangible exposure safety concerns towards the operation of a high voltage detector, provided that the detector exhibits a proper operating resistance.

The computational results of a high-resolution anatomically realistic model provide the estimations of the spatially averaged peak induced E-field in the human brain, heart and body. Through a comparison with the basic restrictions provided in ICNIRP-2010 [2] and IEEE Std. C95.6-2002 [3], the ICNIRP-2010 reference levels are found to be conservative while more safety margins are recommended for the IEEE Std. C95.6-2002 maximum permissible exposure limits. The investigation of the impact of skin layer dielectric property variation indicates that a less conductive skin layer represents a more conservative set-up for an E-field induction exposure assessment. The research findings presented in this chapter path the way towards a better understanding of the induction characteristics of E-field exposure and form the basis for further research activity pertaining to the assessment of the worst-case E-field induction scenario.

6 Mobile Device Antenna Optimization with Genetic Algorithms

6.1 Introduction

With the ever increasing demand for novel hand held wireless devices such as mobile phones and tablet personal computers, the design cycle has to be shortened in order to reduce the product delivery time. This introduces great challenges as product engineers have to realize a design in a rather short time frame while achieving complex design requirements including compliance with the Over The Air (OTA) [113] performance, Specific Absorption Rate (SAR) [114] and Hearing Aid Compatibility (HAC) [115] product standards.. With the trend of slimmer and smaller mobile devices, the available space for antenna placement also shrinks. Inevitably, antenna engineers face great difficulty implementing multi-band antenna for mobile phone with a short chassis and small antenna volume. In recent years, emphasis has been placed on computer-aided antenna optimization methods [42–44].

In this chapter, Genetic Algorithms (GAs) [45] in conjunction with a Finite Difference Time Domain (FDTD) [48] solver are employed for the design and optimization of mobile phone antennas in a Computer Aided Design (CAD) environment. On the basis of an up-to-date commercial mobile phone CAD model, three types of embedded multi-band antenna are designed and optimized within a fixed volume. The research objective is to achieve optimum antenna performance efficiently for all three designs by employing a well devised numerical optimization approach. This chapter is organized in the following manner: a network distribution scheme for the genetic algorithms is introduced first, followed by a discussion of the antenna design concepts. Next, a description of mobile device antenna modelling and optimization approach is presented. The computational results are discussed with respect to the near-field and far-field performance of the optimized antenna designs. Finally, a conclusion is provided on the use of computer-aided numerical modelling for mobile device antenna optimization.

6.2 Methods and Materials

6.2.1 FDTD-based Simulation Platform

The antenna simulations are performed with a FDTD-based full-wave electromagnetic simulation software package “SEMCAD X” [48]. Powered with “Graphic Processing Unit” (GPU) acceleration technology, this simulation platform has achieved simulation speed boost beyond the limit of mere “Central Processing Unit” (CPU) accelerations [116]. A complex structure, e.g. a full scale mobile phone with detailed components, can be simulated across a broadband frequency range in a matter of minutes instead of hours. The suitability and accuracy of the FDTD-based simulation tool for mobile device antenna design has been investigated in [117–120]. The Specific Anthropomorphic Mannequin (SAM) head phantom and a posable CTIA (Cellular Telephone Industries Association) compliant hand model are available in the employed software package for the numerical simulations of mobile phones under real usage conditions. The antenna-related parameters, for instance, the reflection coefficient of an antenna (S_{11}), Total Radiated Power (TRP), radiation pattern, Specific Absorption Rate (SAR) and Hearing Aid Compatibility (HAC), can be acquired through a single broadband simulation process. Compared to a frequency-domain solver which requires multiple simulation runs to acquire a broadband response, the time-domain simulation capability of the FDTD method is particularly beneficial for a multi-band antenna design. In addition, compared to the boundary element method (e.g., the method of moments), the FDTD method (a volume-discretization method) tends to be more efficient for complex structure with inhomogeneous mediums (e.g., with device plastic housing, human head and hand phantoms). The aforementioned factors render the FDTD time-domain solver a suitable candidate for the computer-automated optimization of mobile phone antennas.

6.2.2 Genetic Algorithms and Network Distributed Optimization

Optimization algorithms such as the Genetic Algorithms (GAs) have been experimentally applied to antenna design in the past decade [44, 46, 47, 117, 121, 122]. With the advancement of computer hardware such as multi-core CPUs and GPUs, coupled with efficient computational electromagnetic modelling techniques, complex antenna optimization problems can now be solved efficiently. GAs belong to a particular class of evolutionary algorithms which utilize techniques inspired by evolutionary biology [45]. It was formally introduced in the 1970s and has since been widely used to optimize antenna and other microwave structures. Even though GAs are known to be computationally costly, the method becomes increasingly attractive for complex optimizations due to the continuing price and performance improvements of computer systems. GAs work very effectively on combinatorial problems and are less susceptible to pitfalls such as *stuck at local optima* than the traditional algorithms, e.g., gradient search methods. In addition, GAs are more suitable for an optimization task with unknown suboptimal initial parameters.

When a GA is applied to an optimization task, the problem is structured into a population of abstract representations (known as chromosomes) of candidate solutions (known as individuals). These candidate solutions are to be evolved towards optimum solutions. Typically, solutions are represented in binary forms as strings of 0s and 1s. The evolution normally initiates from a population of stochastically generated individuals and occurs in generations. In each generation, after evaluating the fitness of every individual in the population, several individuals are chosen from the current population based on their fitness and then modified (mutated) to create a new population. The new population is used in the next iteration of the algorithm. The optimization process terminates when either a predefined maximum number of generations has been produced or a satisfactory fitness level has been achieved for the population.

Based on GA's unique evolution-like optimization process, parallelization is realized in the FDTD solver [48] by utilizing network clustered computer systems. In general, the chromosomes from a population are grouped and evenly distributed to multiple computer systems. Each computer will then solve for the fitness values of the assigned individuals. A master computer collects all the fitness information at the end of each generation cycle and creates the next population based on this information. As a result, the optimization time is reduced proportionally by the number of computer systems utilized. This study focuses on the assessment of the suitability of GAs (with network parallelization) in conjunction with the FDTD method for mobile device antenna design. The research objective is to validate that the combination of GAs with FDTD method provides promising practical performance in terms of simulation time and optimization result.

6.2.3 Antenna Optimization Methodology

In a mobile phone, the antenna is one of the key components that has direct impact on product functionality and user experience. A poorly designed mobile phone antenna could cause shorter battery life, inadequate signal coverage and frequent call drops. A mobile phone antenna design cycle consists of initial concept validation, prototyping and numerous optimization iterations based on the product's mechanical and electrical design changes. The traditional optimization process requires an antenna engineer to tweak the antenna design and matching circuit for optimum performance. This approach demands engineering expertise, measurement equipments (e.g., vector network analyzer, anechoic chamber) and hours of measurement time. In light of the ever shortening design cycle, a computer-aided antenna optimization approach serves as an important complement to the traditional method.

Antenna optimization normally focuses on tuning the physical dimensions of an antenna (e.g., the length of radiator element, distance to ground plane, etc.) to achieve bandwidth and efficiency requirements. Performing such optimization iterations in a simulation environment demands a proper choice of optimization goals and variables. On the employed simulation platform, the embedded optimization module allows its user to perform optimization with an

arbitrary number of parameters and a combination of goal functions with different weights. Far-field and near-field parameters such as S_{11} , TRP, SAR, HAC etc. are offered as antenna optimization goals. Since the optimization time is exponentially proportional to the number of variables to be optimized, the antenna parameters to be included should be carefully identified based on their sensitivity and impact to the overall design.

6.3 Antenna Models

In this study, a bar type mobile phone (see Figure 6.1) is analyzed. This mobile device structure incorporates several challenges faced in a mobile phone antenna design: low profile, short chassis and close proximity to electrical components. To establish its corresponding numerical model, a highly detailed CAD database of the phone is imported into the simulation platform. The components with dimensions significantly smaller than the wavelength of the highest frequency of interest are neglected. The entire CAD phone consists of over two hundred parts, providing a “near final hardware” simulation model.



Figure 6.1: The mobile phone model employed in this study: the photograph of the actual phone (far left) and the CAD derived model.

It is known that the radiation characteristics of a mobile phone are better understood and described by considering the antenna element, the printed circuit board (PCB) and the metal chassis frame as a single radiating structure [54]. However, in this study, only the antenna is considered for optimization since for industrial products, form factor and antenna volume are usually locked down in the initial stage of development. The original antenna design for the selected phone model is a folded monopoles antenna (FMA) as shown in Figure 6.2. Alternative antenna designs are realized in the same volume ($45 \text{ mm} \times 14.5 \text{ mm} \times 8 \text{ mm}$) occupied by this antenna. The electrically conductive components near to or within the assigned antenna volume include polyphonic speaker, metal screws, battery and metal battery door. No matching circuit is considered in this evaluation, i.e., the study is conducted purely on the assessment of antenna performance. The antennas are designed to operate in the

frequency bands of GSM850, GSM900, DCS1800 and PCS1900, covering frequencies from 824 MHz to 960 MHz and from 1710 MHz to 1990 MHz. In addition to the folded monopoles antenna design, the antenna types investigated in this study are the Planar Inverted F Antenna (PIFA) [123] (see Figure 6.3) and the Folded Inverted Conformal Antenna (FICA) [124] (see Figure 6.4). These antenna designs have been widely implemented in commercial mobile phones and their respective design methodology has been well documented [54].

6.3.1 Folded Monopoles Antenna (FMA)

This antenna structure is derived from the Inverted L Antenna [54], which is essentially a monopole antenna with its radiator arm bent parallel to the printed circuit board (PCB). By incorporating two branch arms as shown in Figure 6.2, two resonance modes can be excited to cover the required frequency bands. The attainable bandwidth of a FMA largely depends on its distance to the ground plane (PCB and metal chassis). To realize an antenna-to-ground distance, a $45 \text{ mm} \times 12 \text{ mm}$ “ground clearance area” is implemented on the PCB by removing all conductive layers in this clearance region. The resonances are tuned mainly by adjusting the lengths of the arms and the coupling between them. The FMA is relatively easy to implement due to its simple construction in which antenna tuning can be achieved by adjusting the lengths of the branch arms and the gaps between them. However, a matching circuit is crucial for such design as the antenna impedance exhibits strong capacitive characteristic due to the parallel radiator section.

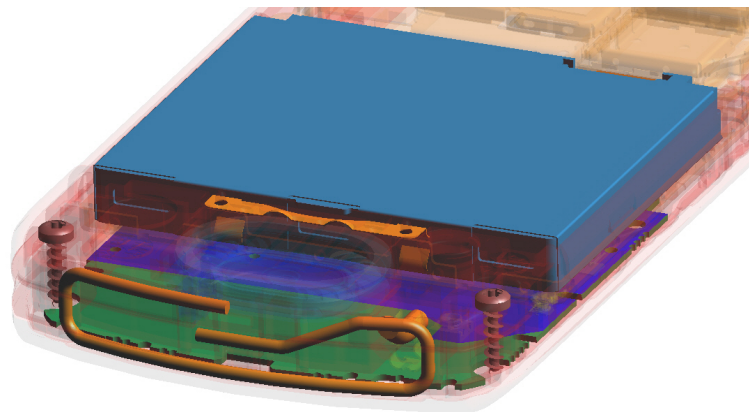


Figure 6.2: The Folded Monopoles Antenna (FMA).

6.3.2 Planar Inverted F Antenna (PIFA)

The Inverted F Antenna (IFA) [54] is a variant of the monopole antenna similar to the Inverted L antenna. The antenna element is folded down to be parallel with the ground plane. A short circuit stub is introduced to provide inductive matching to the structure and this compensates the capacitive input impedance caused by the parallel section. The PIFA can be considered as an Inverted F Antenna (IFA) with the wire radiator element replaced by a plate to expand its

bandwidth. The input impedance of a PIFA can be tuned to achieve an appropriate value and matched to the load impedance (i.e., usually at 50Ω) without using any additional matching circuit. This characteristic is known as *self-matching* [49]. To obtain a desired resonance and bandwidth, various parameters of PIFA are available for tuning. In general, a PIFA design focuses on the following parameters: the locations of the feed pin and short-circuit stub, the antenna patch-to-ground-plane distance (antenna height), and the design of the slot pattern. The U-shape slot as shown in Figure 6.3 produces two arms on the patch. The longer arm governs the GSM band (i.e., 824 to 960 MHz) resonance and the shorter arm determines the DCS/PCS band (i.e., 1710 to 1990 MHz) resonance. The resonances can be tuned by adjusting the lengths and widths of these arms. A “ground clearance area” is also introduced in the PIFA design to broaden the achievable bandwidth by enhancing the fringing field effect.

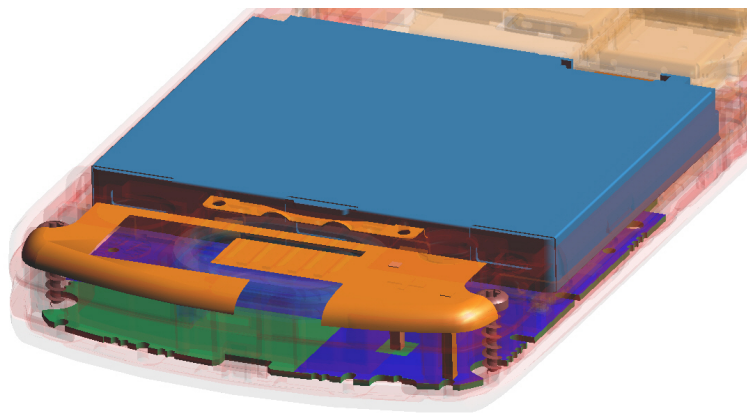


Figure 6.3: The Planar Inverted F Antenna (PIFA).

6.3.3 Folded Inverted Conformal Antenna (FICA)

The Folded Inverted Conformal Antenna (FICA) [124] is a multiple-resonance antenna which generates different resonance modes based on the radiating mechanisms of its physical construct. It offers three resonance modes, namely the “common mode”, the “differential mode”, and an additional “slot mode” created by the folded slot as shown in Figure 6.4. A FICA antenna exhibits broad bandwidth coverage for the DCS/PCS bands by having dual resonance modes present across the 1710-1990 MHz range. The unbalanced feeding structure comprises of one feed stub and one short-circuit stub that are oriented symmetrically with respect to the center of the ground plane. It is more challenging to realized a FICA design compared to other two antenna designs due to its multiple-resonance characteristics. The “differential mode” and “slot mode” must be tuned properly to achieve usable DCS/PCS band resonance. In general, the parameters considered for the tuning of a FICA design include the followings: the distance between the feed and short-circuit stubs, the length and width of the slot, and the antenna height (i.e., the distance from the antenna patch to the nearest ground plane). Two “ground clearance” regions are implemented in the FICA design following its symmetrical structure.

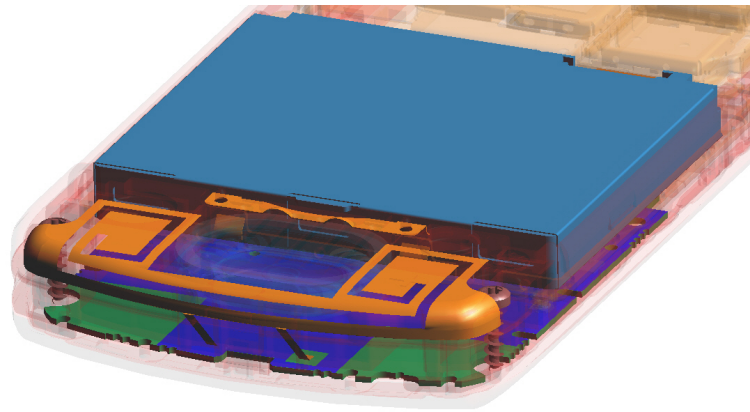


Figure 6.4: The Folded Inverted Conformal Antenna (FICA).

6.4 Parametrization and Optimization

6.4.1 Antenna Modelling and Parametrization

An efficient antenna optimization scheme is initiated by identifying the most critical antenna parameters, e.g., feed and ground pin locations in the case of a PIFA design. The antenna elements subjected to optimizations are modelled as parametrized objects as shown in Figure 6.5 for the PIFA design. In this design, the parameters selected for optimization include the dimensions of the U-shape slot and the distance between the feed and ground pins. These are the critical parameters related to the antenna impedance and resonant frequency. Due to the difference in design complexity for each antenna structure, the number of parameters to be included in the optimization process varies for each design. In this study, 5 optimization parameters are selected for the FMA design, 8 parameters for the PIFA design and 9 parameters for the FICA design. Since the overall optimization time is exponentially proportional to the number of variable parameters and their resolutions (i.e., the number of variants in the parameter range), a well-planned setting allows fast convergence to target goals without sacrificing the best available solution.

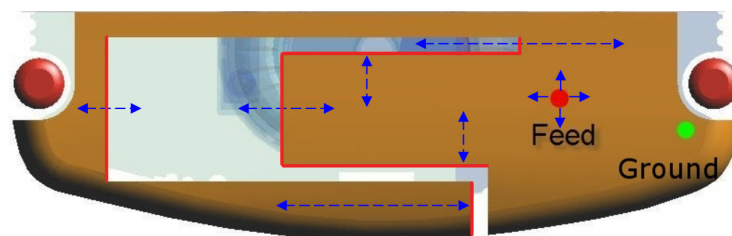


Figure 6.5: The parametrization configuration for the optimization of the Planar Inverted F Antenna (PIFA) design.

6.4.2 Optimization Process

The numerical optimizations are performed in two stages. In the first stage, optimizations are carried out for the mobile phone antennas in a free space environment and initiated from arbitrary antenna geometries. The parametrized antennas are simulated targeting a S_{11} of -5 dB at band edges which serves as the primary goal for a quad-band operation covering the GSM850, GSM900, DCS1800 and PCS1900 frequency bands. The secondary goal targets minimum field intensity above the acoustic point for the HAC compliance. Subsequently, the optimized antenna geometries are subjected to a head-and-hand phantom loading environment to evaluate their performance in real usage conditions. A homogeneous Specific Anthropomorphic Mannequin (SAM) head phantom and a CTIA-compliant anatomical hand model as shown in Figure 6.6 are employed. SAM Head phantom cheek placement and CTIA-compliant mono-block hand grip are considered. The dielectric properties of the head and hand phantoms, given in Table 6.1, are based on the human tissue measurements data described in [114] and [125], respectively.

The second stage of the optimization aims at rectifying the detuning effect when the mobile phone is placed in close proximity to the head and hand phantoms. The optimization for the SAR compliance is also introduced in the head-only condition (i.e., without the hand phantom) by considering the minimum achievable SAR value as a secondary goal (i.e., with less weight than the primary reflection coefficient goal). For the optimization (i.e., reduction) of the head-and-head loading effect, the optimization iterations can be significantly reduced by using the optimized antenna geometry from the free space case as the starting point since the dynamic range of parameter sweep can be reduced considerably.



Figure 6.6: The SAM head phantom cheek placement and a CTIA-compliant hand phantom grip for the investigated mobile phone.

Table 6.1: The relative permittivity ϵ_r and conductivity σ (S/m) of the SAM head and hand phantoms.

Dielectric Property	Head	Hand
ϵ_r at 900 MHz	41.5	30
σ at 900 MHz	0.97	0.62
ϵ_r at 1800 MHz	40	27
σ at 1800 MHz	1.4	0.99

6.5 Optimization Results and Discussions

6.5.1 Radiation Performance in Free Space

The optimizations are successfully performed for the antenna designs in free space. The optimized antenna structures achieved the desired bandwidth coverage for a quad-band operation following the predefined reflection coefficient goal. The S_{11} plots of the optimized antennas are shown in Figure 6.7. The TRP values of the transmit channels for the respective frequency bands are averaged based on the conducted power of 33 dBm (for GSM850/GSM900) and 30 dBm (for DCS1800/PCS1900) and presented in Figure 6.8. From the bandwidth and radiation performance requirement aspects, all three designs serve as suitable internally embedded antennas for the selected bar type phone model.

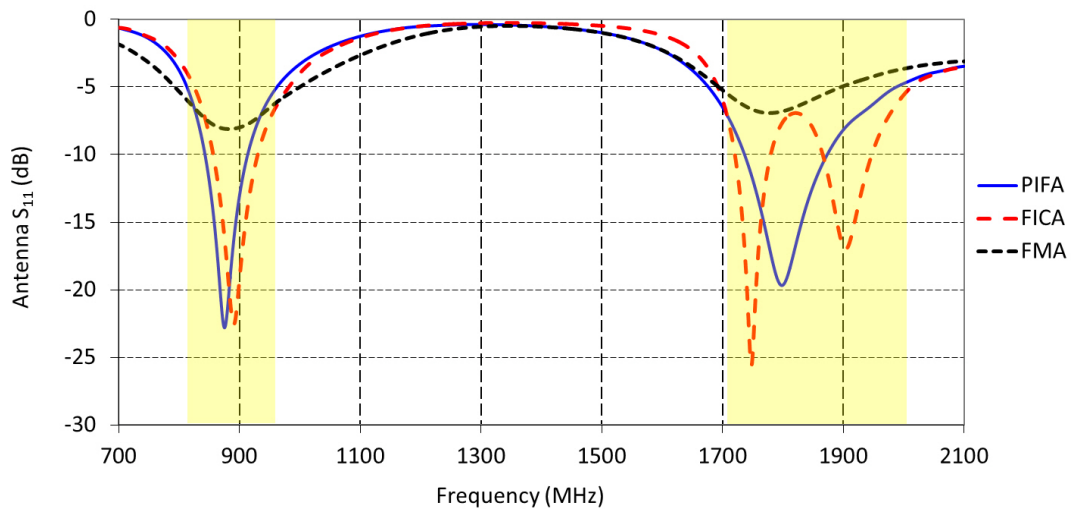


Figure 6.7: The antenna S_{11} of the optimized antennas in free space.

In Figure 6.9, the PIFA geometries before and after the free space optimization are presented together with the total fitness plot. In Figure 6.10, the corresponding antenna S_{11} is presented. As observed in the fitness plot, the first 100% fitness occurred after approximately 70 iterations. The optimization module was configured to continue through the entire generations even after achieving the first 100% fitness. This ensures the coverage of all available optimum solutions. All simulated geometries and results are automatically recorded for further evaluation.

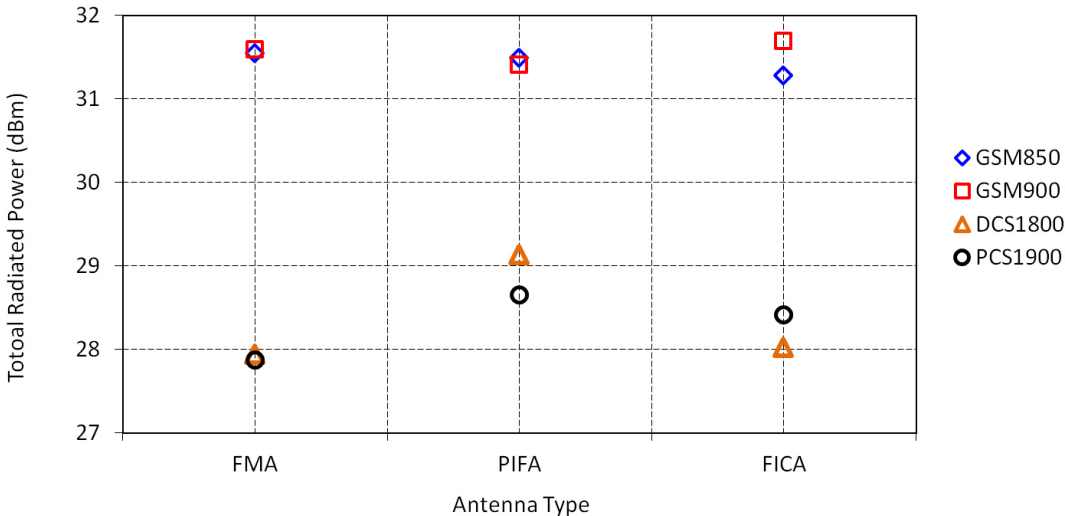


Figure 6.8: The band-averaged total radiated power values of the optimized antennas in free space.

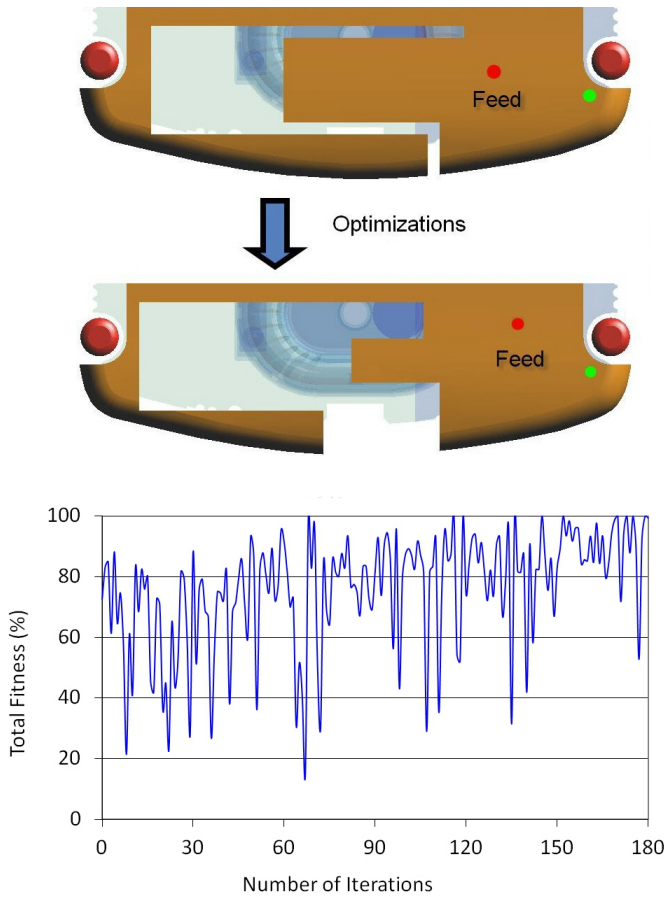


Figure 6.9: The PIFA geometries before and after optimization with the total fitness chart.

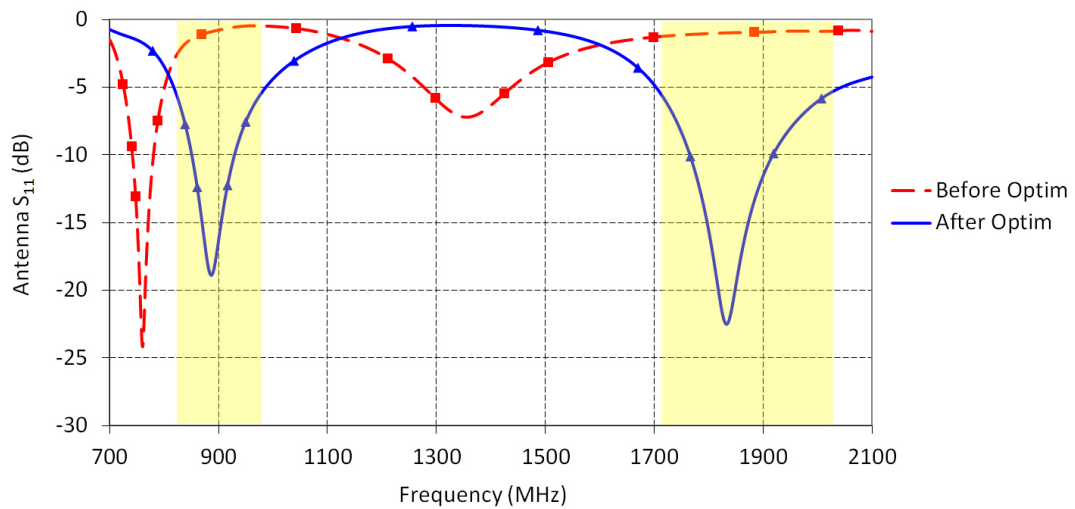


Figure 6.10: The antenna S_{11} of the PIFA design in free space before and after optimization.

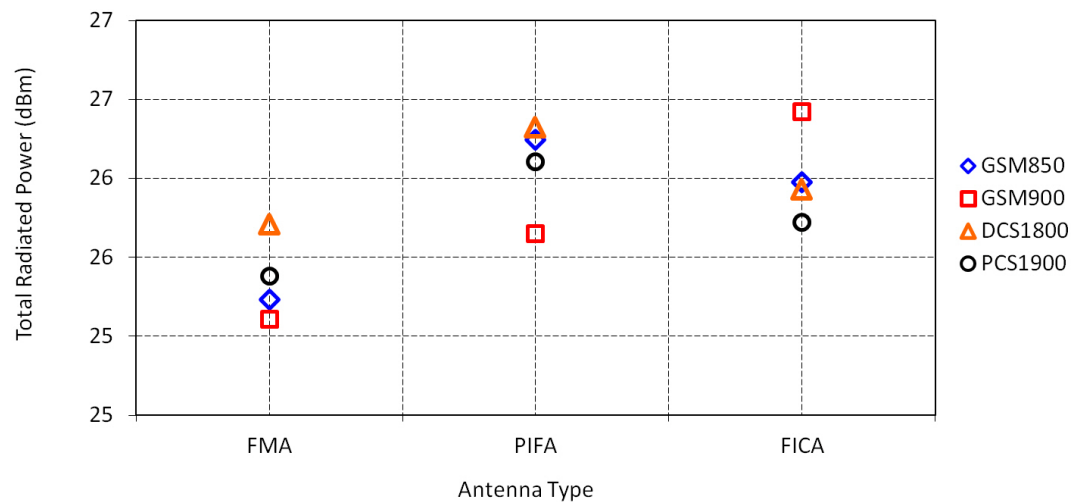


Figure 6.11: The band-averaged total radiated power values of the optimized antennas with SAM head phantom only.

6.5.2 Radiation Performance with Head and Hand Phantoms

Frequency detuning often occurs for the antenna S_{11} when a mobile phone is held in an user's hand and placed next to the ear. The antenna geometries optimized in the free space condition are simulated with the SAM head and CTIA-compliant hand phantoms to evaluate the amount of frequency detuning. Only the right-hand-side head-and-hand phantom placement is investigated in this study. The band-averaged TRP values for the SAM head phantom alone and the SAM head with hand phantoms are presented in Figures 6.11 and 6.12, respectively. The degree of frequency detuning and the amount of power absorption vary for each antenna design under the SAM head phantom loading condition. The PIFA design is selected to demonstrate the optimization for the head-and-hand phantom loading condition, targeting

Chapter 6. Mobile Device Antenna Optimization with Genetic Algorithms

the same S_{11} goal and optimum head-and-hand phantom TRP. By initializing the optimization with the optimized antenna parameter values obtained in the free space case, the parameter sweep range is reduced, hence allowing a shorter optimization convergence time. Upon the completion of optimization, the frequency detuning effect is rectified as shown in Figure 6.13. The antenna band-averaged TRP under the head-and-hand phantom loading condition enjoys an increase of up to 3 dBm for the GSM bands.

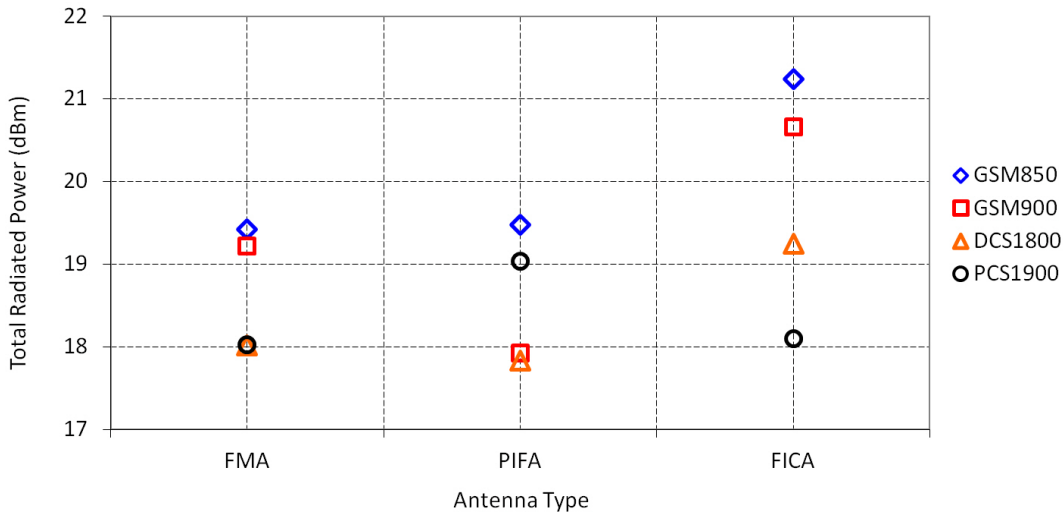


Figure 6.12: The band-averaged total radiated power values of the optimized antennas with head-and-hand phantom loading.

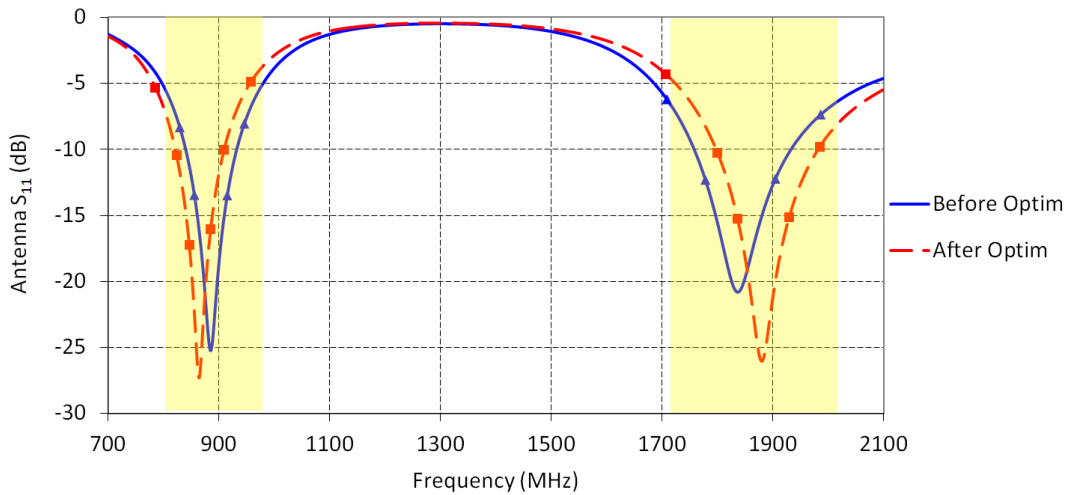


Figure 6.13: The antenna S_{11} optimized against head-and-hand phantom frequency detuning for the PIFA design.

6.5.3 Specific Absorption Rate (SAR)

As mandated by the safety compliance for mobile phones, the Specific Absorption Rate (SAR), defined as the rate at which energy is absorbed by the body when exposed to a radio frequency (RF) electromagnetic field, is investigated for each optimized antenna design. The employed mobile phone has an approximate size of 49 mm × 117 mm × 11 mm. This thin phone profile brings the main current carrying components (e.g., the antenna element and PCB) close to the user's head. This could lead to a high SAR level as the absorption of RF energy in lossy biological tissues is directly associated with the current distribution of the excitation source [126]. The optimized antenna geometries which provide the lowest SAR values are selected for comparison. The peak SAR values for the GSM900 and DCS1800 bands, averaged in a volume of one gram of tissue according to the specification provided in [114], are normalized to the conducted powers which are required to achieve equal TRP performance under the head-only phantom loading condition and are presented in Figure 6.14.

The FMA design exhibits higher SAR in the GSM900 band compared to the PIFA and FICA designs. As shown in Figure 6.15, the magnetic field distributions at 849 MHz (a frequency point in the first transit band of GSM900) of the three antenna designs reveals higher current concentration near the antenna element for the FMA design. The SAR hot spots (the red-color squares) for all three designs are found near the navigation keypad region, where the mobile phone touches the head phantom. These simulation results indicate that the choice of antenna design presents a high impact on the resultant SAR performance. To reduce the SAR value of a mobile phone, a variety of device parameters such as antenna location, phone length and width, shielding and grounding of components, should be taken into consideration.

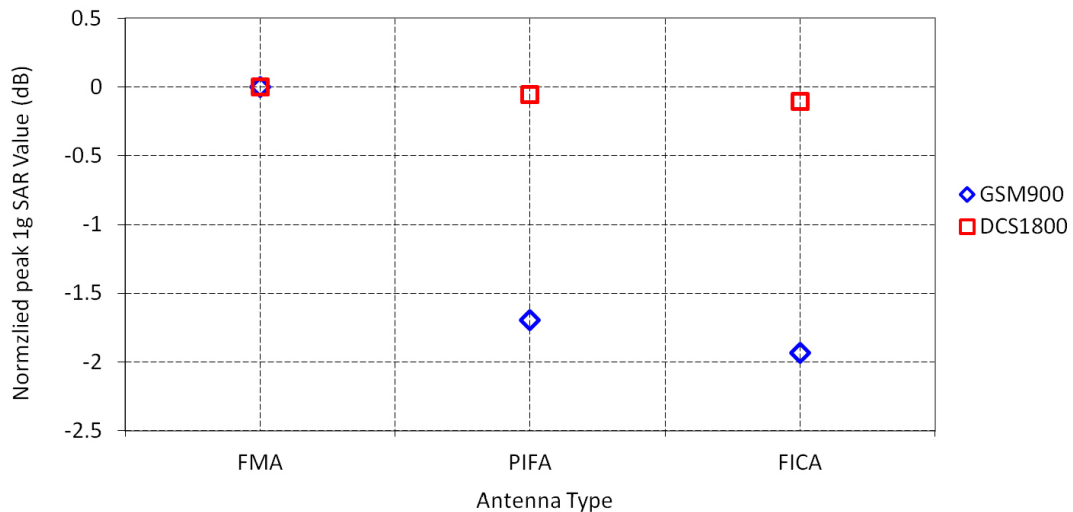


Figure 6.14: The peak 1-gram SAR values normalized to the conducted powers for equal total radiated power under the SAM head phantom loading condition for the GSM900 and DCS1800 bands.

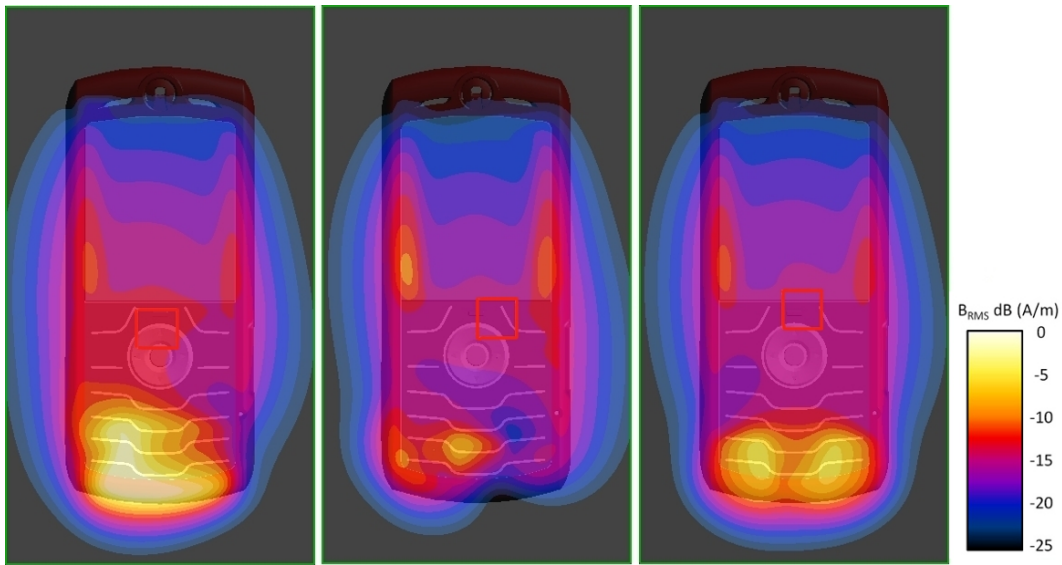


Figure 6.15: The magnetic field distributions extracted at the frontal (keypad side) phone surface at 849 MHz for the FMA (left), PIFA (center) and FICA (right) under the SAM head phantom loading condition; the red-color squares indicate the SAR hot spot locations.

6.5.4 Hearing Aid Compatibility (HAC)

For hearing aid users, a transmitting mobile phone can cause annoying buzz noise in the hearing aid unit due to the lower order harmonics generated by a pulse-like modulation scheme employed by some communication systems (e.g., the Global System for Mobile Communications, GSM). To reduce the possible interference from a mobile phone to a hearing aid device, a compatibility standard known as the Hearing Aid Compatibility (HAC) [115] is proposed to limit the electromagnetic field intensity generated by a mobile phone. Since the introduction of the HAC requirement by the U.S. Federal Communications Commission (FCC) in 2003, mobile phone manufacturers are mandated to deliver a certain number of HAC-compliant phone models to the U.S. market per annum. The HAC standard puts a threshold on the near fields generated by mobile devices due to the potential electromagnetic compatibility (EMC) problems between hearing aids and mobile devices. The electric and magnetic fields are measured on a $5\text{ cm} \times 5\text{ cm}$ area (HAC area), located 1.5 cm above and centered over the mobile phone speaker point. The HAC area is divided into nine grids, and three contiguous outer grids with the highest field strength can be excluded. The center sub-grid and three contiguous outer grids which are not excluded must be common between the electric and magnetic field measurements. The HAC rating given to a mobile phone is based on the worst score across air interfaces, frequency bands, and channels.

The optimized antenna geometries which provide the lowest HAC field intensity values are selected for comparison. The electric and magnetic fields (on the HAC area) of the investigated antennas at 849 MHz and 1910 MHz are presented in Figures 6.16 and 6.17, respectively. For the GSM900 band, the HAC field distributions are similar in all three antenna designs. A

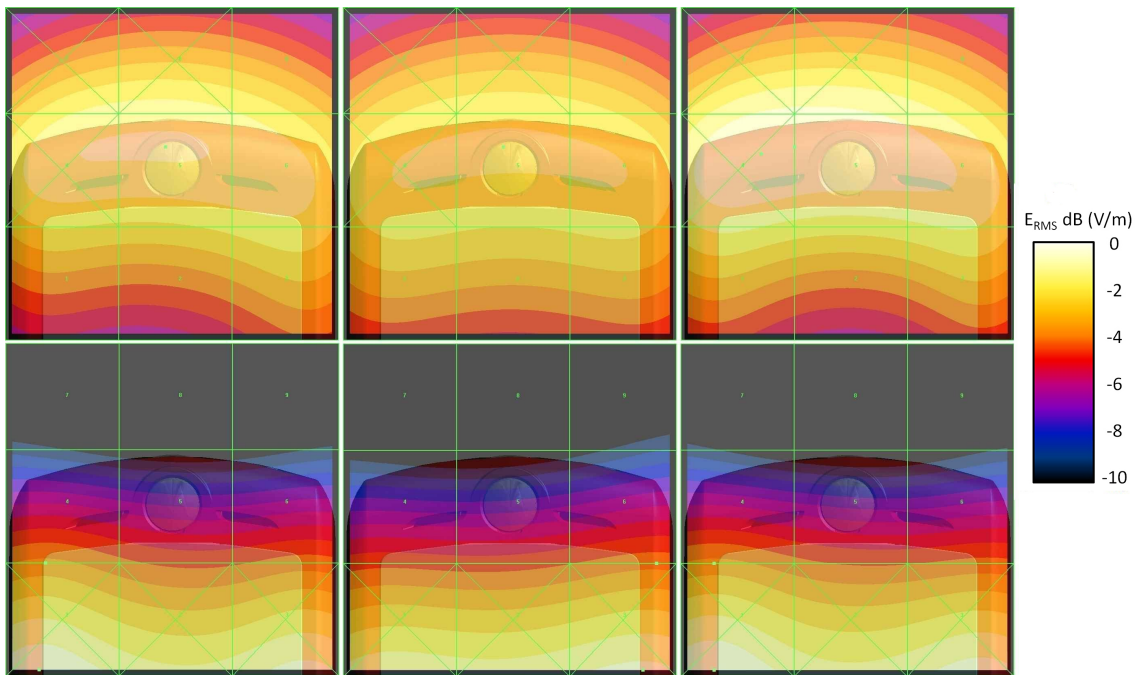


Figure 6.16: The HAC electric (upper row) and magnetic (lower row) field distributions at 849 MHz for the FMA (left), PIFA (center) and FICA (right).

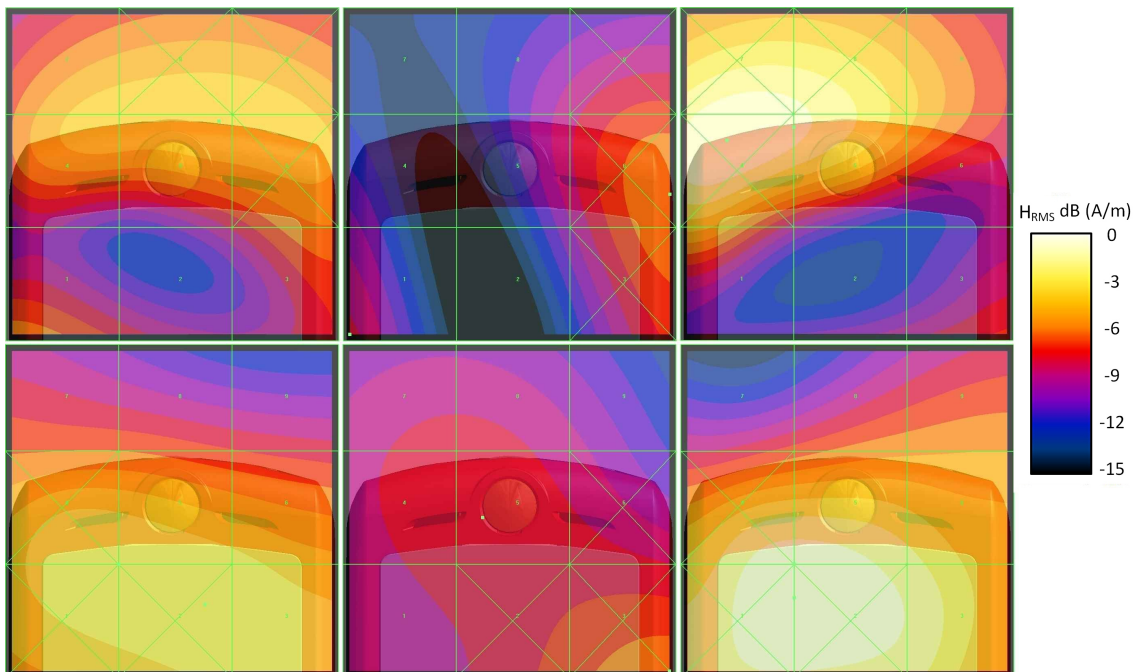


Figure 6.17: The HAC electric (upper row) and magnetic (lower row) field distributions at 1910 MHz for the FMA (left), PIFA (center) and FICA (right).

high electric field distribution is observed in the central grid, which is located near the PCB edge where low current and high voltages are present. In contrast, HAC distribution patterns vary significantly among different antenna designs for the DCS1800 band. This is mainly due to the fact that the mobile phone ground plane (i.e., the PCB and metal chassis) acts as a quarter-wave radiator element in the low cellular band and the entire phone structure behaves as a half-wave dipole regardless of which antenna element is employed. However in the high cellular band, the antenna element has a greater impact on the current flow excited on the ground plane based on the antenna feed location and the current flow on the antenna patch. As a result, different antenna design leads to distinct HAC patterns. In this study, the PIFA design is found to offer favourable HAC performance in the high cellular band. It should be noted that the current HAC compliance test judges the level of potential interference based on the peak near field intensity generated by a mobile phone in free space. When a phone is placed next to an user's ear, the strong perturbation and absorption of the near field energy can in fact cause higher near field intensity around the ear region (i.e., near the hearing aid device). Hence, a revision of the HAC compliance test is recommended to consider the potential field enhancement due to the presence of user head.

6.5.5 Computation Requirement and Optimization Time

A practical optimization process can be concluded when the first 100% fitness is achieved, in this study the optimization was allowed to continue until all optimum antenna geometries within the predefined parameter range are obtained. The numerical simulations are performed on two workstations each equipped with a NVIDIA Quadro FX5600 GPU acceleration card. The resulting grids for the mobile phone alone contain about 4 million FDTD cells, while the grids for the phone with head and hand phantoms contain around 20 million cells. With GPU acceleration, each broadband simulation (for individual antenna design) can be completed in approximately 15 minutes (phone only) and 25 minutes (phone, head and hand phantoms), respectively. The statistics concerning the computation performance of the optimization is shown in Table 6.2. Based on the respective parametrization settings of the three investigated antenna designs, the numbers of simulations required for a 100% fitness in the free space condition and the head-and-hand loading condition are 100 and 50, approximately. This is equivalent to a total of 22 hours of simulation time.

Table 6.2: Computation settings and optimization time requirement.

	Free Space	Head and Hand
Min. grid size (μm)	250	250
Computation domain	4 million cells	20 million cells
Simulation time	≤ 15 minutes	≤ 25 minutes
Total no. of simulations	100	50
Total simulation time	12 hours	10 hours

6.5.6 Optimization Validation

The GA-optimized PIFA geometry is implemented in an actual prototype of the employed mobile phone design. Due to the numerical uncertainties associated with the component dielectric property and exact device geometry, approximately 5 MHz frequency detuning occurs between the numerical and the physical models. This frequency detuning is rectified by trimming the low-band and high-band radiator arms of the physical model. The adjusted PIFA antenna is measured to obtain band-averaged TRP, peak spatial 1g SAR and HAC rating. A comparison between simulation and measurement data shows approximately $\Delta 0.5$ dBm for TRP, $\Delta 0.2$ W/kg for SAR and same rating (e.g., M4) for HAC. Hence, the GA-optimized antenna structure is proven to be suitable for practical implementation.

6.6 Conclusion

In this chapter, the suitability of virtual prototyping and optimization for a mobile phone antenna system design is investigated. Compared to the traditional development approach, i.e., iterations of cutting and trimming the antenna elements, the FDTD-based simulation software powered with genetic algorithms, GPU acceleration and cluster network parallelization offers an excellent alternative for automated analysis and optimization. Three typical mobile phone multiple-resonant antenna designs are numerically simulated and optimized for the free-space, head-only and head-and-hand operating conditions. The antenna performance with respect to Over the Air (OTA) communication capacity (i.e., the Total Radiated Power, TRP), RF exposure limit (i.e., the Specific Absorption Rate, SAR) and device-to-device EMC (i.e., the Hearing Aid Compatibility, HAC) are optimized and compared among the investigated antenna designs. The computational results reveal that in order to comply with the OTA, SAR and HAC design requirements, the selection of a suitable antenna design with respect to the target mobile device structure can be numerically determined based on the optimized antenna performance.

The design characteristics of each of the investigated antenna structure is evaluated to facilitate the selection of the optimization parameters. The final optimization results show that the antenna of a complex commercial mobile device can be improved with respect to various performance criteria in less than 24 hours; thus reducing substantially the development time and improving the device quality during the development process. Computer-aided optimization is proven to be effective and efficient in terms of cost reduction and design quality, especially considering the increasing complexity of modern mobile phone architectures and the reduced antenna volumes that must cover expanding frequency bands while achieving TRP performance coupled with SAR and HAC compliances.

7 Analysis and Design of Mobile Device Antenna-Speaker Assembly

7.1 Introduction

With the rising trend of slim mobile device form factor, the efficient utilization of available device volume for component packaging becomes essential. By integrating electronic components such as speaker, vibrator, camera and microphone in the vicinity of an antenna element, the antenna volume of a mobile device can be efficiently re-utilized. Among the integrated components, an antenna-speaker combination is often employed [50–53]. Such antenna-speaker integration, however, could lead to various Electromagnetic Compatibility and Interference (EMC, EMI) issues, e.g., severe antenna radiation degradation. As a result, the decoupling of antenna and speaker becomes a critical design requirement for an antenna-speaker assembly in a mobile device. To address this problem, the Radio Frequency (RF) characteristics of an antenna-speaker assembly must be closely analyzed.

In [55–58], antenna systems which incorporate integrated speakers have been studied. The speakers in these studies are often modelled as simplified structures, e.g., floating metallic blocks enclosed by dielectric frames. Such simplification corresponds to an idealistic design scenario in which the speaker model represents an isolated non-resonant structure which leads to antenna impedance mismatch and dielectric/ohmic loss to an antenna system. In a practical product design, antenna-speaker isolation is often a non-trivial task. For instance, a speaker design which works well in a particular antenna-speaker assembly (i.e., causes negligible performance issues) could lead to significant performance degradation in another assembly design. An additional practical issue is that mobile device manufacturers generally require multiple component supply sources. While speakers provided by different suppliers may exhibit very similar acoustic performance, they can be drastically different in terms of their RF characteristics. This could lead to inconsistency in antenna radiation performance. To overcome the aforementioned design pitfalls, it is imperative to gain the insights of antenna-speaker interaction mechanisms and provide clear design guidelines to address the EMC and EMI issues.

A preliminary study of speaker RF resonance and its impact to antenna radiation performance has been reported by us in [127]. In that study, the antenna radiation efficiency and speaker resonance for the assembly of a single-resonant monopole antenna and a speaker were investigated. As a follow-up study, both simplified and detailed antenna-speaker assembly models are analyzed in this paper based on numerical simulations and fixture measurements. The detailed Computer-Aided-Design (CAD) speaker model employed in this study was derived from a commercially available speaker design. This paper is organized as follows: first, simplified speaker models are investigated with various single-resonant and dual-resonant antenna designs to address the mutual coupling conditions in an intuitive manner. Next, based on a detailed speaker model and a dual-resonant antenna system, simulations and measurements are performed to analyze and verify the influence of critical design parameters in a realistic design environment. The objective of this study is to provide practical design guidelines to achieve cost-effective antenna-speaker co-existence and optimum antenna radiation performance.

7.2 Background

7.2.1 Moving-Coil Speaker Model

A speaker is essentially an acoustic transducer which converts electrical signals to sound waves. A dynamic moving-coil speaker is investigated in this study. As shown in Figure 7.1, the employed speaker model consists of the following components: a voice coil (i.e., a multi-turn coil), a diaphragm, a permanent magnet, spring contacts, yoke, top-plate and a frame. The voice coil is made of copper (Cu), the frame is made of a plastic material, the permanent magnet is constructed from neodymium magnet (NdFeB) and the yoke and top-plate are made of ferromagnetic materials. In Table 7.1, a list of the RF conductivity and relative dielectric constant values of the speaker components is presented. These values are provided by the component suppliers.

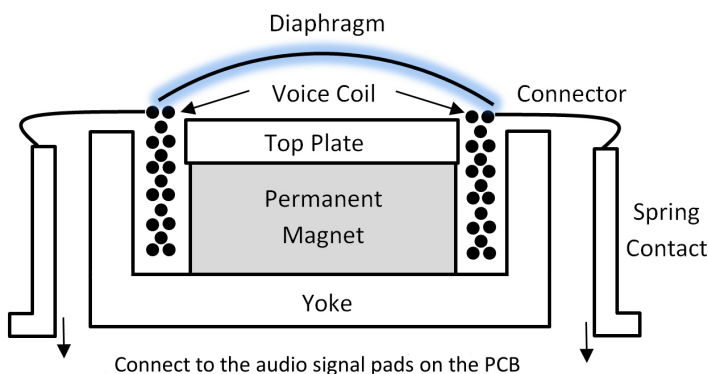


Figure 7.1: The basic structure and components of the investigated moving-coil speaker (components are not drawn to scale and plastic frame is not shown).

Table 7.1: The conductivity (σ) and relative permittivity (ϵ_r) of the speaker components

Component	σ (S/m)	ϵ_r
Voice Coil	5.7×10^7	-
Permanent Magnet	1.9×10^5	-
Top Plate and Yoke	9.3×10^5	-
Spring Contacts	4.7×10^5	-
Frame and Cover	2.0×10^{-3}	2.5

To achieve a desirable audio performance, the voice coil of a speaker is typically designed to resonate at around 700 Hz and has a corresponding resistance of about 7Ω . The voice coil is constructed by winding a long and thin metal wire around the permanent magnet core. The turns of the wire are stacked closely together and the insulation between turns are provided by coating the metal wire with an extremely thin non-conductive layer. The resistance and resonant frequency of the voice coil are mainly determined by wire radius, wire length, number of turns and winding style. For the employed speaker model, the wire radius and wire length are approximately 0.035 mm and 1.5 m.

When an alternating current passes through the voice coil, a time-varying magnetic field is established. This magnetic field interacts with the static magnetic field produced by the permanent magnet and results in a controlled movement of the voice coil. With a piece of light-weight diaphragm supported by the voice coil, the vibration of the flexible diaphragm leads to the production of sound waves. The voice coil ends are connected to two spring contacts which lead to the "audio signal line-in" and the "ground" terminals, respectively. Based on the audio circuitry design and speaker location associated with a particular device platform, audio signal lines which connect the speaker terminals to the audio amplifier are often implemented on a Printed Circuit Board (PCB).

7.2.2 Equivalent Circuit of an Antenna-Speaker Assembly

To illustrate the potential interaction between an antenna and a moving-coil speaker, an equivalent circuit is presented in Figure 7.2. Both the antenna and the speaker are modelled as series-resonant circuits. The quantity R_0 denotes the source resistance, the quantities $R_a(R_s)$, $L_a(L_s)$ and $C_a(C_s)$ are the resistance, inductance and capacitance of the antenna (and speaker), respectively. The equivalent circuit in Fig. 2 bears a close resemblance to the 2-coil inductive link circuit employed in wireless power transmission (WPT) studies [128–130]. However, a fundamental difference is observed in the antenna-speaker circuit: the coupling mechanism is no long limited to the mutual inductance between 2 resonators as in a WPT system. Instead, both free-space coupling (capacitive and inductive), M_{fs} , and conductive coupling (due to physical connections), M_{cond} , can be present. As a result, analytical circuit modelling approach based on the coupled-mode theory [128] or the reflected load theory [129]

cannot be applied without a significant simplification of the coupling mechanisms. In addition, the self-resonance of a practical speaker and the mutual coupling coefficients (M_{fs} , M_{cond}) are functions of the design characteristics (e.g., physical geometry and relative position) of the respective antenna system and speaker model. Therefore, a detailed numerical modelling can provide more insightful information pertaining to the exact coupling mechanisms in a realistic design environment.

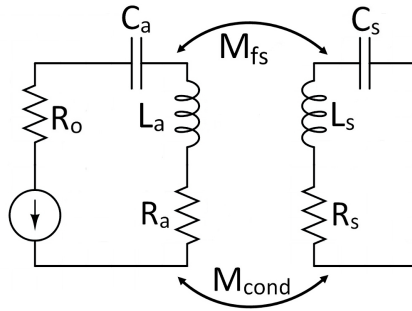


Figure 7.2: The equivalent circuit of a single-resonant antenna-speaker assembly, the mutual couplings are classified as free-space and conductive couplings.

7.2.3 Mutual Coupling and EMC/EMI Issues

In an antenna-speaker assembly, a speaker is typically mounted in an antenna support frame such that the frame also serves as an acoustic chamber. As a result, the distance between the antenna element and the speaker can be extremely close. Such design requirement inherently leads to difficulty in achieving RF isolation. At radio frequency, due to skin effect, proximity effect and parasitic capacitance, a moving-coil speaker becomes a lossy and self-resonant structure. Hence, unlike parasitic elements which are introduced for antenna bandwidth enhancement [131], a speaker exhibits practically no radiation capability at high frequency.

As a speaker is designed to be an audio transducer, its RF characteristics have not been well quantified. Based on practical design observations, several EMC and EMI issues associated with antenna-speaker integration are summarized as follows: (1) In the strong-coupling regime, detuning of antenna impedance match and/or degradation of antenna radiation efficiency could occur. (2) Spurious interference could be coupled through the speaker to the antenna during the RF signal reception stage. This would lead to desensitization (i.e., a reduction of RF receiver radiated sensitivity). (3) The audio performance of a speaker can also be affected by the antenna-speaker coupling. A speaker could pick up unwanted RF energy and produce audible buzz. This is particularly problematic for a mobile communication system which utilizes packet burst transmission, e.g., a Global System for Mobile communications (GSM) system. The aforementioned EMC and EMI issues can be suppressed with a properly devised antenna-speaker integration. In this study, the design objective is focused on the preservation of antenna radiation efficiency.

7.2.4 Existing Design Techniques and Limitations

Various antenna-speaker assembly design techniques have been proposed recently. In [132], decoupling through RF filter is suggested. Prevention of conductive coupling can be achieved by introducing filters at the speaker terminals to block RF energy from entering the voice coil through the PCB ground. The filter configurations include parallel-connected capacitor (i.e., RF bypass), series-connected inductor (i.e., RF block), frequency-selective filter (e.g., tank circuit) and RF ferrite beads. These RF filters can be positioned inside or outside of the speaker box. Caution must be exercised while selecting the appropriate filter components. For instance, a series-connected inductor must exhibit low Direct Current (DC) resistance such that it does not significantly alter the voice coil resistance at the audio frequencies. It should be noted that the filtering technique only addresses conductive coupling issues. However, in a practical design environment, capacitive and inductive coupling could also occur.

A decoupling technique which utilizes variable voice coil connector length is disclosed in [133]. The resonance generated by the speaker, which falls in the mobile device operating frequency range, is identified as the source of antenna performance deterioration. The proposed technique relies on varying the electrical length of the voice coil connector in order to shift the resonance frequency of the speaker. It should be noted that unlike the speaker type described in [133] which utilizes external voice coil connectors, the investigated speaker model employs internal voice coil connectors. This implies that for the latter, the length of the voice coil connector cannot be conveniently varied. To apply the aforementioned design techniques, a prerequisite is the speaker resonance characteristics. Analyses are performed in Sections 7.3 and 7.4 to determine the influence of the voice coil connector length, speaker location and antenna design on the antenna radiation performance and the associated speaker resonance frequency.

7.3 Numerical Analysis of a Simplified Speaker Structure

In this section, the antenna mismatch and radiation performance of an antenna-speaker assembly model is numerically investigated with simplified speaker structures. The analysis is focused on the following design parameters: antenna type, speaker position, voice coil connector length and mutual coupling mechanisms.

7.3.1 CAD Model and Simulation Tool

A Computer-Aided-Design (CAD) speaker model with detailed component dimensions based on a practical moving-coil speaker design is employed in this study. The overall size of the speaker is 18 mm × 13 mm × 5 mm. As shown in Figure 7.3(a), the speaker model is mounted on a single-ground-layer 60 mm × 110 mm × 1 mm FR4 substrate which represents the PCB of a mobile device. The speaker is secured within a support frame with a dimension of 60 mm × 15 mm × 6 mm. The thickness of the frame is 1 mm. The left, center and right speaker

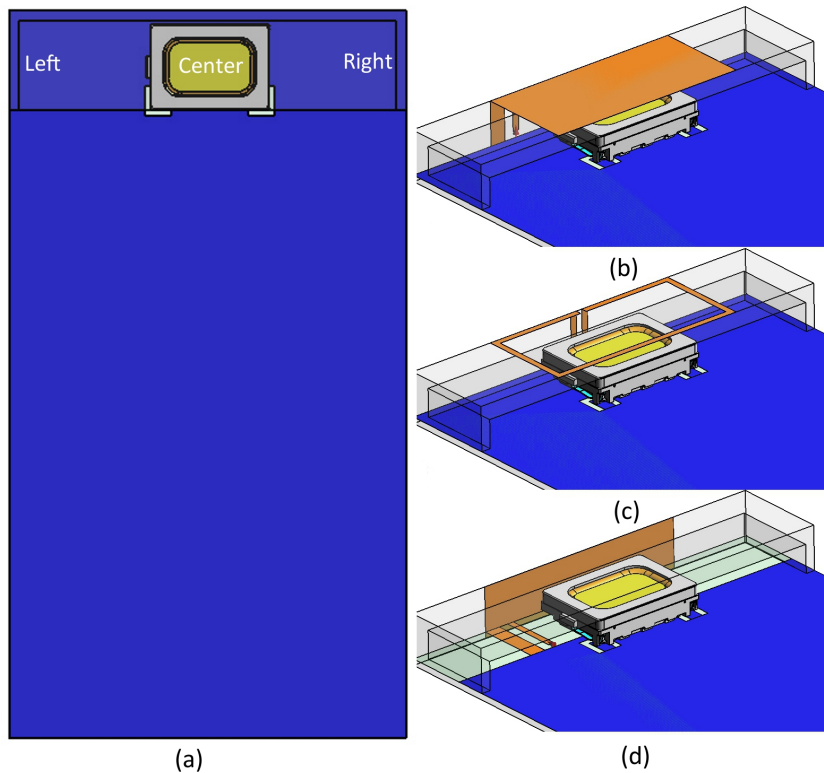


Figure 7.3: (a) A printed circuit board with a center-positioned speaker and an antenna-speaker assembly with (b) a PIFA, (c) a conformal loop antenna and (d) a vertical PIFA, the speaker is conductively-coupled to the PCB ground.

positions are indicated in Fig. 7.3(a) and this orientation definition is applied throughout this study. The material dielectric property values of the speaker components are assumed to be non-dispersive in the investigated frequency range and follow the values listed in Table 7.1. The antenna patch and PCB ground plane are modelled as copper. The material property for the antenna support is the same as the speaker frame. The PCB substrate (FR4) has a relative permittivity value of 4 and a conductivity value of 0.002 S/m.

In this section, the multi-turn voice coil model is replaced by a single-turn loop model. This loop occupies the same overall physical volume as the multi-turn voice coil. Even though the resonance characteristics of a single-turn loop (e.g., resonance frequency, quality factor and ohmic loss) are different from a multi-turn coil, a simplified model can be employed to investigate the coupling mechanisms with minimum computational resource. Five speaker models, namely Speaker 1 to Speaker 5, are employed based on five different voice coil connector lengths. The overall connector length is incrementally reduced from Speaker 1 to Speaker 5 by approximately 6-8 mm from one speaker to the next. Besides the connector length, the remaining components are identical among the speaker models. A Finite Difference Time Domain (FDTD) based commercial electromagnetic computational software SEMCAD-X 14.8 [48] is employed for all the numerical simulations.

7.3.2 Conductively Coupled or Isolated Speaker

In this section, the conductive coupling (M_{cond}) scenario (due to the physical connections between the speaker terminals and PCB ground) and the terminal isolated (M_{fs}) scenario is investigated. As shown in Figure 7.3(b) to 7.3(d), three 1.5 GHz single-resonant antennas mounted on a single-layer PCB are considered. In Figure 7.3(b), a planar inverted-F antenna (PIFA) [134] is employed. The PIFA patch is centred along the width of the antenna support with the feed line on the right and the ground line on the left. A loop antenna with a 1 mm patch width is presented in Fig. 3(c) while a vertically-oriented PIFA with a 10 mm PCB ground clearance is shown in Fig. 3(d). The speaker terminals are either conductively coupled to the PCB ground through the spring contacts or isolated from the PCB. In the isolated case, each spring contact is connected to a 2 mm \times 2 mm floating conductive pad with a 1 mm gap clearance from the PCB ground. The input resistance of an audio signal line-in terminal is typically around 10 Ω , in this study, 0 Ω (i.e., short-circuit to the ground) is assumed when the conductively-coupled scenario is investigated. In addition, the resistance and electric delay introduced by the audio signal lines are neglected, i.e., the speaker spring contacts are assumed to be directly connected to the respective audio circuitry terminals.

As shown in Figure 7.4(a), a terminal-isolated center-positioned speaker leads to about 50 MHz frequency detuning for the PIFA antenna. Negligible radiation loss ($\approx 5\%$) is observed in the isolated case. With a conductively-coupled speaker, the PIFA antenna mismatch becomes more severe (see Fig. 4(b)). This indicates a stronger coupling between the antenna and speaker. Furthermore, a parasitic resonance occurs near the antenna resonance in the conductively-coupled case. The parasitic resonant frequency behaves as a function of the voice coil connector length. The shorter the connector length, the higher the resonance. For the loop antenna, parasitic resonances similar to the PIFA case are observed at approximately the same frequency locations while the antenna mismatch becomes less severe due to the reduced antenna-speaker overlap area. For the vertical PIFA, the parasitic resonance frequency is shifted significantly compared to the PIFA and loop antennas. The computational results indicate that with a terminal-isolated speaker, no parasitic resonance or radiation degradation occurs in the investigated frequency range (i.e., M_{fs} is negligible). With a conductively-coupled speaker, the parasitic resonance frequency can be tuned by varying the voice coil connector length or the antenna design.

In Figure 7.5(a) and Figure 7.6(a), the antenna radiation efficiency of the PIFA and vertical PIFA designs with a center-positioned conductively-coupled speaker are presented. The speaker input reactance at the left terminal (with the right terminal grounded to the PCB and the antenna feed terminated at 50 Ω) are shown in Fig. 5(b) and Fig. 6(b), respectively. The loop antenna case is not presented because the results are practically the same as the PIFA case. From the efficiency and reactance plots, it is observed that when a series resonance occurs at the speaker terminal, a significant deterioration of antenna radiation efficiency ($\approx 70\text{-}90\%$) is encountered near the speaker resonance frequency. It should be noted that this resonance frequency is different from the self-resonance frequency of a speaker structure (which is

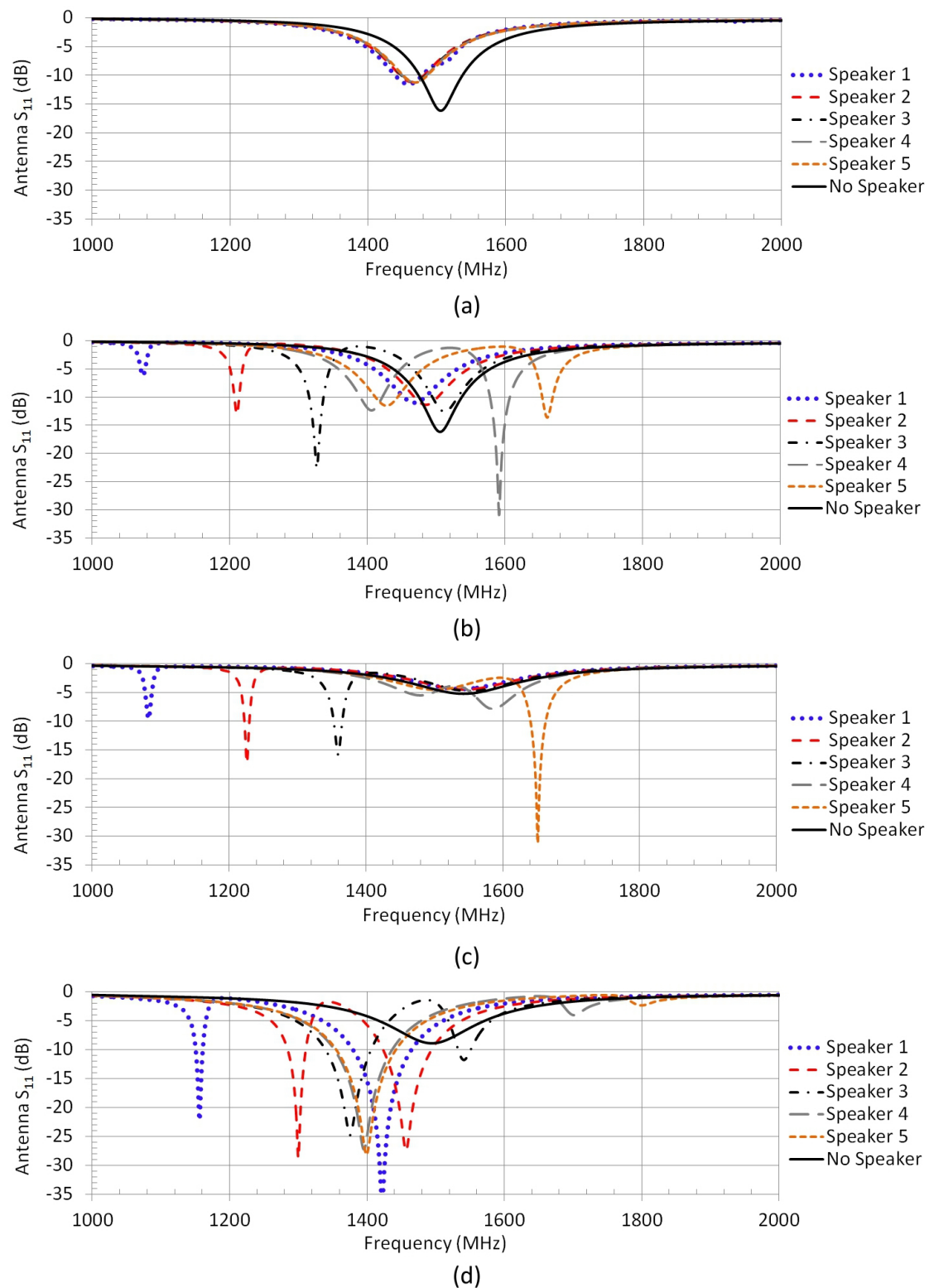


Figure 7.4: The antenna S_{11} for (a) PIFA with a center-positioned terminal-isolated speaker, and (b) PIFA, (c) loop antenna and (d) vertical PIFA, each with a center-positioned conductively-coupled speaker.

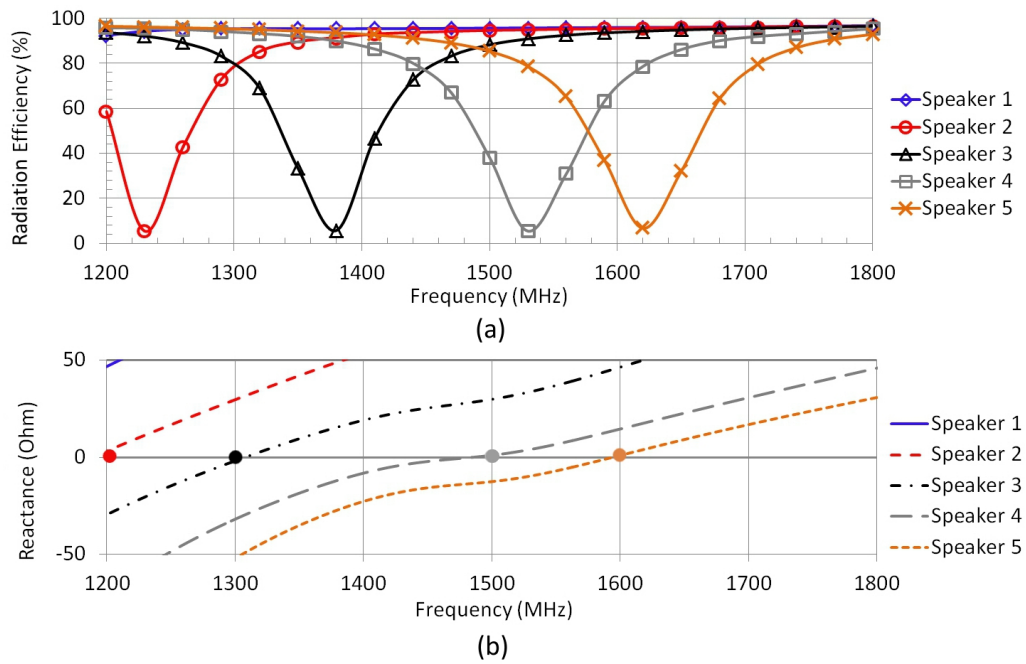


Figure 7.5: (a) The radiation efficiency of the PIFA with a center-positioned conductively-coupled speaker and (b) the voice coil reactance of the respective speaker.

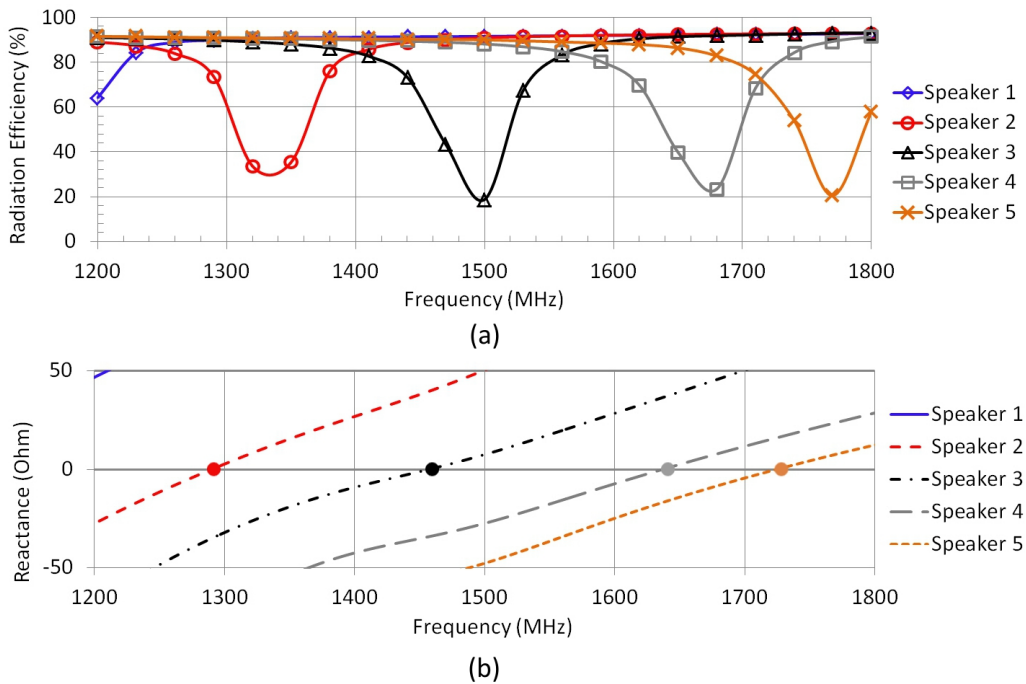


Figure 7.6: (a) The radiation efficiency of the vertical PIFA with a center-positioned conductively-coupled speaker and (b) the voice coil reactance of the respective speaker.

independent of the source of excitation). Unlike a two-port configuration where parameters such as the coupling coefficient (e.g., S_{21}) can be employed as a figure of merit for coupling and isolation, an antenna-speaker assembly is a one-port device which provides no clear port definition for the speaker terminals. Hence, the conductively-coupled speaker resonance in this study is approximated by the input impedance at one excited speaker terminal while keeping the other terminal at PCB ground potential.

7.3.3 Capacitively Coupled Speaker

In this section, two dual-resonant antenna designs and a dual-ground-layer PCB are employed to represent a more practical design environment. As shown in Figure 7.7 and Figure 7.8, dual-resonant (i.e., 820-960 MHz, 1719-1990 MHz, $S_{11} \leq -5\text{dB}$) PIFA and Folded Inverted Conformal Antenna (FICA)[135], are considered. The two PCB ground layers are electrically connected through multiple vias. The simulations of the conductively-coupled speaker scenario yield similar results as the single-resonant antenna case, i.e., antenna radiation deterioration occurs near the parasitic resonance frequency. The investigation is extended to a capacitively-coupled speaker case in which the speaker-PCB configuration is similar to the terminal-isolated case except that a capacitive coupling exists between the lower PCB ground and the speaker pads. This coupling structure corresponds to a practical design scenario in which the ground plane beneath the speaker terminals cannot be removed due to certain design constraints (e.g., an electronic component which requires shielding or grounding is mounted on the opposite side of the PCB directly below the speaker terminals).

In the capacitively-coupled case, one speaker model (Speaker 1) and three speaker locations (center, left and right) are investigated. As shown in Figure 7.8(b), a capacitively-coupled speaker is also capable of introducing noticeable parasitic resonance in the antenna S_{11} . On the other hand, a parasitic resonance could merge with the antenna resonance and become unnoticeable from the antenna S_{11} (see Figure 7.7(b)). It is observed that the low-band (820-960 MHz) antenna radiation efficiency is negligibly affected by the speaker. The high-band (1710-1990 MHz) radiation efficiency is affected under specific coupling conditions. The high-band radiation efficiency due to different coupling conditions and speaker locations are presented in Figure 7.7(c) and Figure 7.8(c). In the PIFA case, significant radiation deterioration occurs with the left-positioned capacitively-coupled speaker while in the FICA case, deterioration occurs when a capacitively-coupled speaker is center-positioned. This indicates that, similar to the conductively-coupled case, a capacitively-coupled speaker is capable of achieving parasitic resonance and causing significant radiation degradation to an antenna system. The speaker resonance frequency is dependent on the antenna-speaker assembly configurations, e.g., speaker position, PCB layout and antenna structure. The simulations of the other four speaker models (Speaker 2 to Speaker 5) reveal that varying the voice coil connector length has the same frequency-shift effect on the speaker resonance as the conductively-coupled case.

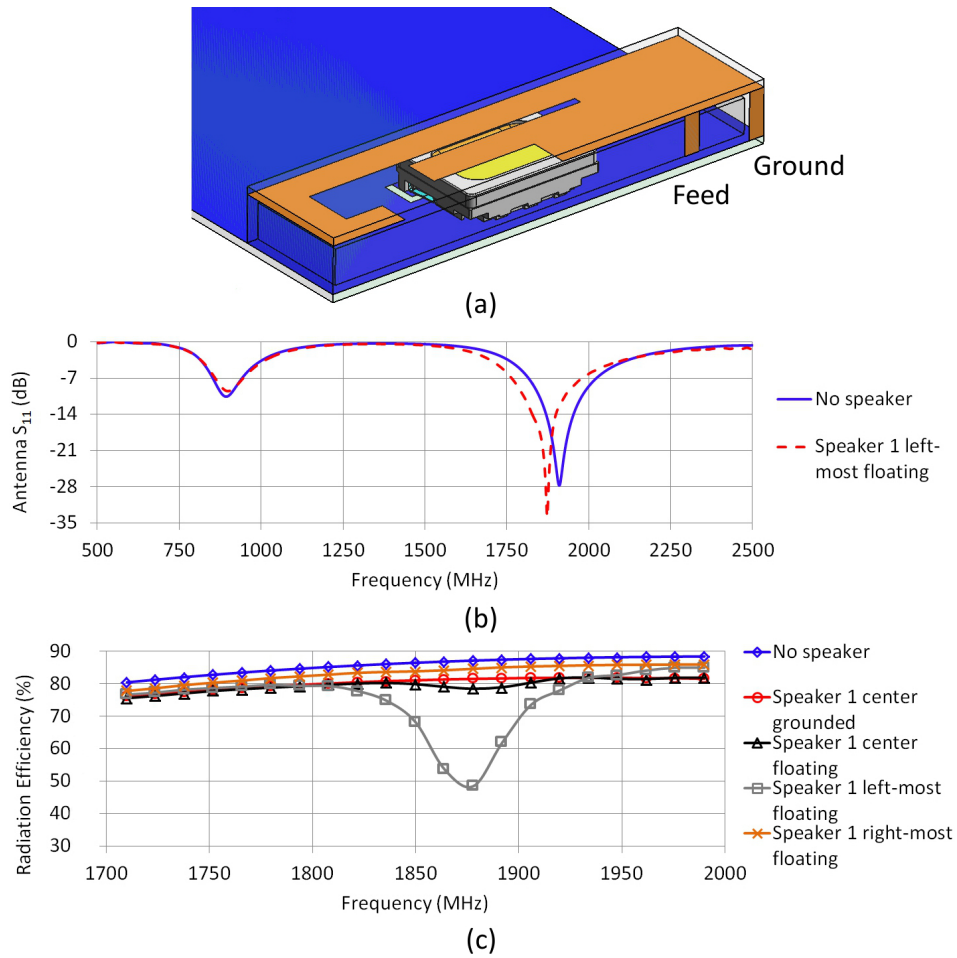


Figure 7.7: (a) The dual-band PIFA antenna with a center-positioned speaker, (b) PIFA antenna S_{11} and (c) antenna radiation efficiency due to a conductively-coupled (grounded) or a capacitively-coupled (floating) speaker.

To analyze the mechanisms behind an antenna radiation degradation, the near-field distributions of the FICA antenna system are investigated. In Figure 7.9 and Figure 7.10, the slice views of the peak root-mean-square (RMS) electric field (E-field) and magnetic field (H-field) distributions of the FICA antenna at 1875 MHz are presented for the capacitively-coupled and conductively-coupled cases, respectively. The frequency 1875 MHz is selected because a significant radiation degradation is observed (see Figure 7.8(c)) at this frequency point. As shown in Figure 7.9, the peak E-field in the capacitively-coupled case occurs at the speaker terminals and within the speaker box while the peak E-field in the conductively-coupled case appears on the FICA antenna element. This shows that RF energy is coupled through the speaker pads from the PCB ground to the speaker when capacitive coupling is present at the speaker terminals. Similarly, as shown in Fig. 10, the peak H-field is observed around the voice coil in the capacitively-coupled case while a H-field distribution equivalent to the case of no speaker presence occurs in the conductively-coupled case.

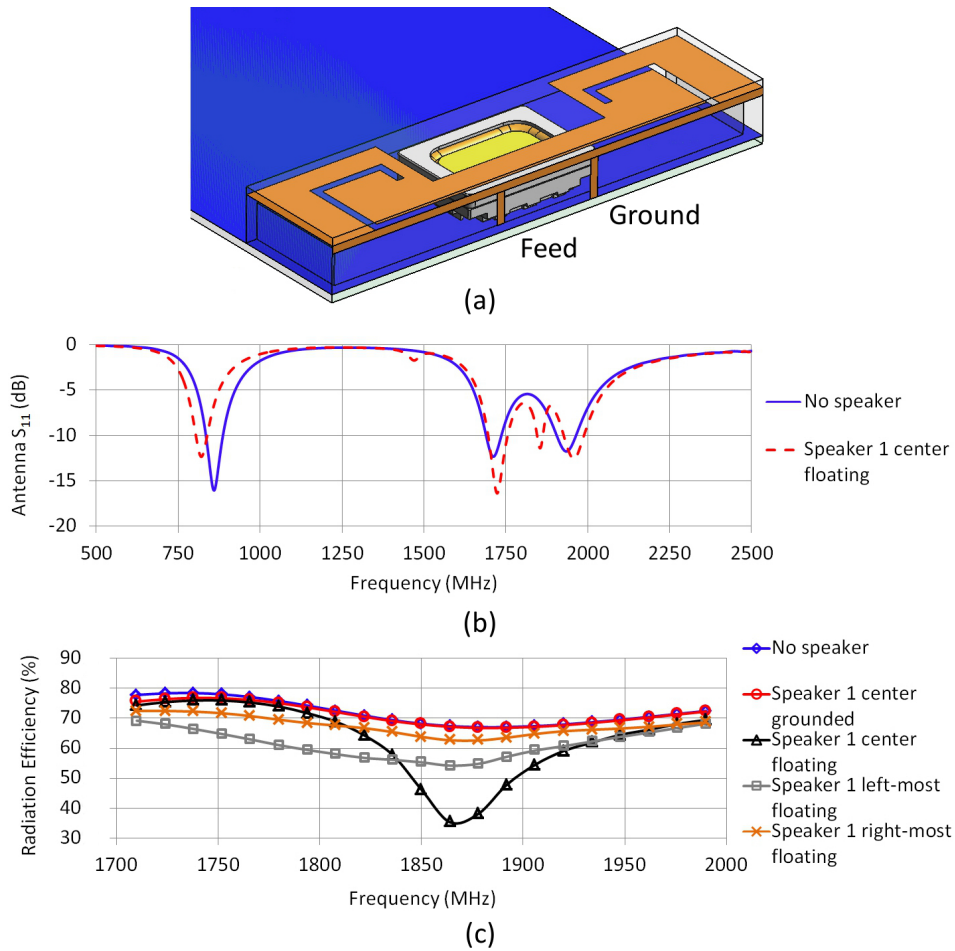


Figure 7.8: (a) The dual-band FICA antenna with a center-positioned speaker, (b) FICA antenna S_{11} and (c) antenna radiation efficiency due to a conductively-coupled (grounded) or a capacitively-coupled (floating) speaker.

Compared to the conductively-coupled case, the peak RMS field value in the capacitively-coupled case is 15 dB higher for the E-field and 18 dB higher for the H-field, respectively. The enhancement of near field intensity serves as a clear indication of strong mutual coupling and the presence of speaker resonance. At 1875 MHz, the total time-averaged stored energy in the FICA antenna system with a center-positioned capacitively-coupled speaker is 6 dB higher than the conductively-coupled speaker case. This indicates that a resonant speaker disrupts the near fields of an antenna system by causing significant field concentration within the speaker structure. The energy stored in the speaker becomes part of the non-radiative energy which “suck up” the RF energy that could potentially be radiated away by the antenna. In addition, the increase of the dielectric and ohmic loss in the speaker components also contributes to radiation degradation.

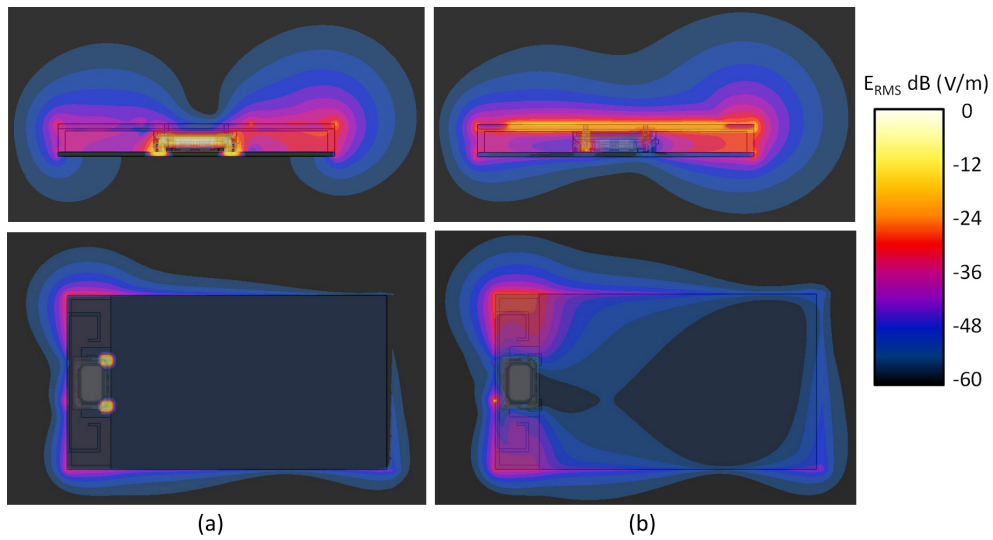


Figure 7.9: The RMS E-field distributions of the FICA at 1875 MHz with a center-positioned (a) capacitively-coupled speaker and (b) conductively-coupled speaker, the E-field values are normalized to the peak value in the capacitively-coupled case.

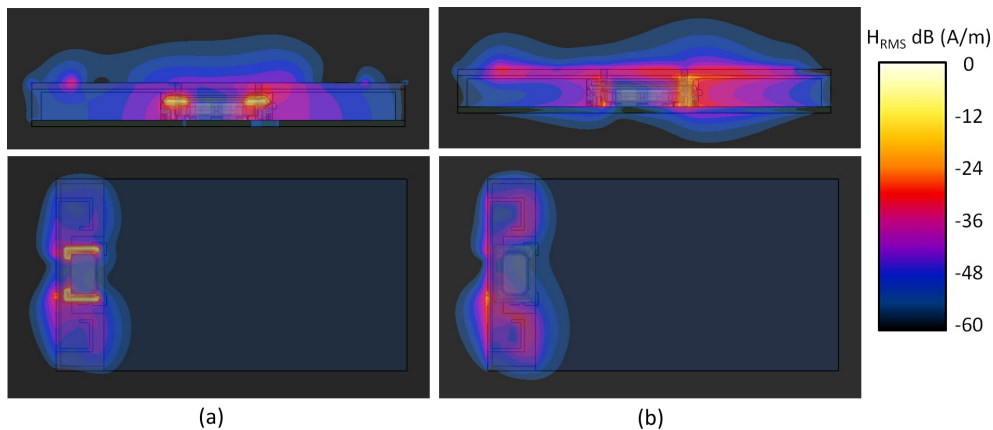


Figure 7.10: The RMS H-field distributions of the FICA at 1875 MHz with a center-positioned (a) capacitively-coupled speaker and (b) conductively-coupled speaker, the H-field values are normalized to the peak value in the capacitively-coupled case.

7.4 Investigation of a Practical Antenna-Speaker Assembly

In this section, a detailed speaker model (with multi-turn voice coil) based on a practical speaker design is first investigated through numerical simulations. Next, prototypes of a PIFA-speaker assembly are constructed by incorporating speakers with different voice coil connector lengths and positions. The antenna radiation efficiency and speaker impedance of these fixtures are measured to validate the findings from the simulation results.

7.4.1 Numerical Simulation of a PIFA-Speaker Assembly

As shown in Figure 7.11(a), a dual-resonant PIFA antenna is simulated with a detailed speaker CAD model. Instead of the simplified single-turn loop employed in the previous section, a multi-turn voice coil (44 turns, 0.035 mm wire radius and 1.5 m long) is modelled. The conductively-coupled and terminal-isolated cases are simulated with respect to the center, left and right speaker positions (see Figure 7.3(a)). The simulated antenna S_{11} , radiation efficiency and speaker impedance are presented in Figure 7.12. In Figure 7.12(a), it is observed that the amount of antenna frequency detuning is associated with the relative position of the speaker. For instance, less high-band resonance shift occurs when the speaker is right-positioned (i.e., closer to low-band arm and away from high-band arm). In Figure 7.12(b), the antenna radiation efficiency curves confirm that a variable speaker location corresponds to a tunable coupling between the antenna and the speaker. The impedance of a center-positioned conductively-coupled speaker extracted at the left speaker terminal is shown in Figure 7.12(c). Two series speaker resonances occur within the antenna operating frequency bands; one at around 1000 MHz and another one at around 1900 MHz. With reference to the radiation efficiency curves, it is clear that a series speaker resonance, by itself, does not warrant radiation degradation. A strong mutual coupling (M_{fs} , M_{cond}) serves as an additional criterion. To predict radiation deterioration prior to a radiation efficiency assessment, the antenna input impedance should be analyzed. As shown in Fig. 12(d), the variation of the PIFA input impedance occurs only in the high frequency band; this serves as an indication of potential radiation efficiency degradation due to a strong antenna-speaker near-field interaction.

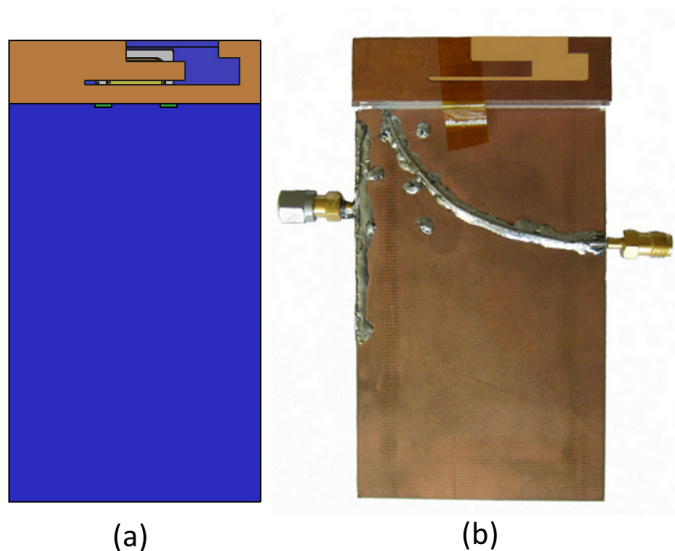


Figure 7.11: (a) The CAD model of a PIFA-speaker assembly for numerical simulation and (b) the corresponding physical model.

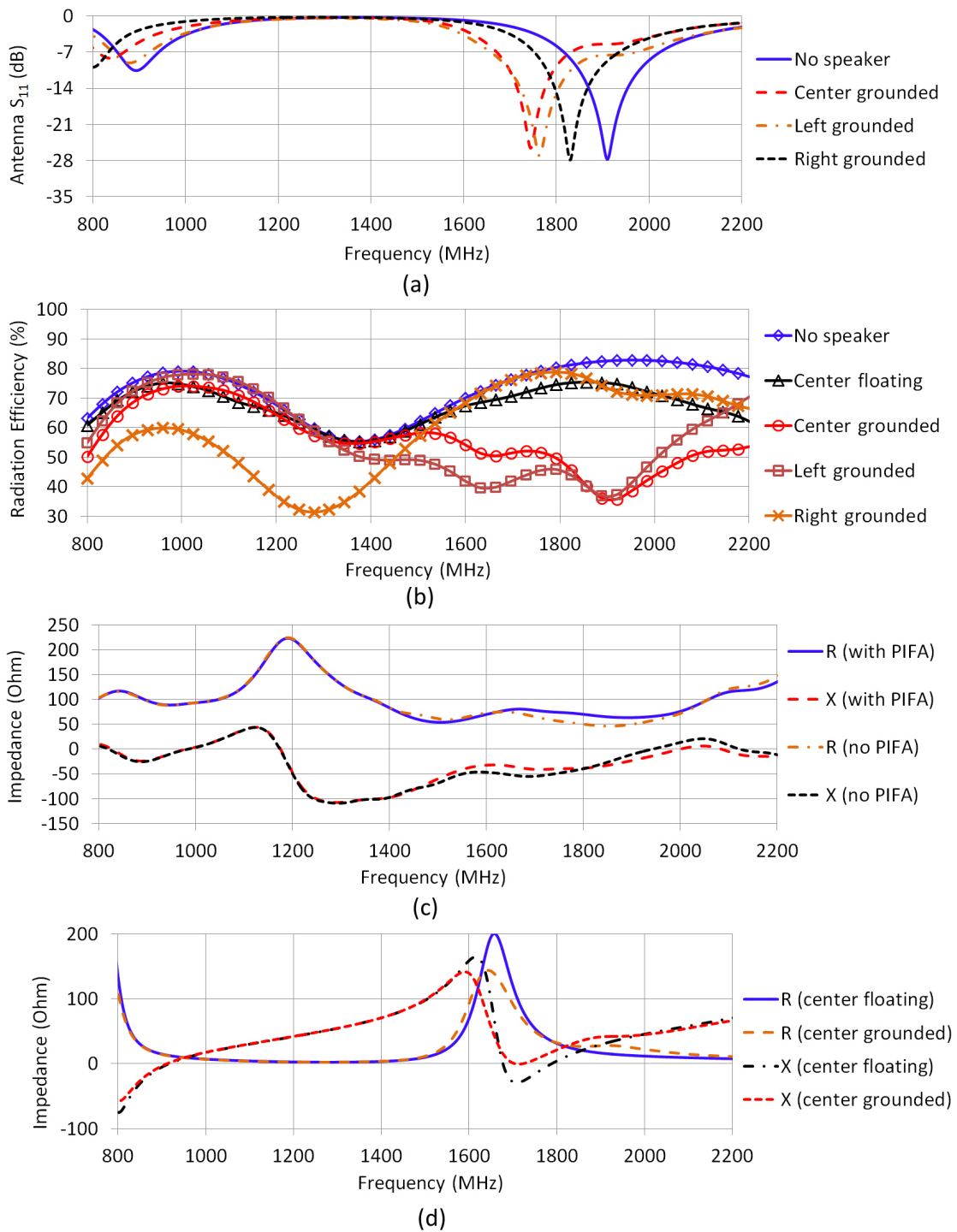


Figure 7.12: The simulation results of (a) PIFA S_{11} , (b) PIFA radiation efficiency, (c) speaker impedance (R for resistance, X for reactance) and (d) PIFA input impedance with a center-positioned terminal-isolated (floating) or conductively-coupled (grounded) speaker.

7.4.2 Measurement of a PIFA-Speaker Assembly

As shown in Figure 7.11(b), the PIFA-speaker assembly model simulated in the previous section is realized as a prototype fixture. Due to the complexity of a practical speaker structure and the uncertainties associated with speaker component material dielectric properties, a frequency shift between the simulated and measured results is expected [127]. As a result, the measurements performed in this section aim at validating the trend of design characteristic observed in the simulation results, instead of verifying the accuracy of the simulated models. The antenna radiation efficiency with a conductively-coupled speaker and the corresponding speaker impedance are measured. Five speaker designs (Speaker A to Speaker E), with voice coil connector length variation similar to the simulated speaker models (Speaker 1 to Speaker 5), are employed. The speaker impedance measurement is performed on the left speaker terminal with the right terminal short-circuited to the PCB ground and the antenna feed terminated with a 50Ω load. Three antenna support frames are constructed such that a speaker can be fixed within the antenna chamber at the center, left and right positions.

The measurement results indicate that when a speaker is terminal-isolated, antenna radiation performance varies only slightly ($\approx 10\%$) among the different speaker models and locations. Negligible radiation degradation is observed when compared to the antenna-only radiation efficiency. In Figure 7.13, the antenna radiation efficiency with the center- and right-positioned conductively-coupled speakers are presented. The effects of the voice coil connector length and speaker location become prominent in the conductively-coupled case. Significant efficiency degradation occurs with the center-positioned Speaker C and Speaker D in the high band when compared to the other speaker models. As shown in Figure 7.14, the degradation in the high band becomes even more pronounced for the left-positioned Speaker C and Speaker D. In addition, a parasitic resonance is observed in the antenna S_{11} as shown in Figure 7.14(a), similar to cases shown in Figure 7.4 and Figure 7.8. This indicates a stronger mutual coupling for the left-positioned case. It is due to the fact that the antenna feed and ground are located on the left side of the structure. Hence, this region becomes the high current and low impedance region. A conductively-coupled resonant speaker positioned within a high current region will have the tendency to couple more RF energy.

The speaker reactance curves shown in Figure 7.14(d) indicate a gradual shift of the resonance frequency towards the antenna operating frequency band (1710-1990 MHz), this corresponds to the simulation results shown in Figure 7.5 and Figure 7.6. In addition, it is observed that unlike the simplified single-loop case, the variation of the voice coil connector length does not shift the resonance frequency in a predictable manner for the multi-turn voice coil. For instance, the resonance frequencies of Speaker C and Speaker D are almost identical despite a 6 mm overall difference in the connector length. This serves as a clear indication that a simplified voice coil model could not predict the impedance transformation of a complex multi-turn coil. The measurement results of the PIFA-speaker assembly confirm the effects of speaker location and voice coil connector length observed in the simulation results. Furthermore, the measurement results indicate that optimum antenna performance can be achieved even

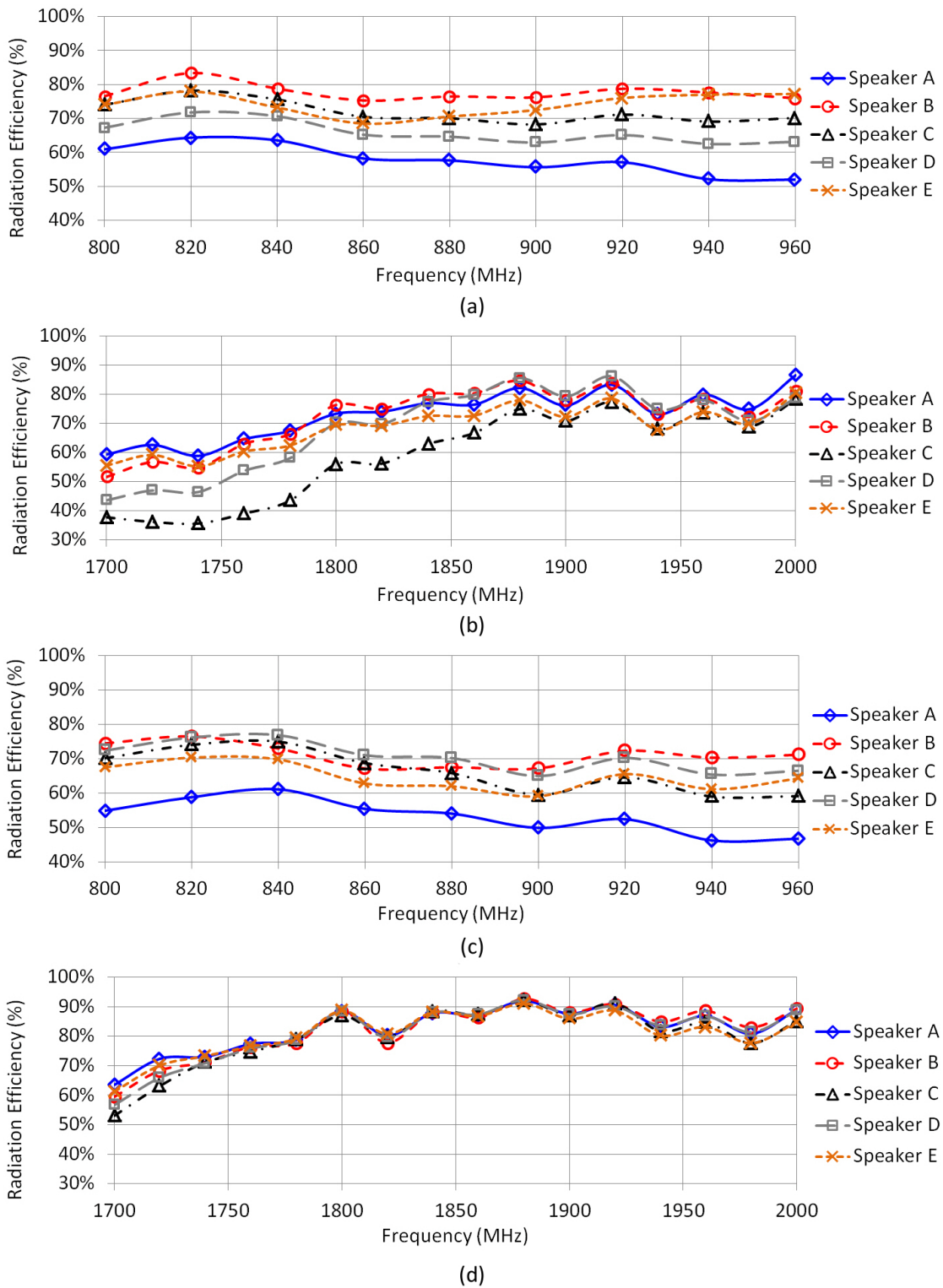


Figure 7.13: The measurement results of PIFA radiation efficiency with a center-positioned conductively-coupled speaker for (a) low band, (b) high band and with a right-positioned conductively-coupled speaker for (c) low band and (d) high band.

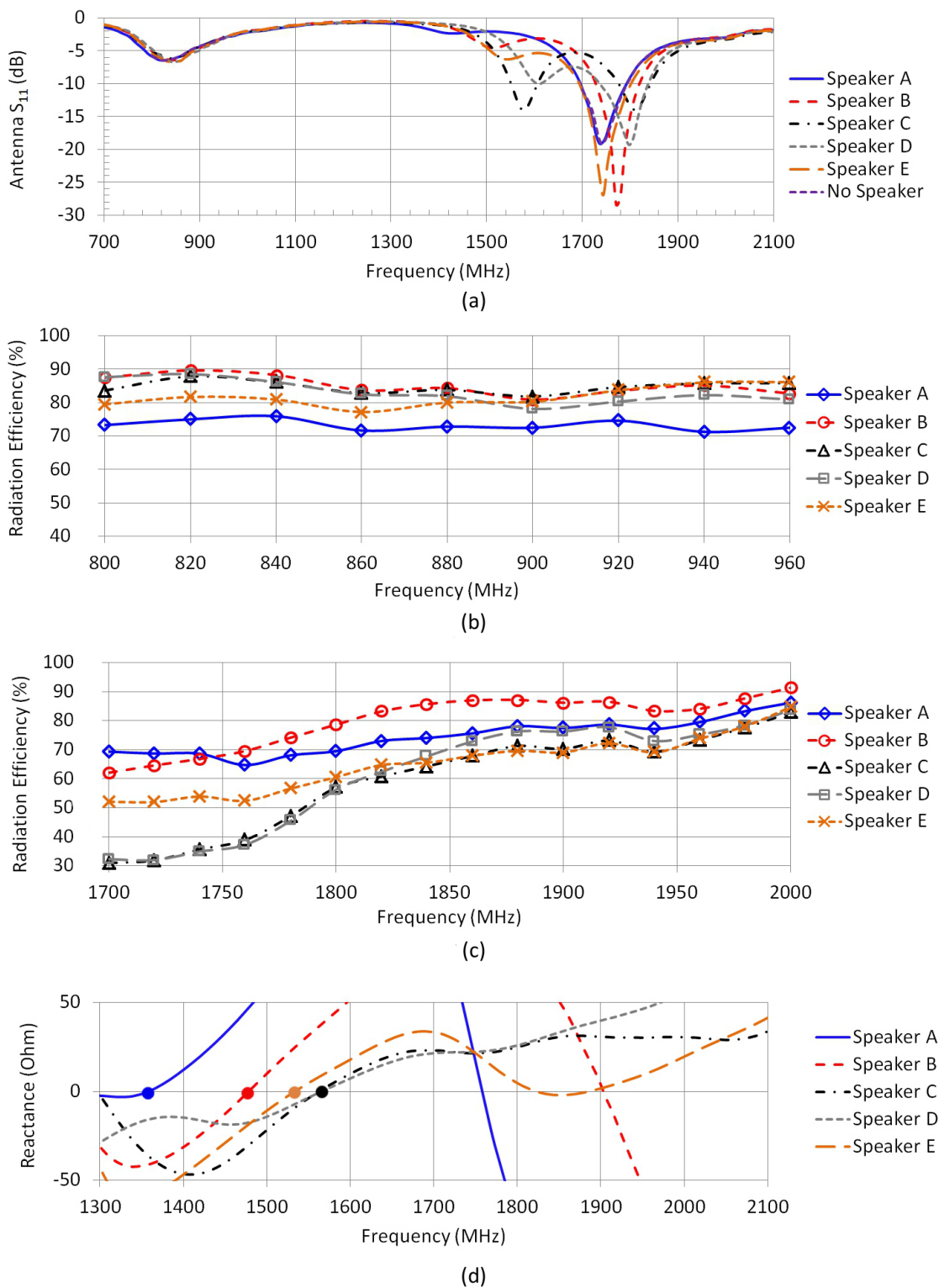


Figure 7.14: The measurement results of (a) PIFA S_{11} , (b) PIFA radiation efficiency for the low band, (c) PIFA radiation efficiency for the high band and (d) speaker coil reactance for the high band, with left-located conductively-coupled speakers.

with a conductively-coupled speaker. For instance, a conductively-coupled Speaker B results in only 10% radiation efficiency degradation in the high band and 5% radiation efficiency degradation in the low band, compared to the antenna-only case. This shows that even without isolation, a non-resonant speaker does not introduce significant impact on the antenna radiation performance. This design concept can be adapted together with the existing design techniques, e.g., RF filtering and controlled voice coil connector length.

7.5 Summary and Proposed Design Guidelines

The antenna-speaker coupling characteristics derived from the simulation and measurement results are summarized as follows:

- A completely isolated speaker (i.e., with negligible M_{fs} and M_{cond}) pose negligible impact on antenna radiation efficiency regardless of the speaker impedance.
- The frequency at which radiation degradation occurs is closely associated with speaker resonance, antenna design and available coupling mechanisms.
- A conductively-coupled or capacitively-coupled resonant speaker could lead to drastic radiation efficiency reduction due to the non-radiative energy stored in the speaker.
- The mutual coupling coefficients (M_{fs} and M_{cond}) can be tuned by varying antenna type and speaker location.
- The speaker resonance frequency can be effectively controlled by adjusting the voice coil connector length.
- By tuning the speaker impedance, a conductively-coupled speaker can be employed with minimum detrimental effect on the antenna radiation performance.

Based on the aforementioned coupling characteristics, practical design guidelines are proposed as follows:

- An isolated (i.e., without conductive or capacitive coupling) speaker should be the priority design goal. This can be achieved by introducing RF filters and removing any potential capacitive coupling sources at the speaker terminals (e.g., PCB ground beneath the speaker pads and audio signal lines).
- A non-resonant speaker due to a properly adjusted speaker impedance can be employed under the capacitive or conductive coupling conditions without any RF filters. The desirable audio frequency response and RF impedance of a speaker can be concurrently achieved within a single speaker structure.

- If capacitive coupling cannot be completely eliminated due to design constraints and speaker resonance is encountered within the antenna operating frequency band, three countermeasures can be applied:
 1. adjust the voice coil connector length.
 2. reposition the speaker.
 3. alter the antenna pattern or employ a different antenna structure.

It should be noted that the audio signal lines can be considered as part of the voice coil connector if the RF chokes are placed at the audio circuitry terminals, instead of the speaker terminals. In this case, adjusting the length of the audio signal lines serves the same purpose as varying the voice coil connector length.

7.6 Conclusion

In this study, the design of an antenna-speaker assembly is investigated through numerical simulations and prototype measurements. Based on the analysis, several critical design parameters are identified. It is concluded that a speaker resonance in the antenna operating frequency band or any potential mutual coupling mechanisms must be prevented to avoid the enhancement of non-radiative RF energy which could lead to the degradation of antenna radiation efficiency. Based on the simulation and measurements results, design guidelines are proposed to achieve optimum antenna radiation performance without compromising speaker audio performance for an antenna-speaker assembly. A cost-effective solution which requires no RF filtering (i.e., less design effort and component counts) is revealed: a conductively-coupled (i.e., speaker terminals directly connected to audio circuitry) non-resonant speaker can be closely integrated with an antenna element with minimum detrimental effect on the antenna radiation performance.

8 Conclusions and Future Work

The research conducted in the framework of this thesis lead to the enrichment of existing knowledge of low frequency exposure safety assessment, cross-frequency component integration and mobile device antenna optimization. For each research topic, the focus is placed on critical open issues which were poorly or inadequately addressed within the literature in the past. Based on the operating frequency range of the investigated wireless applications, the content of this thesis can be structured into the following three research areas:

- Low frequency Electric and Magnetic Field Exposure Safety Assessment
- Mobile Device Antenna Optimization with Network-Distributed Genetic Algorithms
- Analysis and Design of Antenna-Speaker Integration

Being an industrial oriented doctoral thesis, topical issues related to the designs and operations of wireless technologies are investigated with emphasis on the practical applications of computational electromagnetic techniques. The research results presented in this thesis are primarily based on the analyses of complex electromagnetic environments performed on a simulation platform (SEMCAD X) co-developed with our industrial partner Schmid & Partner Engineering AG (SPEAG). The applied numerical techniques (e.g., the SPFE solver for low frequency applications and the FDTD solver for high frequency applications) were integrated in a single software platform to facilitate a smooth transition from one specific application to another. Owing to the advancements in computer processing capability, anatomical model segmentation and electromagnetic computational techniques, realistic models (e.g., a human body) and excitation sources (e.g., a wireless power transfer unit) were analyzed with unprecedented accuracy and complexity. Such technological advancements present an unique opportunity for novel scientific investigations which were absent prior to the work of this thesis. In this chapter, summaries on the original research contributions and future perspectives are presented and discussed.

8.1 Thesis Assessment

Among the various aspects of the investigated wireless applications, the achievements of this thesis can be classified according to the following topics:

Chapter 8. Conclusions and Future Work

- Revision Recommendations for the Existing Low Frequency Exposure Guidelines
- Exposure Safety Analysis for Emerging Wireless Technologies
- Virtual Prototyping of Antenna Optimization in a Complex Design Environment
- Design Guidelines for Cross-Frequency Component Integration

The detail assessments associated with each part are summarized and discussed below.

8.1.1 Recommendations for the Existing Low Frequency Exposure Guidelines

In Chapter 2, the review of existing low frequency exposure guidelines (ICNIRP and IEEE) brought forward several research questions regarding the validity of exposure limits based on outdated dosimetry data (especially for IEEE C95.6-2002 which was established 10 years ago). To ensure that the scientific evidence employed by the aforementioned exposure guidelines stay relevant with the state-of-the-art numerical dosimetry techniques, vigorous analyses were conducted in the current study to provide an up-to-date database for uniform E-field and B-field exposure scenarios.

By investigating simplified canonical models, some of the fundamental induction mechanisms between a human body and external fields are outlined and proven to be critical for the assessment of exposure thresholds. With the analysis of body posture effect on the induced field intensity, an indispensable research foundation is paved for future investigations. Critical revision recommendations are derived for the existing exposure guidelines to achieve scientifically sound exposure limits.

8.1.2 Exposure Safety Analysis for Emerging Wireless Technologies

With the constant development and introduction of new wireless technologies, the demand for novel exposure compliance assessment tailored for specific wireless application is on the rise. To address public concern over the operation safety of one of the emerging low frequency wireless technologies: wireless power transfer (WPT), practical and theoretical analyses of WPT system exposure were conducted.

Through a collaboration with our industrial partners, a commercial close-range WPT unit is investigated for the first time to determine the exposure compliance of such system with respect to the published exposure guidelines. In addition to compliance assessment, the induction characteristics of a human body are derived to facilitate an easy-to-adapt approach which estimates the peak induced field intensity based on known system profiles. Furthermore, the optimum WPT operating frequency range which leads to improved exposure compliance (e.g., additional margin below stimulation or tissue heating thresholds) is determined to equip the wireless power industry with an essential understanding of the frequency-dependence effects. By providing the estimation of the maximum obtainable power in a mid-range WPT

set-up based on exposure limits, this study also leads to a clear baseline for future mid-range WPT implementations in terms of the theoretically achievable power limit with the presence of a human body.

8.1.3 Virtual Prototyping of Antenna Optimization

To accelerate the optimization process of a mobile device antenna design, a computer-aided numerical optimization scheme is favoured by the industry than the traditional empirical optimization approach. To this aim, an antenna optimization approach based on network-distributed generic-algorithms is examined with a detail numerical mobile phone model. By identifying sensitive design parameters and utilizing a networked computer cluster, several internal antenna designs are optimized with the identical goal of achieving OTA/SAR/HAC standard compliance.

The numerical optimization analysis revealed several product development pitfalls, e.g., with an ill-defined antenna structure, concurrent fulfillment of multiple standard requirements become impractical due to the limitations imposed by the radiating mechanisms (e.g., high SAR due to strong RF currents excited on the device chassis). In addition to reviewing the practicability of antenna optimization by virtual prototyping, the research also leads to the characterization of radiation performance based on antenna structural variations. The optimized antenna structure is validated with measurements and the proposed optimization scheme is proven to be superior than empirical approach, i.e., with the possibility of achieving optimization time inversely proportional to the number of employed simulation instances.

8.1.4 Design Guidelines for Cross-Frequency Component Integration

To address a frequently encountered design issue (i.e., radiation degradation) during a mobile device antenna integration process, research is conducted based on a collaboration with industrial partner to derive design guidelines for optimum antenna-speaker integration. The coupling mechanisms between an electro-mechanical coil structure and a small antenna are first determined with simplified and detail speaker coil models. The impacts of speaker coil design and relative speaker location are analyzed with numerical modelling and validated with hardware prototyping.

Based on the simulation results, the precise radiative energy dissipation mechanism, i.e., the concentration of reactive near fields within the voice coil, is identified. Following that, the design parameters responsible for speaker harmonic resonance and inter-component coupling are summarized. The outcome of this research is a systematic design guideline which addresses individual integration stage and provides clear outlines of effective countermeasures in a potentially hostile integration environment. This allows an efficient and cost-effective integration process for antenna-speaker co-existence and optimum radiation performance.

8.2 Perspectives

In this thesis, several aspects of the design and exposure safety of wireless technologies have been addressed. Nevertheless, there are potential improvements and open issues that should be further investigated.

8.2.1 Stimulation Threshold of Biological System

In addition to the revisions recommended in this thesis, other aspects of the published exposure guidelines can be improved. Currently, the scientific evidence of stimulation threshold is based on human volunteer experiments, numerical nerve modelling such as the spatially extended non-linear node model (SENN model) and numerical dosimetry. Further research in the nerve fibre stimulation threshold could be conducted to provide a better understanding of the potential biological effects.

8.2.2 MRI Gradient Coil Peripheral Nerve Stimulation

The adverse biological effects experienced by a patient undergoing magnetic resonance imaging (MRI) scan remains as an important safety issue. In addition to the tissue heating effect (SAR) due to the RF coils, the potential peripheral nerve (and cardiac) stimulation due to the exposure to intensive low frequency gradient fields should also be addressed. Further research is required to understand the impact of gradient coil design and pulse sequence on the stimulation threshold of a target patient.

8.2.3 Reduce the Exposure Level of a Wireless Power Unit

The emerging utilization of wireless power transfer will soon push the application from the conventional low and medium power regime to higher power regime. Hence, the techniques of exposure reduction is expected to be an important research direction with respect to safety compliance. One of the potential solution is to direct the magnetic flux away from an exposed body without affecting the fundamental power coupling mechanisms. Further research should be undertaken to achieve a well balanced received power and induced field ratio.

8.2.4 Alternative Antenna Optimization Algorithms

Besides the Genetic Algorithms examined in this thesis, several alternative optimization schemes should be investigated to understand the optimum choice with regard to specific antenna design requirement. For instance, a gradient-based optimization approach can be applied for optimization refinement after the initial local optimums were determined by GAs.

Bibliography

- [1] ICNIRP, “Guidelines for limiting exposure to time-varying electric, magnetic and electromagnetic fields (up to 300 GHz).” *Health Phys.*, vol. 74(4), pp. 494–522, 1998.
- [2] —, “Guidelines for limiting exposure to time-varying electric and magnetic fields (1 Hz - 100 kHz).” *Health Phys.*, vol. 99, pp. 818–36, 2010.
- [3] *IEEE Std C95.6 Standard for Safety Levels with Respect to Human Exposure to Electromagnetic Fields, 0-3 kHz*, IEEE Standards Coordinating Committee 28 Std., 2002.
- [4] *IEEE Std C95.1 Standard for Safety Levels with Respect to Human Exposure to Radio Frequency Electromagnetic Fields, 3 kHz to 300 GHz*, IEEE Standards Coordinating Committee 28 Std., 1992.
- [5] *IEEE Std C95.1 Standard for Safety Levels with Respect to Human Exposure to Radio Frequency Electromagnetic Fields, 3 kHz to 300 GHz*, IEEE Standards Coordinating Committee 28 Std., 2005.
- [6] T. W. Dawson, K. Caputa, and M. A. Stuchly, “A comparison of 60 Hz uniform magnetic and electric induction in the human body,” *Phys. Med. Biol.*, vol. 42, no. 12, pp. 2319–2329, 1997.
- [7] —, “High-resolution organ dosimetry for human exposure to low-frequency magnetic fields,” *IEEE Trans. Magn.*, vol. 34, no. 3, pp. 708–718, May 1998.
- [8] T. W. Dawson, M. Potter, and M. A. Stuchly, “Accuracy evaluation of modeling of low frequency field interactions with the human body,” *ACES J.*, vol. 16, pp. 162–72, 2001.
- [9] K. Caputa, P. J. Dimbylow, T. W. Dawson, and M. A. Stuchly, “Modelling fields induced in humans by 50/60 hz magnetic fields: reliability of the results and effects of model variations,” *Phys. Med. Biol.*, vol. 47, pp. 1392–1399, 2002.
- [10] P. J. Dimbylow, “Induced current densities from low-frequency magnetic fields in a 2 mm resolution, anatomically realistic model of the body,” *Phys. Med. Biol.*, vol. 43, no. 2, pp. 221–230, 1998.
- [11] —, “Development of the female voxel phantom, NAOMI, and its application to calculations of induced current densities and electric fields from applied low frequency magnetic and electric fields,” *Phys. Med. Biol.*, vol. 50, no. 6, pp. 1047–1070, 2005.

Bibliography

- [12] P. Dimbylow, "Development of pregnant female, hybrid voxel-mathematical models and their application to the dosimetry of applied magnetic and electric fields at 50 Hz," *Phys. Med. Biol.*, vol. 50, pp. 2383–2394, 2006.
- [13] P. J. Dimbylow and R. Findlay, "The effects of body posture, anatomy, age and pregnancy on the calculation of induced current densities at 50 Hz," *Radiation Protection Dosimetry*, vol. 139, pp. 532–538, 2009.
- [14] A. Hirata, K. Wake, S. Watanabe, and M. Taki, "In-situ electric field and current density in Japanese male and female models for uniform magnetic field exposures," *Radiation Protection Dosimetry*, vol. 135, pp. 272–5, 2009.
- [15] A. Hirata, Y. Takano, Y. kamimura, and O. Fujiwara, "Effect of the averaging volume and algorithm on the *in situ* electric field for uniform electric- and magnetic-field exposures," *Phys. Med. Biol.*, vol. 55, pp. 243–252, 2010.
- [16] A. Hirata, Y. Takano, O. Fujiwara, T. Dovan, and R. Kavet, "An electric field induced in the retina and brain at threshold magnetic flux density causing magnetophosphenes," *Phys. Med. Biol.*, vol. 56, pp. 4091–4101, 2011.
- [17] I. Laakso and A. Hirata, "Reducing the staircasing error in computational dosimetry of low-frequency electromagnetic fields," *Phys. Med. Biol.*, vol. 57, pp. N25–N34, 2012.
- [18] J. Bakker, M. Paulides, E. Neufeld, A. Christ, X. Chen, N. Kuster, and G. van Rhoon, "Children and adults exposed to low frequency magnetic fields at the ICNIRP reference levels: theoretical assessment of the induced electric fields," *Phys. Med. Biol.*, vol. 57, pp. 1815–182, 2011.
- [19] M. H. Repacholi and B. Greenebaum, "Interaction of static and extremely low frequency electric and magnetic fields with living systems: Health effects and research needs," *Bioelectromagnetics*, vol. 20, pp. 133–160, 1999.
- [20] R. J. Lamarine and R. A. Narad, "Health risks associated with residential exposure to extremely low frequency electromagnetic radiation," *Journal of Community Health*, vol. 17, no. 5, pp. 291–301, October 1992.
- [21] W. T. Kaune and W. C. Forsythe, "Current densities measured in human models exposed to 60 Hz electric fields," *Bioelectromagnetics*, vol. 6, pp. 13–32, 1985.
- [22] M. J. Hagmann and T. M. Babij, "Noninvasive measurement of current in the human body for electromagnetic dosimetry," *IEEE Trans. Biomed.*, vol. 40, no. 5, pp. 418–423, May 1993.
- [23] M. J. Hagmann, O. P. Gandhi, and C. H. Durney, "Numerical calculation of electromagnetic energy deposition for a realistic model of man," *IEEE Trans. Microw. Theory Techn.*, vol. MTT-27, no. 9, pp. 804–809, September 1979.

- [24] W. T. Kaune, J. L. Guttman, and R. Kavet, "Comparison of coupling of humans to electric and magnetic fields with frequencies between 100 Hz and 100 kHz," *Bioelectromagnetics*, vol. 18, pp. 67–76, 1997.
- [25] S. Ozen, "Low-frequency transient electric and magnetic fields coupling to child body," *Radiation Protection Dosimetry*, vol. 128, no. 1, pp. 62–67, 2008.
- [26] A. Zupanic, B. Valic, and D. Miklavcic, "Numerical assessment of induced current densities for pregnant women exposed to 50 Hz electromagnetic field," *11th Mediterranean Conference on Medical and Biomedical Engineering and Computing*, vol. 16, pp. 226–229, 2007.
- [27] R. Cech, N. Leitgeb, and M. Padiaditis, "Current densities in a pregnant woman model induced by simultaneous elf electric and magnetic field exposure," *Phys. Med. Biol.*, vol. 53, p. 177–186, 2008.
- [28] N. L. R. Cech, "Dosimetric assessment of simultaneous exposure to ELF electric and magnetic fields," *IEEE Trans. Biomed.*, vol. 55, no. 2, pp. 671–674, February 2008.
- [29] W. T. Kaune and M. F. Gillis, "General properties of the interaction between animals and ELF electric fields," *Bioelectromagnetics*, vol. 2, pp. 1 – 11, October 2005.
- [30] A. Barchanski, M. Clemens, H. D. Gersem, and T. Weiland, "Efficient calculation of current densities in the human body induced by arbitrarily shaped, low-frequency magnetic field sources," *Journal of Computational Physics*, vol. 214, p. 81–95, 2006.
- [31] T. W. Dawson, K. Caputa, and M. A. Stuchly, "Magnetic field exposures for UK live-line workers," *Phys. Med. Biol.*, vol. 47, p. 995–1012, 2002.
- [32] M. Taki, Y. Suzuki, and K. Wake, "Dosimetry considerations in the head and retina for extremely low frequency electric fields," *Radiation Protection Dosimetry*, vol. 106, pp. 349–356, 2003.
- [33] C. Gonzalez, A. Peratta, and D. Poljak, "Pregnant woman exposed to extremely low frequency electromagnetic fields," in *16th International Conference on Software, Telecommunications and Computer Networks*, September 2008, pp. 11–15.
- [34] R. Cech, N. Leitgeb, and M. Padiaditis, "Fetal exposure to low frequency electric and magnetic fields," *Phys. Med. Biol.*, vol. 52, p. 879–888, 2007.
- [35] T. W. Dawson, K. Caputa, and M. A. Stuchly, "Electric fields induced in humans and rodents by 60 Hz magnetic fields," *Phys. Med. Biol.*, vol. 47, p. 2561–2568, 2002.
- [36] P. J. Dimbylow, "Current densities in a 2 mm resolution anatomically realistic model of the body induced by low frequency electric fields," *Phys. Med. Biol.*, vol. 45, pp. 1013–1022, 2000.

Bibliography

- [37] M. A. Stuchly and T. W. Dawson, "Interaction of low-frequency electric and magnetic fields with the human body," *Proceedings of the IEEE*, vol. 88, pp. 643–664, 2000.
- [38] M. Stuchly and O. Gandhi, "Inter-laboratory comparison of numerical dosimetry for human exposure to 60 Hz electric and magnetic fields," *Bioelectromagnetics*, vol. 21, pp. 167–174, 2000.
- [39] T. Matsumoto, N. Hayashi, and K. Isaka, "Analysis of induced current density in ellipsoidal human model exposed to concurrent elf electric and magnetic fields with phase differences," *Transmission and Distribution Conference and Exhibition 2002: Asia Pacific. IEEE/PES*, vol. 3, pp. 2343 – 2347, 2002.
- [40] A. Chiba, K. Isaka, Y. Yokoi, M. Nagata, M. Kitagawa, and T. Matsuo, "Application of finite element method to analysis of induced current densities inside human model exposed to 60-hz electric field," *Power Apparatus and Systems, IEEE Transactions on*, vol. PAS-103, no. 7, pp. 1895 –1902, July 1984.
- [41] D. Poljak and Y. F. Rashed, "The boundary element modelling of the human body exposed to the ELF electromagnetic fields," *Engineering Analysis with Boundary Elements*, vol. 26, pp. 871 – 875, 2002.
- [42] S. Benkler, N. Chavannes, and N. Kuster, "FDTD subcell models powering computational antenna optimization," in *The Second European Conference on Antennas and Propagation (EuCAP 2007)*, 2007.
- [43] D. I. Olcan and B. M. Kolundzija, "Adaptive random search for antenna optimization," *IEEE Antennas and Propagation Society International Symposium*, vol. 1, pp. 1114–1117, 2004.
- [44] S. Ooi and D. Thompson, "Antenna optimization technique using parametric analysis with distributed computing," in *The First European Conference on Antennas and Propagation (EuCAP 2006)*, 2006.
- [45] J. H. Holland, *Adaptation in Natural and Artificial Systems : An Introductory Analysis with Applications to Biology, Control, and Artificial Intelligence*. the MIT Press, 1992.
- [46] D. S. Linden, "Using a real chromosome in a genetic algorithm for wire antenna optimization," *IEEE Antennas and Propagation Society International Symposium*, vol. 3, pp. 1704–1707, July 1997.
- [47] J. M. Johnson and Y. Rahmat-Samii, "Genetic algorithm optimization and its application to antenna design," *IEEE Antennas and Propagation Society International Symposium*, vol. 1, pp. 326–329, 1994.
- [48] SEMCAD-X. (2012) Electromagnetic/Thermal Simulation Platform. [Online]. Available: www.semcad.com

- [49] B. S. Yarman, *Design of Ultra Wideband Antenna Matching Networks - Via Simplified Real Frequency Technique*. Springer Science Business B.V., 2008.
- [50] B.-H. Ryou, W.-M. Sung, and D.-S. Lee, "Antenna and speaker assembly and wireless communication device," United States of America Patent US 8 194 906 B2, 2012.
- [51] G. J. Hayes, "Internal antenna and flat panel speaker assembly and mobile terminals including the same," United States of America Patent US 0 024 273 A1, 2005.
- [52] D. Voth and D. Taylor, "Antenna and speaker configuration for a mobile device," United States of America Patent US 7 123 734 B2, 2006.
- [53] K.-S. Kim, I.-S. Baek, and S.-H. Jeong, "Built-in antenna module in portable wireless terminal," United States of America Patent US 0 089 184 A1, 2006.
- [54] Z. N. Chen, *Antennas for Portable Devices*. John Wiley & Sons Ltd, 2007.
- [55] Y.-W. Chi and K.-L. Wong, "Half-wavelength loop strip capacitively fed by a printed monopole for penta-band mobile phone antenna," *Microw. Opt. Technol. Lett.*, vol. 50, pp. 2549–2554, 2008.
- [56] C.-H. Wu and K.-L. Wong, "Internal shorted planar monopole antenna embedded with a resonant spiral slot for penta-band mobile phone application," *Microw. Opt. Technol. Lett.*, vol. 50, pp. 529–536, 2008.
- [57] C.-H. Chang, K.-L. Wong, and J.-S. Row, "Multiband surface-mount chip antenna integrated with the speaker in the mobile phone," *Microw. Opt. Technol. Lett.*, vol. 50, pp. 1126–1132, 2008.
- [58] K.-L. Wong, M.-F. Tu, T.-Y. Wu, and W.-Y. Li, "Small-size coupled-fed printed pifa for internal eight-band lte/gsm/umts mobile phone antenna," *Microw. Opt. Technol. Lett.*, vol. 52, pp. 2123–2128, 2010.
- [59] M.-R. Hsu and K.-L. Wong, "Wwan ceramic chip antenna for mobile phone application," *Microw. Opt. Technol. Lett.*, vol. 51, pp. 103–110, 2009.
- [60] P. Hasgall, E. Neufeld, M. Gosselin, A. Klingenbock, and N. Kuster. (2012, May 30th) IT'IS database for thermal and electromagnetic parameters of biological tissues.
- [61] J. Clarys, A. Martin, and D. Drinkwater, "Gross tissue weights in the human body by cadaver dissection," *Hum Biol.*, vol. 56(3), pp. 459–473, 1984.
- [62] F. Liu, H. Zhao, and S. Crozier, "On the induced electric field gradients in the human body for magnetic stimulation by gradient coils in MRI," *IEEE Trans. Biomed. Eng.*, vol. 50, pp. 804–815, 2003.
- [63] W. R. Adey, "Tissue interactions with nonionizing electromagnetic fields," *Physiological Reviews*, vol. 61, pp. 435–514, 1981.

Bibliography

- [64] M. J. Suess and D. A. Benwell-Morison, Eds., *Nonionizing Radiation Protection*. WHO Regional Publications, European Series, No. 25, 1989.
- [65] J. Michaelis, J. Schüz, R. Meinert, M. Menger, J. P. Grigat, P. Kaatsch, U. Kaletsch, A. Miesner, A. Stamm, K. Brinkmann, and H. Kärner, "Childhood leukemia and electromagnetic fields: Results of a population-based case-control study in Germany," *Cancer Causes and Control*, vol. 8, no. 2, pp. 167–174, March 1997.
- [66] C. Stenlund and B. Floderus, "Occupational exposure to magnetic fields in relation to male breast cancer and testicular cancer: a Swedish case-control study," *Cancer Causes and Control*, vol. 8, no. 2, pp. 184–191, March 1997.
- [67] R. J. Lamarine and R. A. Narad, "Health risks associated with residential exposure to extremely low frequency electromagnetic radiation," *Journal of Community Health*, vol. 17, no. 5, pp. 291–301, October 1992.
- [68] W. R. Adey, "Cell membranes: The electromagnetic environment and cancer promotion," *Neurochemical Research*, vol. 13, no. 7, pp. 671–677, July 1988.
- [69] ICNIRP, "Guidelines for limiting exposure to time-varying electric, magnetic and electromagnetic fields (up to 300 GHz)." *Health Phys.*, vol. 74(4), pp. 494–522, 1998.
- [70] J. P. Reilly, *Applied Bioelectricity: From Electrical Stimulation to Electropathology*. Springer-Verlag New York, Inc, 1998.
- [71] J. P. Reilly and A. M. Diamant, *Electrostimulation: Theory, Applications, and Computational Model*. Artech House, Boston, London, 2011.
- [72] J. P. Reilly and A. M. Diamant, "Spatial relationships in electrostimulation: application to electromagnetic field standards," *IEEE Trans. Biomed.*, vol. 50(6), pp. 783–785, 2003.
- [73] E. L. Carstensen, *Biological Effects of Transmission Line Fields*. Elsevier, New York, 1987.
- [74] *IEEE Recommended Practice for Instrumentation: Specifications for Magnetic Flux Density and Electric Field Strength Meters-10 Hz to 3 kHz*, IEEE Power & Energy Society Std., Rev. IEEE Std 1308-1994, 1995.
- [75] The Visible Human Project. [Online]. Available: http://www.nlm.nih.gov/research/visible/visible_human.html
- [76] A. Christ, W. Kainz, E. G. Hahn, K. Honegger, M. Zefferer, E. Neufeld, W. Rascher, R. Janka, W. Bautz, J. Chen, B. Kiefer, P. Schmitt, H. P. Hollenbach, J. Shen, M. Oberle, D. Szczerba, A. Kam, J. W. Guag, and N. Kuster, "The virtual family project - development of anatomical whole-body models of two adults and two children," *Phys. Med. Biol.*, vol. 55, pp. 23–38, 2010.

- [77] E. Cherubini, N. Chavannes, and N. Kuster, "Realistic skeleton based deformation of high-resolution anatomical human models for electromagnetic simulation," in *the 31st annual meeting of The Bioelectromagnetics Society*, 2009.
- [78] D. Andreuccetti and N. Zoppetti, "Quasi-static electromagnetic dosimetry: From basic principles to examples of applications," *International Journal of Occupational Safety and Ergonomics (JOSE)*, vol. 12, no. 2, p. 201–215, 2006.
- [79] K. Yee, "Numerical solution of initial boundary value problems involving maxwell's equations in isotropic media," *IEEE Trans. Antennas Propag.*, vol. 14, p. 302–307, 1966.
- [80] J. D. Moerlose, T. W. Dawson, and M. A. Stuchly, "Application of the finite difference time domain algorithm to quasi-static field analysis," *Radio Science*, vol. 32, no. 2, pp. 329–341, March-April 1997.
- [81] G. Pelosi, "The Finite-Element Method, Part I: R. L. Courant [Historical Corner]," *IEEE Antennas Propag. Mag.*, vol. 49, no. 2, pp. 180–182, April 2007.
- [82] A. Peratta, C. Gonzalez, and D. Poljak, "Geometrical aspects of 3D human body exposed to extremely low frequency high voltage electric fields. a bem approach." in *International Conference on Software in Telecommunications and Computer Networks*, 2006, pp. 17–21.
- [83] D. M. J. Young, *Iterative Solution of Large Linear Systems*, N. York, Ed. Academic Press, 1971.
- [84] M. R. Hestenes and E. Stiefel, "Methods of conjugate gradients for solving linear systems," *Journal of Research of the National Bureau of Standards*, vol. 49, no. 4, pp. 409–436, December 1952.
- [85] A. F. Stevenson, "Solution of electromagnetic scattering problems as power series in the ratio (dimension of scatterer)/wavelength," *Journal of Applied Physics*, vol. 24, no. 9, pp. 1134–1142, 1953.
- [86] H. Massoudi, C. H. Durney, and C. C. Johnson, "Long-wavelength analysis of plane wave irradiation of an ellipsoidal model of man," *IEEE Trans. Microw. Theory Techn.*, vol. 25, pp. 41–46, 1977.
- [87] F. X. Hart and A. A. Marino, "Elf dosage in ellipsoidal models of man due to high voltage transmission lines," *Electromagnetic Biology and Medicine*, vol. 1, no. 1, pp. 129–154, 1982.
- [88] J. P. Reilly, "Review of icnirp draft: Guidelines for limiting exposure to time-varying electric and magnetic fields (1 to 100 khz)," *The International Committee on Electromagnetic Safety (ICES)*, vol. Document MT 09-123, 2009.
- [89] J. Reilly and A. Diamant, "Spatial relationships in electrostimulation: application to electromagnetic field standards," *IEEE Trans. Biomed.*, vol. 50(6), pp. 783–785, 2003.

Bibliography

- [90] J. A. McGrath, R. A. J. Eady, and F. M. Pope, *Anatomy and Organization of Human Skin, in Rook's Textbook of Dermatology, Eighth Edition*. Wiley-Blackwell, Oxford, UK, 2010.
- [91] T. L. Moore, M. Lunt, B. McManus, M. E. Anderson, and A. L. Herrick, "Seventeen-point dermal ultrasound scoring system - a reliable measure of skin thickness in patients with systemic sclerosis," *Rheumatology*, vol. 42, pp. 1559–1563, 2003.
- [92] S. Neerken, G. W. Lucassen, M. A. Bisschop, E. Lenderink, and T. A. Nuijs, "Characterization of agerelated effects in human skin: A comparative study that applies confocal laser scanning microscopy and optical coherence tomography," *Journal of Biomedical Optics*, vol. 9, pp. 274–281, 2004.
- [93] J. Sandby-Møller, T. Poulsen, and C. Wulf, "Epidermal thickness at different body sites: Relationship to age, gender, pigmentation, blood content, skin type and smoking habits," *Acta Derm Venereol*, vol. 83(6), pp. 410–413, 2003.
- [94] T. Lahtinen, J. Nuutinen, and E. Alanen, "Dielectric properties of the skin," *Phys. Med. Biol.*, vol. 42, pp. 1471–2, 1997.
- [95] C. Gabriel, A. Peyman, and E. Grant, "Electrical conductivity of tissue at frequencies below 1 Mhz," *Phys. Med. Biol.*, vol. 54, pp. 4863–4878, 2009.
- [96] S. Gabriel, R. W. Lau, and C. Gabriel, "The dielectric properties of biological tissues: II. Measurements in the frequency range 10 Hz to 20 GHz," *Phys. Med. Biol.*, vol. 41, pp. 2251–2269, 1996.
- [97] C. Gabriel, "Comments on 'dielectric properties of the skin.'" *Phys. Med. Biol.*, vol. 42, no. 8, pp. 1671–1674, 1997.
- [98] V. Raicu, N. Kitagawa, and A. Irimajiri, "A quantitative approach to the dielectric properties of the skin," *Phys. Med. Biol.*, vol. 45, p. L1–4, 2000.
- [99] E. Marzec and K. Wachal, "The electrical properties of leg skin in normal individuals and in-patients with ischemia," *Bioelectrochem. Bioenerg.*, vol. 49, p. 73–5, 1999.
- [100] A. Karalis, J. Joannopoulos, and M. Soljagic, "Efficient wireless nonradiative mid-range energy transfer," *Annal. Phys.*, vol. 323, no. 1, p. 34–48, 2008.
- [101] A. Kurs, A. Karalis, R. Moffatt, J. D. Joannopoulos, P. Fisher, and M. Soljagic, "Wireless power transfer via strongly coupled magnetic resonances," *Science*, vol. 317, no. 5834, p. 83–86, 2007.
- [102] Q. Yuan, Y. Chen, L. Li, and K. Sawaya, "Numerical analysis on transmission efficiency of evanescent resonant coupling wireless power transfer system," *IEEE Trans. Antennas Propag.*, vol. 58, no. 5, p. 1751–1758, May 2010.

- [103] B. L. Cannon, J. F. Hoburg, D. D. Stancil, and S. C. Goldstein, "Magnetic resonant coupling as a potential means for wireless power transfer to multiple small receivers," *IEEE Trans. Power Electron.*, vol. 24, pp. 1819–1825, 2009.
- [104] S. Cheon, Y.-H. Kim, S.-Y. Kang, M. L. Lee, J.-M. Lee, and T. Zyung, "Circuit-model-based analysis of a wireless energy-transfer system via coupled magnetic resonances," *IEEE Trans. Ind. Electron.*, vol. 58, no. 7, pp. 2906–2914, July 2011.
- [105] M. Kiani, U.-M. Jow, and M. Ghovanloo, "Design and optimization of a 3-coil inductive link for efficient wireless power transmission," *IEEE Trans. Biomed. Circuits Syst.*, vol. 5, no. 6, pp. 579–591, Dec. 2011.
- [106] A. Christ, M. G. Douglas, J. M. Roman, E. B. Cooper, A. P. Sample, B. H. Waters, J. R. Smith, and N. Kuster, "Evaluation of wireless resonant power transfer systems with human electromagnetic exposure limits," *IEEE Trans. Electromagn. Compat.*, vol. PP, pp. 1–10, 2012.
- [107] L. Ilkka, T. Shogo, H. Akimasa, and K. Yoshitsugu, "Evaluation of SAR in a human body model due to wireless power transmission in the 10 MHz band," *Phys. Med. Biol.*, vol. 57, pp. 4991–5002, 2012.
- [108] J. Nadakuduti, M. Douglas, L. Lu, A. Christ, P. Guckian, and N. Kuster, "Compliance demonstration of wireless power transmission systems with respect to human safety limits," *IEEE Trans. Electromagn. Compat.*, vol. submitted, 2013.
- [109] The wireless power consortium. [Online]. Available: <http://www.wirelesspowerconsortium.com/index.html>
- [110] F. W. Grover, *Inductance Calculations Working Formulas and Tables*. Dover Publications, Inc. New York, NY, 1946.
- [111] The consumer electronics association. [Online]. Available: www.ce.org/
- [112] E. Waffenschmidt, "Wireless power for mobile devices," in *Telecommunications Energy Conference (INTELEC), 2011 IEEE 33rd International*, Oct. 2011, pp. 1–9.
- [113] CTIA-Certification, *Test Plan for Mobile Station Over the Air Performance - Method of Measurement for Radiated RF Power and Receiver Performance*, Std., Rev. 2.2.2, 2008.
- [114] *IEEE Recommended Practice for Determining the Peak Spatial-Average Specific Absorption Rate (SAR) in the Human Head From Wireless Communications Devices: Measurement Techniques Amendment 1: CAD File for Human Head Model (SAM Phantom)*, IEEE Std 1528a-2005 (Amendment to IEEE Std 1528-2003) Std., 2006.
- [115] *American National Standards Methods of Measurement of Compatibility Between Wireless Communications Devices and Hearing Aids*, ANSI C63.19-2007, 2007, pp. 1–145 Std.

Bibliography

- [116] G. D. Castillo, C. Mason, N. Chavannes, and M. Okoniewski, "High performance, high accuracy fdtd implementation on gpu architectures," 2010, pp. 2–6.
- [117] F. Nunez, E. Ofli, N. Chavannes, and N. Kuster, "Multi-Goal (S-Parameter, OTA, SAR) Optimization of industrial mobile phones using Genetic Algorithms," in *The Second European Conference on Antennas and Propagation (EuCAP 2007)*, 2007.
- [118] N. Chavannes, R. Tay, N. Nikoloski, , and N. Kuster, "Suitability of fdtd-based tcad tools rf design of mobile phones," *IEEE Antennas Propag. Mag.*, vol. 45, no. 6, p. 52–66, 2003.
- [119] N. Chavannes, R. Tay, F. Nuez, E. Ofli, and N. Kuster, "Virtual prototyping & failure mode and effect analysis (fmea) in industrial design processes on the basis of mobile device terminals," in *The Second European Conference on Antennas and Propagation (EuCAP 2007)*, 2007.
- [120] P. Futter, N. Chavannes, R. Tay, M. Meili, A. Kingenbock, K. Pokovic, and N. Kuster, "Reliable prediction of mobile phone performance for realistic in-use conditions using the fdtd method," *IEEE Antennas Propag. Mag.*, vol. 50, pp. 87–96, 2008.
- [121] N. Fichtner, V. Siart, and P. Russer, "Antenna bandwidth optimization using transmission line matrix modeling and genetic algorithms," *International Symposium on Signals, Systems and Electronics (ISSSE)*, vol. 1, pp. pp.79–82, 2007.
- [122] A. Arkko and J. Rahola, "On the optimization of mobile terminal antenna isolation using the genetic algorithm technique," in *The Second European Conference on Antennas and Propagation (EuCAP 2007)*, 2007.
- [123] T. Taga, *Analysis, Design and Measurement of Small and Low Profile Antennas*, K. Hirasawa and M. Haneishi, Eds. Artech House, 1992.
- [124] C. D. Nallo and A. Faraone, "Multiband internal antenna for mobile phones," *Electronics Letters*, vol. 41, pp. 514–515, 2005.
- [125] C. Gabriel, "Tissue equivalent material for hand phantoms," *Phys. Med. Biol.*, vol. 52, no. 14, pp. 4205–4210, 2007.
- [126] N. Kuster and Q. Balzano, "Energy absorption mechanism by biological bodies in the near field of dipole antennas above 300 mhz," *IEEE Trans. Veh. Technol.*, vol. 41(1), pp. 17–23, 1992.
- [127] X. L. Chen, G. H. Ng, Y. S. Tay, N. Chavannes, and N. Kuster, "A preliminary investigation of miniature loudspeaker high frequency resonance and its impact to antenna radiation performance," in *Antennas and Propagation (APSURSI), 2012 IEEE International Symposium on*, July 2012.
- [128] M. Kiani and M. Ghovanloo, "The circuit theory behind coupled-mode magnetic resonance-based wireless power transmission," *Circuits and Systems I: Regular Papers, IEEE Transactions on*, vol. 59, no. 9, pp. 2065–2074, sept. 2012.

- [129] M. Kiani, U.-M. Jow, and M. Ghovanloo, "Design and optimization of a 3-coil inductive link for efficient wireless power transmission," *Biomedical Circuits and Systems, IEEE Transactions on*, vol. 5, no. 6, pp. 579–591, dec. 2011.
- [130] S. Cheon, Y.-H. Kim, S.-Y. Kang, M. L. Lee, J.-M. Lee, and T. Zyung, "Circuit-model-based analysis of a wireless energy-transfer system via coupled magnetic resonances," *Industrial Electronics, IEEE Transactions on*, vol. 58, no. 7, pp. 2906–2914, july 2011.
- [131] H. Chattha, Y. Huang, M. Ishfaq, and S. Boyes, "Bandwidth enhancement techniques for planar inverted-f antenna," *Microwaves, Antennas Propagation, IET*, vol. 5, no. 15, pp. 1872–1879, 9 2011.
- [132] L. Zhu, Y. Qi, M. Corrigan, K. Bandurska, and Y. T. Man, "Mobile wireless communications device having improved antenna impedance match and antenna gain from RF energy," United States of America Patent US 0 223 597 A1, 2006.
- [133] M.-S. Choi, C.-K. Lee, and W.-I. Do, "Method construction for reducing interference between antenna and peripheral device," United States of America Patent US 0 088 542 A1, 2012.
- [134] Z. D. Liu, P. S. Hall, and D. Wake, "Dual-frequency planar inverted-f antenna," *IEEE Trans. Antennas Propag.*, vol. 45, no. 10, pp. 1451–1458, 1997.
- [135] C. Di Nallo and A. Faraone, "Multiband internal antenna for mobile phones," *Electronics Letters*, vol. 41, no. 9, pp. 514–515, April 2005.



Curriculum Vitae

Chen Xi Lin

Singapore Address	Switzerland Address
28 Bukit Batok East Ave 2, #12-16	101 Bederstrasse, Zurich
Singapore 659921	Switzerland 8002
SG +65 68969221	CH +41 798621086
gaxchen@yahoo.com	xilin.chen@epfl.ch

SUMMARY

Electrical engineer with 8 years of industrial and academic experience in electromagnetic applications related to antenna design, EM compatibility design, EM and bio-EM exposure assessment analysis. Strong hands-on experience, excellent problem solving skills and comfortable working in multi-tiered teams.

EDUCATION

Ph.D Electrical Engineering 2010 - October 2013
Swiss Federal Institute of Technology (Lausanne), EPFL, Switzerland

Focus on antenna optimization, electromagnetic exposure assessment (e.g., magnetic resonant wireless power transfer and bio-compatible wireless device design).
Doctoral Thesis: Multidisciplinary Electro-Magnetic-Compatibility Analyses: Optimized Antenna Integration and Low-Frequency Bio-Electromagnetic Assessment.

M.Sc Hardware for Wireless Communications 2003 - 2004
Chalmers University of Technology, CTH, Gothenburg, Sweden

Focus on hardware design for wireless communications (Ericsson Research Lab)
Master Thesis: The Design of an Ortho-mode Transducer for Reflector Antenna.

B.Eng (Hons) Electrical Engineering 1999 - 2003
National University of Singapore, NUS, Singapore

Major in electrical and electronic engineering.
Final Year Project: Direction of Arrival (DoA) Estimation based on MUSIC (Multiple Signal Classification) Algorithm.

EXPERIENCE

Senior Application Engineer 2010 - present
Schmid and Partner Engineering AG (SPEAG), Zurich, Switzerland

- Responsible for the development of novel wireless technologies with an emphasis on bio-medical applications, e.g., near-field sensor, exposure assessment, bio-compatible antenna and electromagnetics computational tools.
- Provide training and technical support for electromagnetic applications, e.g., mobile phone, on-body and implantable antenna designs, customized computational tools and virtual prototyping of commercial wireless products.
- Concurrently undergoing an industrial sponsored doctoral study in *the Laboratory of Electromagnetics and Acoustics (LEMA), Swiss Federal Institute of Technology (Lausanne), EPFL, Switzerland*.

Research Assistant 2008 - 2010
The Foundation for Research on Information Technologies in Society, Swiss Federal Institute of Technology (Zurich), ETHZ, Switzerland

- Completed various research projects in the field of bio-compatible antenna design, exposure assessment for emerging wireless technologies (e.g., wireless power transfer), cross-frequency component integration for mobile devices, implant safety and exposure compliance of bio-medical applications (e.g., magnetic resonance imaging (MRI) and transcranial magnetic stimulation (TMS)).

Antenna/RF Engineer

2005 - 2008

Motorola Electronics Pte Ltd, Singapore

- Product engineer for commercial mobile phone antenna and RF designs.
- Provide novel antenna solutions, antenna feasibility analysis, SAR/OTA/HAC assessments for new product development.
- Experienced with numerical simulation and practical prototype mock-up for multi-band antenna systems.
- Responsible for the antenna designs of Motorola Rokr E8, Slvr L7, L6.
- Inventor of a U.S. Patent (US 20080272970) on multiple-resonance antenna structure, familiar with patent generation and application procedures.
- In charge of anechoic chamber and SAR laboratory in terms of system maintenance and calibration.

SKILLS**Languages**

Fluent in English and Mandarin (mother tongue).

SoftwareMatlab, Ansoft HFSS, CST Microwave Studio, XFDTD, SEMCAD-X, Feko, Agilent ADS, AWR Microwave Office, Optenni, \LaTeX , Python, Microsoft Office.**Hardware**

Network Analyzer, Anechoic Chamber, Dosimetry Assessment System (DASY5), Spectrum Analyzer, Signal Generator, Power Amplifier, Soldering Station, Base Station Emulator (CMU).

PATENT

U.S. patent (US 20080272970) Communications Assembly and Antenna Radiator Assembly.

List of Publications

JOURNAL PUBLICATIONS

1. X.L. Chen, E. Ofli, Y.S. Tay, N. Chavannes, N. Kuster, "A Novel Approach for Mobile Device Design: GA-Based Distributed Optimization to Comply with OTA, SAR, and HAC Standards," *IEEE Antennas Propag. Mag.*, vol.54, no.1, pp.22-31, Feb. 2012 (Feature Article).
2. X.L. Chen, S. Benkler, N. Chavannes, V. De Santis, J. Mosig, N. Kuster, "Analysis of Human Brain Exposure to Low-Frequency Magnetic Fields: a Numerical Assessment of Spatially Averaged Electric Fields and Exposure Limits," *Bioelectromagnetics*, (published online ahead of printing on Feb 2012).
3. J. Bakker, M. Paulides, E. Neufeld, A. Christ, X.L. Chen, N. Kuster, G. van Rhoon, "Children and Adults Exposed to Low Frequency Magnetic Fields at the ICNIRP Reference Levels: Theoretical Assessment of the Induced Electric Fields," *Phys. Med. Biol.* 57, 1815-182, 2012.
4. X.L. Chen, Y.S. Tay, N. Chavannes, J. Mosig, N. Kuster, "Analysis and Design of Mobile Device Antenna-Speaker Integration for Optimum Over-the-Air Performance," *IEEE Antennas Propag. Mag.*, (submitted).
5. X.L. Chen, A.E. Umenei, V. De Santis, N. Chavannes, J. Mosig, N. Kuster, "Human Exposure to Close-Range Resonant Wireless Power Transfer Systems as a Function of Design Parameters," *IEEE Trans. Electromagn. Compat.*, (submitted).
6. V. De Santis, M. Douglas, J. Nadakuduti, S. Benkler, X.L. Chen, N. Kuster, "Assessment of the Induced Fields produced by Therapeutic Magnetic Field Mats," *Bioelectromagnetics* (submitted).
7. V. De Santis, X.L. Chen, I. Lakkso, A. Hirata, "On the Issues Related to Compliance of LF Pulsed Exposures with Safety Standards and Guidelines," *Phys. Med. Biol.* (submitted).

CONFERENCE PUBLICATIONS

1. X.L. Chen, E. Ofli, N. Chavannes, N. Kuster, "Simulation Platform for Electromagnetic Optimization of Wireless Environments," *Antennas and Propagation (APS/URSI), 2013 IEEE International Symposium on*, 8-14 July 2013.
2. X.L. Chen, A.E. Umenei, J. Taylor, N. Chavannes, N. Kuster, "User Hand Exposure Assessment of a Highly Resonant Power Transfer System," *Antennas and Propagation (APS/URSI), 2013 IEEE International Symposium on*, 8-14 July 2013.
3. X.L. Chen, Y.S. Tay, N. Chavannes, N. Kuster, "Numerical Analysis of a Detailed Moving-Coil Speaker Model for Antenna-Speaker Integration," *Antennas and Propagation (EuCAP), 2013 7th European Conference on*, 8-12 April 2013.
4. X.L. Chen, N. Chavannes, G.H. Ng, Y.S. Tay, N. Kuster, "A Preliminary Investigation of Miniature Loudspeaker High Frequency Resonance and its Impact to Antenna Radiation Performance," *Antennas and Propagation (APS/URSI), 2012 IEEE International Symposium on*, 8-14 July 2012.
5. X.L. Chen, E. Ofli, M. Fuetterer, M. Minana, N. Chavannes, N. Kuster, "Computational Platform for Multidisciplinary Electromagnetic Simulations," *Antennas and Propagation (APS/URSI), 2012 IEEE International Symposium on*, 8-14 July 2012.
6. X.L. Chen, V. De Santis, N. Chavannes, N. Kuster, "Computation of *in situ* Electric Field in the Brain during Transcranial Magnetic Stimulation," *Electromagnetic Compatibility (APEMC), 2012 Asia-Pacific Symposium on*, pp.369-372, 21-24 May 2012.
7. X.L. Chen, N. Kuster, Y.C. Tan, N. Chavannes, "Body Effects on the GPS Antenna of a Wearable Tracking Device," *Antennas and Propagation (EuCAP), 2012 6th European Conference on*, pp.3313-3316, 26-30 March 2012.
8. X.L. Chen, N. Kuster, Y.C. Tan, N. Chavannes, "The Design of a Miniature Antenna for Wi-Fi Enabled Memory Card," *Antennas and Propagation (APS/URSI), 2011 IEEE International Symposium on*, pp.1215-1218, 3-8 July 2011.
9. X.L. Chen, S. Benkler, C.H. Li, N. Chavannes, N. Kuster, "Low Frequency Electromagnetic Field Exposure Study with Posable Human Body Model," *Electromagnetic Compatibility (EMC), 2010 IEEE International Symposium on*, pp.702-705, 25-30 July 2010.
10. X.L. Chen, E. Ofli, N. Chavannes, N. Kuster, "Optimization of Mobile Phone Antennas using Generic Algorithms and Network Parallelization," *Antennas and Propagation (APS/URSI), 2010 IEEE International Symposium on*, pp.1-4, 11-17 July 2010.